The Abrasive Wear of Plasma Sprayed Nanoscale Tungsten Carbide-Cobalt (WC-Co)

Graham A. Tewksbury
B.A., Lawrence University, Appleton, Wisconsin, 1995

A dissertation submitted to the faculty of the
OGI School of Science & Engineering
Oregon Health & Science University
in partial fulfillment of the
requirements for the degree
Doctor of Philosophy
in
Materials Science and Engineering

June 2002

The dissertation "The Abrasive Wear of Plasma Sprayed Nanoscale Tungsten Carbide-Cobalt (WC-Co)" by Graham A. Tewksbury has been examined and approved by the following Examination Committee:

Dr. David Atteridge
Thesis Advisor
Director Laboratory Science
Columbia Basin College

Dr. Milton Scholl
Associate Professor
OGI School of Science & Engineering
Oregon Health & Science University

Dr. Jack McCarthy
Assistant Professor
OGI School of Science & Engineering
Oregon Health & Science University

Dr. Jack Devletian
Professor
Portland State University

Dr. Martin Becker
Professor Emeritus
OGI School of Science & Engineering
Oregon Health & Science University

Acknowledgments

I would like to acknowledge the support and patience of a number of individuals. First and foremost, my advisor, Dr. D. G. Atteridge whose advice, guidance and patience made this endeavor possible. I would also like to thank the members of my committee for their time and helpful advice. Myself and anyone who reads this thesis owes a debt of gratitude to Roxanne Workman for her efforts in making this document appear as it does.

I would also like to thank Jim Young at Environmental Molecular Science Laboratories for his help with the FESEM.

Table of Contents

List of Figures

List of Tables

ABSTRACT

The Abrasive Wear of Plasma Sprayed Nanoscale Tungsten Carbide-Cobalt (WC-Co)

Graham A Tewksbury

Ph.D.
OGI School of Science & Engineering
Oregon Health & Science University
June 2002

Thesis Advisor: Dr. David Atteridge

Thermal spray coatings composed of a variety of carbide sizes and cobalt contents were sprayed with a high energy plasma spray system. The size of the carbides used fell into three rough groupings, micrometer scale carbides (1-2 μm), submicrometer (700-300 nm), and nanoscale ($\approx$100 nm). The feedstock powder was evaluated in terms of their size distribution, external morphology, internal morphology, and initial carbide size. Two different fixtures were used in spraying to evaluate the effect of cooling rate on the wear resistance of the coatings. The microstructures of the sprayed coatings were examined using optical metallography, SEM, FESEM, TEM, XRD and chemical analysis. The coatings were evaluated in low stress abrasive wear by the ASTM G-65 Dry Sand Rubber Wheel test. Furthermore, the porosity and hardness of the coatings were evaluated. The cobalt content was found to be the predominant influence on the wear rate of the coatings. The decrease in the carbide size was not found to effect the wear rate of the coatings. Coatings sprayed on the 'hot' fixture were found to have slightly improved wear resistance as compared to coatings sprayed on the 'cold' fixture. The wear rates of the coatings were found to be a function of the WC/Co volume ratio.

The Abrasive Wear of Plasma Sprayed Nanoscale Tungsten Carbide-Cobalt (WC-Co)

1.0 INTRODUCTION

Thermal spray coatings can be used to modify the surfaces of materials. Through the use of sprayed coatings it is possible to have combinations of material properties that might not otherwise be possible. In general, the mechanical strength and fracture toughness are being provided by the substrate while the coating provides protection against environmental degradation processes including wear, corrosion, erosion, biological or thermal attack. Through the use of coatings it is possible to improve the resistance of the base material to surface degradation, thereby extending service life, reducing down time, frequency of repairs, and the need for replacement parts. One of the common properties that coatings are used to modify is wear resistance. One of the most common coating materials used for wear resistance is tungsten carbide-cobalt (WC-Co). A recent development in WC-Co materials has been the reduction of the size of the carbides to the nanoscale. This reduction in carbide size has the potential to substantially improve the properties of the composite. This study focuses on the abrasive wear resistance of plasma sprayed coatings containing different carbide sizes and cobalt contents.

1.1 Introduction to Materials

The tungsten carbide-cobalt (WC-Co) system was originally developed in Germany during the early 1920's by Schroter [1, 2]. Powders of tungsten carbide and cobalt were mixed and dense parts prepared by compacting and heating the mixture above the melting point of the binder. Today the majority of the composite is still prepared by liquid phase sintering. The WC-Co materials have been used in a variety of applications, most well known is the use in wear coatings and cutting tools. For most applications WC-Co is sintered from a green ceramic to a near net shape.

The success of the system is due in part to near perfect wetting of the WC particles by the cobalt binder phase in liquid phase sintering [1]. Considerable research has been undertaken to improve the properties of this system. This effort has focused on either the altering of the matrix [3-8] or the WC grain size [9-13] to maximize the relevant properties of the composite. While there has been a considerable amount of research on WC-Co, much has been focused on sintered structures. Nanoscale grains have been shown to have higher strengths and hardness then the same materials with larger grains as predicted by the Hall-Petch equation[14-22]. This increase in the strength and hardness of the material will result in improved abrasion resistance [23].

1.1.1 Formation of WC

Tungsten carbide (WC) melts incongruently and therefore cannot be produced by melting, as shown in Figure 1.1. The preferred way to produce WC is the reaction of pure tungsten powder with carbon black of low ash content. The tungsten powder used in cemented carbide technology is usually produced by the reduction of the tungsten trioxide, tungsten hydratic acid (H_2WO_4) blue tungsten oxide (W_4O_{11}) or ammonium paratungstenate ($5NH_3 \bullet 12WO_3 \bullet 5H_2O$). Coarse and polycrystalline WC Powders (particle size >2 μm) are obtained from coarse tungsten powders (>6 μm) at relatively high carburization temperatures of about 1600°C, while fine and essentially monocrystalline WC of less than 1um in size is produced from submicrometer W powders at 1350-1400°C.

The Nanodyne™ process [11-13] by which nanoscale carbides are produced is a spray conversion process. This is fundamentally different from the conventional reduction processes mentioned previously. The essential process is comprised of three unit operations: an aqueous solution mixing operation in which the final composition of the powder is established; a spray drying which converts the aqueous precursor solution to an easily fluidized solid solution powder having good flow characteristics; and a gas/solid reaction operation that converts the precursor powder to a nanostructured WC-Co powder in a high temperature fluidized bed reactor.

The first step in the process, mixing and aqueous solution, determines the final composition of the powder. Early production relied on compound formation to achieve the atomic scale mixing of the tungsten and the cobalt that was desired. For example, the chemical compound $Co(en)_3WO_4$ where en= ethlenediamine, was precipitated from the solution and used as a precursor to form nanostructured WC-23Co powder. The discovery that amorphous solid solutions could be created allowed the WC-Co to be prepared in non-stoichiometric ratios. The range of attainable cobalt percentages is 3% to 30% but for most practical applications the cobalt contents from 6% to 18% are produced. [11]

The activity of the carbon is controlled in the final step of the process, a gas/solid carburization reaction, by varying the potential of the CH_4/H_2 gas environment in the fluidized bed and by controlling the reaction temperature. It is possible to control the WC+ β Co composition by controlling the carbon activity.

1.1.2 Properties of WC

There are a number of other carbides that could be used instead of WC in a cemented carbide. Table 1.1 shows the relative hardness of various carbides. It is clear that WC (2200HV) is not as hard as TiC (3000HV) or VC (2900HV). Even though other carbides are harder, WC-Co is used in more than 90% of all cemented carbide applications [1]. The properties of a variety of carbides is shown in Table 1.1. The most significant property of WC is its high elastic modulus, which at 696 GPa is almost double that of the other carbides. Tungsten carbide's high modulus of elasticity combined with it's ability to undergo plastic deformation at room temperature, as well as the near perfect wetting with Co, make WC the best compromise.

Tungsten carbide's crystalline structure is a simple hexagonal lattice of tungsten atoms with the carbon atoms located either at 1/3, 2/3, and 1/2 positions or at 2/3, 1/3, and 1/2. The c/a ratio is nearly one (a=0.29065 nm, c=0.28366 nm). An analysis of the slip traces around hardness indentations in single crystal WC indicated that the slip planes are of the {1100} type with slip directions of <1120>, <1123> and <0001>. These slip systems and a number of others have been observed in TEM studies.[1, 24-28] Unit dislocations with Burgers vectors <0001>, 1/3<1120> and 1/3<1123> have all been observed and claimed to be glissible on a number of different planes.

1.1.3 Phase Diagrams of WC

The phase diagrams are a necessary starting point for an understanding of the phase composition of the coatings. The phase diagrams show the narrow range of phase stability of the WC + Co region, as well as some of the other possible phases that might occur due to the decarburization of the WC, (Figures 1.2-1.4). These isopleths show the very narrow range of carbon contents in which WC-Co can be obtained from melting.

In general the phases that are seen in the sprayed material are on the carbon deficient side of the isopleth. The width of the phase field for 6% Co is 44.6-45.2 at.%C at its maximum. The boundaries at 10 wt% Co are 41.4-42.4 at.%C. The boundaries for the 16wt% Co are 37.5 to 38.1 at.%C. The region of interest in the binary phase diagram is the WC+L phase field which transforms to WC + Co. In this narrow range it is possible to perform liquid phase sintering and yield a structure that has only WC and Co. Excess carbon results in formation of graphite. Carbon deficiency results in formation of the eta phase, W_2Co_4C. In general, all the carbon deficient phases are of the form M_6C or $M_{12}C$. The exact ratio of W to Co and C will vary based on processing of the material.

The isopleths (Figures 1.2-1.6) focus on the narrow range of phase stability of WC for cobalt weight percentages that are relevant to work done in the thesis. Furthermore the WC-Co isopleth, Figure 1.5, gives a much broader view of the regions of phase stability complementing the individual Co wt% isopleths.The C-Co-W ternary diagram at 1800°C shows the solid solubility limits of WC in cobalt at high temperature, which is particularly relevant to the plasma spray process (Figure 1.7).

1.1.4 Cobalt

Cobalt exists in one of two phases, either a fcc with a lattice parameter of a = 0.35447 nm, or as a hcp structure with parameters of a = 0.2505 nm and c = 0.4060 nm. The equilibrium structure of cobalt at room temperature is hexagonal close packed, with the hcp to fcc phase transformation occurring at 422°C [24]. However, the amount of hcp cobalt which forms on cooling from a high temperature fcc is dependent on the purity and grain size of the starting material; impure cobalt and/or large cobalt grains will inhibit the fcc to hcp reaction from going to completion. Subsequent deformation of the fcc material below 390°C will push the reaction to completion. In the WC-Co composite the cobalt binder shows an increase in flow stress with the addition of C and W which appears to be more important than the fcc/hcp ratio in determining strength. The increase in the flow stress of the binder was about 100 MN m^{-2} for each 1.0 atomic% addition of either W or C [24].

1.1.5 The Rule of Mixtures

One way to evaluate the properties of a composite material is through the rule of mixtures. This rule states that the properties of the composite will be a mix of the properties of the individual components. This is frequently used in polymer matrix composites (PMC) and is just as applicable to metal matrix composites (MMC). A statement of the rule of mixtures based on the hardness of the WC-Co System would be as follows, where HV is hardness in vickers and V_f is volume fraction:

$$HV_{\text{comp}} = HV_{\text{matrix}} * V_{f\,\text{matrix}} + HV_{\text{reinforcement}} * V_{f\,\text{reinforcement}} \qquad (1)$$

One of the assumptions of the rule of mixtures is a perfect interface between matrix and reinforcement. While this assumption works well in the homogenous sintered materials, sprayed coatings are inhomogeneous and do not always have perfect interfaces, especially between splats. To accurately model the properties of the sprayed composite it would be necessary to include several other phases such as porosity and oxides, and the effects of the various interfaces.

A number of researchers have attempted to relate the hardness of the composite to grain size and volume fraction [29, 30]. The Vickers hardness of the composite could be determined by the following equation where H_{wc} and H_{co} are the in-situ hardness of the WC and cobalt phases respectively, V_{wc} is the volume fraction of the carbide grains and C is a contiguity factor:

$$H_v = H_{wc} F_{wc} + H_{co}(1 - V_{wc} C) \tag{2}$$

In a sintering operation there are two parameters that are important that are not generally considering in plasma sprayed applications. These parameters are contiguity and binder mean free path. In order to be able to reference the data that has been collected over the years for the sintered product it is necessary to understand some of the parameters that are important in the sintered product even though they are not generally considered for the thermally sprayed product.

At this time there are no articles on thermal spraying that have looked at the parameters which are frequently considered to be the controlling factors in determining the physical properties of the cemented carbides. These assumptions make it necessary to understand the parameters and how they relate to sintered and sprayed material. This information makes it possible to use of the vast body of information on the sintered product. The contiguity of the sample is determined by a mean linear intercept method. Contiguity is defined as follows, where N_{aa} is the number of carbide/carbide interfaces intersecting a unit length test line, and N_{ab} is the carbide/matrix interfaces:

$$C = \frac{2N_{aa}}{2N_{aa} + N_{ab}} \tag{3}$$

Binder mean free path is defined as the following, where d is the grain size of the carbide particle, V_b is the volume fraction of the binder phase, and C is the coefficient of contiguity:

$$BMF = \frac{d\,V_b}{(1-V_b)(1-C)} \tag{4}$$

1.1.6 Sintered Nanoscale Material

The nanometer size of the WC grains increases the solubility as well as the diffusivity of the WC in the cobalt matrix [22]. In some small regions the cobalt matrix has been found to be amorphous [32]. The alloy strengthened binder phase, combined with the small carbide grain size gives the sintered nanostructured WC-Co composites high hardness with high fracture toughness. This has implications on the behavior of a WC-Co microstructure under abrasive wear conditions.

The abrasion resistance of the conventional materials increases linearly with the hardness; while that of the nanostructured materials is higher than predicted by hardness alone [33]. To a first approximation, the wear abrasive resistance increases linearly with the hardness of the materials. Departures from this were observed in the sense that the sliding wear rate increases with the higher WC content and larger grain size [34]. The sliding wear resistance of conventional sintered WC-Co composite depends on cobalt content and grain size of the composite [34]. In a conventional sintered WC-Co, wear occurs on a very small scale and no conventional fracture, plastic deformation or uprooting of carbide grains is observed. Jia proposed a mechanism for nanoscale WC-Co in which material is removed by dislocations sliding across the carbide grains followed by the removal of the material at the steps on the surface created by the emerging dislocations [32]. There has been considerable TEM work done on WC which helps to explain this proposed mechanism. Jia theorized that these observations explained the formation of steps on wear surface of the nanoscale WC grains.

In the conventional sintered WC-Co there is a noticeable improvement in the sliding wear resistance of the composite when the grain size of the WC is large. In sliding wear, it has been observed that the cobalt matrix can be worn away from the surface and the sides of the grains and still hold the particles if the grains are large enough. A rough, not quite connected, surface of WC is presented to the wearing surface. Larger carbides and lower cobalt contents create a surface which is predominantly WC, protecting the Co matrix.

The cobalt mean free path is the predominant microstructural parameter in the abrasion process of sintered nanoscale WC-Co. The mechanism for the abrasive wear of the composite is dominated by the removal of the binder material. Fragmentation or uprooting for the carbide grains is the second step in the abrasion process. In low stress abrasion there was no indication of how the binder was removed; while under high stress abrasion evidence of binder extrusion was observed [32]. Under abrasive conditions, Jia concluded that decreasing the carbide grain size is more effective in increasing the wear resistance than lowering the cobalt content. The nanoscale WC-Co retained very good surface uniformity in the process of surface plastic deformation which significantly enhances the high stress abrasion resistance by decreasing the material extrusion and carbide fragmentation. The move to the nanoscale has at least two positive effects: one is reducing the material removal by carbide fracture and the second is the increase in the resistance to microfracture of the nanoscale carbide relative to a conventional carbide.

1.2 Sintered vs. Thermally Sprayed Nanoscale WC-Co

All of the work by Jia and Fischer involved sintered WC-Co, therefore extrapolating to thermally sprayed coatings would be difficult. One of the important differences between sintering and spraying are the temperatures involved and the time spent at temperature. It is difficult to retain the nanoscale grain size of the WC during sintering. Fang and Eason, on the effects of sintering on the nanostructured material, indicate that most of the particles are less the 200 nm in size though occasionally there are WC particles as large as 600 nm [12]. The driving force for densification of the nanoscale material is approximately 20 times higher than in the conventional material.

Furthermore, they found that even after an extremely short time (five minutes) there had already been a significant increase in the nominal size of the WC grains. They theorized that the process by which this growth was taking place was coalescence; where WC grains that are in contact reorient themselves and when their grain boundaries match, the grain boundary moves through the grains.

Grain growth can be limited through the use of VC additions to the material. VC slows down the growth of the WC grains so that they only reach their thermodynamically stable size during sintering. The exact mechanism for this inhibition of growth is not known, though it is assumed that VC interferes with the alignment of the WC grains.

The plasma spray process allows these thermodynamic limitations on minimum grain size to be avoided due to the very short time that the material is at temperature. Another important consequence of the short time at temperature is that a large portion of the matrix is amorphous. Only a small portion of the matrix is amorphous in the sintered material. While in thermally sprayed WC-Co coatings the matrix ranges from partially to completely amorphous [35, 36] there does not seem to be enough peak broadening in the XRD spectra to indicate that the amorphous material is common in sintered WC-Co [32]. The amorphous regions are reported to be approximately 43% W unlike the rest of the matrix which has approximately 20% W dissolved in it.

In thermal spraying, the molten cobalt dissolves the smaller WC grains and becomes supersaturated with W and C. In the literature on thermal spraying, there is a significant body of work that recognizes the incidence of nanometer size particles that are developed as a result of the spraying. It has been assumed that these extremely small crystals are the result of the dissolution of the smaller carbides in the cobalt during the spraying process and then precipitation of the small WC particles during solid state cooling. The exact composition of these very small particles is not known, though it is assumed that they are one of the W-Co-C compounds [37].

Many of the principles which govern how sintered cermets behave are not applicable to the thermally sprayed coatings since the two differ greatly in terms of micro-composition and microstructure. Furthermore, the exact mechanism by which thermally sprayed WC-Co coatings are formed is not clearly understood, and there have been many different theories proposed. It can be stated, however, that the final coating will probably have suffered carbon loss during the deposition process and will likely contain phases which were not present in the starting powder [38].

One of the fundamental differences between the sintered and the sprayed coating (in terms of their microstructure), are the WC/WC interfaces. Sintered WC-Co with high values of Contiguity (C) may have a continuous interlinked network of WC grains. This network is often referred to as a skeleton and as such represents an important load bearing element in the structure. It is now generally accepted from TEM studies that WC/WC interfaces exist in the sintered material [25]. Not every WC particle takes part equally in the skeleton structure and it has been proposed that the sintered material is comprised of a partially connected structure with the number of grains participating in the long range continuous network being determined by the product of CV_{wc}.

1.3 Effects of the Nanoscale Carbides on the Cobalt Matrix

The Hall-Petch relationship for metals predicts an increase in hardness as the grain size decreases. This relationship has been shown to work well for metals with grain sizes in the millimeter range. The applicability of this relationship to ceramics and nanoscale materials has been questioned [39]. The Hall-Petch relationship would predict that a reduction in grain size would substantially increase the hardness of the cobalt matrix. The data on Ni-W electrodeposited alloys indicates that there is a minimum size for the strengthening effects of the Hall-Petch relationship [39]. As grain size decreases, the percentage of the grain that is in the grain boundary increases. Some researchers indicate that the size of the grain boundary increases significantly in nanoscale grains. In nanoscale grains, the grain properties are governed by the properties of the grain boundary and not the grains themselves. Thus grain boundary slip should become the major means of deformation at small sizes. There is a minimum grain size, below which, an inverse Hall-Petch relationship is observed. The increase in the intercrystalline volume is so large at nanoscale grain sizes that it swamps out the strengthening effect of the small grains. The hardness of very small grains could be predicted by the following: (and shown graphically in Figure 1.8 for Equations 6-8)

$$H_{cal} = V_f^{tj} H_{tj} + (1 - V_f^{tj}) H_{HP} \qquad (5)$$

$$V_f^{ic} = 1 - \left[\frac{(d - D)}{d} \right]^3 \qquad (6)$$

where:

$$V_f^{gb} = \frac{3D(d-D)^2}{d^3} \tag{7}$$

$$V_f^{tj} = V_f^{ic} - V_f^{gb} \tag{8}$$

d = grain diameter

D = grain boundary thickness

H_{HP} = the hardness predicted by Hall-Petch

tj = triple junction

ic = intercrystalline

gb = grain boundary

Part of the reason for the drive to understand nanoscale grains are the properties predicted by the Hall-Petch relationship. Lee and Gurland [30] originally investigated the relationship between the Hall-Petch relationship and the rule of mixtures as it might apply to sintered WC-Co. Equations 10 and 11 predict the hardness of the WC and Co. They can be substituted into Equation 9 to calculate a theoretical hardness based on the grain size of both WC and Co. In these equations an important parameter in calculating the hardness of the Co is not the grain size but the cobalt mean free path. In the sintered material it is assumed that the actual grain size of the cobalt will be on the order of a millimeter. The hardening effects of the cobalt are due to the constraint of the carbides rather than the true grain size.

$$H_c = H_{wc}V_{wc}C + H_m(1 - V_{wc}C) \tag{9}$$

$$H_{wc} = 1382 + 23.1d^{-1/2} \tag{10}$$

$$H_m = 304 + 12.7\lambda^{-1/2} \tag{11}$$

C = contiguity
d = grain size (mm)
λ = cobalt mean free path

Milman, et al. have expanded on this work to include submicrometer and nanoscale WC grains as well as temperature effects [40, 41]. The focus of their work was the observed decrease in hardness with increasing temperature which they approximated by a Hall-Petch type relationship. They reported that up to about 600°C, the decrease in hardness with increasing temperature appears to be mostly due to a decrease in the intrinsic hardness of the individual phases. Above 600°C the decrease in hardness appears to be mostly due to easier slip transfer across grain boundaries. Finer grained alloys (0.6 μm), have been found to preserve their hardness at high temperature better than coarser grained alloys (2.6 μm). Equations 12-17 were used by Milman et al. to calculate the hardness of the WC-Co composites. Equation 12 shows the hardness of the composite as it was effected by grain size.

$$H = H_0 + K_y d^{1/2} \tag{12}$$

$$H_0 = H_{wc}V_{wc}C + H_m(1 - V_{wc}C) \tag{13}$$

$$K_y = K_{wc}V_{wc}C + K_m(1 - V_{wc}C)B^{-1/2} \tag{14}$$

Where,

V = volume fraction

C = contiguity

K = material specific hardness factor

H = hardness

m = matrix

$$B = \frac{1 - V_{wc}}{V_{wc}(1 - C)} \tag{15}$$

Milman, et al.[40] found that the contiguity factor did not change much with carbide size but changed with the cobalt fraction. This provides a simplifying assumption that allows

$$\lambda = B \cdot d \tag{16}$$

Where ,

$$B = \frac{1 - V_{wc}}{V_{wc}(1 - C)} = 0.28 \tag{17}$$

The simplifying assumption in Equation 17 works for the data gathered by Milman. Other studies have found the value for B to be between 0.2-0.4. The value of the simplifying assumption in Equation 17 is that it allows an easy comparison between cobalt mean free paths for materials with different carbide sizes. It should also be noted that the calculated values for cobalt mean free path tend to differ from the measured values.

The estimation of cobalt mean free path does not take into account processing variables and due to this tends predict cobalt mean free paths that are smaller then the measured values. To be certain of cobalt mean free path it is necessary to measure it for the sample in question.

1.4 Thermally Sprayed WC-Co

Thermal spray is a broad category of coating application techniques. Some of the similarities between the techniques are that they all involve high temperatures which are used to cause partial or full melting in the feedstock and some kind of accelerating gas jet. The feedstock can be liquid, powder or wire or some combination of all three. The molten or partially molten feedstock material is accelerated towards the substrate, where it is quickly quenched to a solid. These molten or partially molten of material tend to pancake out before solidification and form thin nominally circular deposits and are generally referred to in the literature as 'splats'. Splat formation after droplet impingement onto the substrate surface has important influence on the development of the structure and properties of the sprayed coating [42, 43]. Coating-substrate adhesion is most strongly influenced by splat formation [44-46]. Depending on the cooling rate and whether the splat is a single phase material or a multiphase material, the grains in the splats themselves will either be columnar or cellular [47, 48]. Entrained gases, unmelted and oxidizes particles, and voids are mixed with the particle splats and between splats, and tend to degrade the coating properties because they provide points of stress concentration during surface loading that will act as crack initiation centers [49]. Particles with sizes substantial larger than the mean size do not melt completely to their core and thus do not spread appreciably on impact. In their wake porosity can build up as well as trains of other only partially melted particles. This porosity will detrimentally effect the mechanical properties of the coating [50, 51]. Particles with sizes substantially smaller then the mean size may be vaporized in flight, or undergo other unwanted transformations due to overheating.

Specific thermal spray techniques vary greatly in their temperature ranges, velocities and deposition rates. For the deposition of WC-Co coating two techniques are most frequently used, plasma spray and high velocity oxygen fuel (HVOF). Plasma spray runs at a much higher temperature than HVOF, with plume temperatures of 15,000°K versus 3,200°K [49, 52].

The spray system that is used in this research is a high energy plasma system. Like all plasma spray systems the heat source is an arc generated thermal plasma where the plume reaches temperatures in excess of 15,000°K. It differs from conventional air plasma systems in that it has a much greater gas flow rate and is capable of much higher velocities. This reduces particle dwell time in the plume and presumably limits degradation of the feedstock. The velocity range of the plume is high subsonic to Mach 3. The resultant coating structure of the plasma spray process is governed by kinetics and not thermodynamics. The reason for this is the high cooling rate of the molten feedstock, which is on the order of 10^6 C per second. This results in the feedstock material being at temperature for extremely short times even though the plume is at a very high temperature.

1.5 Wear of thermal sprayed coatings

The vast majority of the literature on the wear of WC-Co coatings involved the coatings being sprayed with the HVOF process. This means that the bulk of the literature on the wear of thermal sprayed coatings is not directly applicable to plasma sprayed coatings. However, the trends that the various authors discuss provide background and context to better understand the plasma sprayed coatings.

Usamani, et al. reported that the ideal grain size of the WC particles varies for different wear regimes for sprayed WC-Co [10]. Fine grain sizes provide the best combination of hardness and toughness for relatively hard grades, however for soft grades the opposite is true. Sampath, et al. has reported that a decrease in the carbide size in the starting powder leads to an increase in the carbide decomposition [48]. A finer carbide size distribution in the starting powders leads to an increase in the W_2C phase in the coating. Coatings with finer carbides show higher hardness and lower indentation fracture toughness. This trend is similar to a trend observed in conventional sintered WC-Co cermets.

The abrasion resistance of the sprayed coating is dominated by the fracture toughness of the coating as opposed to its hardness. Sampath, et al., came to the conclusion that the abrasion resistance of the coating followed an inverse trend with hardness, which is the opposite of the trend observed in sintered WC-Co [48]. The reasons for this inversion of the traditional hardness wear resistance trend was the greater anisotropy and decomposition in the sprayed coatings.

Under sliding wear conditions carbide size was found to have only a minor effect. Coatings with the fine carbide grain size distributions fractured primarily by matrix crack propagation with minimum "tortuosity." The fracture in coatings with large carbides occur by propagation of cracks at the carbide/matrix interface and into the carbide. Most of the cracks were observed to initiate at pores or on the interface.

The binder phase has been reported by various authors to be amorphous, nanocrystalline, or microcrystalline [37, 53-55]. The differences in the crystallinity of the binder phase are probably due to differences in the cooling rate of the different coatings.

The amorphous and nanocrystalline resulting from the higher cooling rate and the microcrystalline binder phase resulting from a lower cooling rate. The degree of crystallinity in the binder may also be dependent on the amount of W and C dissolved in the binder phase.

1.6 Carbide Degradation

There are three major mechanisms for the degradation of the carbide, two involving decarburization and a third involving oxidation. Decarburization is a high temperature reaction and would only be occurring in the plume during spraying. The high velocity of the high energy plasma spray system decreases dwell time of the powder in the plume to a few tenths of a millisecond [56]. It has been shown that substantial decarburization still occurs.

In the thermal spray process it is common to develop carbon deficient phases in the coatings that were not present in the starting powder. The following reactions are some of the suggested steps in the decarburization of WC [56].

$$2WC \rightarrow W_2C + C \tag{18}$$

$$W_2C + O \rightarrow W_2(C,O) \tag{19}$$

$$W_2(C,O) \rightarrow 2W + CO \tag{20}$$

Or

$$4Co + 4WC + O_2 \rightarrow 2Co_2W_4C + 2CO \tag{21}$$

$$3Co + 3WC + O_2 \rightarrow Co_3W_3C + 2CO \tag{22}$$

$$12Co + 12WC + 5O_2 \rightarrow 2Co_6W_6C + 10CO \tag{23}$$

The first three reactions are thought to only occur on the surface of the particle. These reactions proceed at a very slow rate until liquid WC is present. The second three reactions are diffusion limited and occur primarily in the presence of liquid Co and solid WC. The melting and boiling points of the materials are such that a significant loss of Co could also occur when the powder is heated sufficiently to melt the carbide. These two reactions result in different types of compounds being formed in the coating. The first set of reactions (Eq. 18-20) will result in the presence of W in the coating. The second set of reactions (Eq. 21-23) would result in the formation of one of the eta carbides. In both reactions, oxygen plays a significant role.

The work by Khan compares the phase decomposition of WC-Co when sprayed by air plasma spray (APS) and vacuum plasma spray (VPS) [54]. The APS had significant amounts of decarburization with W_2C, W, and η phases present. Whereas, the VPS showed no traces of W_2C or W in the coating. This suggests that oxygen plays a role in decomposition of the carbide during spraying.

Jarosinski concluded that finer carbides produced coatings with higher hardness and lower surface roughness [57]. Jarosinski also concluded minimization of carbide degradation and maximization of fine carbides in the coating were mutually exclusive.

Usmani thought that the WC grain size strongly effected the kinetics of dissolution during spraying, and thus strongly effect the nature of the resulting microstructure; i.e. large carbides tend to undergo less decomposition during spraying than fine carbides [10].

Wang, et al. stated that the use of air cooling increased the decarburization in the spraying of WC-Co powders with plasma or detonation gun [58]. The decarbonization seems to occur mostly during and after the powders in the flame strike the substrate. The increase in the decarburization due to air cooling indicates that at least some of the decarburization is occurring on the substrate after the splats have landed.

1.7 Oxidation of WC

While decarburization occurs in the plume at high temperatures, WC can also be decomposed through a lower temperature oxidative mechanism. There are two stable oxides WO_2 and WO_3, with WO_3 being the most stable at room temperature and pressure. Roebuck, et al. showed the potential for oxidation of the WC particles [59-62]. It was found by Roebuck et al. that the temperature of oxidation of the carbides was related to the size of the carbides. The isochronal experiments showed oxidation of the WC particles at temperatures as low as 390°C for submicrometer carbides. Roebuck calculated a decreasing activation energy for the oxidation reaction as a carbide size was reduced [60]. However, it seems more likely that the decrease in reaction temperature was actually related to the increased surface area of the carbides. Table 1.2 shows the relative increase in the surface area of the carbides as the size of the carbides are reduced.

The oxidation reaction of the WC to WO_3 is shown by the following equation:

$$2WC + 5O_2 \rightarrow 2WO_3 + 2CO_2 \qquad (24)$$

Other investigations on the oxidation behavior of WC and WC-Co have focused on the presumed upper temperature limit due to oxidation at 500°C. Nolan, et al. discuss the oxidation of WC-Co coatings at 450°C in air [63]. Webb, et al. suggested that at higher temperatures the oxidation rate for WC can be greater than that of W (700°C-1000°C). Warren noted at temperatures of over 400°C there is a marked increase in the thickness of the oxide film [64]. Tungsten-Carbide (WC) had a thinner oxide layer at low temperatures due to its covalent bonding. Warren's data indicates that WC slowly oxidizes in water and the oxide on the sample's surface breaks down revealing a fresh layer of WC. Test results of the water used in the experiment showed significant traces of W, which indicates that the WO was dissolving and not being regenerated by the solution.

1.8 Heat Treatments of WC-Co

There have been a number of studies that examined the effect of heat treatment on the sprayed WC-Co composite. These studies are useful for two reasons; heat treatments can be used to improve the properties of the coatings, and, as noted by Roebuck, it is possible through rapid cooling to suppress the development of certain phases [24]. The heat treatment studies will give insight into some of the phases that were suppressed due to the rapid quenching of the coatings.

A variety of different heat treatments have been studied. Some of the post spray heat treatments that have been investigated were heat treatments in inert atmospheres [37, 65, 66], vacuum annealing [36, 67, 68], flame heating, and laser remelting [68] [37]. Guo claimed that of all the treatments possible, vacuum heat treatment had the greatest effect on the properties in terms of the highest density, strongest bond, and lowest residual stress.

Work by Nerz compared WC-12Co coatings sprayed with HVOF and high energy plasma using DTA. They found that there was a strong exothermic reaction in the coatings at 853°C for HVOF coatings and 860°C for high energy plasma sprayed coatings. Since the feedstock did not exhibit this exotherm, they concluded that this reaction was due to the recrystallization of the binder phase. Chemical analysis of the coatings revealed that both of the coatings contained the same percentage of carbon, though XRD revealed that there had been more decarburization of the carbides in the high energy plasma sprayed coating. There was also a reduction in the percentage of cobalt in the high energy plasma sprayed coating; this was thought to be caused by the greater temperature involved in the high energy plasma spraying process. XRD after DTA showed the presence of large amounts of eta carbides and a recrystallized matrix.

Li, et al. performed DTA and DSC of sprayed WC-18Co [37]. The DTA work showed exothermic reactions at 671°C and 831°C while the DSC showed a reaction occurring at 600°C. They argued that the lower exothermic reaction in the DTA investigation corresponded with the DSC results and was attributed to the recrystallization of the amorphous binder phase even though a very fast scanning rate of 4°/minute was used. After the annealing at 600°C, XRD showed that the diffuse diffraction halo was no longer present. It is also interesting to note that both free carbon and eta carbide were present in the same sample. The eta carbide and the free carbon are on opposite sides of the WC phase field in the phase diagram. The presence of both is either a fluke or indicates that there is a great deal of local inhomogeneity in the samples. This is not unexpected in a sample generated with a thermal spraying technique but is a testament that the system is very complex and that mutually exclusive phenomena can be occurring in a sample in different locations at the same time. The exotherm at 831°C was thought to be the reaction of the cobalt with the W and C to form the eta carbide. They argued that the 853°C exotherm reported by Nerz was not a recrystallization but a compound formation reaction.

The differences in the work done by Nerz and Li may be due to the different annealing times that they used. Nerz used times ranging from five minutes to one hour while Li annealed for six hours. Nerz commented that the recrystallization was temperature and time dependent and so differences are not unexpected.

Schweke, et al. annealed HVOF coatings at 400°C, 500°C, 600°C, 700°C, and 800°C for one hour and studied the changes in the microstructure and hardness [66]. Both Schweke and Li found that heat treatment between 600°C and 800°C resulted in the formation of $M_{12}C$, and the transformation of M_6C to $M_{12}C$. They also noted that W and WC precipitated in the matrix. The peak hardness of the coatings was achieved after annealing at 600°C.

Stewart performed vacuum annealing heat treatments of HVOF coatings containing micron and submicrometer carbides at 250°C, 550°C, 600°C, 800°C, and 1100°C. The heat treated coatings showed improvement in the wear resistance, even at temperatures as low as 250°C, which resulted in a 35% improvement in the wear resistance over a conventional coating. The nano-WC-Co coating did not show an improvement in the wear resistance until 600°C. Stewart related this to the precipitation of eta carbides. Furthermore it was found that the maximum hardening of the coatings was achieved at 600°C as well as maximum improvement in wear resistance [69]. No phase change occurred before 600°C according to the XRD results, however, after 600°C there was a reduction in the intensity of the amorphous halo and new peaks corresponding to Co_6W_6C appeared. The nanocarbides also showed greater decomposition of the WC and subsequent decarburization during flight in spraying. The decomposition reaction was more pronounced in the nano-WC-Co due to the small size of the carbides. Stewart concluded that while the nanoscale carbides improved the sintered material, the greater decomposition of the carbides in thermal spraying resulted in the loss of those improvements.

1.9 Abrasive Wear

Abrasive wear can be divided into two body and three body wear processes. The terms high stress and low stress abrasion are used as further classification. In high stress abrasion, the abrasive particles are crushed during the process, in low stress abrasion these particles do not fracture. Abrasive wear resistance is not an intrinsic property of the material, but depends on tribological system [70, 71]. Misra and Finnie have shown that many variables affecting abrasive wear resistance are the same for two body and three body abrasion [72]. With increasing depth of indentation of the abrasive particles, the volume properties of the wearing material becomes increasingly important. The abrasives themselves have several factors which are used in evaluating the type of abrasive; these are hardness, acuteness, shape, size, and wear resistance [71].

For this study only three body low stress abrasive wear was evaluated. Even in this very specific wear process there are a number of variables: relative hardness of the abrasive to the surface, the shape of the abrasive, (sharp or rounded) and the size of the abrasive. ASTM-G65, the recommended dry-sand-rubber-wheel (DSRW) abrasion test procedure, specifies the use of 50-70 Ottowa silica sand and specifies the load at which the tests should be performed. However, different researchers have studied the effects of changing some of these variables.

Stewart performed a series of modified DSRW tests in which the abrasive type, abrasive size, and load were varied [69]. The materials tested were HVOF sprayed WC-Co with micron and submicrometer carbide sizes. He found that the wear rate increased with an increase in abrasive size and load. Alumina and silica were used as abrasives, with the alumina found to cause greater wear than the silica. Larsen-Basse suggested that the WC-Co cermets exhibited a scale effect [73]. If the hardness of the WC is taken as 2400 HV and the harness of the cobalt as 125 HV then, depending on the exact composition, the cermet may have a hardness in the range of 800-1500HV.

The hardness value which determines whether a specific abrasive acts as hard or soft abrasives becomes dependent on the size of the area of contact between the abrasive and the cermet. For example, under low loads and fine grit sizes, an individual abrasive grain will be in contact with only one or, at most, a few carbide grains at a time. Under conditions of a larger abrasive size and greater load , the bulk hardness of the composite becomes the controlling factor because now the contacting surface includes a substantial number of carbide grains. Therefore, it is possible that a medium hardness abrasive like Al_2O_3 can be either a hard or a soft abrasive depending on size and loading conditions.

The mechanisms involved in the three body abrasive wear situation depends on whether it is hard or soft abrasion. In the hard abrasive case, mass removal is high and the material is removed by plastic extrusion from grooves formed in the surface. In the soft abrasive case, wear rates are much lower and a different mechanism is in operation; the binder is preferentially removed leaving carbides unsupported to crack and fall out. In soft abrasion, the binder extrusion is the rate controlling step and the wear rate can be related to the binder free path [73].

1.10 Equal Pressure vs. Equal Wear

Khruschov and Babichev published some of the earliest research relating abrasive wear resistance to the structure of heterogeneous materials [74]. Their results showed a linear relationship between the wear resistance and the volume fraction of hard phase present. Khruschov concluded that abrasive wear resistance of heterogeneous materials was the sum of the phases volume fraction multiplied by that phase's abrasive wear resistance. In later work Khruschov noted that his wear relationship significantly overpredicted the wear resistance of ceramic-containing composites [75]. Garrison concluded that Khruschov's rule was valid when wear is proportional to load and was not valid for conditions when wear is proportional to pressure [76].

The equal wear (EW) and equal pressure (EP) theory is based on proposed micromechanisms involved in the wear process and results in two equations expressing linear and inverse rule of mixtures [77-79]. The two wear modes, EW and EP, constitute upper and lower limits of the wear resistance of a composite or a multiphase material, provided that assumptions of the model are fulfilled [78]. The two models relate the distribution of the load across the phases to the wear rate. The equal pressure process is defined as the condition in which each phase is loaded uniformly. The equal wear process is defined as the condition in which both phases wear at the same linear rate with the reinforcement phase carrying the greater portion of the load. The micromechanisms that this derivation is based on provides insight into the wear of multiphase materials, which are worn in the equal wear mode, produce flat wear scars, each phase has been worn the same amount. Materials that worn in the equal pressure mode produce a rough wear surface where the harder phase stands out above the surface of the matrix. Materials that are worn in the equal pressure mode tend to be strongly influenced by the matrix properties of the composite. A small increase in the properties of the matrix can result in a significant increase in the wear resistance. The wear of sprayed coatings has been shown to follow at least some version of Archard's wear equation which states that an increase in load increases the wear rate. Archard's wear equation is stated in equation 25, and restated in equation 26 in terms of the load specific wear rate. Equation 27 is Khruschov's wear equation, restated in terms of load specific wear resistance.
Equation 28 is the equal pressure equation in which each phases of the composite is loaded equally.

Archard's wear equation

$$\frac{dV}{dS} = K\frac{L}{H} \tag{25}$$

Where V is the volume loss caused by wear, S is the sliding distance, L is the load, and H is the hardness of the worn material. K is a material constant that depends on the wear system and the material being worn, k is K/H or the load specific wear rate, Ω is the load specific wear resistance or 1/k, and A is the nominal contact area,

or

$$\frac{dV}{dS} = kL \tag{26}$$

for EW for multiphase materials:

$$\frac{dV}{dS} = \frac{LA}{\sum_i (A_i \Omega_i)} \tag{27}$$

while for EP for multiphase materials:

$$\frac{dV}{dS} = \frac{L}{A}\sum_i \frac{A_i}{\Omega_i} \tag{28}$$

Figure 1.9 shows the relationship between Eqs. 27 and 28.

The WC-Co coating worn with DSRW tester is going to be in the EP mode several reasons: 1) the size of the reinforcement is much smaller than the wearing particle, 2) three body abrasive wear with a compliant rubber wheel allows conformity of the surfaces, and 3) unfragmented reinforcing particles may be removed as a part of larger wear debris and, since they are removed without direct contact against the abrading particles, they have no practical effect on the wear resistance for the matrix or the load distribution. When the matrix surrounding the reinforcing phase is removed by wear, the particles are gradually exposed to higher stresses and gradually receive diminished support from the matrix. At some point the particles either fracture or loosen and subsequently are easily removed from the surface.

The wear of sprayed coatings have been shown to follow at least some version of Archard's wear equation which states that an increase in load increases the wear rate. Archard's and Khruschov's wear equations work best for monolithic heterogenous materials. Wayne and Sampath developed a relationship for wear in abrasive and erosive conditions specifically for sprayed coatings [9, 31]. In this equation, K_{1c} is the indentation fracture toughness, H is hardness and Vf_{Co} is the volume fraction of cobalt:

$$\text{Wear resistance} = (K_{1c}^{3/8} H^{1/2})(\frac{Vf_{Co}}{1\text{-}Vf_{Co}}) \tag{29}$$

This equation provides a means for assessing the wear resistance of sprayed WC-Co coatings intended for industrial applications requiring abrasion and erosion resistance. The indentation fracture toughness (IFT) is determined through the following equation, where H is the Knoop microhardness (GPa) under a 10-Kg load, D is the diagonal for the Vickers indentation (micrometer), and Cl is the total crack length:

$$IFT = \frac{(0.113HD^{1/2})}{(1+Cl/2D)^{3/2}} \tag{30}$$

1.11 Conclusions

The use of nanoscale carbides open new opportunities in thermal sprayed WC-Co, as well as presents new challenges. The nanoscale material has the potential to significantly enhance the properties of the coating. However, due to their small size, the carbides would also be more prone to diffusion controlled degradation. The optimism that accompanies any new material must be tempered with the knowledge of previous materials and where constraints lie. Nanoscale materials do offer new opportunities for improvement in properties but they are still governed by the same basic laws. To evaluate the effect of the nanoscale carbides on the abrasive wear of WC-Co a combination of carbide sizes of cobalt contents were sprayed using the high energy plasma spray system. These coatings were evaluated using the dry sand rubber wheel abrasion test to measure the effect of change of cobalt composition and carbide size.

Table 1.1. Some properties of refractory carbides used in cemented carbides.

Carbide	**Crystal Structure**	**Melting Point (°C)**	**Nominal carbon content (wt%)**	**Microhardness HV (50g)**	**Modulus of elasticity GN m^{-2}**
TiC	fcc	3100	20.05	3000	451
ZrC	fcc	3400	11.64	2700	34
HfC	fcc	3900	6.30	2600	352
VC	fcc	2700	19.08	2900	422
NbC	fcc	3600	11.45	2000	338
TaC	fcc	3800	6.23	1800	285
Cr_2C_3	orthorombic	1800	13.33	1400	373
Mo_2C	hexagonal	2500	5.89	1500	533
WC	hexagonal	2800	6.13	(0001) 2200 (1010) 1300	696

Table 1.2. Increase in surface area of carbides as size decreases for a constant volume of carbide.

Carbide Size	**Relative surface area**
1 µm	1 µm^2
250 nm	16 µm^2
100 nm	100 µm^2
10 nm	10,000 µm^2

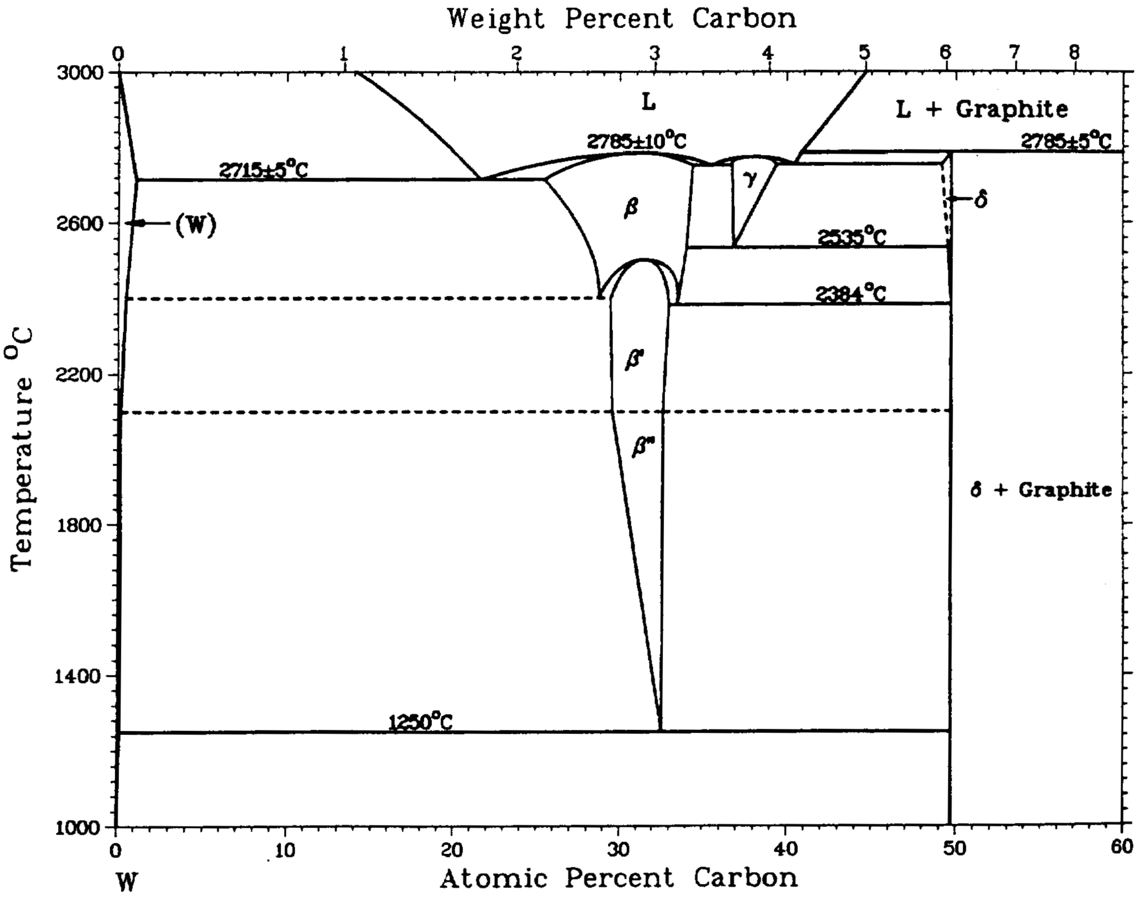

Figure 1.1. Binary phase diagram of W-C [80]. Reprinted with permission from ASM International.

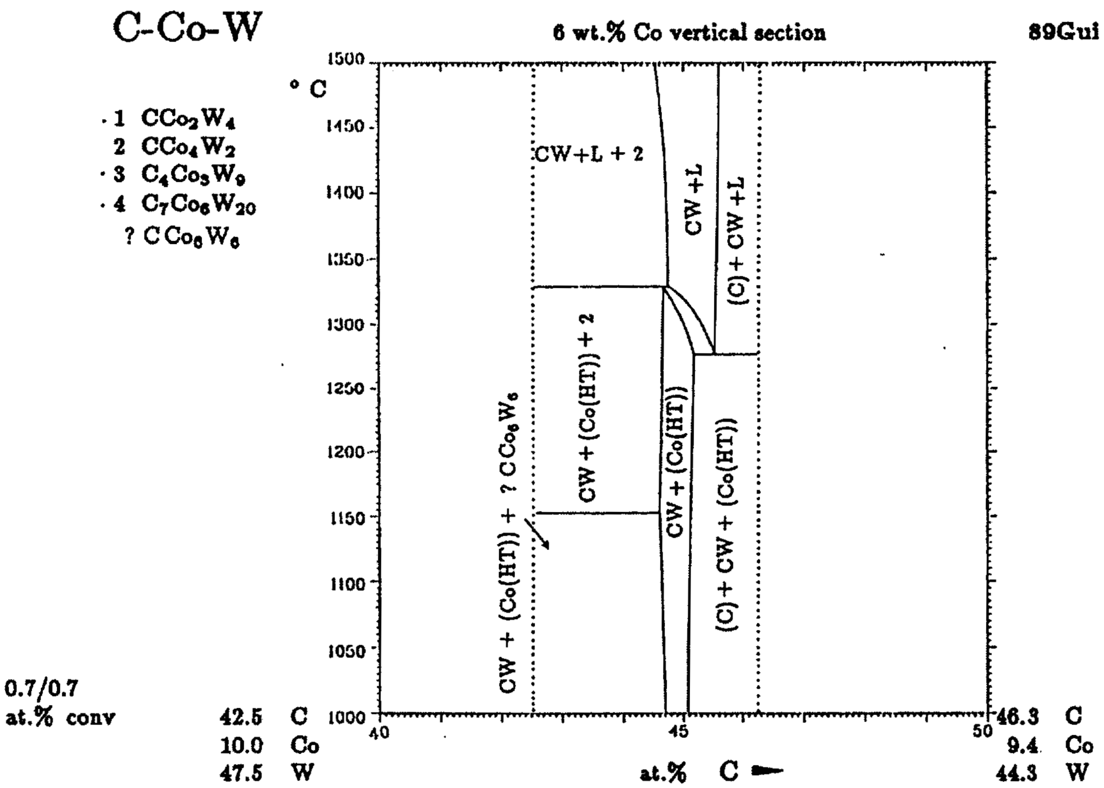

Figure 1.2. Isopleth of WC-Co at 6 wt% Co [81]. Reprinted with permission from ASM International.

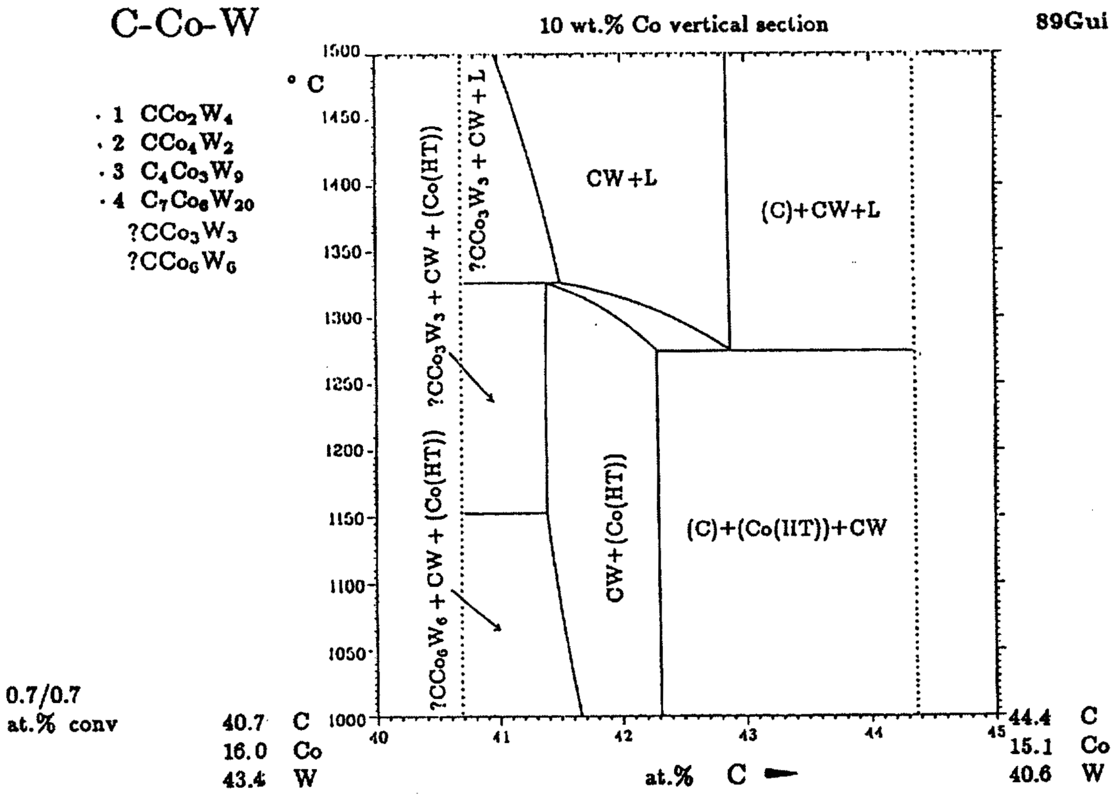

Figure 1.3. Isopleth of WC-Co at 10 wt% Co [81]. Reprinted with permission from ASM International.

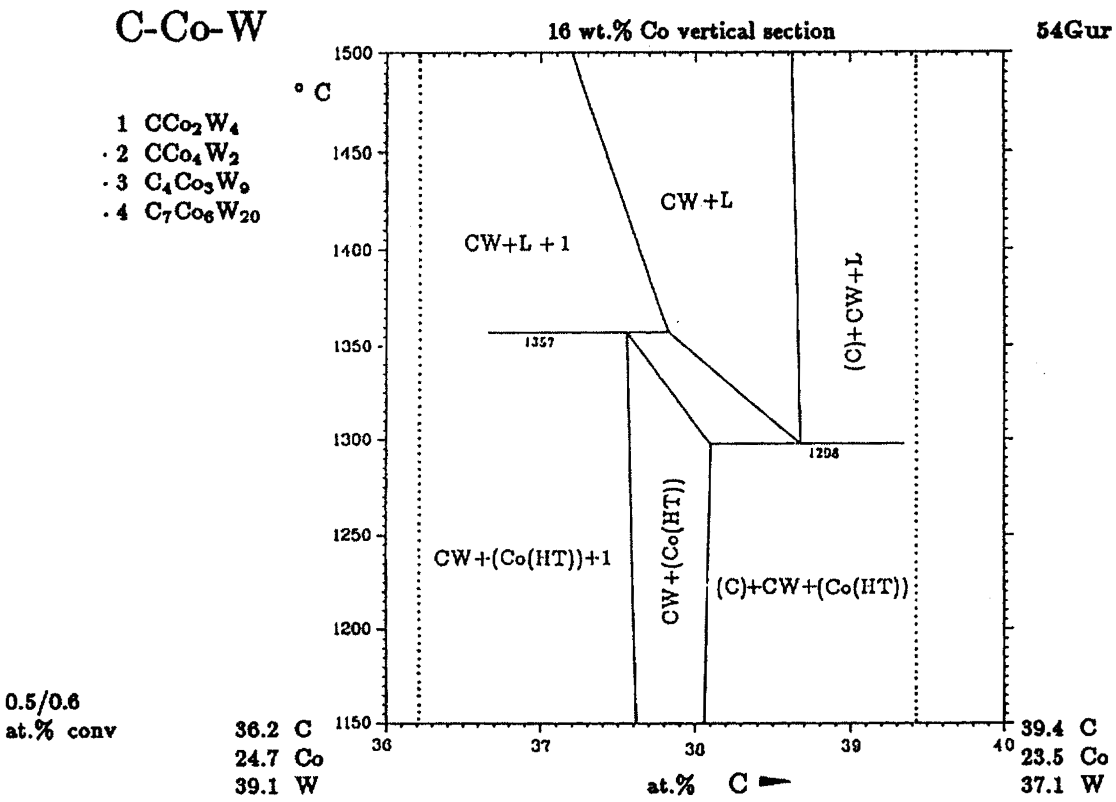

Figure 1.4. Isopleth of WC-Co at 16 wt% Co [81]. Reprinted with permission from ASM International.

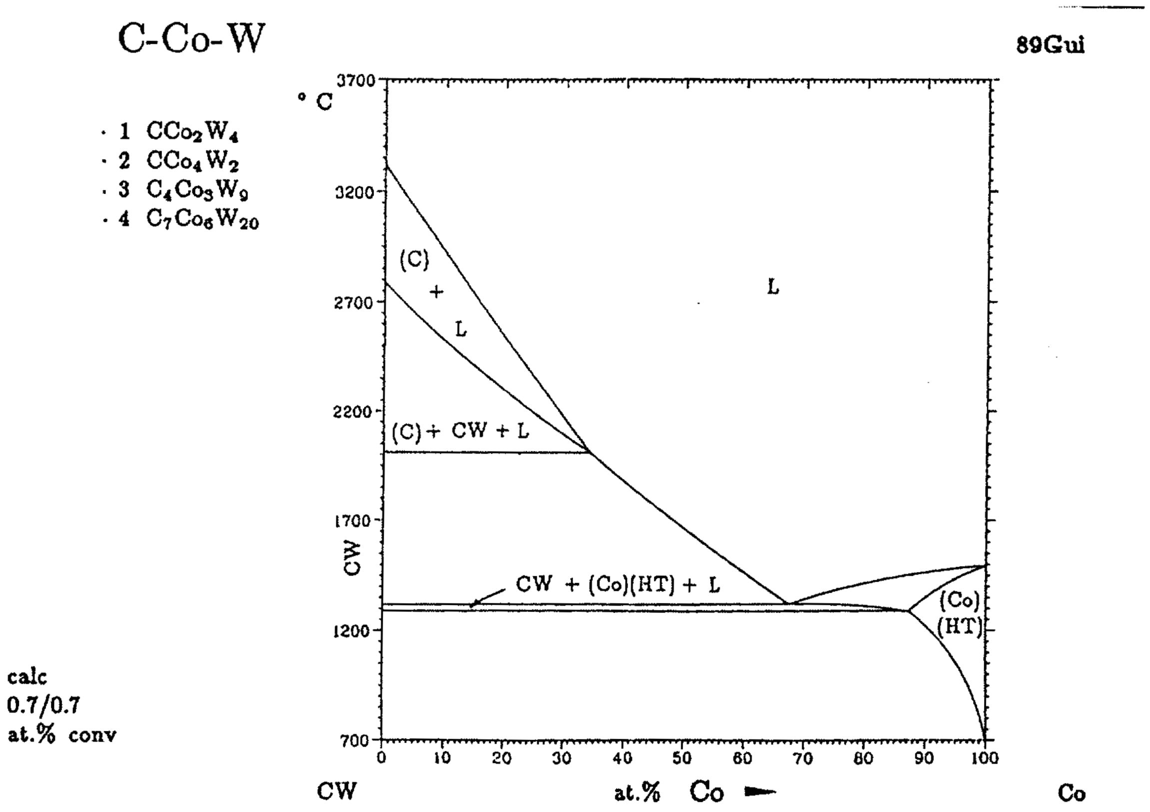

Figure 1.5. Binary phase diagram of WC and Co [81]. Reprinted with permission from ASM International.

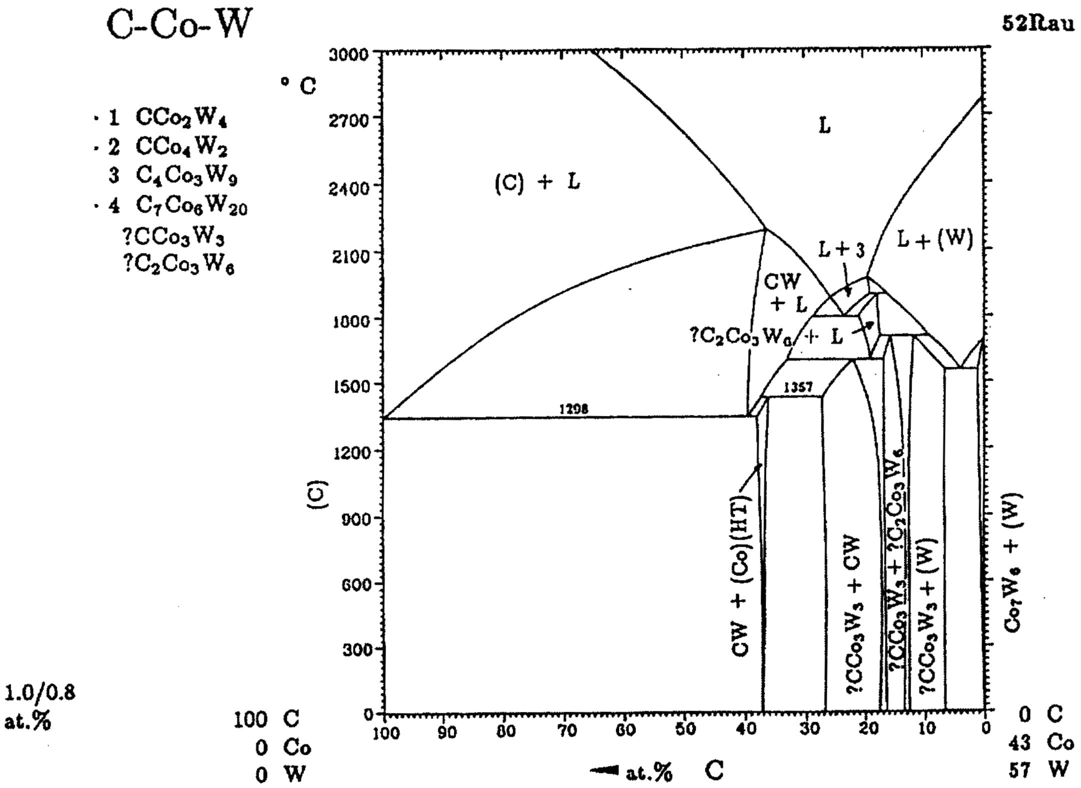

Figure 1.6. Binary phase diagram of WC-Co [81]. Reprinted with permission from ASM International.

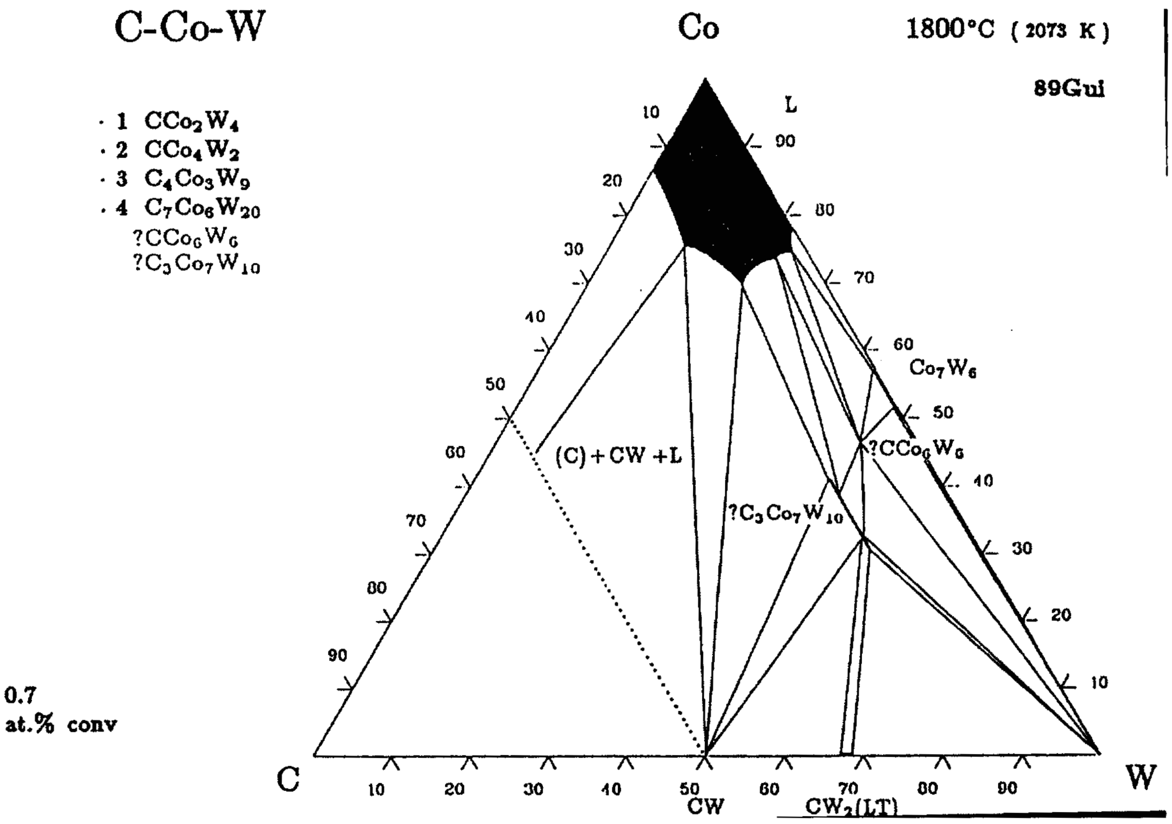

Figure 1.7. Ternary phase diagram of WC-Co [81]. Reprinted with permission from ASM International.

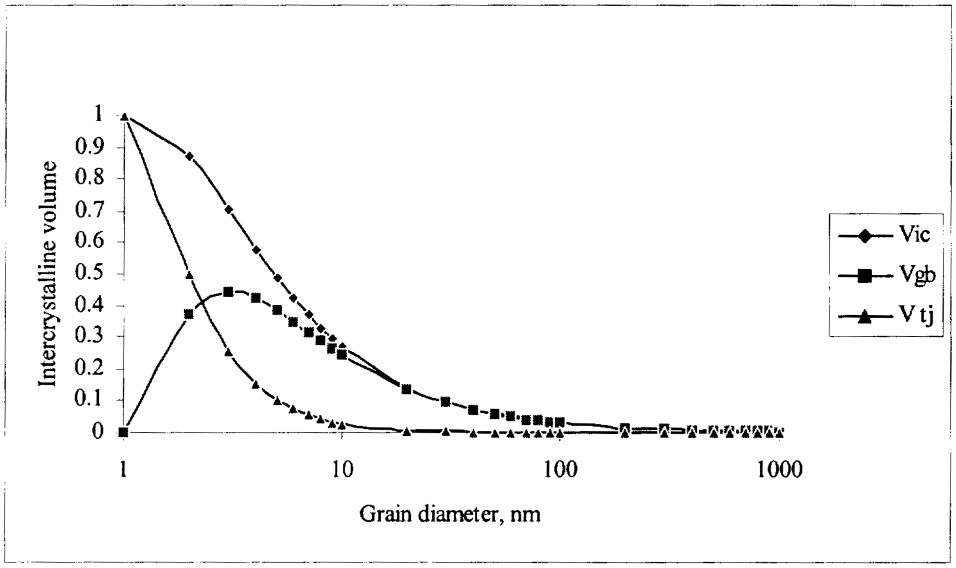

Figure 1.8. Intercrystalline volume of a material versus grain diameter, V_{ic} is intercrystalline volume, V_{gb} is the volume of the grain boundaries, V_{tj} is the volume of the triple junction.

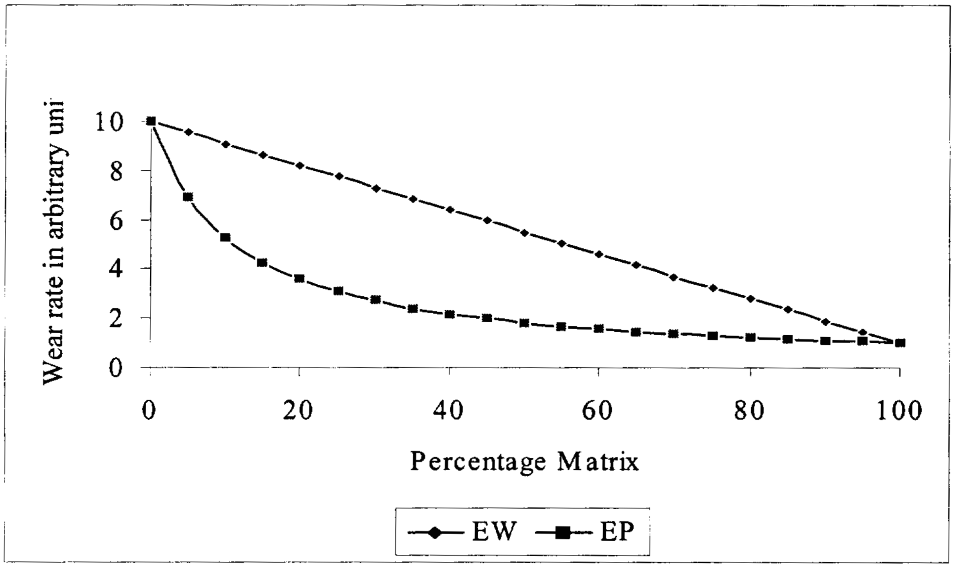

Figure 1.9. The relative wear resistance, Equal Wear (EW) and Equal Pressure (EP) modes.

2.0 EXPERIMENTAL

2.1 Introduction

The experimental process and procedure description is divided into two major sections: microstructural characterization and performance evaluation. The emphasis of the thesis was on microstructural characterization and hence those associated processes make up the bulk of the techniques that were used. A substantial effort was made to completely evaluate the powders that were used to make the coatings. A full examination of the feedstock was deemed necessary in order to gain a better understanding of the relationships between the starting material, spray parameters, and the properties of the coatings.

2.2 Powders

The WC-Co powders were obtained from several different sources and were manufactured using a variety of techniques. In general, the powders were agglomerated masses of small carbides held together with cobalt. The characterization of the powders included powder size analysis, done by SEM or with a particle size analyzer, chemistry, and X-ray diffraction. Some of the powders had very poor flow characteristics. These powders were dried, sieved, or had flowing agents added as deemed necessary to ensure reasonable dry flow characteristics.

2.3 Substrates

The substrates used for spraying consisted of flat 1/4"x 1"x 4" cold rolled mild steel coupons. These specimens were cleaned and grit blasted with chilled iron shot no more than one hour prior to spraying. This was done to create a clean, roughened surface on the substrate to increase coating adhesion. Immediately prior to deposition of the coatings, the substrates were cleaned with acetone to assure an oil and dust free surface.

2.4 Plasma Spray Equipment

Plasma spraying was performed with a 200 kW PlazJet high energy plasma spray system. This plasma spray system consisted of an energy source, gas source, plasma gun and a control system. The energy source consists of two 100 kW rectified DC power supplies connected in series. The operating range of the system was 200-500 volts and 100-500 amps. The system is capable of using a number of different plasma gases: argon, helium, nitrogen and hydrogen. In this study only nitrogen and hydrogen were used. The gas flow rates were controlled with inline flow meters. The maximum gas flow was 18 cfm at 200psi. A schematic of the plasma gun illustrating the water and gas flow paths is shown in Figure 2.1. One descriptive deposition parameter which was the standoff distance was measured from the nozzle exit of the gun to the surface of the substrate. In almost all cases the standoff distance was 200 mm. The injection angle of the powder was 45 degrees. The powder feeder, a Miller Thermal Rotohopper, used was set at 10 rpm and a gas flow rate of 1 cfm. Coating thickness was controlled by the number of passes. The traverse speed of the gun was approximately 30 cm per second.

2.5 Fixtures

Two different fixtures were used to control the degree of cooling of the substrates. Substrates in the 'cold' fixture were cooled from the back side with compressed air as well as being cooled from the front side with nitrogen (Figure 2.2). The cold fixture could hold two samples. Behind each substrate were five holes, in the centerline of the bar, distributed symmetrically over the length of the substrate. No attempt was made to regulate the air pressure which was nominally 70 psi.

The hot fixture consisted of a 0.5m long piece of angle iron which had small blocks to loosely hold the substrates in place (Figure 2.3). The substrates in this case were cooled from the front side with either compressed air or nitrogen.

2.6 Metallography

In order to characterize the coating and the powder microstructures, they were prepared for metallographic examination. The metallographic coating samples were either cross sections of the as-deposited coating or cross sections of the coating through the wear scar after testing. The wear scar samples were cut so that the surface viewed would be the middle of the wear scar parallel to the direction of abrasive flow. The coating sample cross sections were prepared by first cutting the samples with an abrasive saw.

The cut samples were then vacuum impregnated with cold mount epoxy and auto-polished. The steps used in auto-polishing were: 120 grit SiC until planar, followed by 30 seconds at 240, 400, and 600 grit SiC. They were subsequently polished with 6 μm diamond grit, followed by 1 μm diamond grit for 1 to 2 minutes. The final step was the application of a 0.05 μm silica attack etchant for 1 minute.

The powder samples were vacuum impregnated with cold mount epoxy. These samples were hand polished to planarity with 120 grit then quickly polished with 400 and 600 grit SiC papers, followed by 6 μm and 1 μm diamond, and a final polish using 0.05 μm silica attack etchant.

2.7 Image Analysis

Computer based image analysis was performed to measure the porosity of the as-sprayed coatings. The Definitive Image™ was the image analysis system used in the course of this work. An Optical metallograph was connected to a digital camera which captured the images and imported them into software which was designed for making metallographic measurements. The analysis was performed at 400x, 500x, or 1000x depending on the coating thickness. A minimum of image modification was done to insure that the values acquired were real as opposed to artifacts of the image processing. The sprayed coating contained at least three different phases, matrix, carbides and porosity. The smallest carbides used in this study were not individually resolvable with optical microcopy.

2.8 Scanning Electron Microscopy

A Ziess DSM-960 SEM was used to image the samples in both secondary electron and backscattered electron imaging modes. Several different types of samples were analyzed in the SEM, as well as the powders, coating cross sections, wear scars, and wear scar cross sections. Two different types of powder samples were examined with the SEM. The first was a sample of the as-received powder placed on a carbon adhesive. The overall morphology of the powders was gathered with these samples. The second type of powder sample was a polished cross section of the powders. These sample were used to assess the internal morphology of the powders as well as the as-received carbide size.

The coating cross sections examined in the SEM were prepared as described in the metallography section. These samples were coated with 200-400 angstroms of Au/Pd before they were imaged in the SEM. The coating cross sections were used to gather information about the effects on the microstructure with respect to the spray parameters. Furthermore, in backscatter electron imaging, porosity and carbides could be clearly distinguished from the matrix. This allowed the size and distribution of the carbides in the coating to be assessed. The wear scar specimens were cleaned with air to remove any loose debris from their surface. The worn bars were then examined without being coated and the wear scar cross sections were prepared as described in the metallography section. The structure near the wear surface of these samples were examined.

2.9 Microhardness

A Leco DM-400 microhardness tester with a Knoop microhardness indenter was used to make microhardness indentations in the polished metallographic samples. A 300-500g load with a 15 second dwell time was used. The hardness indentations were made with the long axis of the indent being perpendicular to the coating/substrate interface. This resulted in the indent intersecting as many splat-to-splat boundaries as possible.

2.10 Transmission Electron Microscopy

A Hitachi H800 200 Kev STEM was used to examine some of the samples which were imaged in bright field mode. The purpose of the imaging was to determine the size of the carbides. Both powder samples and coating samples were prepared. The powder samples were prepared by first crushing the powder with a mortar and pestle, and then etching the crushed powder with nitric acid in methanol in an ultrasonic bath for 30 minutes. A carbon-coated copper grid was then used to skim the surface of the solution to gather the small particles held on the surface. This grid was washed with methanol and placed in the TEM.

Other coating samples were prepared with ion milling. Both conventional ion milling and focused ion beam milling were used to prepare samples of the coatings. The focused ion beam milling was done with a FEI 610 Focused Ion Beam workstation. The preparation for samples that were milled with either the conventional or focused ion beam was identical. The samples were first cut from the bulk coating. They were then mechanically ground to less than 150 μm and then milled to electron transparency.

2.11 Dry Sand Rubber Wheel Abrasive Wear Test

The sprayed coatings were tested using a Dry Sand Rubber Wheel (DSRW) abrasive wear test machine, a three body low stress abrasive wear test. The procedure used was slightly modified from ASTM Standard G-65. The procedure was modified in that a small number of revolutions, typically 200, were run and then the weight change was measured. This procedure was carried out step-wise throughout the abrasion test. The stopping point of the test for these coating was at least 1000 revolutions or when the coating had worn through. The force on the sample was 130 Newtons. The abrasive used was 50-70 mesh Ottawa silica sand. The wheel was set to run at 200 rpm. In calculating the volumetric wear rate, density values were assumed. Figure 2.4 shows a schematic drawing of the DSRW machine.

2.12 X-Ray Diffraction

X-ray diffraction was performed using Cu Kα radiation with a Norelco X-ray Diffractometer. Two types of samples were examined: the as-received powers and the sprayed coatings. The coatings had been sprayed on standard sample bars which were cut down to 2" lengths so they would fit in the sample fixture of the XRD. The coatings were not removed from the substrates. In none of the coatings examined did the XRD penetrate to the substrate.

2.13 Chemical Analysis

Chemical analysis was performed on a small number of the coatings. The elements that were expected were W, C, Co, and O. The Carbon was analyzed with a LECO CS-444 carbon analyzer. The amount of Co, W and O in the coatings was assessed with an ARL Spectrospan VI direct current plasma optical emission spectrometer. In the latter samples were dissolved in a mixture of nitric and hydrofloric acid and this solution then diluted with distilled water. Furthermore, in order to assure that only the WC-Co coatings and not the steel substrates were examined, the coating samples were magnetically separated before analysis.

2.14 Field Emission Scanning Electron Microscopy

The powder cross sections and a small group of wear scars were examined using a LECO 982 FESEM. Due to the sensitivity of this microscope to surface coatings, the majority of the powder cross sections were coated with carbon rather than Au/Pd. The wear scar samples were not coated. The FESEM had a high enough resolution such that individual carbides could be resolved.

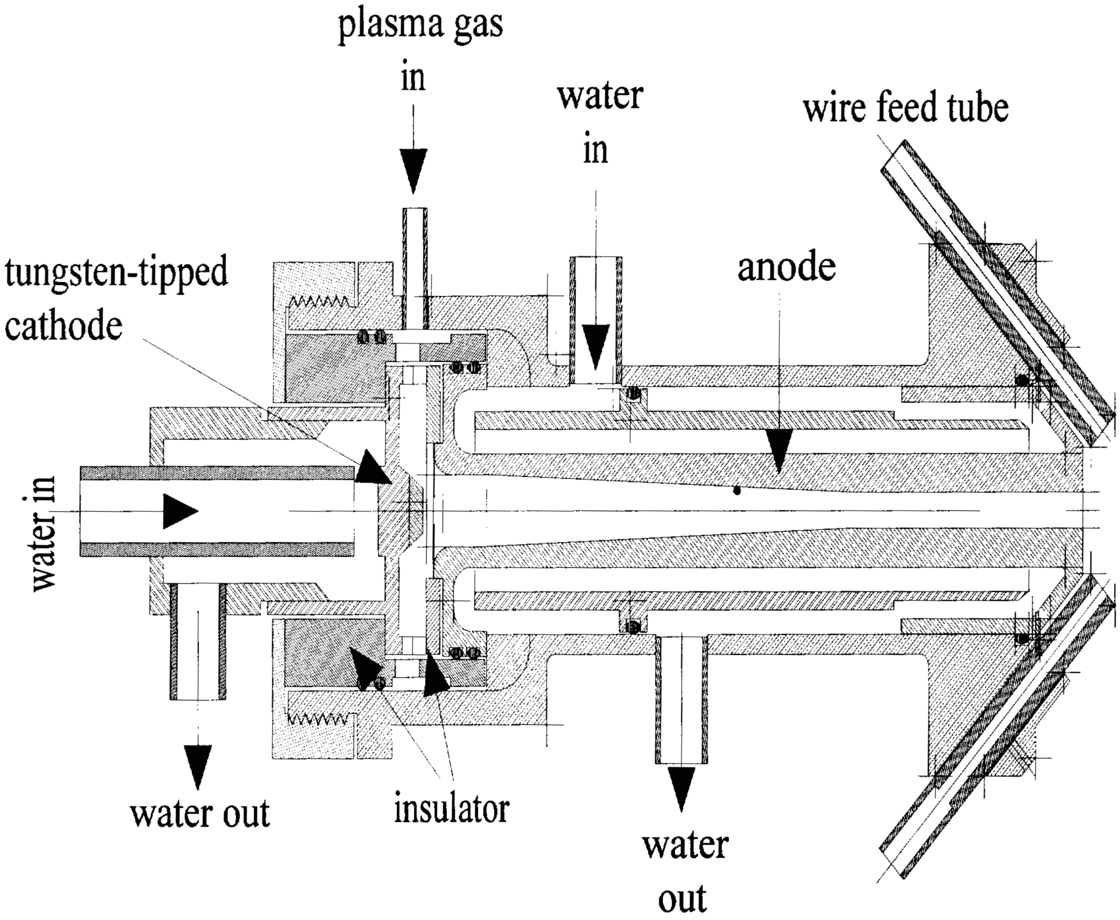

Figure 2.1. Schematic of high energy plasma spray gun.

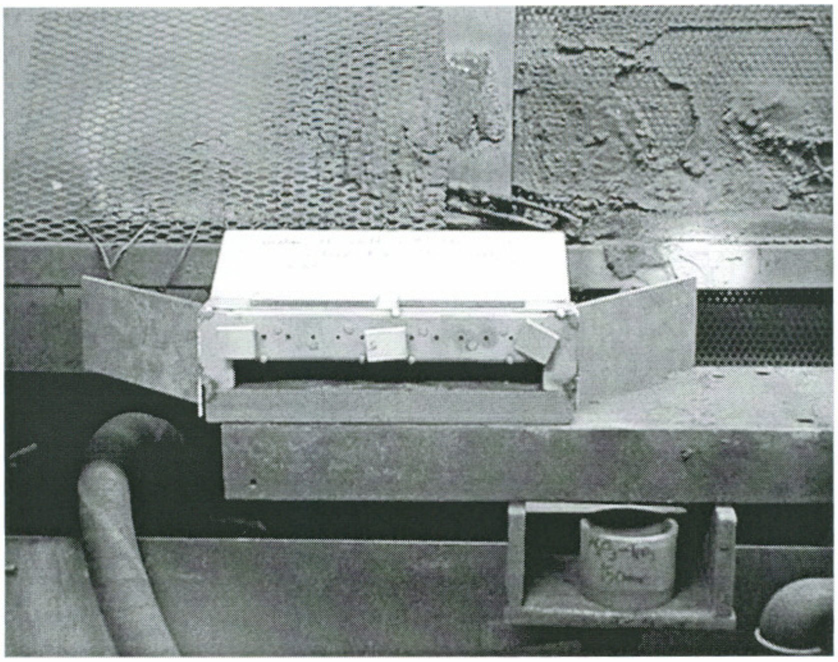

Figure 2.2. High cooling rate fixture.

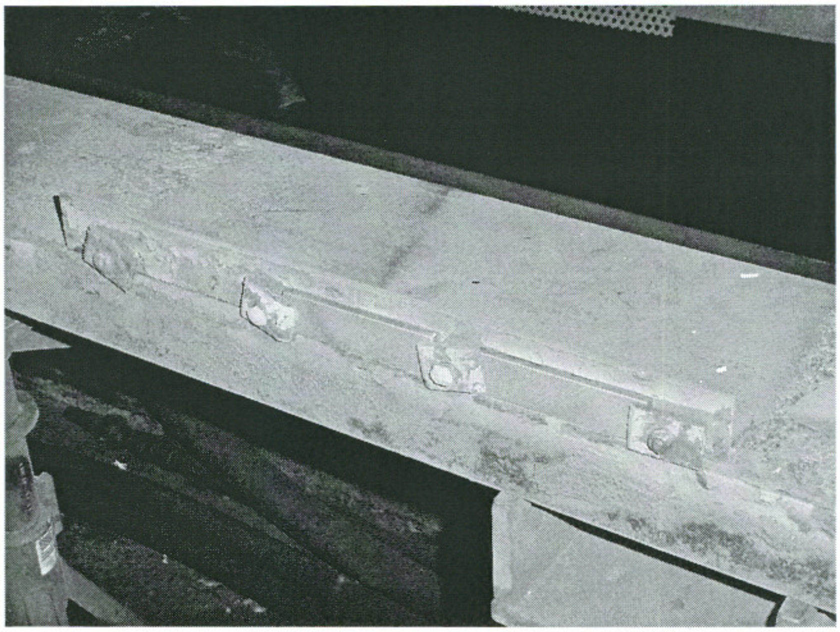

Figure 2.3. Low cooling rate fixture.

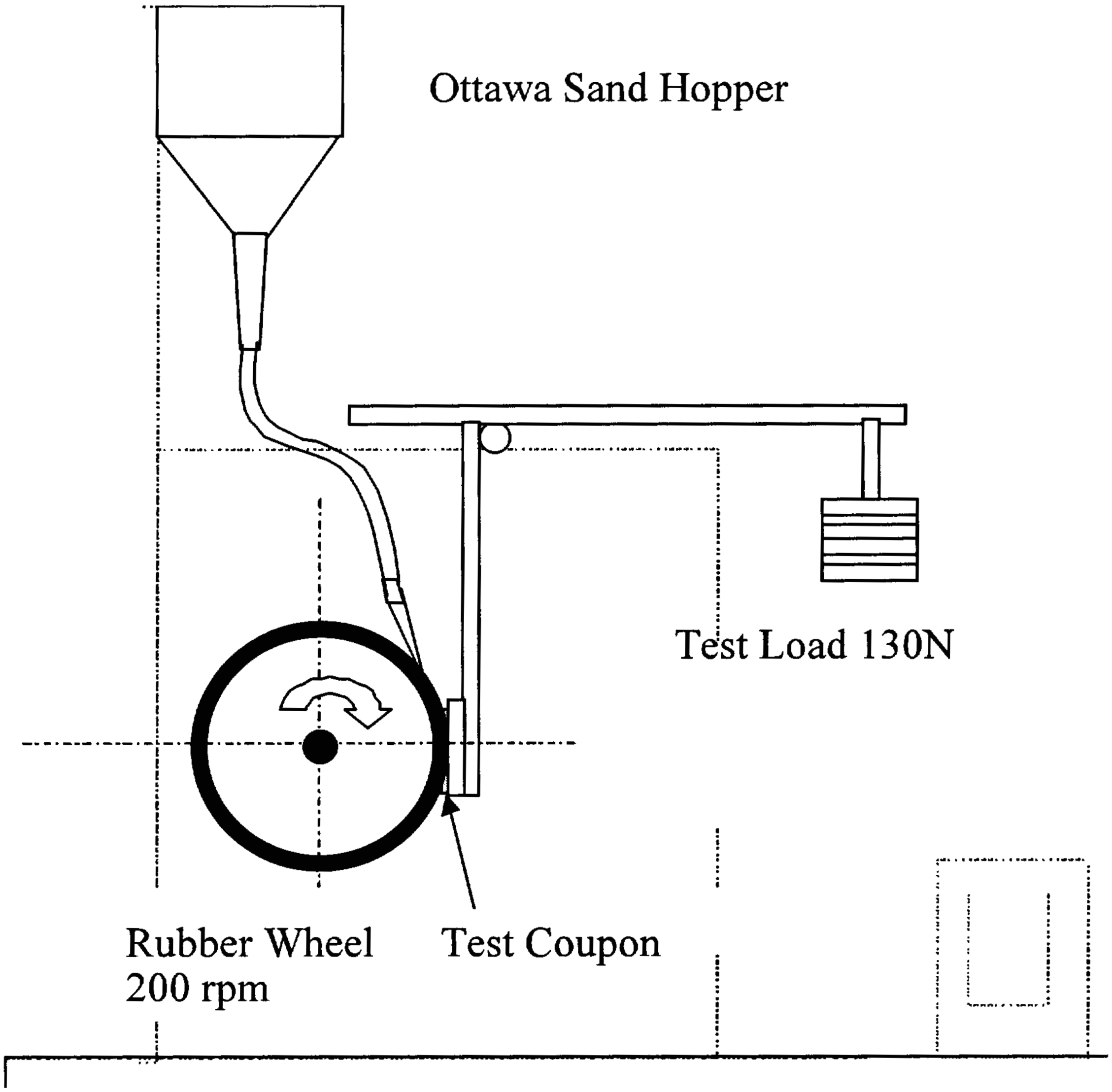

Figure 2.4. Schematic of the Dry Sand Rubber Wheel abrasive wear test machine.

3.0 RESULTS

The powders used for thermal spraying in this study were obtained from a number of different sources and were of a variety of carbide sizes. The size of the carbides was of primary interest. Cross sections of all of the feedstock powder particles were made in order to directly observe the size and morphology of the carbides. Furthermore, not all of the feedstock powders were designed to be thermal spray powders. As a result it was necessary to examine all the powders to determine their fitness as thermal spray powders.

Scanning Electron Microscopy was used to examine the morphology of the starting powders and the images obtained were used to evaluate the shape and the range of sizes of the powder particles. The size distribution of the powder particles was determined with a Lecotrac^{TM} powder size analyzer. The combination of the Lecotrac^{TM} distribution data and the SEM images reasonably characterized the powders particles.

With the powder fully characterized, the effects of changing the plasma spray parameters on the microstructure and properties could be considered. The microstructure of plasma sprayed WC-Co coatings result from a combination of the spray parameters and the starting powder. The influence of the microstructure on the properties of the coating will be more fully addressed in the discussion section. The porosity, hardness and wear rate of each of the coatings will be reported here.

3.1 Powders

Three different methods were used to determine the characteristics of the powders. SEM observations of the powder morphology were made. SEM and FESEM observations of the polished powder cross sections were performed. Most of the powders were analyzed with a Lecotrac™ powder size analyzer. The data of powder size analysis and the images taken together helped develop a fair understanding of the powders.

There were two different particles that were of great interest, the powder particles and the carbide particles. The SEM morphology images and the Lecotrac™ data were used to characterize the as received thermal spray powders due to the information they provided on the powder particle size. The powder cross-sections were primarily used to evaluate the size of the carbide particles in the powders as well as providing information on the internal morphology of the powders.

Images of the powder and coating cross-sections come primarily from the SEM even though all of the powders, coatings and cross sections were also observed using optical microscopy. In general, the SEM images were of higher resolution with greater depth of field and were included in preference to optical microscopy images. FESEM images were used to observe the carbide size and internal morphology of the powder cross sections. The following subsection presents results of the individual powders.

3.1.1 Powder Particle Morphology

Metco 2004^{TM}

This was the only commercially available thermal spray powder in the study. As such it was frequently used as a baseline from which to judge the other powders. Figures 3.1-3.3 shows the powder consisting of solid, nominally spherical or oblong particles with a relatively tight size range. The majority of the particles fell in the size range of 10-70 μms with no fines.

Nanomyte^{TM}

This powder, though not commercially available, was designed for thermal spraying. Figures 3.4-3.6 show a spherical nonporous powder with an average powder particle size estimated at 30 μm. The size range appeared to be 10-50 μm. This powder showed a narrow distribution with few fines.

Nanodyne^{TM} 12 wt% Co Large

The large cut of the powder was found to contain particles ranging from 20-100 μm. Figures 3.7-3.9 are images of the Large cut of the Nanodyne^{TM} 12 wt% Co. The images showed a spherical porous powder, with an average particle size of 75 μm. The particle size distribution was narrow and few fines were in evidence. This powder and the Nanodyne^{TM} 12 wt% Co Small were dramatically different from the other Nanodyne^{TM} powders in that they had fewer shattered particles and the particles appeared to be solid.

Nanodyne™ 12 wt% Co Small

The smaller cut of the Nanodyne™ 12 wt% Co (Figures 3.10-3.12) also had a narrow size distribution ranging from 10-50 µm of a spherical porous powder. This powder did not have a significant amount of fines in evidence and the powder particles appeared to not be hollow.

Nanodyne™ 15 wt% Co

The as-received Nanodyne™ 15 wt% Co powder consisted of porous particles, with a significant amount of fines. The average particle size was estimated at 50 µm (Figures 3.13-3.15). This powder was further sieved to remove the excess fines and to narrow the powder size distribution. The sieved powder can be seen in Figures 3.16-3.18.

Nanodyne™ 5 wt% Co

This powder had a nominal range of particles sizes from 2-250 µm, Figures 3.19-3.21. This powder consisted of a mixture of flakes and spherical particles with a very high percentage of fines. The broken spherical particles appeared to be of low density and highly porous.

Inframat™ 8 wt% Co

This powder had a very small average size and a large amount of fines, Figures 3.22-3.24. This powder was a reprocessed Nanodyne™ power. The original Nanodyne™ powder was found to be unsprayable and was subsequently sent to Inframat™ for re-constitution in hopes of yielding a sprayable powder. Inframat™ used a plasma spray particle consolidation method which reduced the average particle size.

The original low density and/or flake Nanodyne™ particles were condensed into nominally dense, spherical particles by liquid metal (Co) surface tension forces. The Inframat™ powder also contained a reasonable number of fines, as it is presumed that the original Nanodyne™ powder contained a reasonable number of fines. The Inframat™ powder was found to flow well.

Osram-Sylvania - 12 wt% Co and - 18 wt% Co

The two Osram-Sylvania powders had very similar powder morphologies. Both were spherical, nonporous powders with an estimated average particle size of 40 μm. Neither of these powders had any significant amount of fines. Figures 3.25-3.27 show the images of the 12% Co and Figures 3.28-3.30 show the powder images of the 18% Co powder.

3.1.2 Powder Cross Sections

All powders were mounted and polished to 0.05 μm and examined in the SEM to determine the internal structure and to estimate the carbide size. Two images of each of the powders were taken; one to show internal structure; another to show carbide size. Table 3.1 shows a summary of WC grain size and Table 3.2 shows powder characteristic relevant to thermal spray. Images of the powder cross sections of selected powders were taken with the FESEM and show the size and distribution of the carbides.

Metco 2004 12 wt% Co

The Metco 2004 powder was the only conventional powder sprayed in this study and, as such, it clarifies some of the differences between the powders. Figures 3.31 and 3.32 show a wide range in the size of the prismatic carbides. There appears to be cobalt between most of the carbides and to be very little porosity in the powder particle. Figure 3.33 shows the carbides which range from 3 µm to 200 nm in size and are surrounded by cobalt.

Nanomyte^{TM}

The distribution of the carbides in the Nanomyte^{TM} can be seen in Figures 3.34-3.36. The micrometer-sized carbides are interspersed with submicrometer and nanoscale carbides. The images show the distinct mixed sizes in this powder. FESEM work confirmed that the powder was a mix of micrometer and submicrometer carbides.

Nanodyne^{TM} 12 wt% Co Large

The cross section of the Large Cut of the Nanodyne^{TM} 12 wt% Co was more typical of the images taken with the FESEM. Figure 3.37 is a secondary electron image of the powder at 3000X. This image shows the abundance of small carbides, with no large pores in the powder particle itself. The small pores that can be seen in the image may be due to pull out of the carbides that occurred during the polishing of the sample. Figure 3.38 focuses on the carbides, showing that they are submicrometer in size. Figures 3.39 show individual carbide clusters which appear to be attached to particles of cobalt.

Nanodyne™ 12 wt% Co Small Cut

Figures 3.40-3.42 show the clustering of the carbides, which was identical to that observed in the Nanodyne™ 12 wt% Co large powder. In Figure 3.42 discreet nanoscale carbides can be seen in the cobalt. Some of the carbides in this powder were as small as 50 nm, however, it appears that most of the carbides were in the submicrometer range.

Osram-Sylvania 12 wt% Co

The Osram-Sylvania - 12 wt% Co powder examined in FESEM showed carbides that were submicrometer in size, ranging from 200-300 nm, (see Figures 3.43 and 3.44). The cross sectional images revealed that the spray particles contained very small internal pores with an occasional large pore.

Osram-Sylvania 18 wt% Co

Figure 3.45 shows the cross section of a single powder particle. This image revealed that the powder was porous, having a number of small internal pores with an occasional large pore. The grey areas in this image are the regions of cobalt that are free of carbides. Figure 3.46 shows the carbides as mostly being in the range of 200-300nm but with carbides both significantly larger and smaller.

Inframat™ 8 wt% Co

Figure 3.47 shows this powder to have particles that are spherical, porous and widely ranging in carbide size. Figure 3.48 shows the carbides to have both prismatic and rounded morphologies. The carbide size can be seen to range from less than 100 nm up to 750 nm, though most of the carbides appear to be in the 200-400 nm range. There does not seem to be any cobalt holding the clusters of carbide particles together.

Nanodyne™ 5 wt% Co

This powder shows large clusters of carbides and a large amount of porosity, see Figure 3.49. A higher magnification image of the carbide clusters shows carbides ranging from 200-750 nm in size, see Figure 3.50. The average size appeared to be about 500 nm.

Nanodyne™ 15 wt% Co A

Figure 3.51 shows a combination of solid and hollow spheres along with shattered bits of powders. Furthermore, this image highlights the porous nature of this powder. Figure 3.52 and 3.53 shows the bright carbides (due to the high average Z) against the dark porosity. This powder had a very high porosity in the powder itself. Figures 3.53 and 3.54 show the globular shape of the cobalt and carbides. The carbides in these images seem to be forming around the cobalt creating a coral-like pattern for the internal structure of the powder. While carbides in the nanoscale range are present in this powder, there were also a large percentage of particles in the submicrometer range. The extreme friability of this powder can be explained by its internal structure, with the large empty volume of the powder surrounded with a very fine structure of cobalt and carbides.

Nanodyne™ 15 wt% Co B

Figure 3.55 shows the distribution of the carbides in this powder. The powder particles have a large amount of porosity spread evenly throughout the particle. Clusters of carbides appear to be more discreet in this powder than in Nanodyne™ 15 wt% Co A. The carbides do not seem to have the same coral like appearance. There even appears to be areas where cobalt is binding the carbides together. The carbide size is shown in Figures 3.56-3.57 and ranges from 50-200 nm. The average size appears to be about 100 nm.

3.1.3 Lecotrac™ Particle Size Analysis

The particle sizing data, measured by Lecotrac™ , was more accurate at assessing the powder size distribution than the SEM morphology images. There was a tendency with SEM observation, in the case of the powders with a large percentage of fines, to significantly under estimate the percent of fines in the powder. A summary of the following Lecotrac™ data can be found in Table 3.3.

Metco 2004 12 wt% Co

The powder size distribution of the Metco 2004 WC-12 wt% Co with the micron-sized carbides is shown in Figure 3.58. The particle size distribution ranges from 10-75 μm. The most common particle size was 26 μm which accounted for 17% of the total powder volume. The powder distribution from 15-37 μm accounted for 80% of the powder particles. This is a narrow distribution with a high percentage of the particles in what is considered a reasonable spraying size range.

Nanodyne™ 12 wt% Co Large and Small

There were two "cuts" of the submicrometer Nanodyne™ WC-12Co. The larger cut was for conventional plasma spray and the smaller cut was for HVOF. The larger of the cuts had a mode particle size of 75 µm, Figure 3.59. Due to the sieving operation, this powder did not contain particles less than 10 µm in size. The distribution ranged from 25-100 µm. Particles in the range of 55-85 µm were 65% of the total particles. The distributions of the smaller cut can be seen in Figure 3.60. The mode of the particle size distribution was 65 µm. Particles in the range of 45-75 µm accounted for 58% of the powder particles.

Osram-Sylvania 18 wt% Co

The Osram-Sylvania 18 wt% Co powder particle size range was approximately 15-60 µm, see Figure 3.61. The mode for this particle size distribution was 30 µm. The size range for 20-45 µm contained 89% of the powder particles.

Nanodyne™ 5 wt% Co

The Nanodyne™ 5 wt% Co powder sizes distribution can be seen in Figure 3.62. This, like the other powders that did not yield acceptable coatings, had a wide particle size distribution, 10-150 µm. The mode particle size was 90 µm. The particle size range of 75-100 µm contained 30% of the all the particles.

Inframat 8 wt% Co

The Inframat 8 wt% Co powder sizes distribution can be seen in Figure 3.63. This powders that did not yield an acceptable coating though it had a narrow particle size distribution, 4-40 μm. The mode particle size was 15 μm. The particle size range of 5-25 μm contained 60% of the all the particles. Over 60% of the powder particles were less then 10 μm in size.

Nanodyne™ 15 wt% Co A

Nanodyne™ 15 wt% Co A powder particle size distribution can be seen in Figure 3.64. This powder had a particle size range from 10-200 μm. The mode particle size was 62 μm. The particle size range of 50-90 μm contained 35% of the particles. This powder, unlike the Nanodyne™ WC-15 wt% Co B, did not contain nanoscale carbides and no sieving operating was attempted to narrow the particle size distribution.

Nanodyne™ 15 wt% Co B

The Nanodyne™ 15 wt% Co B powder that contained nanoscale carbides had a particle size range from 1 to over 100 μm in size, Figure 3.65. The mode of the particle size distribution was 75 μm. The particle size range of 55-85 μm contained 40% of all the particles. This powder was sieved and the sieved powder had particles that ranged in size from 25-100 μm, Figure 3.16-3.18. The mode of this distribution was 75 microns while 80% of the particles were in the size range from 55-85 μm.

3.2 Coating properties

The data showing various coating properties are presented powder by powder and properties of coating sprayed on the hot fixture and cold fixture are presented together and are summarized in Table 3.4.

3.2.1 Coating Porosity

Figures 3.66-3.72 show the porosity of the coatings. The porosity of the coating was in the lower range for plasma sprayed coatings, 2-5%. The Nanomyte^{TM} powder was the one exception to this trend. Coatings made from the Nanomyte^{TM} powder had a porosity volume fraction up to 25%. The porosity in the Nanomyte^{TM} was not due to voids in the coating but large areas of pullout. This was presumed to be due to an instability in the plume during the deposition as there was no evidence in the powder images of powder characteristics that would give rise to such a large variation from the norm.

3.2.2 Coating Hardness

Figures 3.73-3.79 shows the hardness of the coatings. The hardness of the coatings ranged from a low of 680 Knoop to a high of 1200 Knoop. The hardness varied with the percentage of cobalt; increasing the cobalt decreased the hardness.

3.3 Coating Wear Rate

The following section has been designed to help the reader examine the wear data. Dry sand rubber wheel (DSRW) testing had been shown to work well at predicting the relative ranking of materials under low stress abrasive wear [82, 83].

Depending on the actual wear conditions, the wear rate of the materials will change, however the ranking of the coatings should not change for low stress abrasive wear conditions. A coating that performs better than another coating in this test will, in general, perform better over the range of low stress abrasive wear conditions.

Figures 3.80-3.86 shows the wear rates of the coating obtained in the DSRW abrasive wear test with Ottawa silica sand. This data was the most important of the three data sets; coating porosity, coating hardness and coating wear rate, as the utility of the coatings was evaluated in terms of wear rate. There was substantial variation in wear rate within a single powder depending on the gas parameters used.

Metco 2004 12 wt% Co

The Metco 2004 12 wt% Co powder was chosen as a standard to which the other coatings were compared. Coatings made from Metco 2004 had lower wear rates when sprayed on the hot fixture then sprayed on the cold fixture (Figure 3.80). The lowest hot fixture wear rate for the Metco coating was 0.0023 mm^3/m, while the lowest wear rate for this coating sprayed on the cold fixture was 0.0031 mm^3/m. This wear rate was among the lowest achieved for any of the coatings. In real applications only coatings with good wear resistance would be of interest, so all of the coatings sprayed were compared with the best results for the conventional material. The 6 cfm hot fixture condition was chosen to be the baseline to compare the performance of the coatings.

The Metco 2004 12 wt% Co powder had very reasonable powder flow characteristics and contained micrometer-sized carbide particles. The hot fixture wear rates in all of the compared conditions resulted in better wear rates than the cold fixture coatings, see Figure 3.80. The best wear rate for both the hot and cold fixture was the high nitrogen spraying condition. The lower nitrogen primary gas flow condition with the addition of hydrogen resulted in a decrease in the wear rate due to over melting and decomposition of the powder in flight. The effect of gas flow on the wear rates was limited, and was attributed to powder characteristics; namely the combination of a narrow particle size distribution and an average particle size well suited for plasma spraying. The final characteristic of this powder that made it less sensitive to spray parameters than the other powders was the fully dense powder particles. These characteristics were not shared with all of the other powders. Many of the powders had wide particle size distributions, low particle densities, and/or average sizes that were too small to work well in the time-temperature regime of high energy plasma spraying.

Actual spray parameters established for a commercial application are likely to be different than the ones used in this study. Factors such as the deposition efficiency, adhesion strength, porosity, hardness, or toughness of the resulting coating may be more important for the particular application than wear resistance alone. That being said, this study focuses on the wear resistance of the coatings. Further study would be required correlate the effect of carbide size and cobalt percentage with these other factors.

Nanomyte^{TM} 12 wt% Co

It was found when that spraying with 6 cfm nitrogen plasma gun primary gas on the hot fixture was the best condition for the Nanomyte^{TM} powder with a wear rate of 0.0029 mm^3/m, which is about 25% worse than the wear rate of the conventional powder (Figure 3.81). The rest of the coatings sprayed on the hot fixture all fell into a narrow range of values. The highest wear rate on the hot fixture was 0.0036 mm^3/m, which is 55% higher wear rate than the conventional powder. Coatings sprayed on the cold fixture were distinctly inferior to the coatings sprayed on the hot fixture for this powder. The lowest wear rate obtained for the cold fixture was 0.0036 mm^3/m. The addition of hydrogen increased the wear rate to 0.0047 mm^3/m, which is double the wear rate of the conventional powder.

The Nanomyte™ powder had a mixed mode carbide size distribution containing both micrometer and nanoscale sized carbides. There was very little difference in the wear rate of the coating due to changes in the gas conditions for coatings sprayed on the hot fixture, see Figure 3.81. For all conditions, the hot fixture resulted in a better wear rate than the cold fixture. The wear rate did not change dramatically with the conditions sprayed.

Nanodyne™ 12% wt% Co Large

This coating showed low wear rates when sprayed with or without hydrogen on the hot fixture, Figure 3.82. A wear rate of 0.0024 mm^3/m is not meaningfully different than the lowest wear rate for the conventional powder. The 6 cfm spraying condition for this powder resulted in the highest wear rate rather than the lowest wear rate as was found in the conventional powder. This could be attributed to the large average size of the particles and the range of the spray conditions. Differences between the large and small cut will be discussed later. Cold fixture wear rates were 0.0028 mm^3/m for all the conditions except for the highest the enthalpy conditions which had a wear rate of 0.0025 mm^3/m, a 22% and 9% increase in the wear rate over the hot fixture results.

This powder showed very little difference between the wear rates of the coatings sprayed on the hot fixture or cold fixture, Figure 3.82. The differences in wear rate were small enough in all cases that the differences are within the experimental variation. This powder had consistently good wear rates regardless of gas parameters, including conditions with hydrogen added to the carrier gas. The reason for the lack of distinction between the hot fixture and cold fixture as well as the overall good wear rates can be attributed to the powder characteristics. The powder had a narrow, reasonable particles size distribution with a high mode particle size, essentially a "plasma" cut. The larger powder particle size assured that the powder did not undergo the overheating as did the smaller particles.

Nanodyne™ 12% wt% Co Small

This coating showed very consistent wear rates. For the hot fixture, most of the wear rates were about 0.0032 mm^3/m, a 40% increase in the wear rate when compared to the conventional powder, see Figure 3.83. Coatings sprayed on the cold fixture had a range of 0.0030 mm^3/m to 0.0035 mm^3/m over the range of conditions sprayed. This represents an increase in the wear rate by 27% and 48%, respectively over the conventional Metco 2004 coating. Coatings sprayed on the cold fixture with the addition of hydrogen to the plume had better wear rates than coatings sprayed without hydrogen.

The wear rates of the cold fixture for this powder were as good or a little bit better than the hot fixture, see Figure 3.83. As was shown in Figure 3.11 and 3.8, this powder had a higher percentage of hollow particles than the larger cut of the same powder. This may have exacerbated the differences between the two powders.

Osram-Sylvania - 12 wt% Co

The wear rate of this coating sprayed on the hot fixture with 6 cfm nitrogen condition was 0.0023 mm^3/m, which was identical to the wear rate of the conventional Metco 2004 coating, Figure 3.84. This was distinctly better than the rest of the wear rates for the hot fixture. The highest wear rate of a coating sprayed on the hot fixture was 0.0040 mm^3/m, a 74% increase over the Metco 2004 coatings. Cold fixture results showed an increase in wear rate similar to the hot fixture. The lowest cold fixture wear rate was also the 6 cfm spraying condition. In this case the wear rate was 0.0029 mm^3/m, a 25% increase in the wear rate over the hot fixture. The highest wear rate for the cold fixture was 0.0054 mm^3/m, 135% higher than the conventional Metco 2004 coatings.

The Osram Sylvania powder had a very narrow distribution of powder size. The hot fixture wear rates were always better than the cold fixture wear rates, though not significantly different when sprayed with the high nitrogen conditions, see Figure 3.84. In a reversal of the general trend, the porosity of the coating sprayed on the hot fixture was lower than the coatings sprayed on the cold fixture. The porosity values for coatings sprayed on the cold fixture averaged around 4.5% for all of the conditions sprayed, see Figure 3.70.

Osram-Sylvania - 18 wt% Co

The lowest wear rate of this coating sprayed on the hot fixture was 0.0041 mm^3/m which is a 75% higher wear rate than the Metco 2004 coating, Figure 3.85. The highest wear rate for the hot fixture was 0.0064 mm^3/m, a 175% higher wear rate. The coating sprayed on the cold fixture had higher wear rates than similar coatings sprayed on the hot fixture. The lowest wear rate for this coating sprayed on the cold fixture was 0.0056 mm^3/m, the highest was 0.0082 mm^3/m, 136% and 247% higher than the Metco 2004 coating respectively.

Nanodyne™ 15 wt% Co B

There was very little distinction in the lowest wear rates between the hot and cold fixtures for these coatings, Figure 3.86. The lowest wear rate for this coating was 0.0032 mm^3/m, sprayed on the hot fixture, which resulted in a 40% higher wear rate than the Metco 2004 coating. The highest wear rate was 0.0048 mm^3/m, 108% higher wear rate than the Metco 2004 coating.

This powder did not show any distinctive trend in wear rate between the hot and cold fixture, Figure 3.86. The difference in the two fixtures was greater in the case of the porosity. The nitrogen-only spray condition resulted in large differences between the hot and cold fixture, in the most extreme 5.8% vs. 1.4% porosity, see Figure 3.72. The reason for the large difference in porosity between hot and cold fixture was probably due to oxidation of the carbides. Coatings on the hot fixture were cooled with compressed air; the coatings made with the cold fixture were cooled with nitrogen. Work by Roebuck et al., has shown that the temperature for the oxidation of the carbides decreases with decreasing size [59-62, 84]. The oxides have relatively poor properties and would pull out during polishing, resulting in higher apparent porosity. The 6 cfm condition sprayed on the cold fixture was 20% harder than the same condition sprayed on the hot fixture as well as being 20% harder than the 5 cfm condition with the cold fixture, see Figure 3.81.

3.4 Chemical and Phase Analysis

Since a large number of coating powders were sprayed, it was not possible to fully examine each and every coating. Four coatings were chosen for further analysis. These coatings were selected because they had the lowest wear rate of the coatings in their group. Since the largest change in the wear rate was linked to the change in wt% Co, coatings that represented a range of cobalt contents were chosen, as well as the conventional powder to be used as a benchmark.

The coatings selected were Metco 2004 12 wt% Co, Osram-Sylvania - 12 wt% Co, Osram-Sylvania - 18 wt% Co, and Nanodyne^{TM}-15 wt% Co B. These coatings allowed for differences in cobalt content as well as in carbide size to be examined. The coatings underwent x-ray diffraction and in-depth chemical analysis, beyond the analysis that the rest of the coatings underwent.

3.4.1 Chemical Analysis

Chemical analysis was performed on coatings sprayed on the cold fixture and the chemistry data illustrated several phenomenon. The magnitude of the loss of carbon in the spraying process was apparent , see Table 3.5, as well as the effectiveness of the addition of carbon to the feedstock powder as means for limiting the carbon loss, see Table 3.6. Furthermore, the chemical analysis revealed that the weight percentage of cobalt in the coatings was slightly different than expected based on the weight percentage of cobalt in the starting powders, Table 3.7.

3.4.2 X-ray Diffraction

Cobalt absorbs copper Kα radiation and due to this interaction the peaks for Co are weaker than would be expected for the amount of cobalt in the specimens. The amorphous character of the matrix further broadens this weak peak, and as a result there was no discernable cobalt peak in the sprayed coatings. When examining the powder the cobalt peak was easily seen.

X-ray Diffraction of the Powders

The X-ray diffraction data for the Metco 2004, Osram-Sylvania - 12 wt% Co and Osram-Sylvania - 18 wt% Co powders show the expected peaks for WC and Co with no other phases being present, Table 3.8. The Nanodyne^{TM} 15 wt% Co powder was anomalous in that it had no cobalt peak. The spray drying method used to produce the Nanodyne^{TM} 15 wt% Co powder in non-stoichiometric ratios, like 15 wt% Co, resulted in amorphous cobalt being produced. The amorphous nature was the reason that the cobalt in the powder cross sections had a globular appearance.

X-ray Diffraction of the Coatings

The qualitative nature of the analysis, along with the lack of a cobalt peak in the sprayed coating, limits the information that can be gained from the XRD data. The presence or absence of phases can be seen and discussed with some certainty. The relative amount of the phases can only be qualitatively discussed in terms of the degradation that the WC has undergone, Table 3.9.

The previous heat treatment research [36, 37, 65, 66 , 67, 68] would indicate that at least some of the phases that may be in a heat treated coating might not develop in the sprayed coating due to the thermal cycle. Most of the phases that are that are seen in heat treated coatings but not seen in sprayed coating contain cobalt. In the spraying process, the cobalt is expected to melt and then be quenched rapidly. The temperature was high enough in many of the spray conditions that considerable melting of the carbides occurred as well. Work by both Jia and Stewart [33, 35] showed a high percentage of W dissolved in the matrix. This would impede phase formation, as W diffuses slowly. The phases that are reported to form in WC-Co alloys, all involve W, Co and C in specific ratios. There is likely not enough time in the spraying process for large scale mixing of all the elements necessary to form an eta phase in large enough amounts to be detected by XRD.

3.5 Transmission Electron Microscopy of Coatings

The TEM images of the nanoscale carbides in the matrix can be seen in Figure 3.87 and 3.88. The carbides were found to be in the expected size range (≈100 nm) and to have very distinct rectangular shaped crystals. The matrix around the carbides is glassy and there are few if any carbide/carbide interfaces. Figure 3.89 is of a region of matrix that was free of carbides. The diffraction pattern obtained from the area seen in Figure 3.89 was clearly amorphous (Figure 3.90). The TEM images show that the matrix in the coating was glassy in nature resulting in diffuse rings in the diffraction pattern. These images, combined with the lack of a cobalt peak in the XRD data, indicates that the matrix was amorphous in all the coatings tested. The matrix was likely to have been amorphous in all the coating as the coatings tested were generally the lower enthalpy conditions.

3.6 Hot vs. Cold Fixture Coatings

The most sprayable powders were sprayed on both a hot fixture and a cold fixture as previously described in the experimental section. The Nanodyne^{TM} 5 wt% Co and the Inframat^{TM} reconstituted 8 wt% Co were not sprayed on both of the fixtures because a reasonable coating could not be achieved with these powders. These powders had very poor powder characteristics, i.e. size and distribution of the powder particles, which yielded very thin coatings. Even though wear data was collected on these coatings, it is not reasonable to directly compare them with the other powders as the feedstock characteristics were so far out of the range required for plasma spray. However, it is of potential interest that the WC-5 wt% Co powder was sprayed and did create a coating. This implies that with the right powder characteristics a reasonable coating could be created with the high energy plasma spray system using powders with as little as five weight percent cobalt.

Thermal behavior of the substrates on the fixtures was examined. A thermocouple was welded to the backside of a sample bar and was used to measure the maximum temperature that the substrates achieved during spraying. The room temperature at the time of the test was 22.2° C. For all of the thermocouple tests the primary plasma gas flow of 5 cfm N_2 was used with a standoff distance was the standard 200 mm.

The samples were first passed over a single time to determine the effect on the substrate of a single pass. The sample was allowed to cool back to room temperature and then passed over 50 times by the plasma with no powder being added to the plume. The sample was once again allowed to cool. The sample was then passed over by the plume another 50 times by the plume with the powder feed so that a coating was deposited. This procedure was repeated for both the hot and cold fixture.

The thermocouple data is summarized in Table 3.10. The most important difference between the hot and cold fixture is peak temperature of the substrate when the coating was deposited. The temperature was measured from the backside of the substrate so instead of representing the maximum temperature of the coating, it represents the temperature that the coating was quenched to. The hot fixture yielded a maximum temperature of 512° C, whereas the cold fixture showed a maximum temperature of 145° C. The 367° C difference between the two was enough to effect some of the properties of the coatings.

Samples sprayed on the cold fixture were obviously quenched to a lower temperature and maintained at a lower temperature. Another difference between the hot and cold fixture was the amount of time that the coatings were at temperature. The deposition of the coatings took 2-3 minutes. The thermocouple data was collected on the back side of the substrates, therefore the actual temperature experienced by the coatings was likely higher. The temperature may have been high enough on the hot fixture that eta phase, as discussed in the heat treatment literature, could have started to form. The cold fixture would have suppressed these transformations by cooling the coatings to a temperature below which the transformation would not have occurred in the time available. The matrix in these samples may not have had time to develop grain structure and would presumably be softer than the matrix of the coatings sprayed on the hot fixture. This resulted in the cold fixture samples having higher wear rates than the hot fixture samples sprayed with the same powder and conditions.

3.7 Wear of Heat Treated Coatings

Heat treated samples clarified the observation that the difference in the wear rates between the hot and cold fixture was related to the time that the coatings were at temperature. The heat treated coatings showed significant improvement in wear resistance over the non-heat treated coatings, Figure 3.91. The wear rate of the heat treated bars was improved, in the best case, to the same wear rate as the same coating sprayed on the hot fixture. The change in the wear rate of these coatings indicated that the difference in the wear rate between the hot and cold fixture was an effect of the thermal history of the coatings as they were cooling.

As discussed by Axen et al., a small change it the matrix hardness can have a great effect on the wear resistance [77]. The heat treatment data would suggest that the only difference between the hot and cold fixture is the quenching in the latter of the matrix such that there was not enough time for any matrix structure to evolve, yielding a loss in properties. This loss in matrix hardness would be expected from other data on amorphous materials, and materials that show an inverse Hall Petch relationship [85]. As was shown in Figure 3.92, there is a bow wave of material that builds up in front of the carbides as material is removed from behind the carbide. Any increase in the strength of the matrix, or in its resistance to carbide removal of the carbide could substantially improve the wear resistance of the coating. While the wear rate of the heat treated coatings was not improved beyond that of the coating sprayed on the hot fixture, it seems that with further refinement of the heat treatment procedure this may be possible, especially if the coatings were heat treated in vacuum and not in air. There was significant amounts of oxidation on the surface of the heat treated coatings. Vacuum heat treatment would overcome this problem. Furthermore, Guo et al., suggested that of all the heat treatments available, that vacuum annealing resulted in the best properties in WC-Co coatings [68].

3.8 Large vs. Small Powder Size

The Nanodyne^{TM} 12 wt% Co powders were received as two different "cuts" of the same powder. The larger cut, was designated 'Large'. The smaller cut, 'Small', was meant for HVOF spraying. The Lecotrac™ data illustrates the differences in the size distribution of the powders (Figures 3.59 and 3.60). Since these powders were from the same powder batch, the differences between the coatings produced with these powders can be attributed to the differences in their size distributions.

The Large Cut had better wear rates than the small cut in both hot and cold fixtures, though the differences in the wear rate between these coatings was not large for any specific condition, see Figures 3.93 and 3.94. The porosity differences between the two cuts fabricated on the hot and cold fixtures filters out some of the differences between the powders. Whereas, the Large Cut had the same porosity in the hot and the cold fixture, the Small Cut had a large difference between porosity in the hot fixture and the cold fixture, Figure 3.69 and 3.70. The drop in porosity in the Small Cut indicates a greater degree of melting or increased impact velocity yielding a higher penetration degree in the Small Cut than in the Large Cut. The microstructure of the coatings made from the Large Cut showed less than full melting, Figure 3.95. This is manifested by the relatively low hardness and high porosity values in the coating made with the Large Cut.

Lack of melting is associated with lowered splat-splat adhesion. The DSRW test was not sensitive to splat-splat adhesion, so the increase in the amount of the carbides preserved in the coating gives a slightly better resistance for the Large Cut over the Small Cut.

3.9 Osram Sylvania 12 wt% and 18 wt%

Two other powders that were of interest due to their similarities were the powders produced by Osram Sylvania. These powders had nearly identical size distributions and average carbide sizes. Due to these similarities, it was assumed that the only difference in the coatings was due to the cobalt content. The 18 wt% powder's lowest wear rates was twice as high as the lowest wear rate for the 12 wt% powder, Table 3.4. This was the largest difference in wear rate between any of the coatings. It was expected that as the cobalt percentage was increased the wear rate would also increase. A 200% increase in wear rate was not expected. The volume percentages of cobalt was 23% for the 12 wt% and 38% for the 18 wt%, only 15% volume difference. Khruschov's equation (Eq. 27), predicts a 15% change in the wear rate between coatings produced with the two powders. The change in hardness for the two coatings sprayed on the cold fixture for the same spray conditions was approximately 150 HK, which was the difference predicted.

The Osram-Sylvania - 18 wt% Co coatings consistently had the highest wear rates of any of the thick coatings, see Figure 3.85. Not only was the average wear rate higher but the range of the wear rates was also greater. The difference between the hot fixture and the cold fixture was distinct in the nitrogen-only conditions and less so in conditions with hydrogen. Photomicrographs show a high degree of overmelting in the wear scar for the coatings sprayed with hydrogen, see Figure 3.96. The melting and decomposition of the carbides in this case was likely responsible for the lack of difference in the wear rates in the coatings sprayed with hydrogen.

Though the wear rate was lower with the hot fixture, the porosity fraction was lower with the cold fixture. The hardness of the coatings tended to be higher under low enthalpy spraying conditions, with the hot fixture in most conditions having slightly higher hardness values, see Figure 3.78.

Table 3.1. Tungsten Carbide grain size in the powder particles.

Powder	WC Particle Size Range (nanometer)	Wt% Co
Metco 12 wt% Co	1,000-2,000	12
Nanodyne™ 6 wt% Co	200-1,000	6
Nanodyne™ 5 wt% Co	200-1,500	5
Nanodyne™ 12 wt% Co Small	300-500	12
Nanodyne™ 12 wt% Co Large	300-500	12
Inframat™ 8 wt% Co	100-300	8
Osram-Sylvania 18 wt% Co	200-1,200	18
Osram-Sylvania 12 wt% Co	200-1,200	12
Nanodyne™ 15 wt% Co	10-100	15

Table 3.2. Thermal spray powder characteristics.

Lot No.	**Size Range (μm)**	**Fines**	**Powder Flow**	**Spray Particle Structure**
Metco 12 wt% Co	8 to 110	No Fines	easy	1
Metco 17 wt% Co	9 to 140	No Fines	easy	1
Metco 12 wt% Co	10 to 70	No Fines	Easy	1
Nanodyne™ 12 wt% Co	1 to 205	Few Fines	OK	Thick-walled Spheres
Nanodyne™ 15 wt% Co	10 to 100	Many Fines	Poor	Mostly 1+ also 2, 3, 6
Nanodyne™ 6 wt% Co	50 to 200	Many Fines	Poor	2, 3, 6, 5
Nanodyne™ 15 wt% Co	5 to 300	Many Fines	Poor	5, 3
Nanodyne™ 5 wt% Co	5 to 200	Almost all fines	Poor	2
Nanodyne™ 12 wt% Co Large	20 to 110	Few Fines	Easy	Mostly 5, also 2, 3, 4, 6
Nanodyne™ 12 wt% Co Small	10 to 50	Few Fines	Easy	
Inframat™ 8 wt% Co	2 to 20	No Fines	Easy	5
Osram-Sylvania 18 wt% Co	10 to 70	No Fines	Easy	1
Osram-Sylvania 12 wt% Co	10 to 70	No Fines	Easy	1

1. Solid spheres
2. Thin-walled spheres
3. Thick-walled spheres
4. Multi-layered spheres
5. Porous spheres
6. Thin/thick-walled spheres fill with small particles or debris

Table 3.3. Powder particle size by Lecotrac™ and SEM observation.

Powder Type	Mode Particle Size (μm)	Range of Particle Sizes (μm)	Range Around the Mode (%)
Micrometer Carbides			
Metco 12 wt% Co	26	10-75	80% in 15-37
Nanomyte™ 12 wt% Co	30[1]	10-50[1]	na
Submicrometer Carbides			
Nanodyne™ 12 wt% Co Large	75	25-100	65% in 55-85
Nanodyne™ 12 wt% Co Small	65	1-100	58% in 45-75
Osram-Sylvania 12 wt% Co	30	20-60	90% 20-45
Osram-Sylvania 18 wt% Co	30	20-60	89% in 20-45
Inframat™ 8 wt% Co	15	4-40	60% in 5-25
Nanodyne™ 6 wt% Co	90	10-150	30% in 75-100
Nanodyne™ 5 wt% Co	na	na	na
Nanoscale Carbides			
Nanodyne™ 15 wt% Co	75	1-100	40% in 55-85
Nanodyne™ 15 wt% Co, seived	75[1]	50-85[1]	na

[1] estimation from SEM observations

Table 3.4. Wear rate, porosity, hardness of the coatings.

Powder	**Fixture**	**Condition (CFM)**	**Wear Rate (mm^3/m)**	**Porosity**	**Hardness (HK)**
Metco 2004	hot	7 N2	0.00256	21.6	676.4
		6 N2	0.00236	20.9	680
		5 N2	0.00278	17.3	971.9
		6N2 1H	0.00273	2.5	1077
		5N2 1H	0.00407	2.4	1077
Metco 2004	cold	6 N	0.00354	8.8	1030
		5.5 N	0.00312	8.3	1194
		5 N	0.00329	4.4	1097
		4 N	0.00378	6.7	1073
		5.5 N 1/2 H	0.00361	7.9	1095
		5N 1/2 H	0.00467	3.8	947
Nanomyte™ 12 wt% Co	hot	6N	0.00293	11.1	806
		5N	0.00298	5.5	981
		4N	0.00359	2.2	945
		6N 1/2H	0.0029	3.3	1004
		5N 1/2H	0.00309	5.3	936
Nanomyte™ 12 wt% Co	cold	6N	0.00358	22.6	812
		5N	0.00412	3.3	916
		4N	0.00406	19.0	n.a
		6N 1/2H	0.00475	22.6	n.a.
		5N 1/2H	0.00435	24.7	n.a
Nanodyne™ 12 wt% Co - Large Cut	hot	6N	0.00343	3.5	776
		5N	0.00248	3.7	962
		4N	0.00324	1.0	1113
		6N 1/2H	0.0024	5.7	n.a.
		5N 1/2H	0.00241	2.2	997
		4N1/2H	0.00372	6.5	989
Nanodyne™ 12 wt% Co - Large Cut	cold	6N	0.0029	7.5	867
		5N	0.00282	5.5	1064
		4N	0.0028	2.0	1019
		6N 1/2H	0.0028	4.7	1065
		5N 1/2H	0.00253	2.9	1022

Table. 3.4. Continued.

Powder	Fixture	Condition (CFM)	Wear Rate (mm³/m)	Porosity	Hardness (Kp)
Nanodyne™ 12 wt% Co Small Cut	hot	6N	0.00327	5.7	945
		5N	0.00328	3.8	1163
		4N	0.00418	3.1	1098
		6N 1/2H	0.00308	5.4	1110
		5N 1/2H	0.00357	3.5	1116
Nanodyne™ 12 wt% Co Small Cut	cold	6N	0.0035	5.6	1010
		5N	0.003	4.3	979
		4N	0.00344	2.1	1043
		6N 1/2H	0.00301	1.5	1033
		5N 1/2H	0.00295	1.7	1002
Osram-Sylvania 12 wt% Co	hot	6N	0.00226	1.5	1019
		5N	0.00309	3.7	1139
		4N	0.00317	0.9	991
		6N 1/2H	0.00267	1.2	1158
		5N 1/2H	0.00395	1.4	n.a.
Osram-Sylvania 12 wt% Co	cold	6N	0.00289	4.8	1200
		5N	0.00332	5.1	1052
		4N	0.00472	4.4	1121
		6N 1/2H	0.00366	4.8	997
		5N 1/2H	0.00538	4.3	920
Osram-Sylvania 18 wt% Co	hot	5N	0.00438	6.6	1041
		4N	0.00406	7.0	1015
		5N 1/4H	n.a	2.7	972
		5N 1/2H	0.0064	5.0	865.5
		4N 1/2H	0.00609	3.6	n.a.
Osram-Sylvania 18 wt% Co	cold	5N	0.00557	4.1	1108
		4N	0.00703	3.5	981
		5N 1/4H	0.00821	2.0	854
		5N 1/2H	0.00693	2.6	854
		4N 1/2H	0.00742	1.7	881

Table 3.4. Continued.

Powder	**Fixture**	**Condition (CFM)**	**Wear rate (mm³/m)**	**Porosity**	**Hardness (Kp)**
Nanodyne™ 15 wt% Co	hot	6N	0.00325	5.0	1014
		5N	0.00393	5.9	1041
		4N	0.00485	4.0	n.a.
		6N 1/2H	0.00318	1.4	1111
		5N 1/2H	0.00391	1.9	1096
Nanodyne™ 15 wt% Co	cold	6N	0.00401	2.3	1217
		5N	0.00357	1.6	1024
		4N	0.00468	3.4	971
		6N 1/2H	0.00369	1.4	1029
		5N 1/2H	0.00445	1.8	1014

Table 3.5. Carbon content of selected coatings.

	Osram-Sylvania 18 wt% Co	Osram-Sylvania 12 wt% Co	Metco-2004 12 wt% Co	Nanodyne™ 15 wt% Co
Actual wt%C	2.53	1.76	3.65	1.68
Ideal wt%C	5.0	5.3	5.3	5.2
Difference wt%C	2.47	3.54	1.65	3.52
Percentage carbon lost	49%	67%	30%	67%

Table 3.6. Osram-Sylvania - 18 wt% Co sprayed on cold fixture with carbon added to feedstock powder.

Carbon added to powder	0 wt%	1 wt%	2 wt%	3 wt%	4 wt%
wt % C in coating	2.53	2.80	3.02	3.16	3.29
Increase in wt% C remaining in coating per addition of 1wt% C	0	0.27	0.22	0.14	0.13
Percentage Carbon Retained	49%	56%	60%	63%	65%

Table 3.7. Chemistry of selected coatings sprayed on the cold fixture.

Elements	Osram-Sylvania 18 wt% Co	Osram-Sylvania 12 wt% Co	Metco-2004 12 wt% Co	Nanodyne™ 15 wt% Co
C wt%	2.53	1.76	3.65	1.68
Co wt%	16.80	12.19	12.39	13.70
O ppm	1710	570	1070	1920
W wt%	80.49	84.00	83.69	82.95

Table 3.8. Phases detected in the as-received powders by XRD.

Powder	WC	W_2C	W	Co
Metco-2004 12 wt% Co	Yes	No	No	Yes
Osram-Sylvania 12 wt% Co	Yes	No	No	Yes
Osram-Sylvania 18 wt% Co	Yes	No	No	Yes
Nanodyne™ 15 wt% Co	Yes	No	No	No

Table 3.9. Phases detected in the sprayed coatings by XRD.

Coating	Fixture	WC	W_2C	W	Co
Metco-2004 12 wt% Co	hot	Yes	Yes	No	No
Metco-2004 12 wt% Co	cold	Yes	Yes	No	No
Osram-Sylvania 12 wt% Co	hot	Yes	Yes	Yes	No
Osram-Sylvania 12 wt% Co	cold	Yes	Yes	Yes	No
Osram-Sylvania 18 wt% Co	hot	Yes	Yes	Yes	No
Osram-Sylvania 18 wt% Co	cold	Yes	Yes	Yes	No
Nanodyne™ 15 wt% Co	hot	Yes	Yes	Yes	No
Nanodyne™ 15 wt% Co	cold	Yes	Yes	Yes	No

Table 3.10. Thermocouple readings from Hot and Cold fixture.

	First Pass	**Fifty Passes Plasma**	**Fifty Passes Coating**
Cold Fixture	60 °C	104 °C	145 °C
Hot Fixture	135 °C	443 °C	512 °C

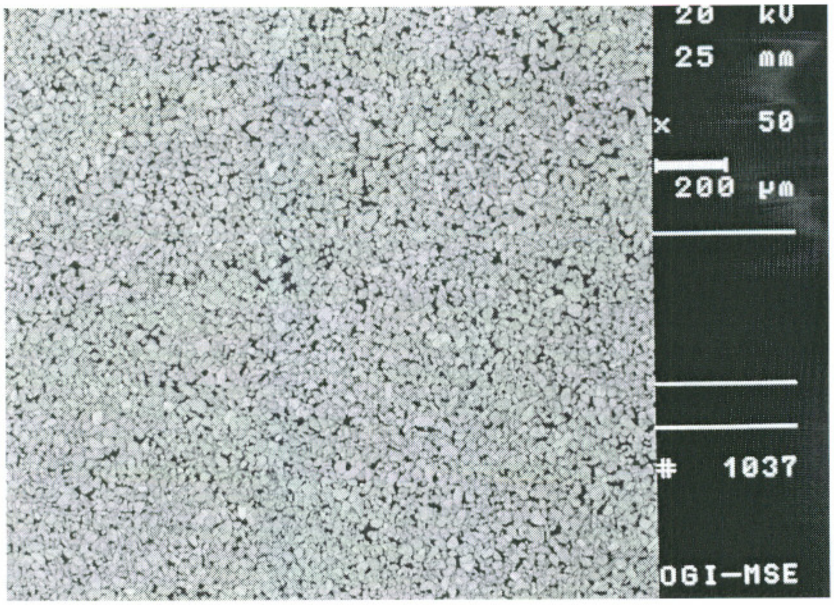

Figure 3.1. SEM image of Metco 2004 WC-12 wt% Co powder, 50X.

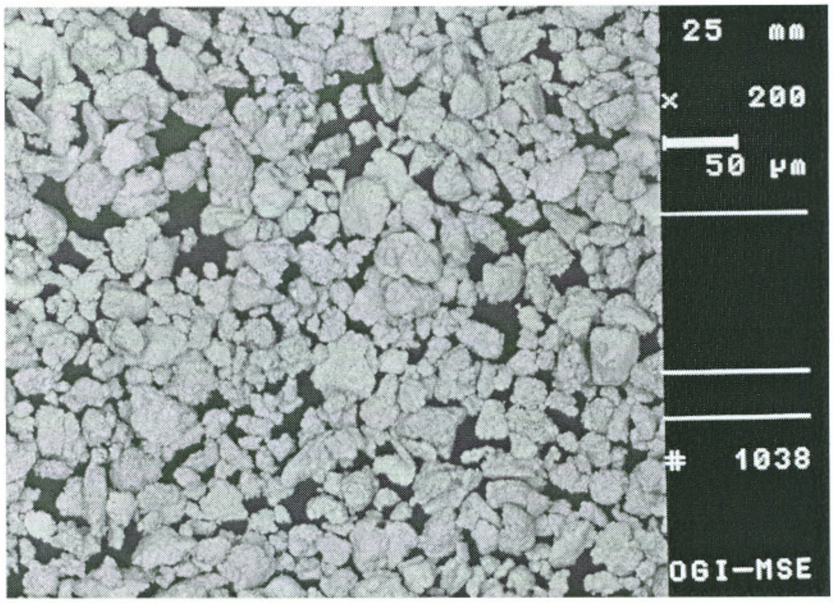

Figure 3.2. SEM Image of Metco 2004 WC-12 wt% Co Powder, 200X.

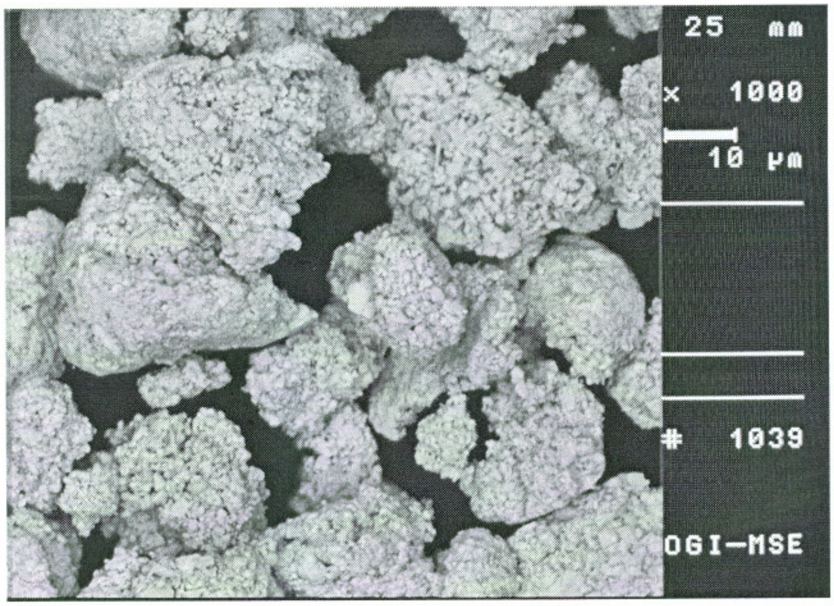

Figure 3.3. SEM image of Metco 2004 WC-12 wt% Co powder, 1000X.

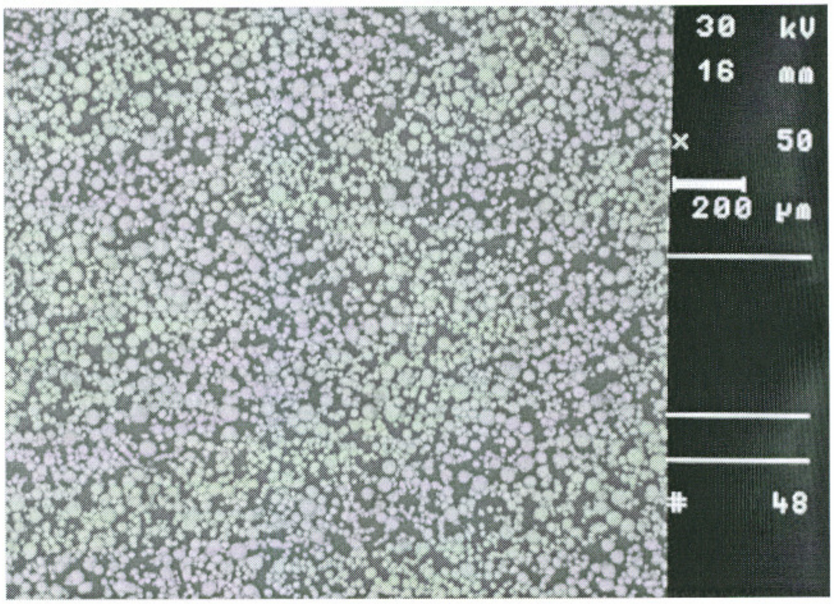

Figure 3.4. SEM image of Nanomyte™ WC-12 wt% Co powder, 50X.

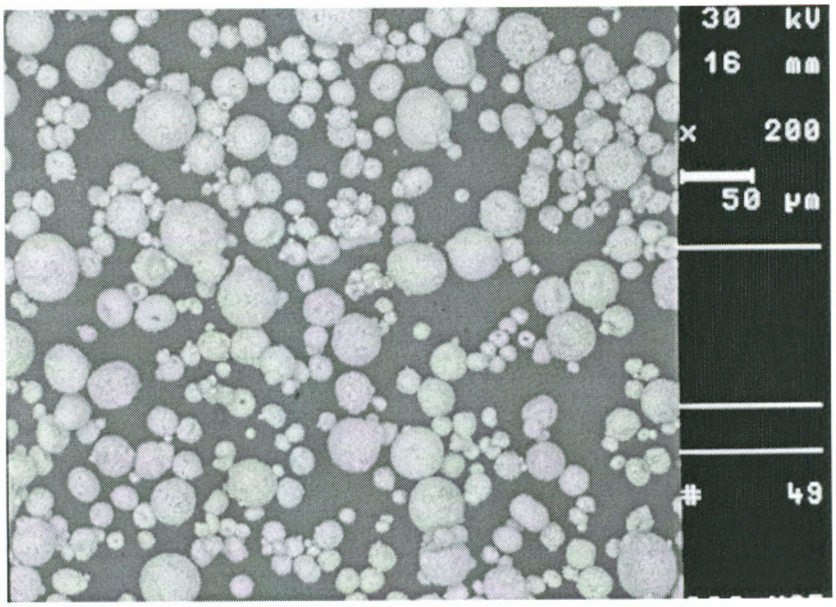

Figure 3.5. SEM image of Nanomyte^{TM} WC-12 wt% Co powder, 200X.

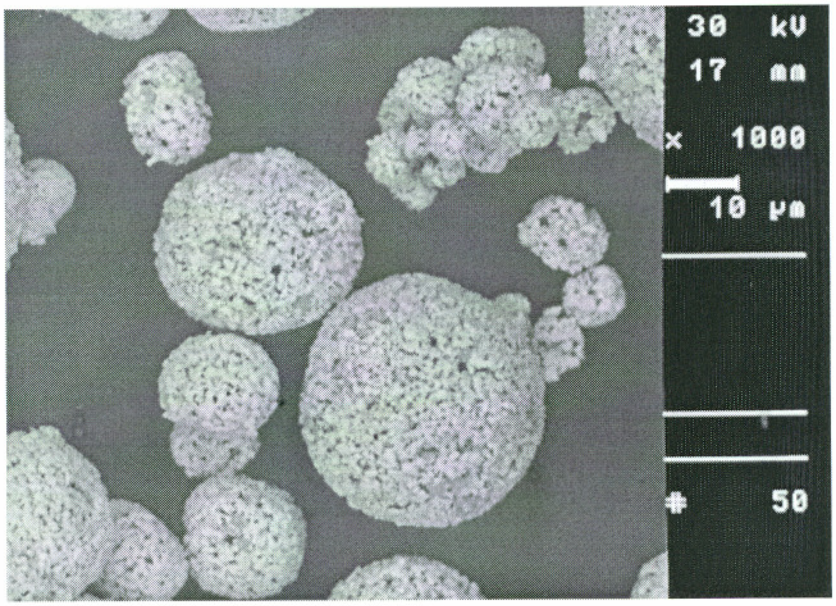

Figure 3.6. SEM image of Nanomyte^{TM} WC-12 wt% Co powder, 1000X.

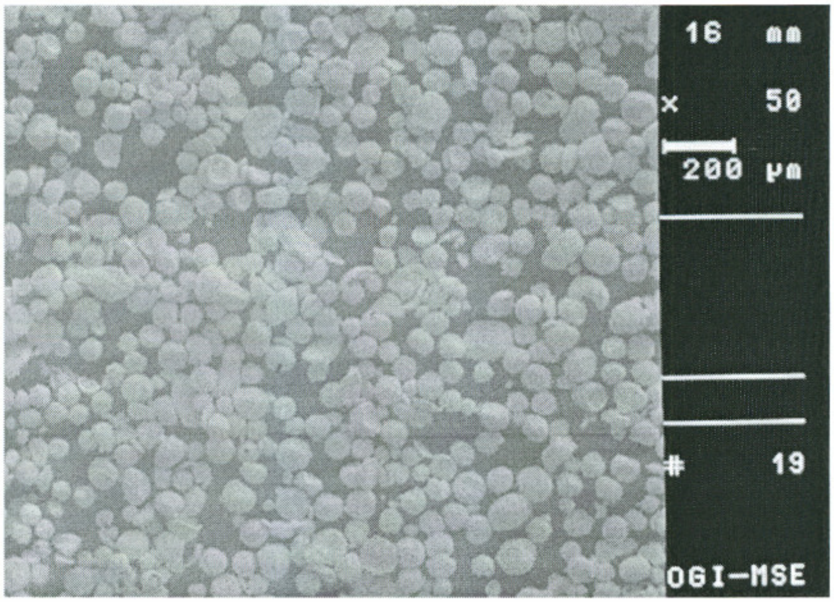

Figure 3.7. SEM image of Nanodyne™ WC-12 wt% Co large cut, 50X.

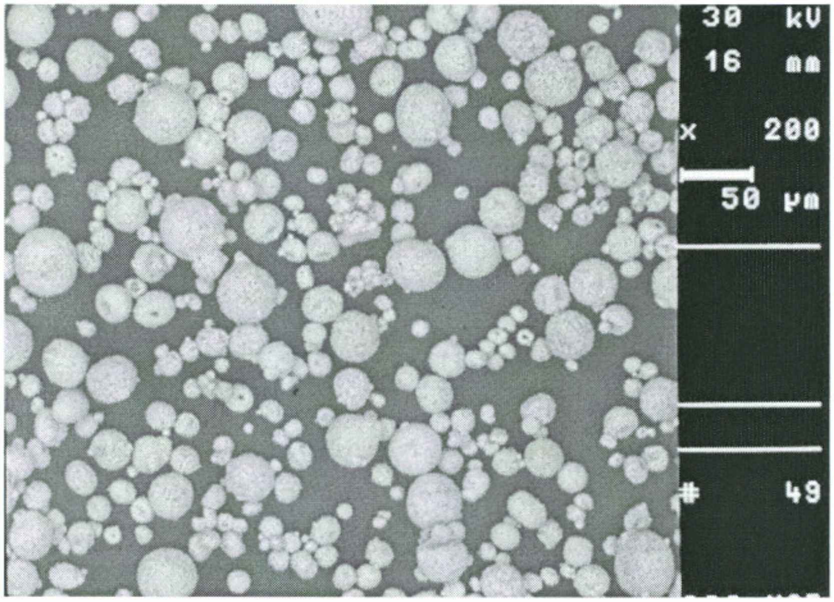

Figure 3.8. SEM image of Nanodyne™ WC-12 wt% Co large cut, 200X.

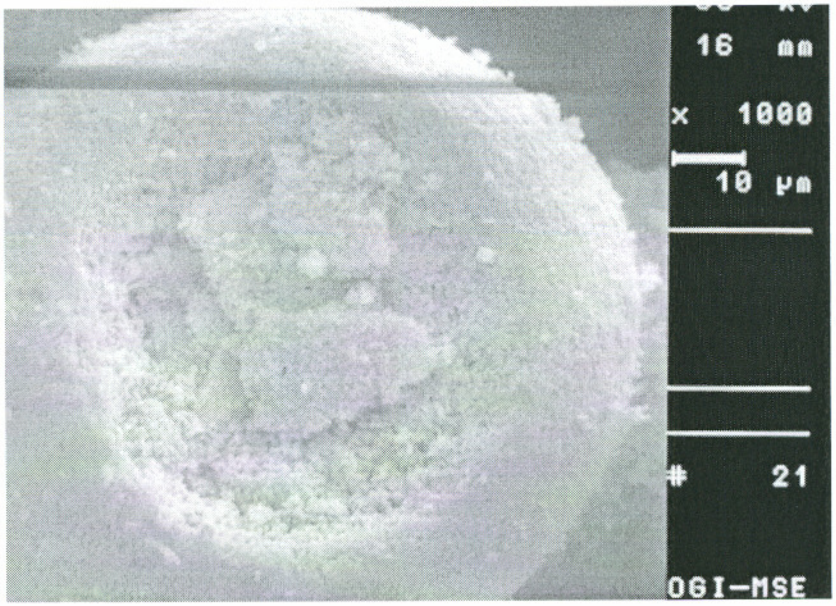

Figure 3.9. SEM image of Nanodyne™ WC-12 wt% Co large cut, 1000X.

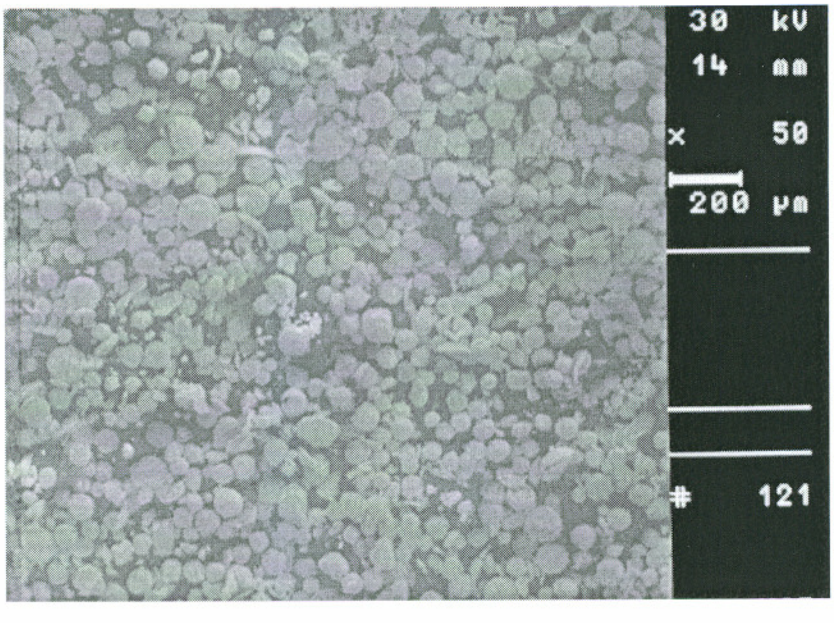

Figure 3.10. SEM image of Nanodyne™ WC-12 wt% Co small cut, 50X.

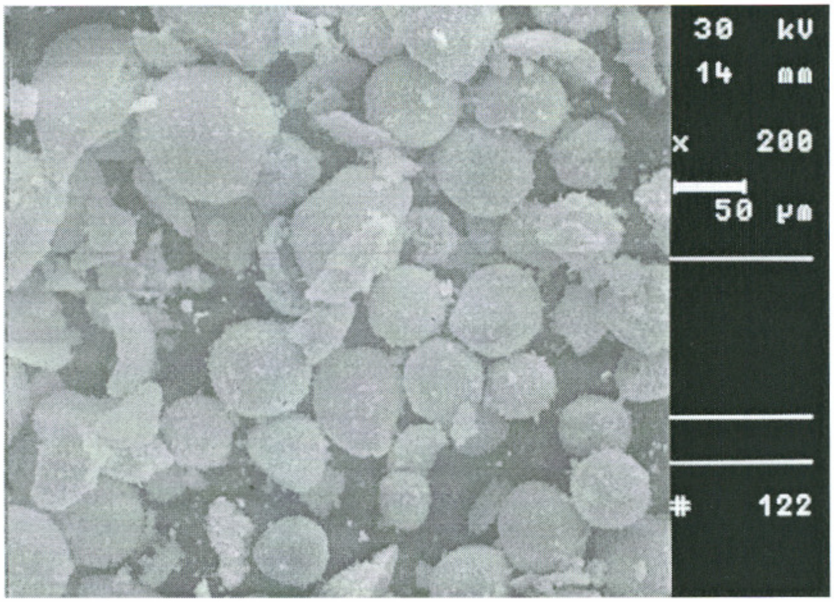

Figure 3.11. SEM Image of Nanodyne^{TM} WC-12 wt% Co small cut, 200X.

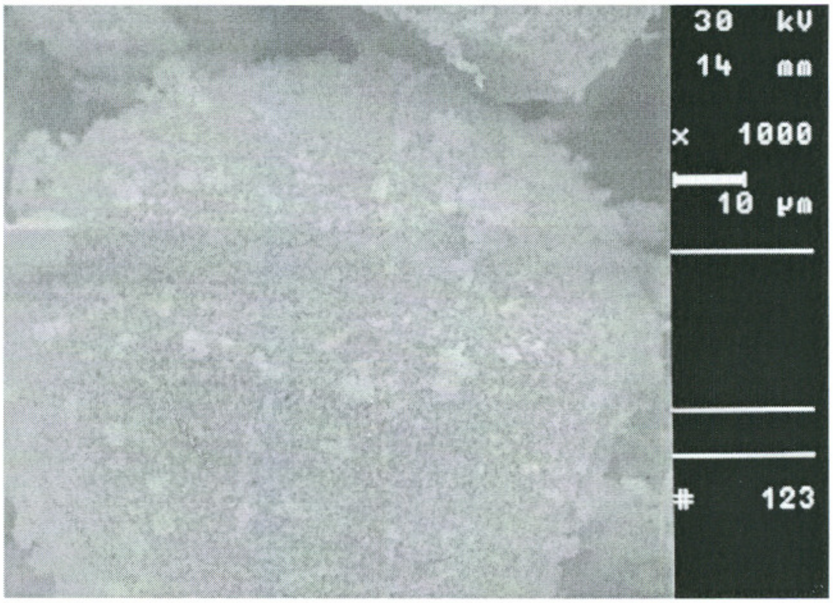

Figure 3.12. SEM image of Nanodyne^{TM} WC-12 wt% Co small cut, 1000X.

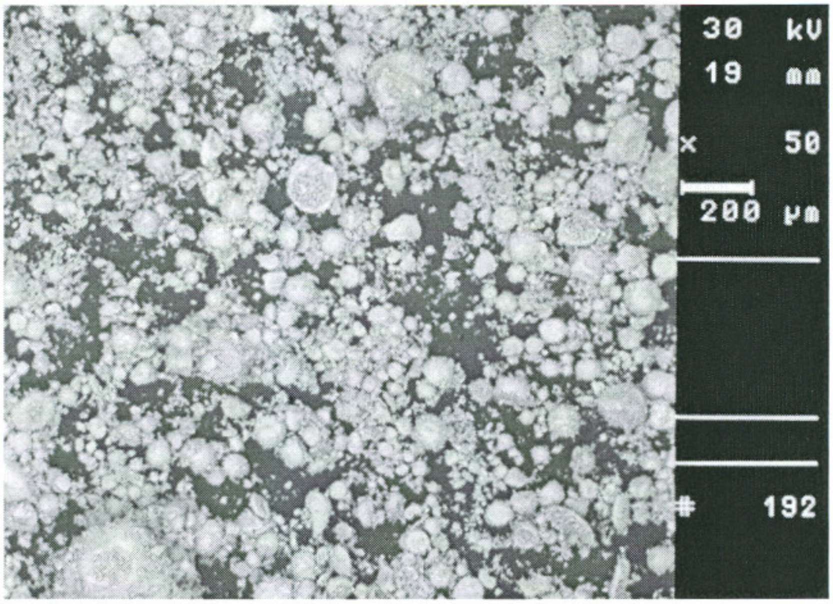

Figure 3.13. SEM image of Nanodyne™ WC-15 wt% Co, as received, at 50X.

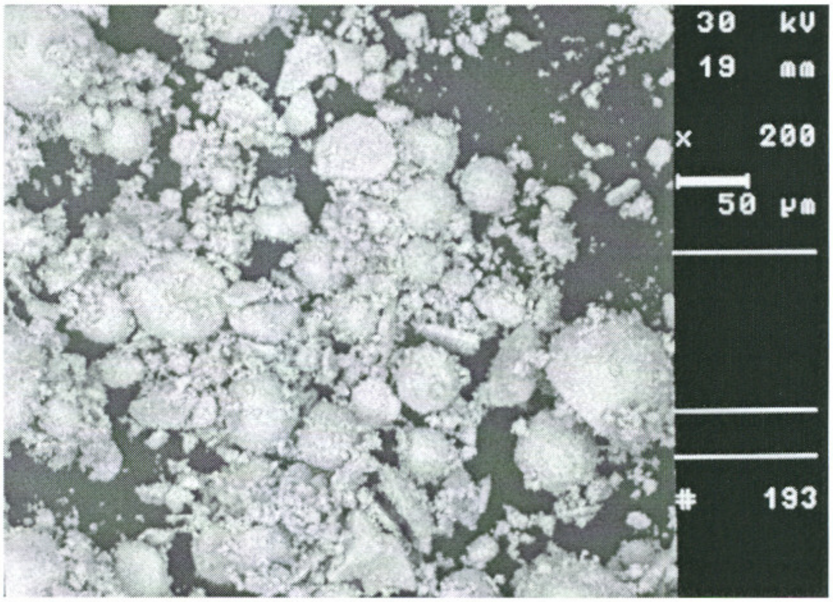

Figure 3.14. SEM image of Nanodyne™ WC-15 wt% Co, as received, at 200X.

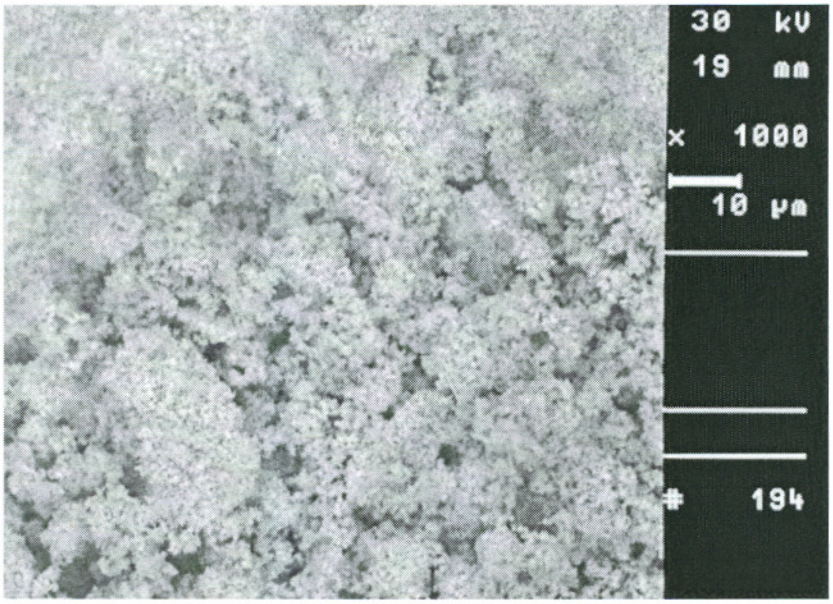

Figure 3.15. SEM image of Nanodyne™ WC-15 wt% Co, as received, at 1000X.

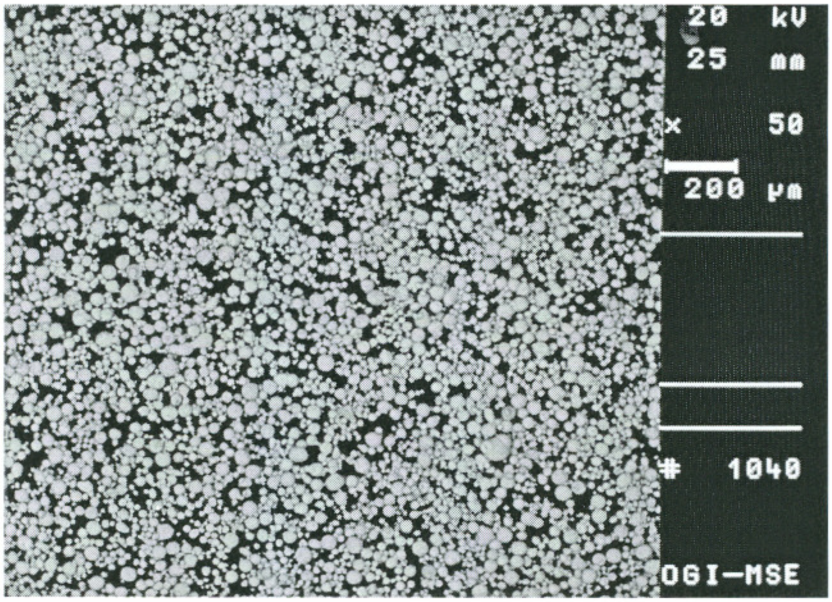

Figure 3.16. SEM image of Nanodyne™ WC-15 wt% Co, sieved, at 50X.

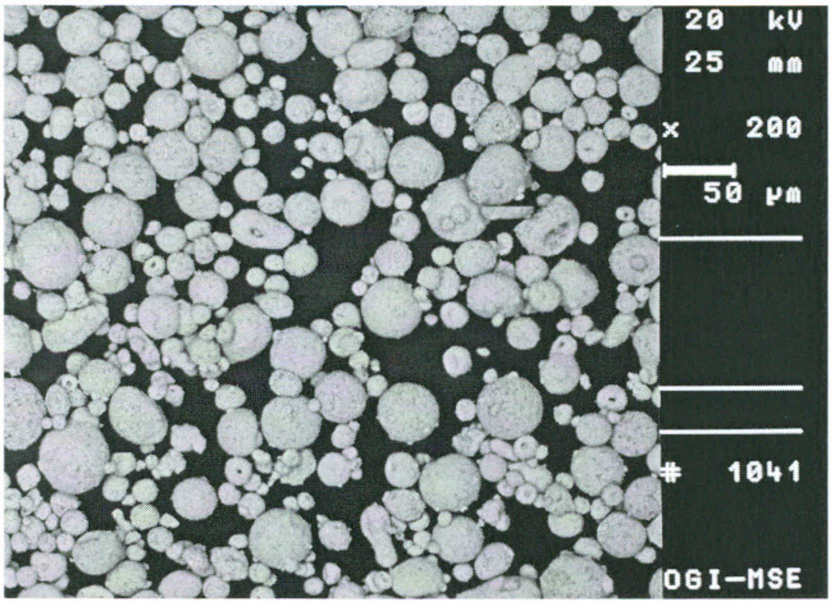

Figure 3.17. SEM image of Nanodyne™ WC-15 wt% Co, sieved, at 200X.

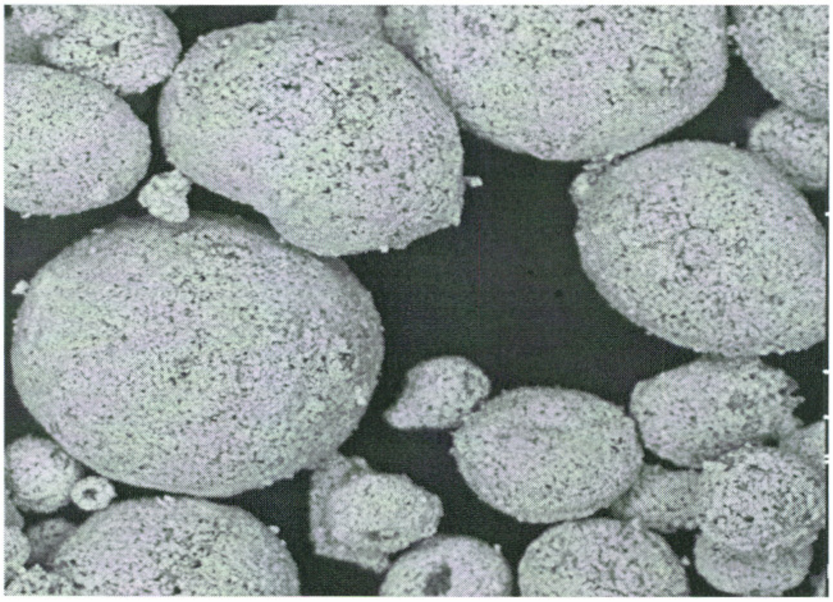

Figure 3.18. SEM image of Nanodyne™ WC-15 wt% Co, sieved, at 1000X.

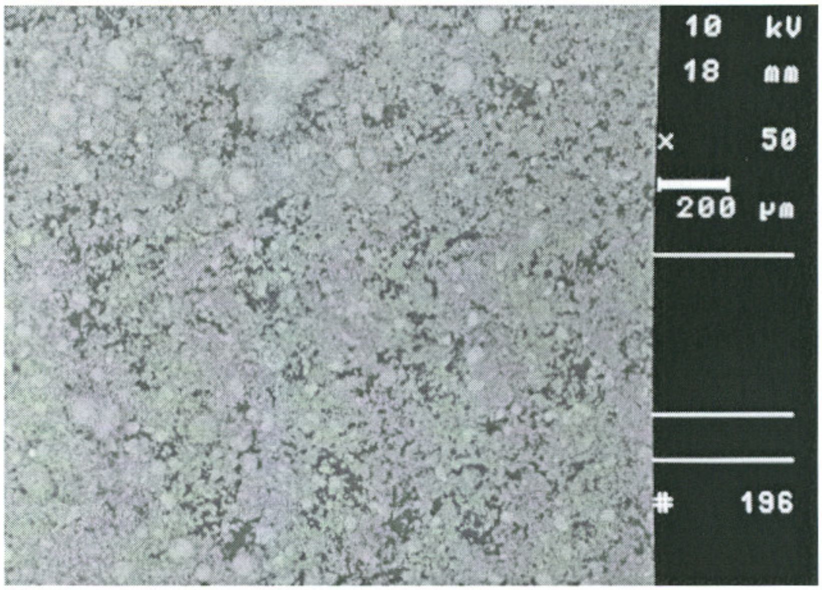

Figure 3.19. SEM image of Nanodyne™ WC-5 wt% Co, at 50X.

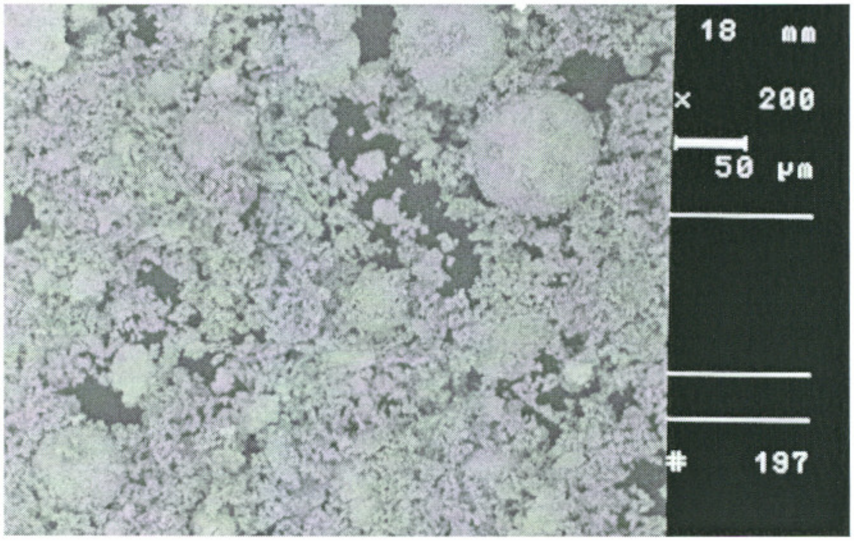

Figure 3.20. SEM image of Nanodyne™ WC-5 wt% Co, at 200X.

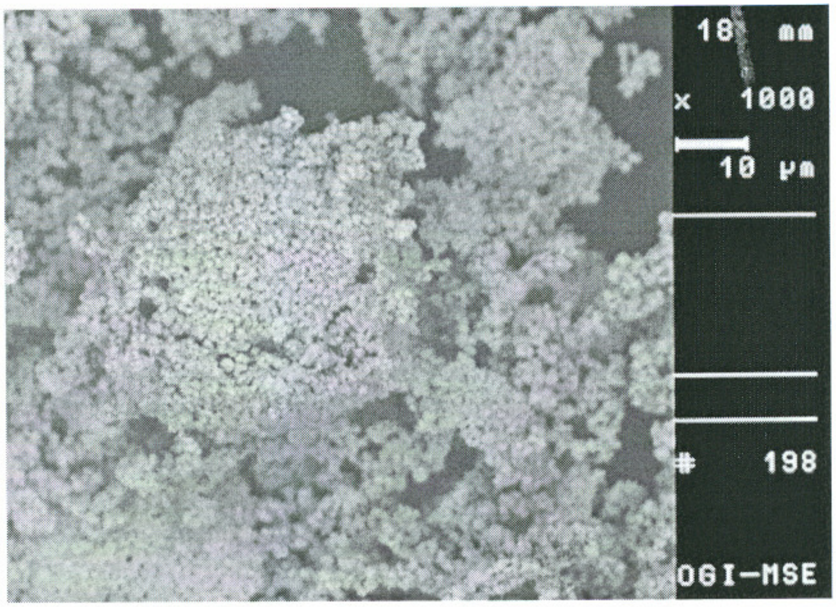

Figure 3.21. SEM image of Nanodyne^{TM} WC-5 wt% Co, at 1000X.

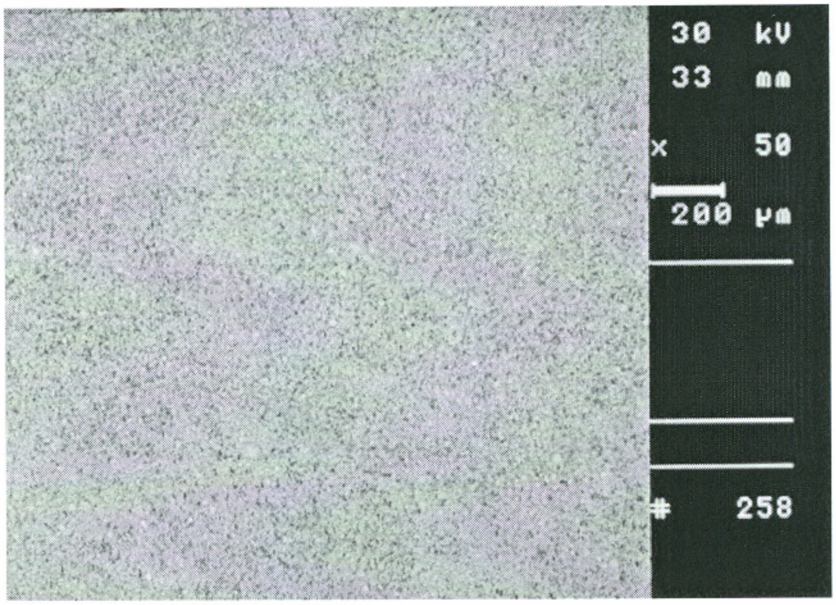

Figure 3.22. SEM image of Inframat^{TM} WC-8 wt% Co, at 50X.

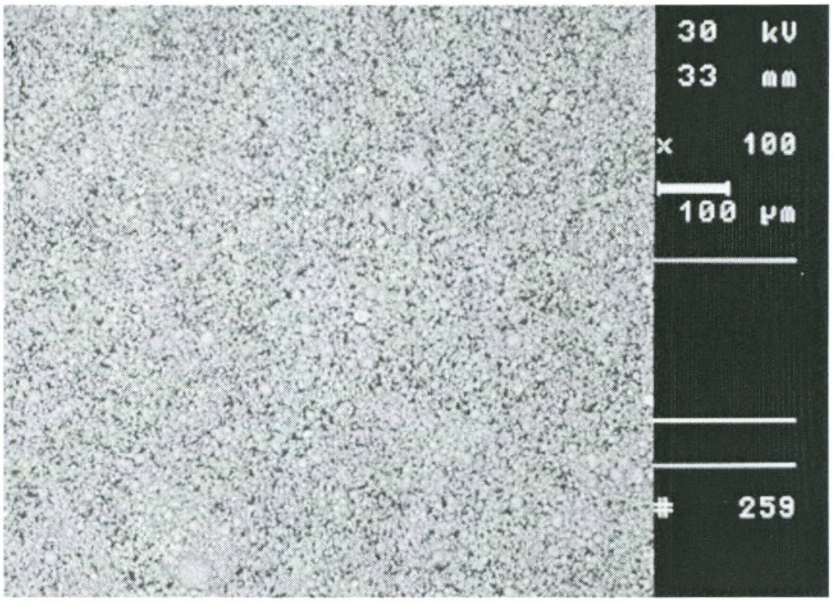

Figure 3.23. SEM image of Inframat™ WC-8 wt% Co, at 100X.

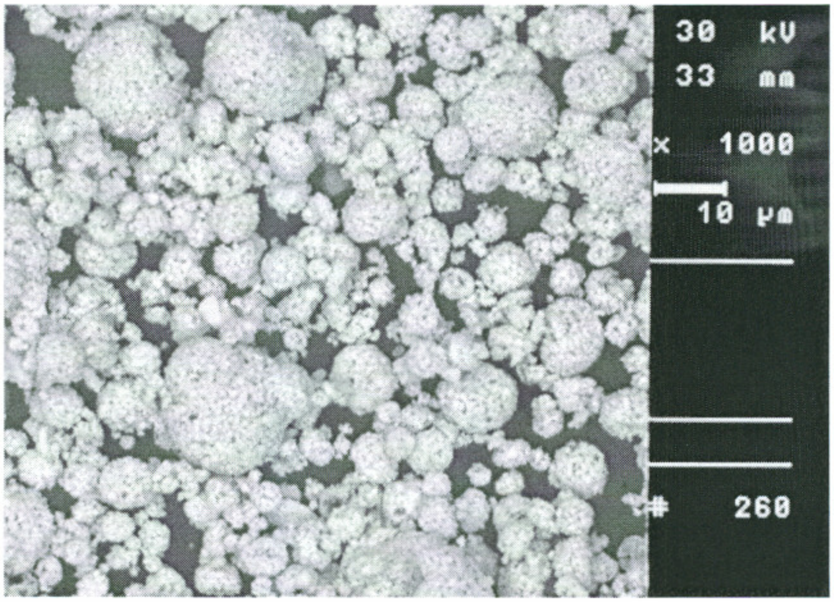

Figure 3.24. SEM image of Inframat™ WC-8 wt% Co, at 1000X.

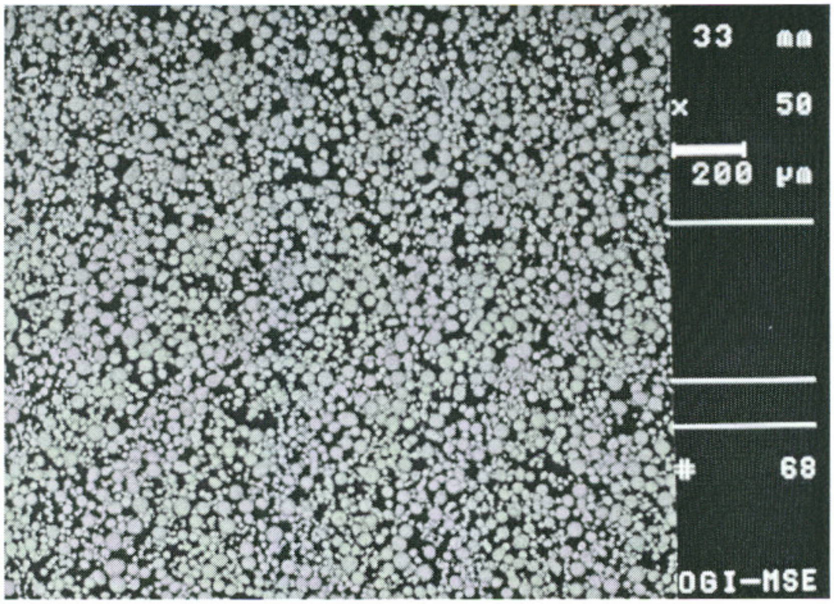

Figure 3.25. SEM image of Osram Sylvania WC-12 wt% Co, at 50X.

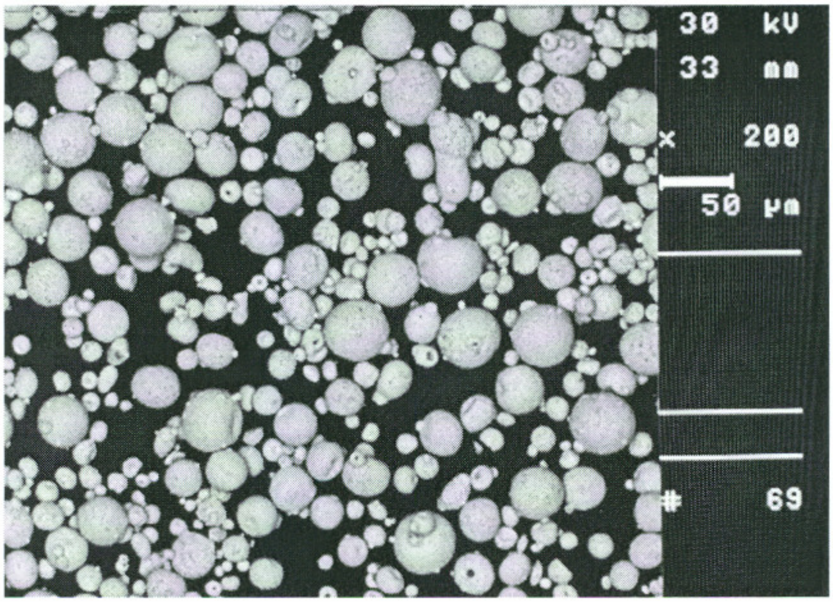

Figure 3.26. SEM image of Osram Sylvania WC-12 wt% Co, at 200X.

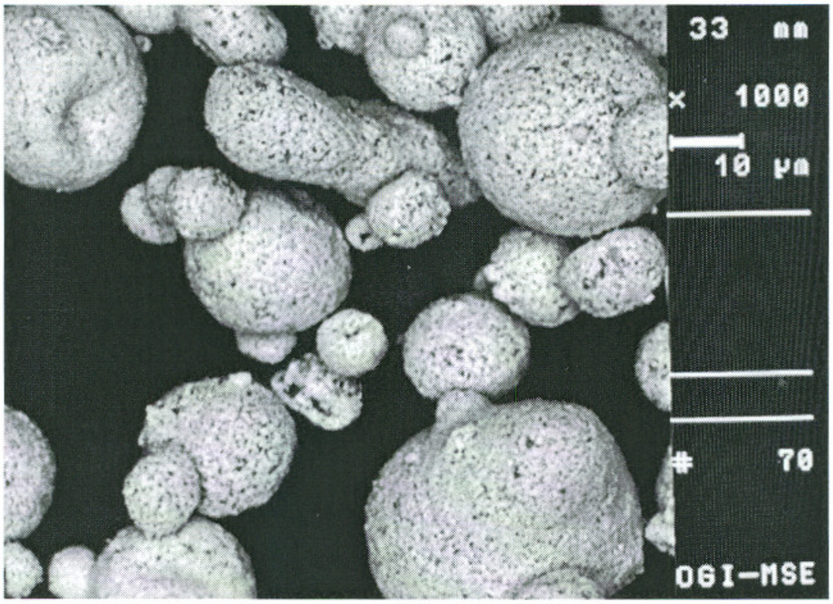

Figure 3.27. SEM image of Osram Sylvania WC-12 wt% Co, at 1000X.

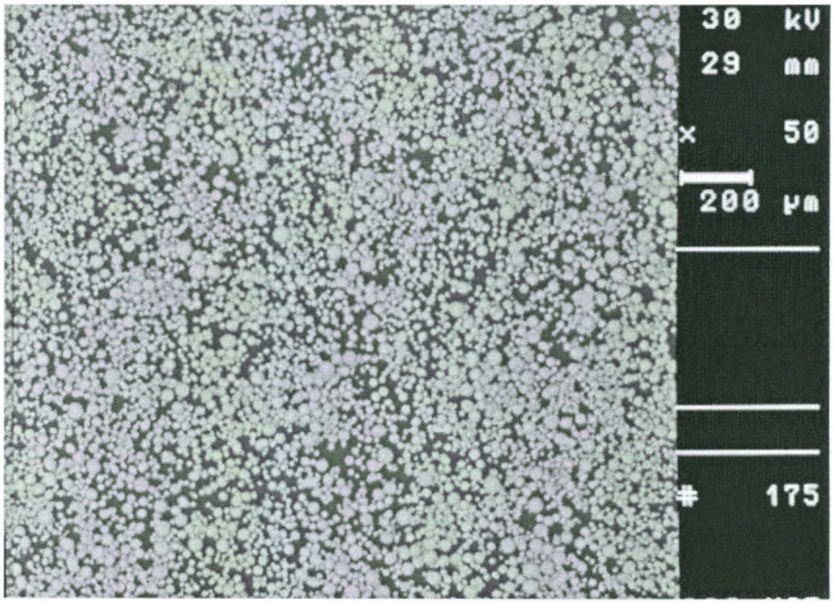

Figure 3.28. SEM image of Osram Sylvania WC-18 wt% Co, at 50X.

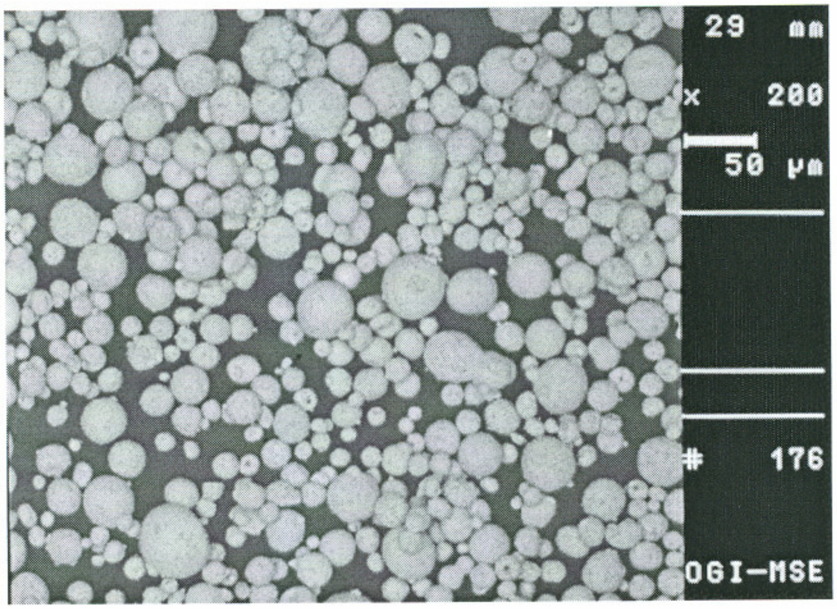

Figure 3.29. SEM image of Osram Sylvania WC-18 wt% Co, at 200X.

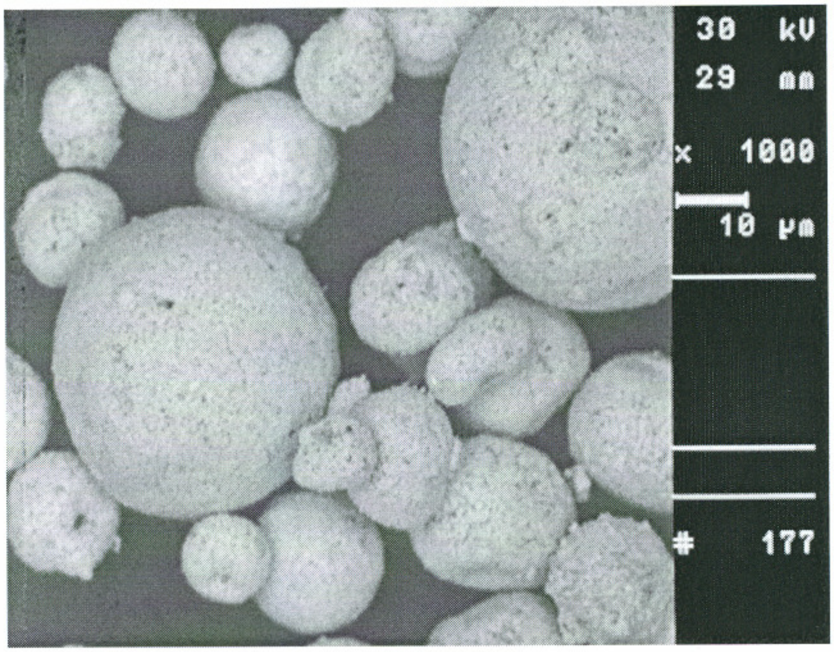

Figure 3.30. SEM image of Osram Sylvania WC-18 wt% Co, at 1000X.

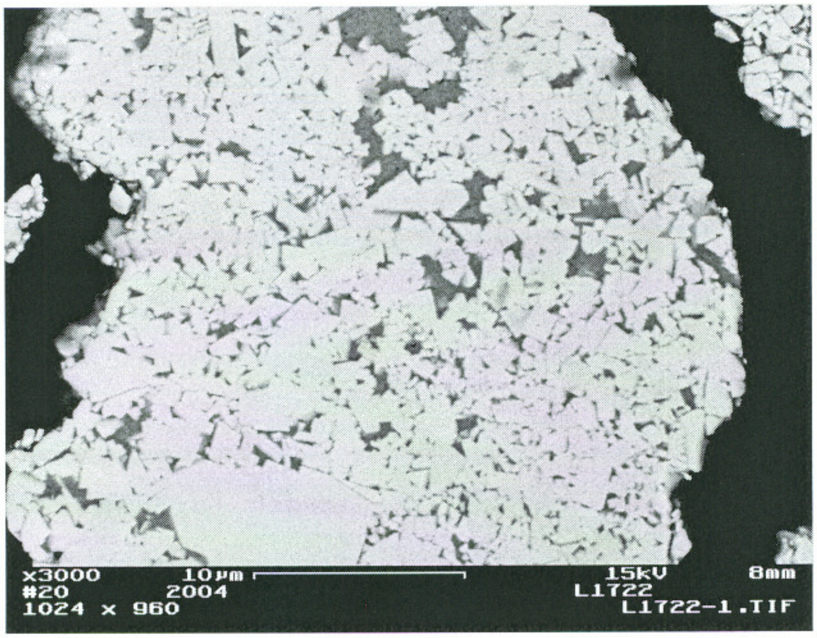

Figure 3.31. FESEM image of Metco 2004 WC-12 wt% Co powder cross section, 3000X.

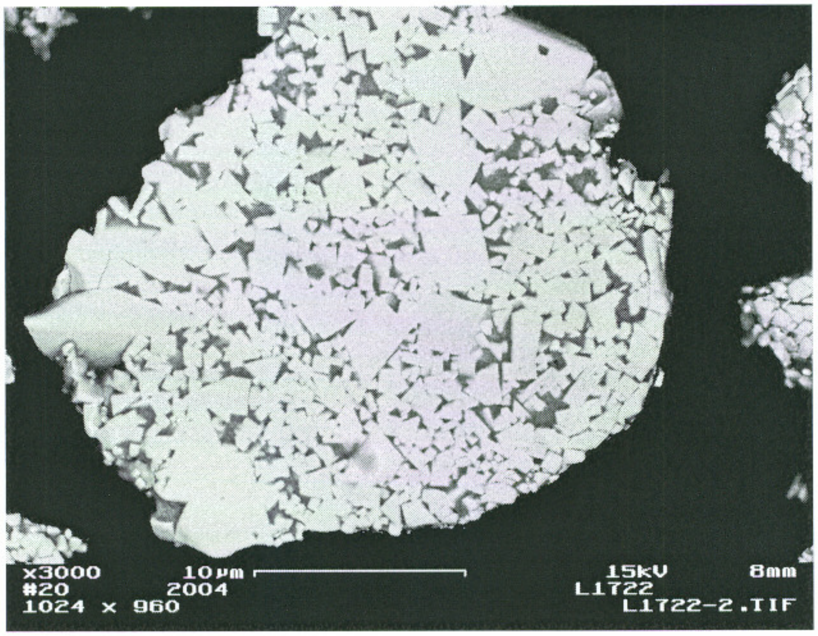

Figure 3.32. FESEM image of Metco 2004 WC-12 wt% Co powder cross section, 3000X.

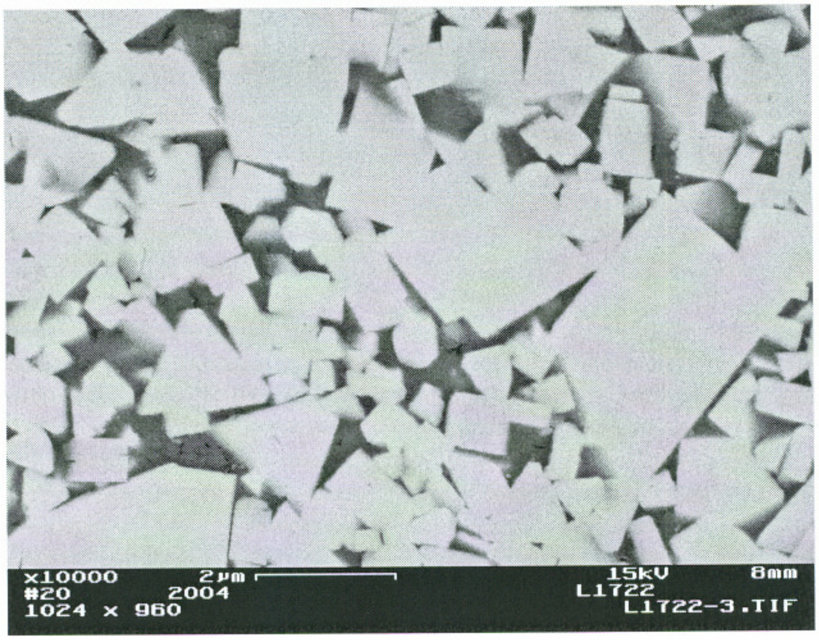

Figure 3.33. FESEM image of Metco 2004 WC-12 wt% Co powder cross section, 10000X.

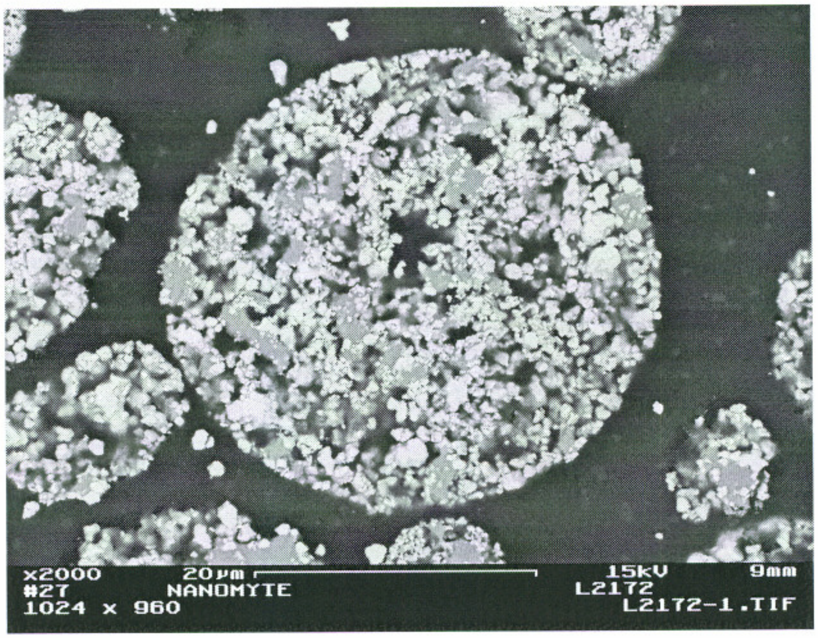

Figure 3.34. FESEM image of Nanomyte^{TM} WC-12 wt% Co powder cross section 2000X.

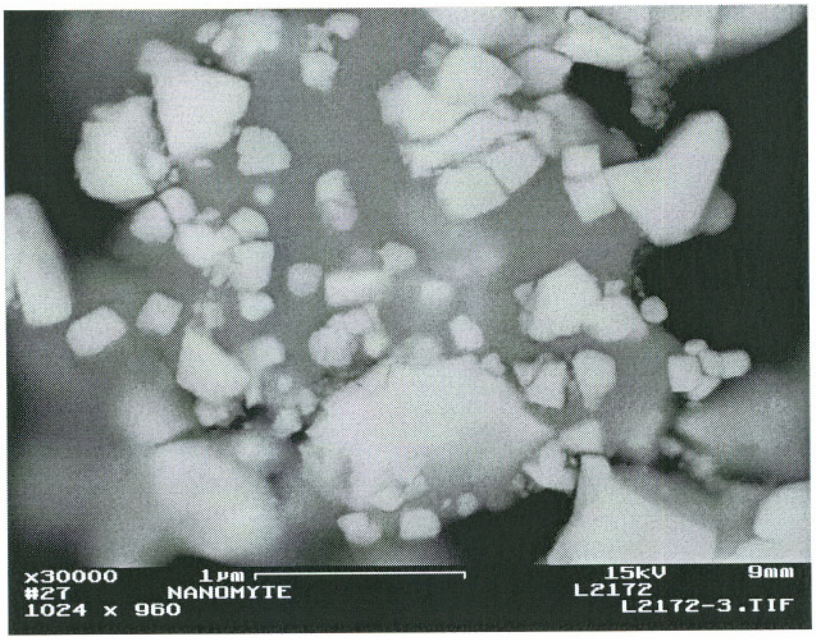

Figure 3.35. FESEM image of Nanomyte^{TM} WC-12 wt% Co powder cross section 30000X .

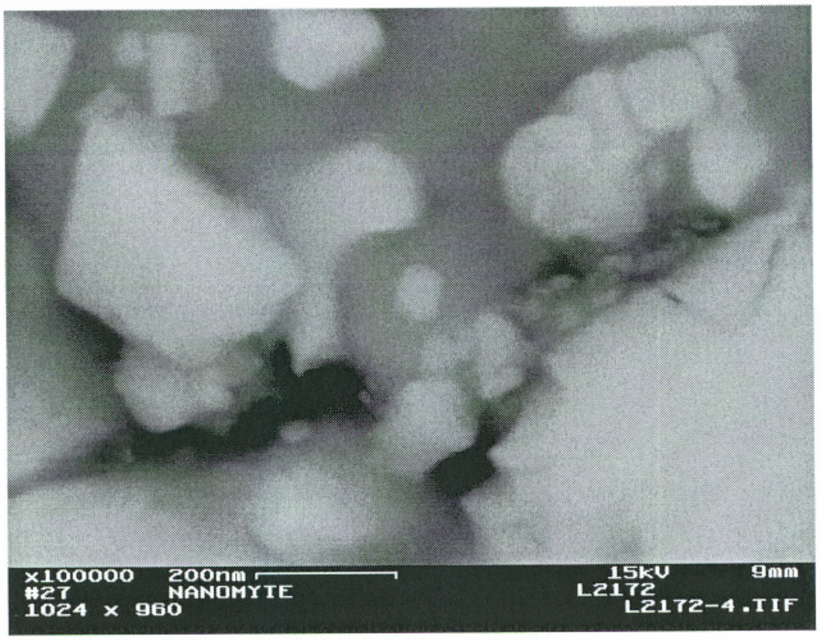

Figure 3.36. FESEM image of Nanomyte^{TM} WC-12 wt% Co powder cross section 100000X .

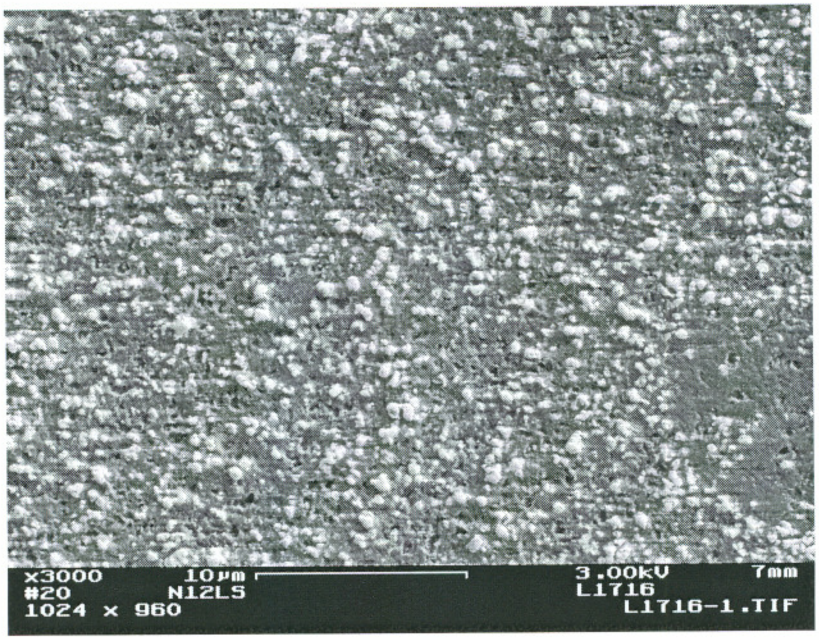

Figure 3.37 FESEM image of Nanodyne™ WC-12 wt% Co, large cut powder cross section, 3000X.

Figure 3.38. FESEM image of Nanodyne™ WC-12 wt% Co, large cut powder cross section, 30000X.

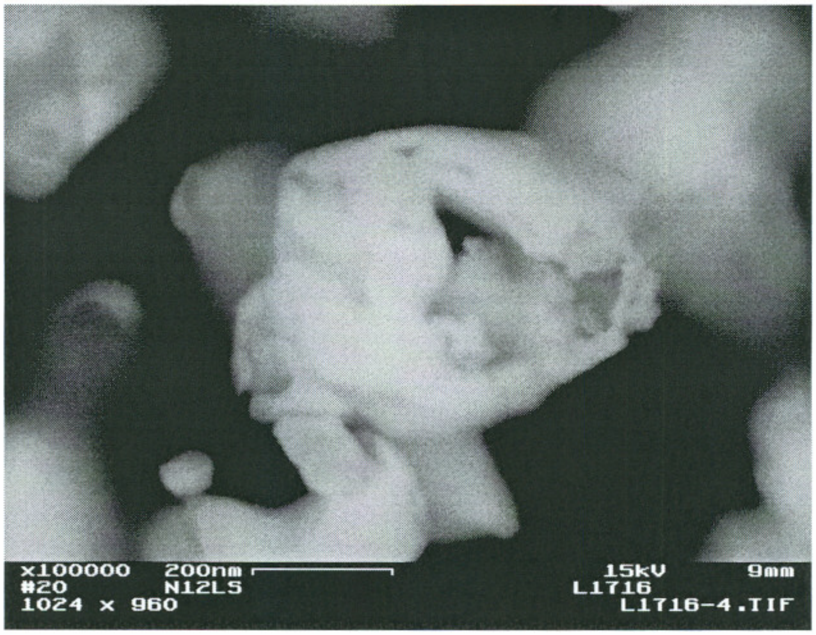

Figure 3.39. FESEM image of Nanodyne™ WC-12 wt% Co, large cut powder cross section, 100000X.

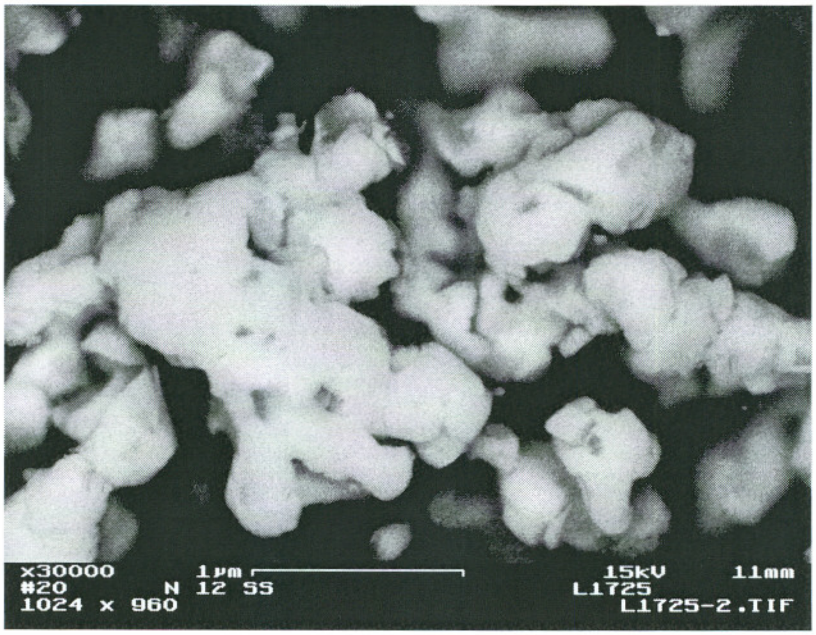

Figure 3.40. FESEM image of Nanodyne™ WC-12 wt% Co, small cut powder cross section, 30000X.

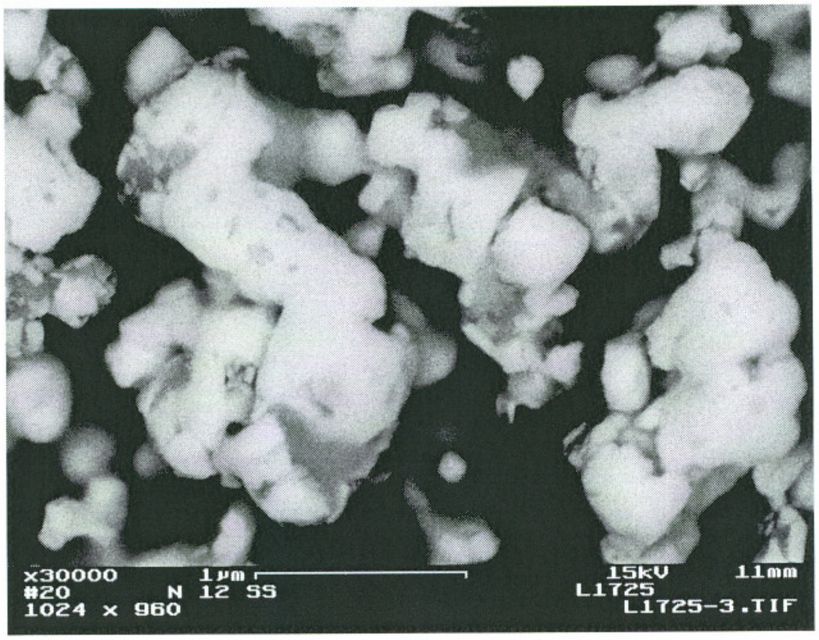

Figure 3.41. FESEM image of Nanodyne™ WC-12 wt% Co, small cut powder cross section, 30000X.

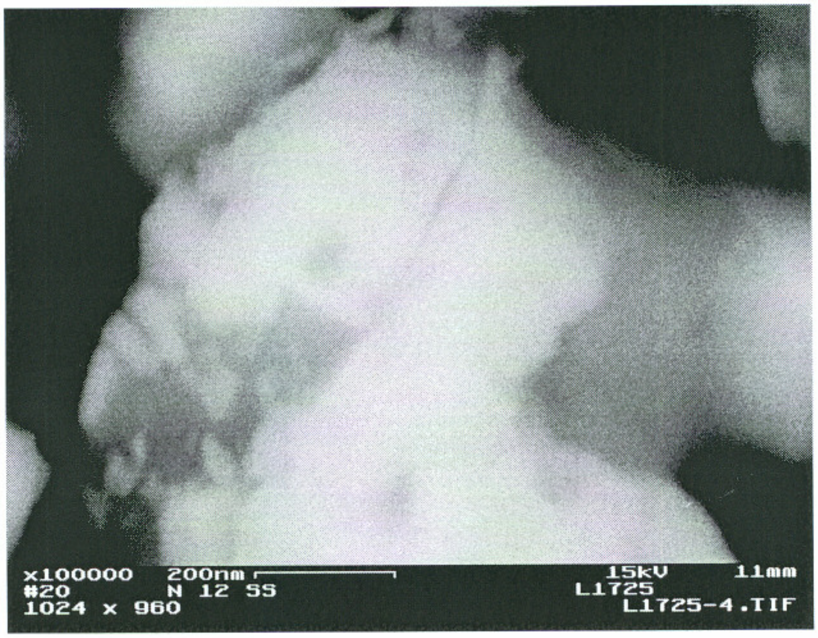

Figure 3.42. FESEM image of Nanodyne™ WC-12 wt% Co, small cut powder cross section, 100000X.

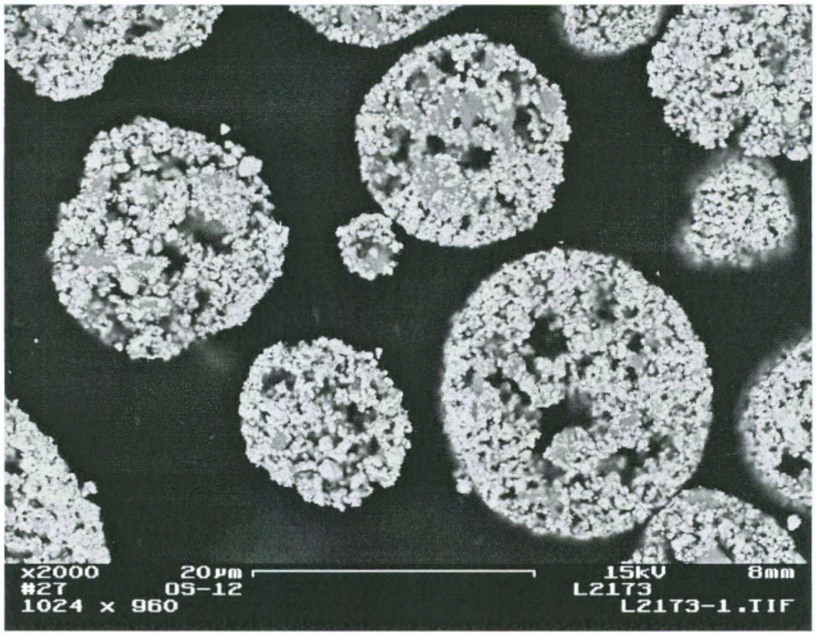

Figure 3.43. FESEM image of Osram Sylvania WC-12 wt% Co powder cross section, 2000X.

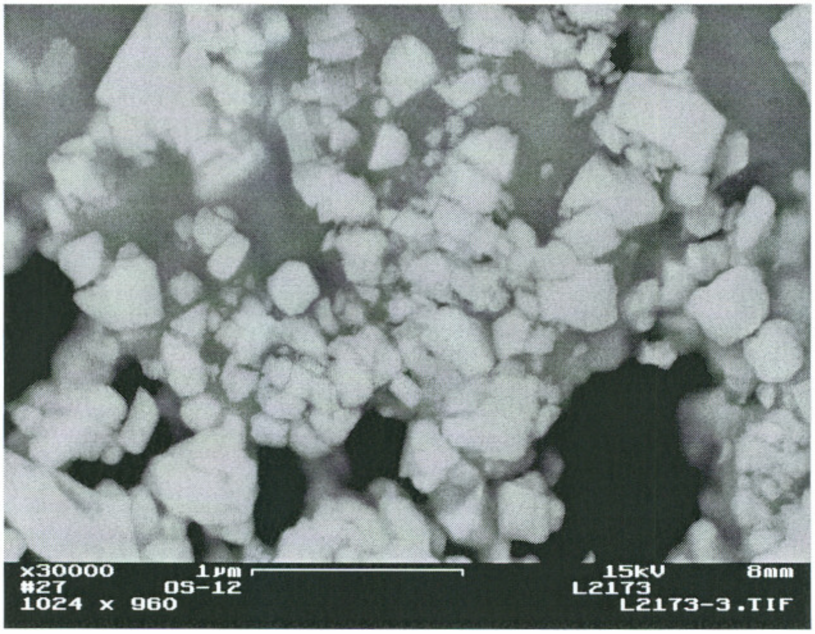

Figure 3.44. FESEM image of Osram Sylvania WC-12 wt% Co powder cross section, 30000X.

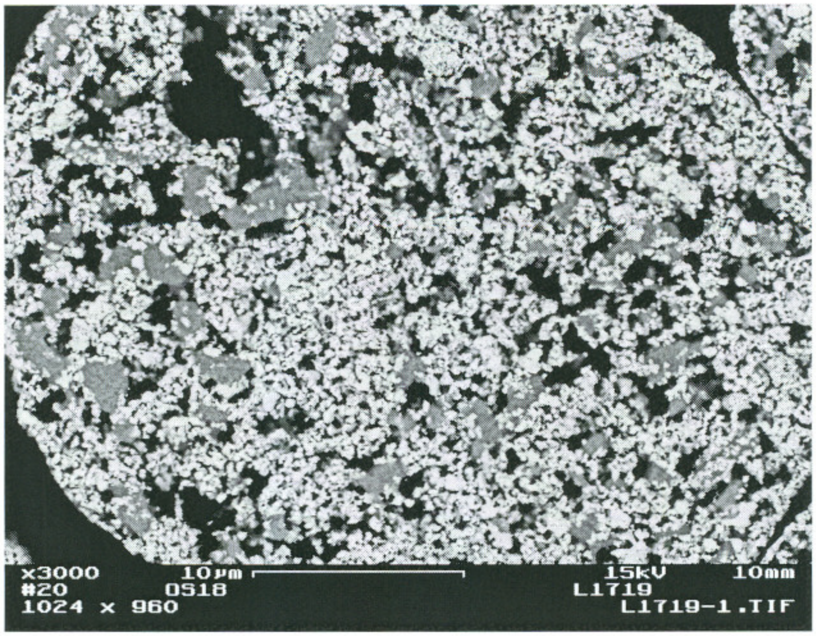

Figure 3.45. FESEM image of Osram Sylvania WC-18 wt% Co powder cross section, 3000X.

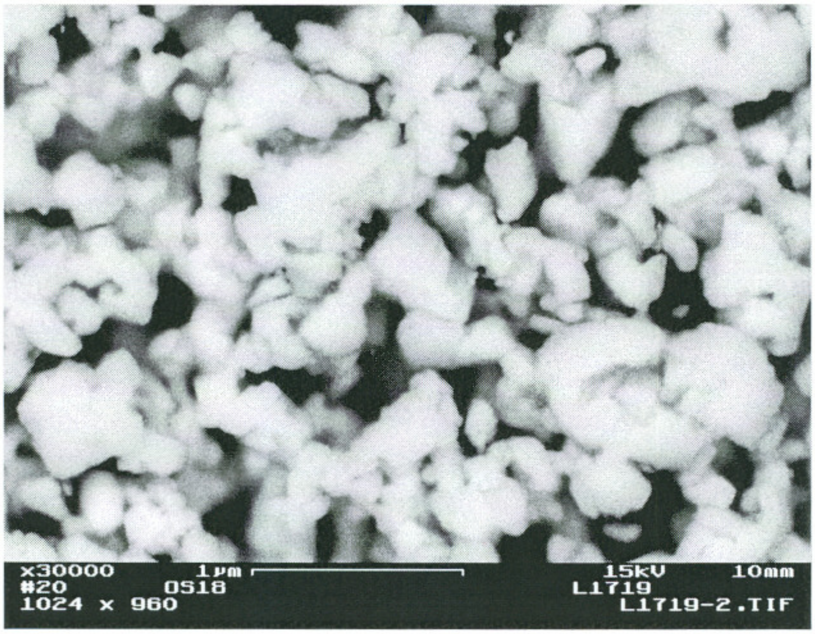

Figure 3.46. FESEM image of Osram Sylvania WC-18 wt% Co powder cross section, 30000X.

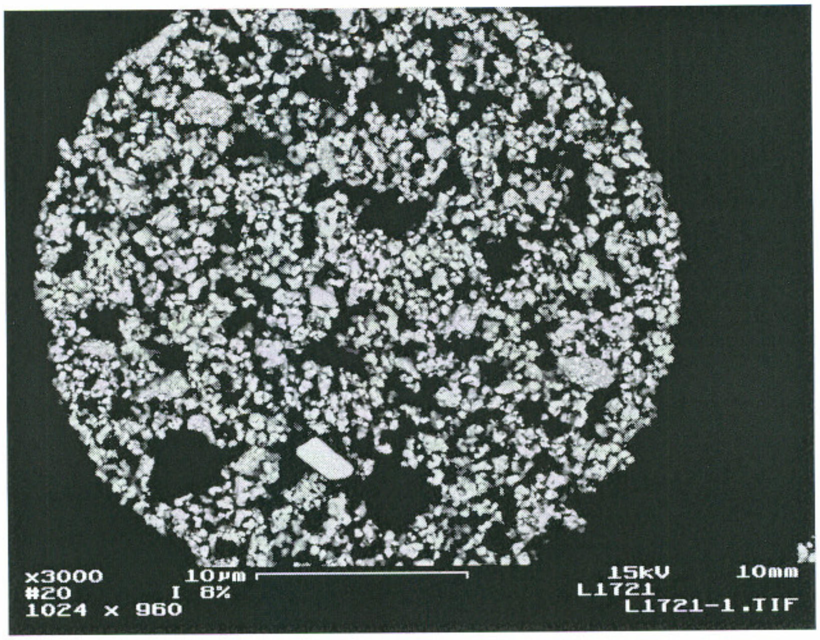

Figure 3.47. FESEM image of Inframat™ WC-8 wt% Co powder cross section, 3000X.

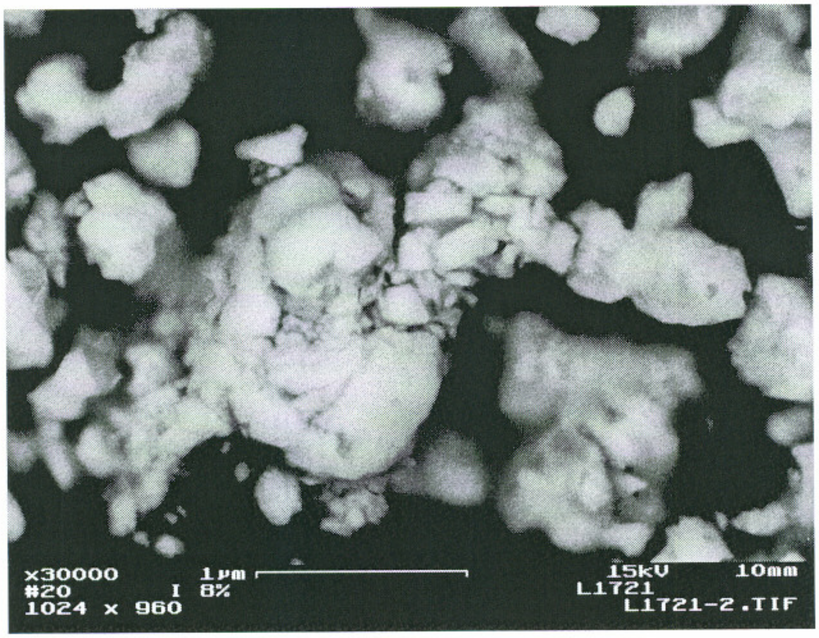

Figure 3.48. FESEM image of Inframat™ WC-8 wt% Co powder cross section, 30000X.

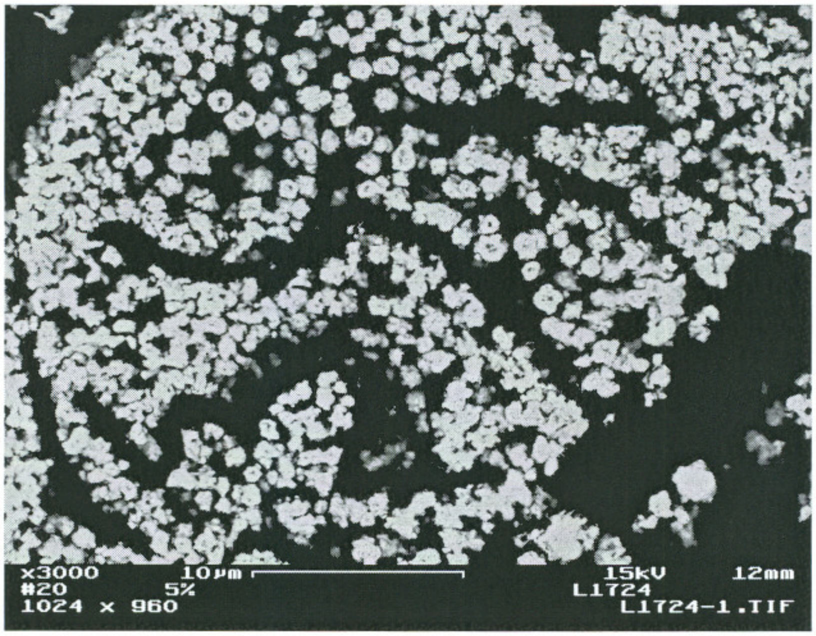

Figure 3.49. FESEM image of Nanodyne™ WC-5 wt% Co powder cross section, 3000X.

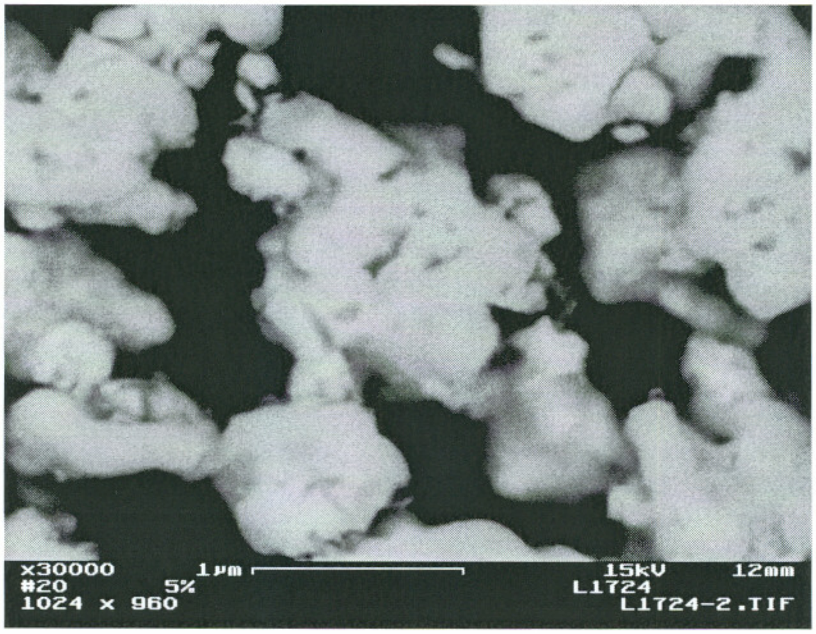

Figure 3.50. FESEM image of Nanodyne™ WC-5 wt% Co powder cross section, 30000X.

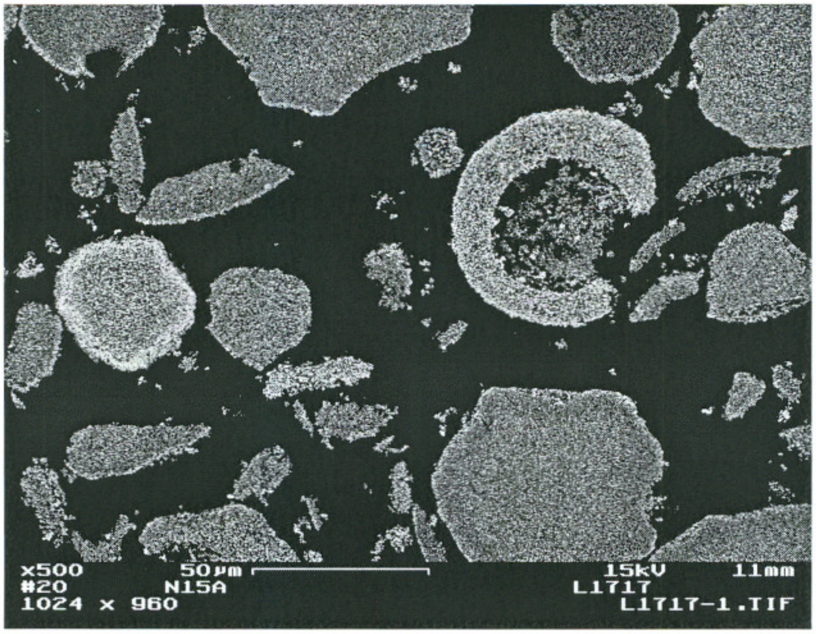

Figure 3.51. FESEM image of Nanodyne™ WC-15 wt% Co, powder A cross section, 500X.

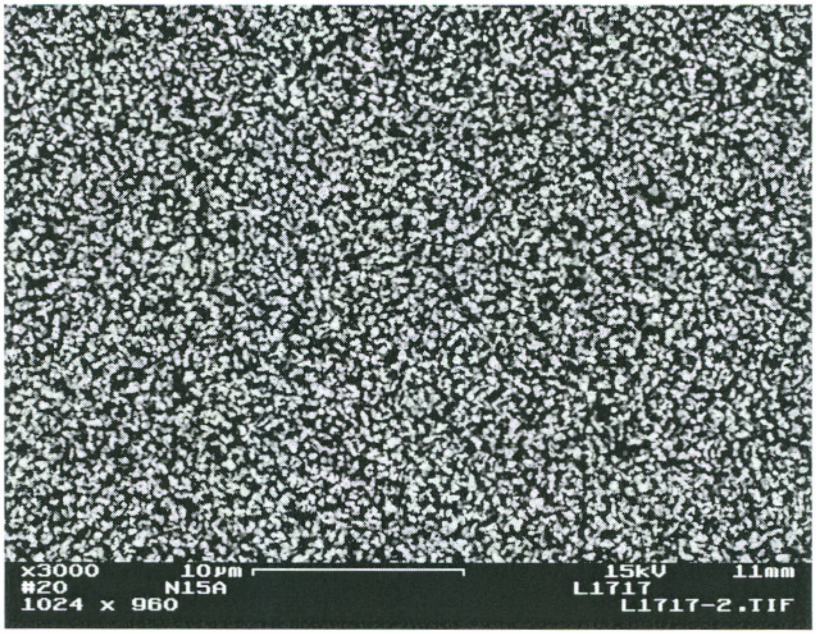

Figure 3.52. FESEM image of Nanodyne™ WC-15 wt% Co,powder A cross section, 3000X.

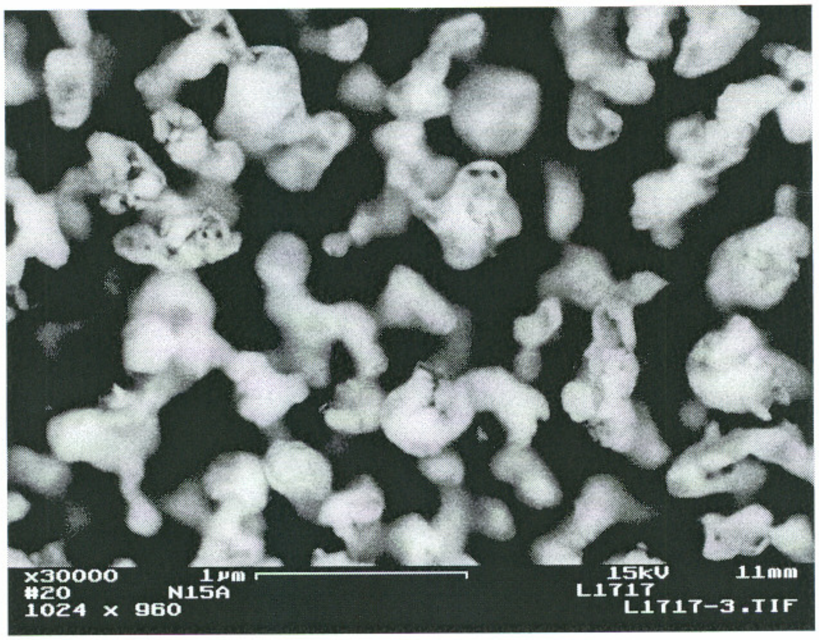

Figure 3.53. FESEM image of Nanodyne^{TM} WC-15 wt% Co,powder A cross section, 30000X.

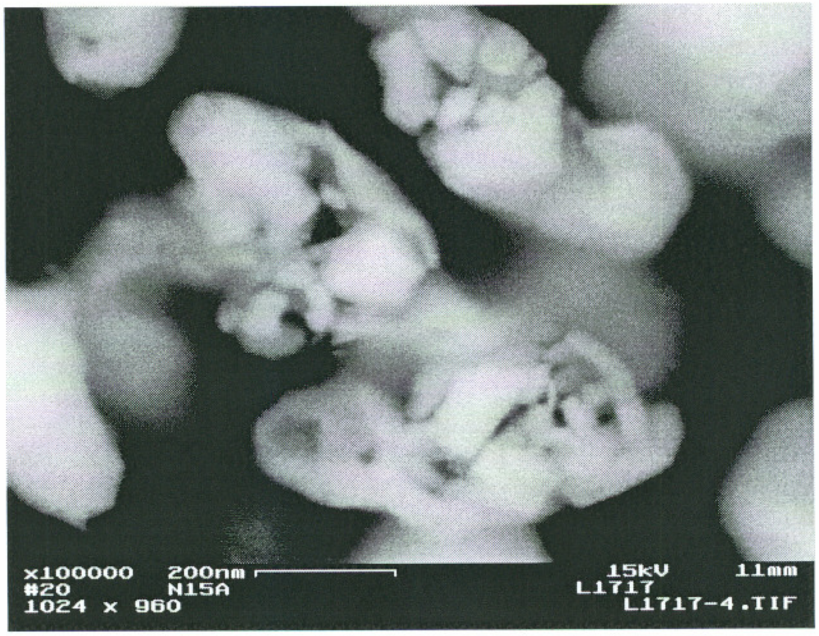

Figure 3.54. FESEM image of Nanodyne^{TM} WC-15 wt% Co,powder A cross section, 10000X.

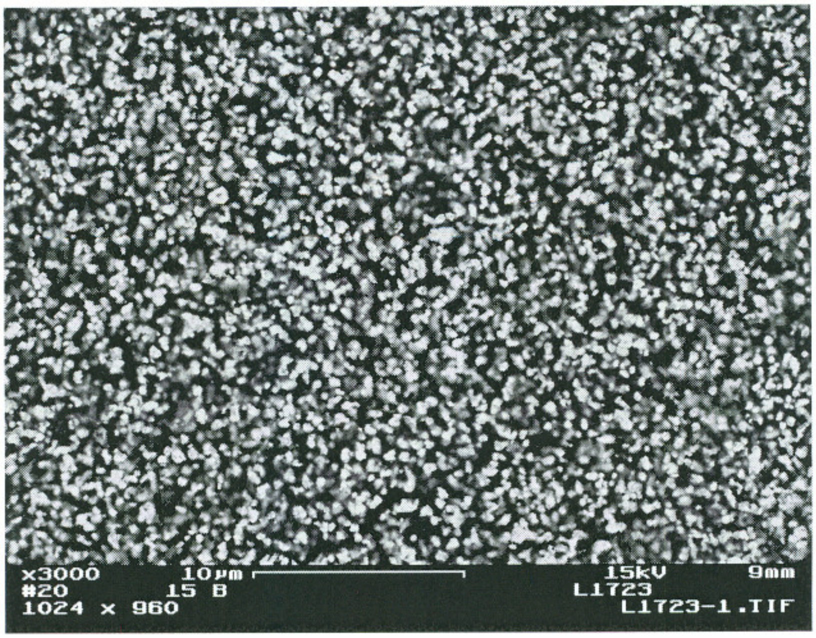

Figure 3.55. FESEM image of Nanodyne™ WC-15 wt% Co powder B cross section, 3000X.

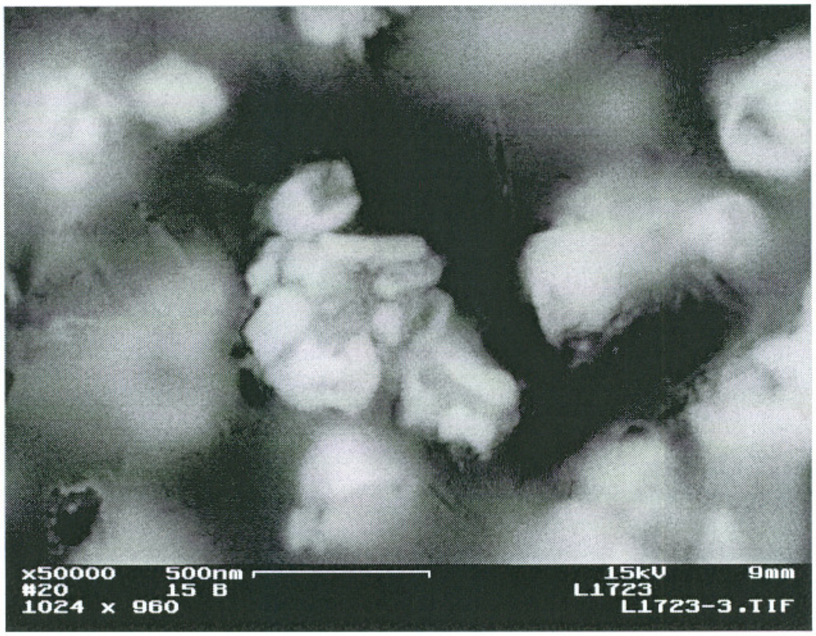

Figure 3.56. FESEM image of Nanodyne™ WC-15 wt% Co powder B cross section, 50000X.

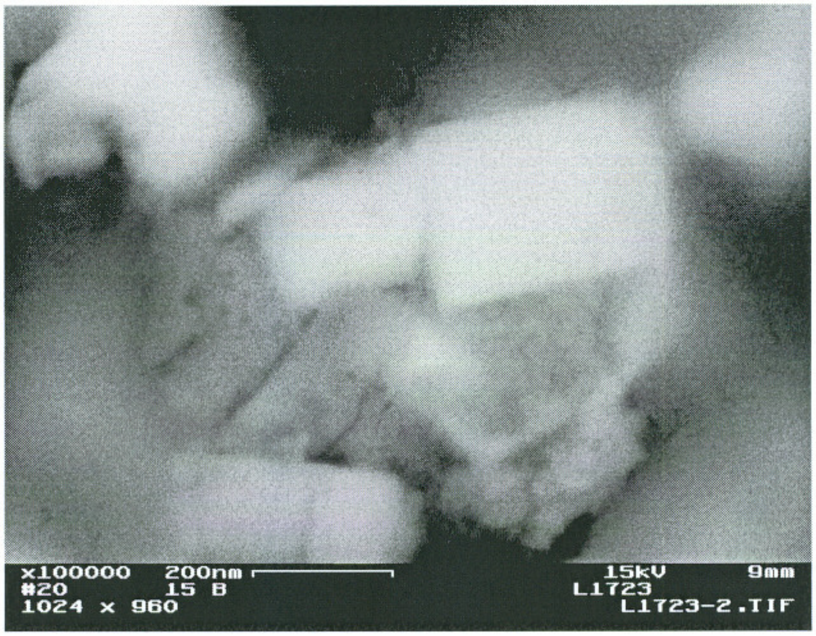

Figure 3.57. FESEM image of Nanodyne™ WC-15 wt% Co powder B cross section, 100000X.

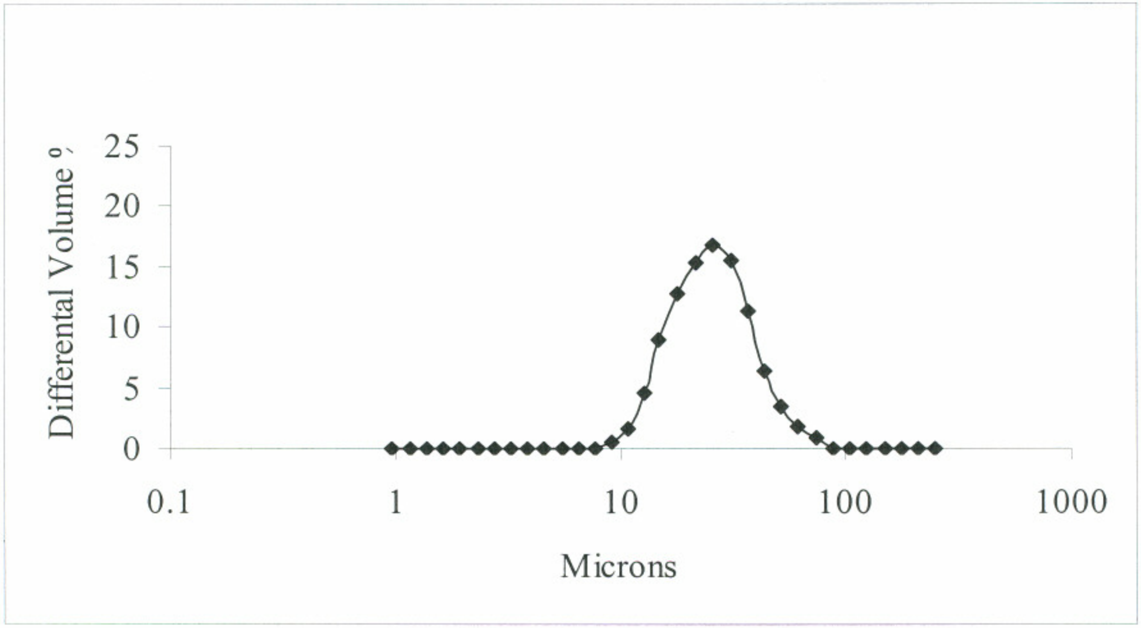

Figure 3.58 Lecotrac™ powder size analysis of Metco 2004 WC-12 wt% Co powder.

Figure 3.57. FESEM image of Nanodyne™ WC-15 wt% Co powder B cross section, 100000X.

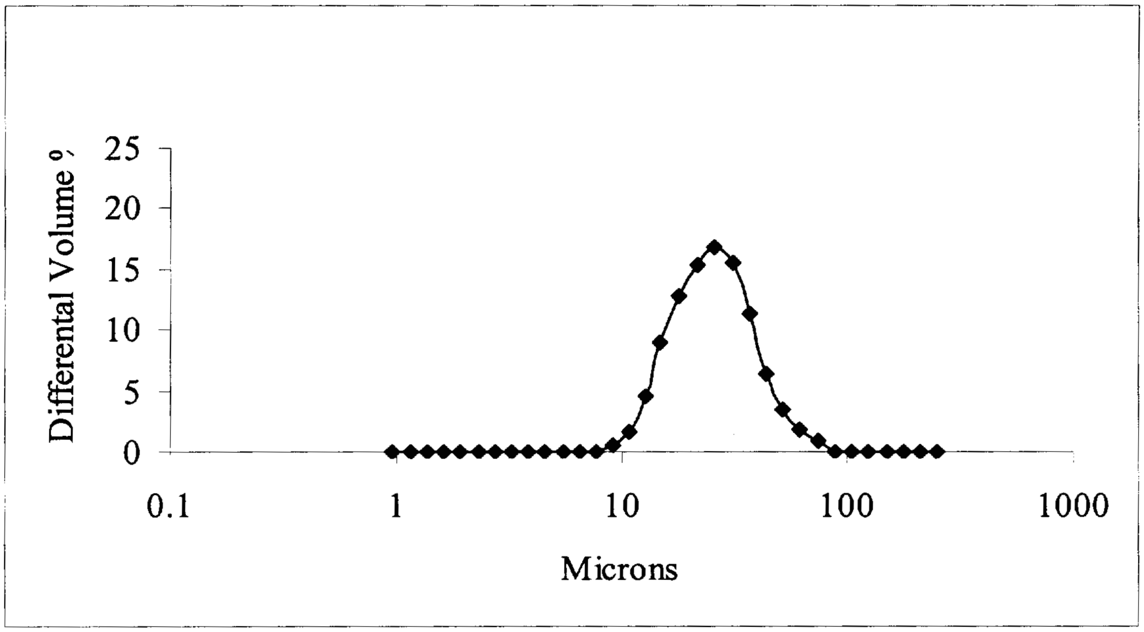

Figure 3.58 Lecotrac™ powder size analysis of Metco 2004 WC-12 wt% Co powder.

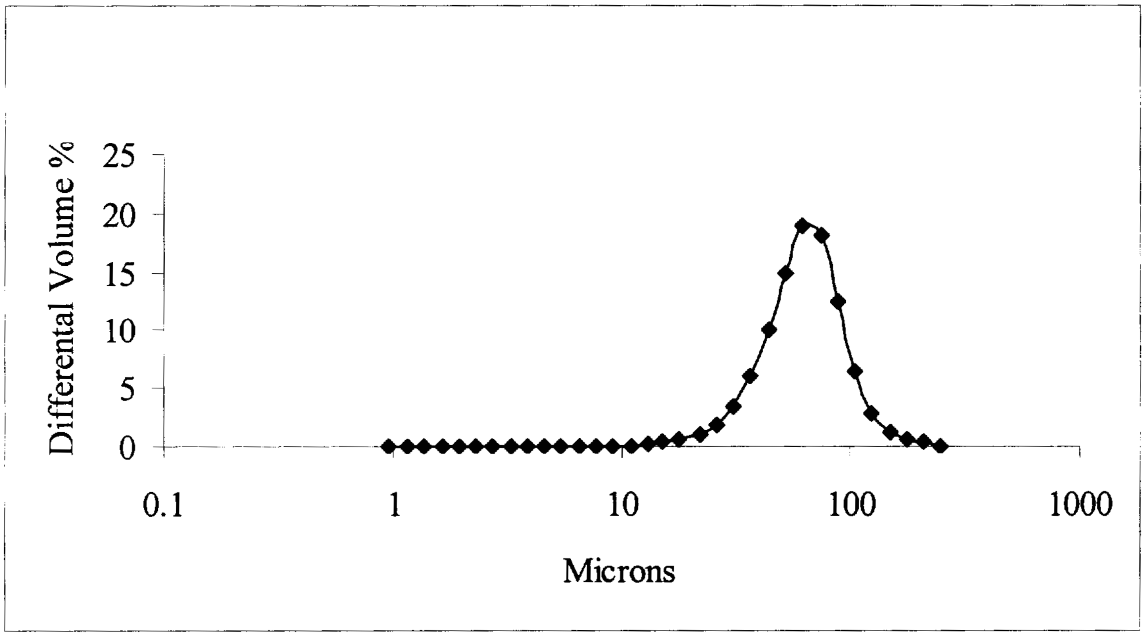

Figure 3.59. Lecotrac™ powder size analysis of Nanodyne™ WC-12 wt% Co, Large cut powder.

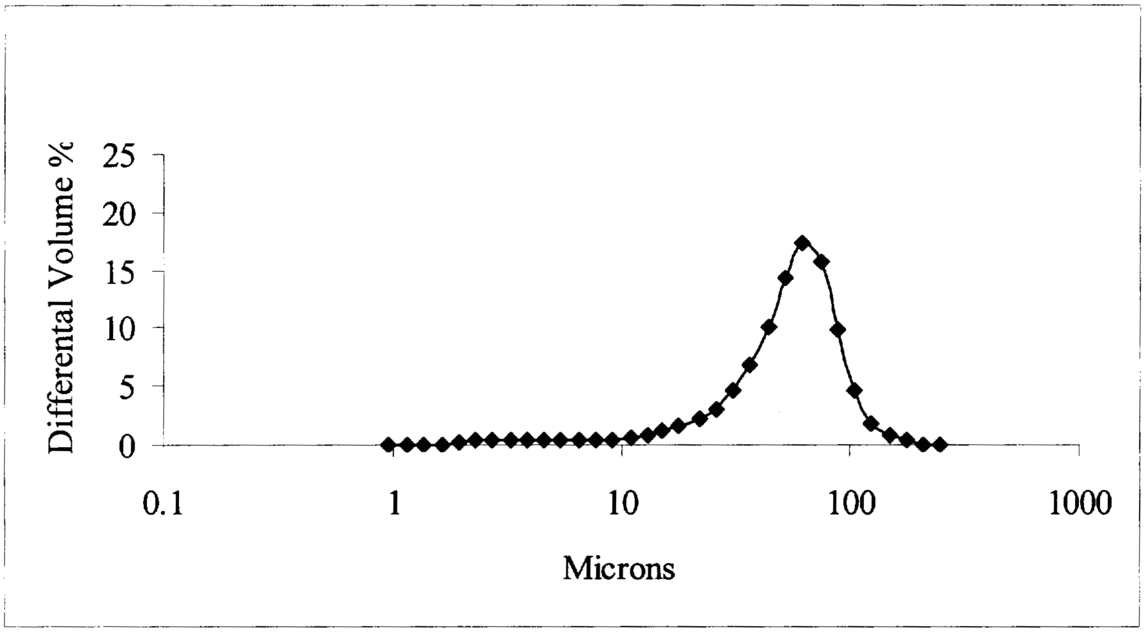

Figure 3.60. Lecotrac™ powder size analysis of Nanodyne™ WC-12 wt% Co, Small cut powder.

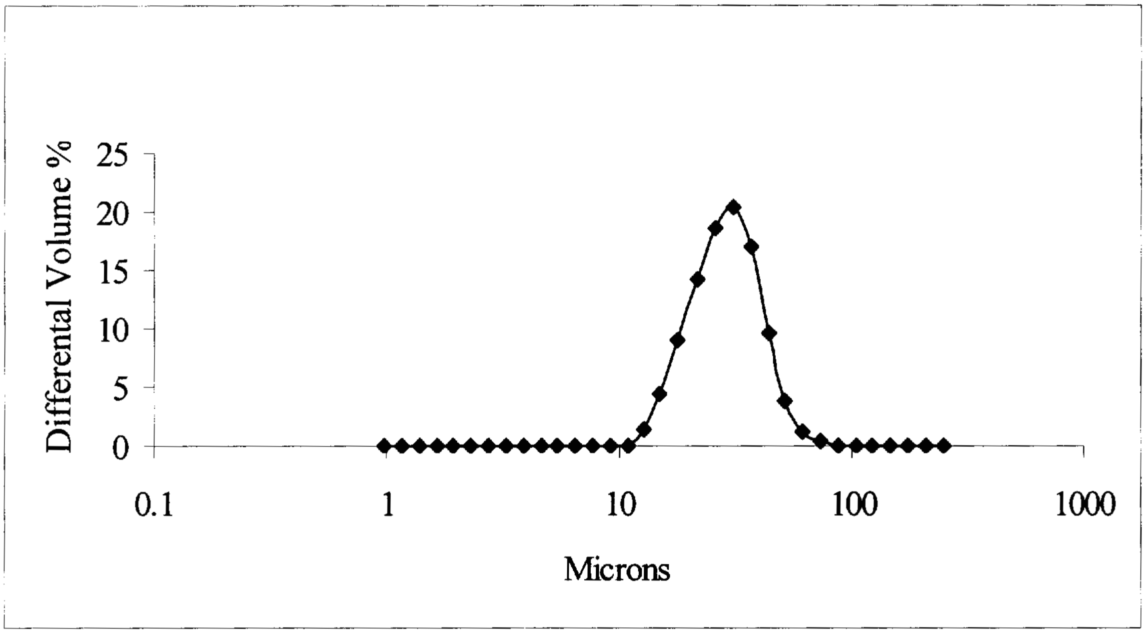

Figure 3.61. Lecotrac™ powder size analysis of Osram Sylvania WC-18 wt% Co powder.

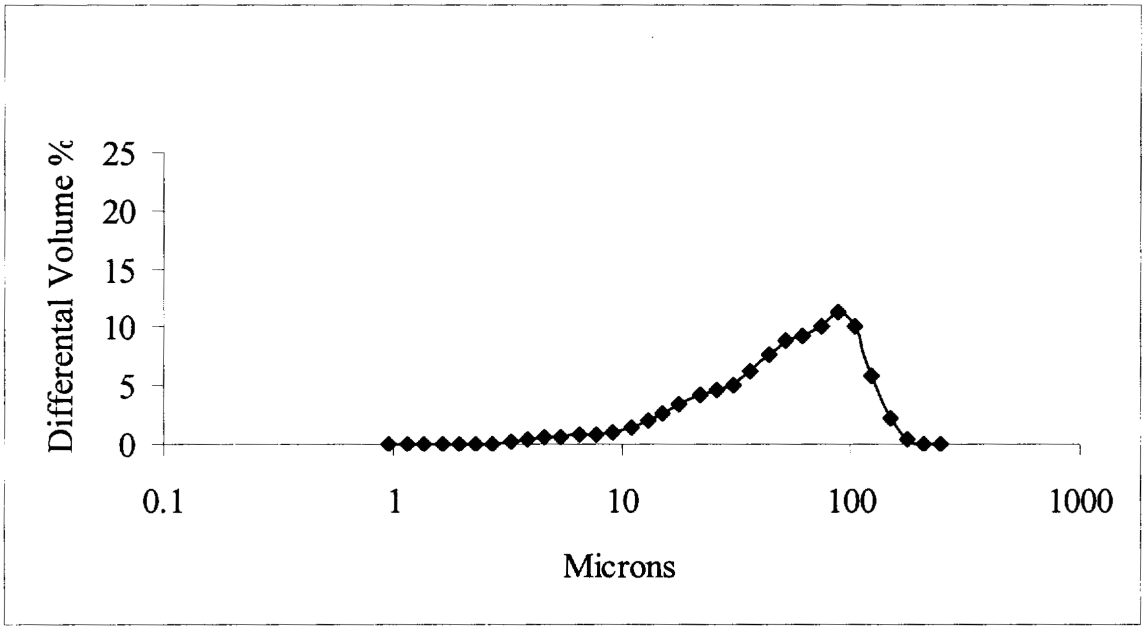

Figure 3.62. Lecotrac™ powder size analysis of Nanodyne™ WC-5 wt% Co powder.

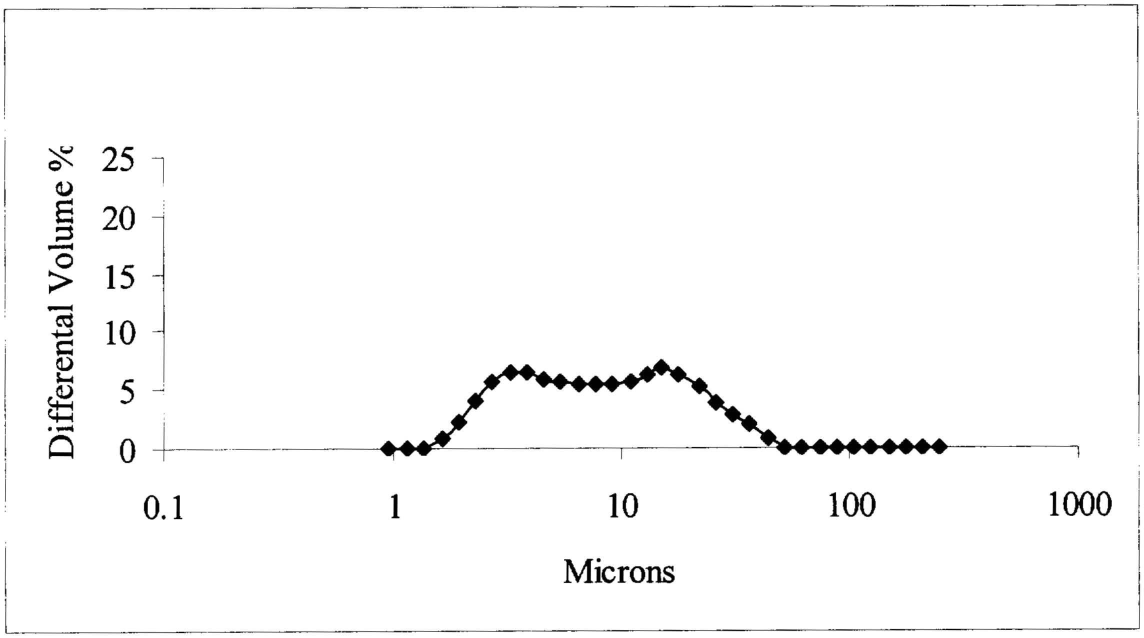

Figure 3.63. Lecotrac™ powder size analysis of reconstituted WC-8 wt% Co by Inframat™.

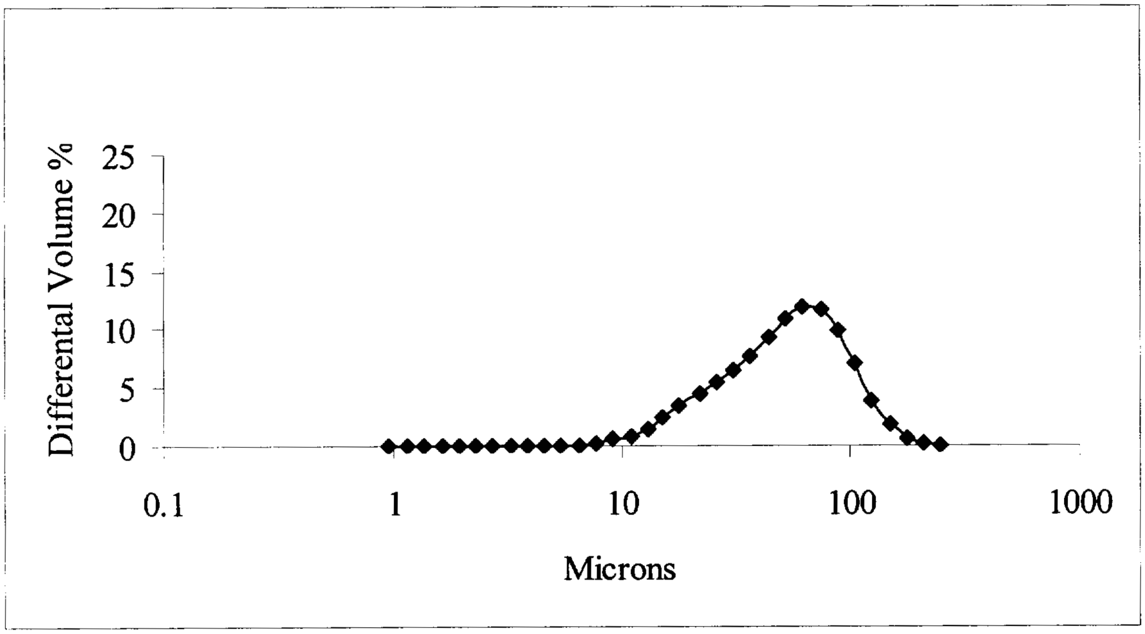

Figure 3.64. Lecotrac™ powder size analysis of Nanodyne™ WC-15 wt% Co A, powder.

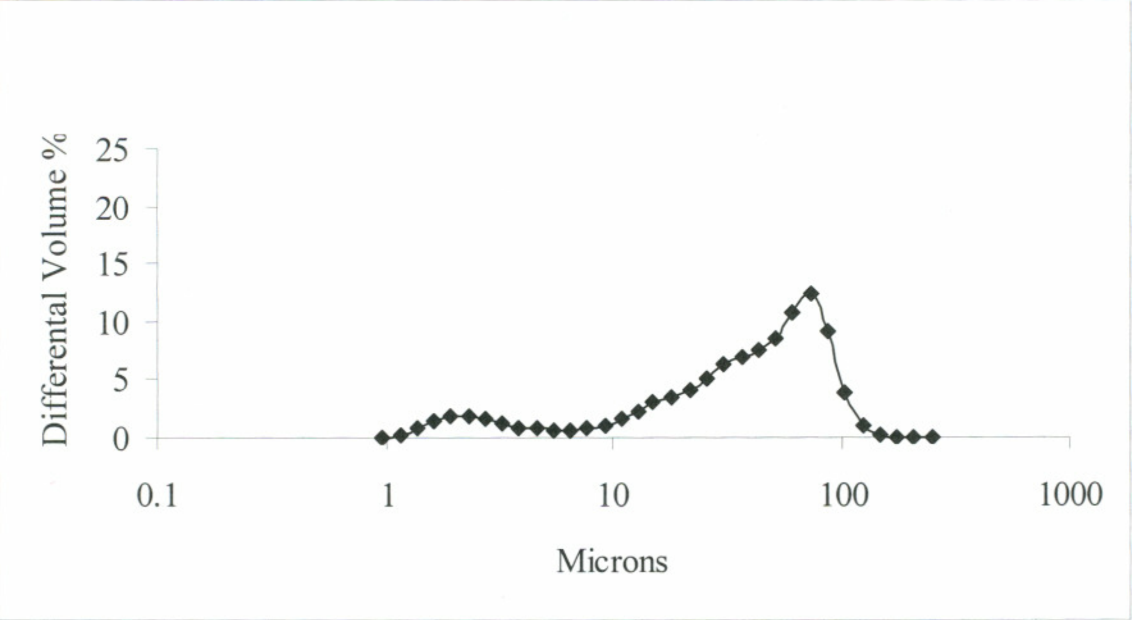

Figure 3.65. Lecotrac™ powder size analysis of Nanodyne™ WC-15 wt% Co B, un-sieved powder.

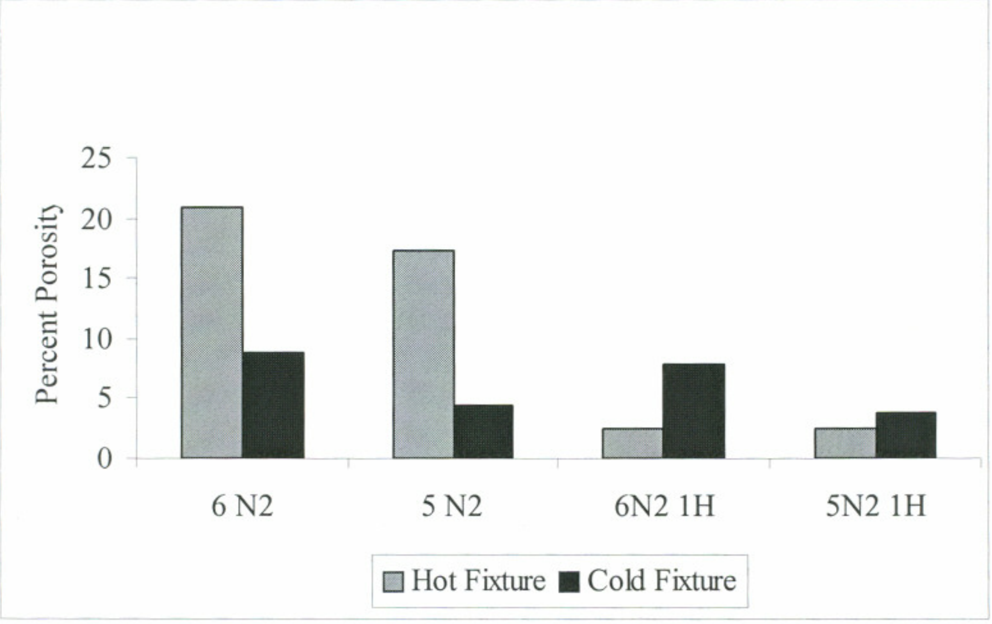

Figure 3.66. Porosity of Metco 2004 WC-12 wt% Co, hot fixture and cold fixture.

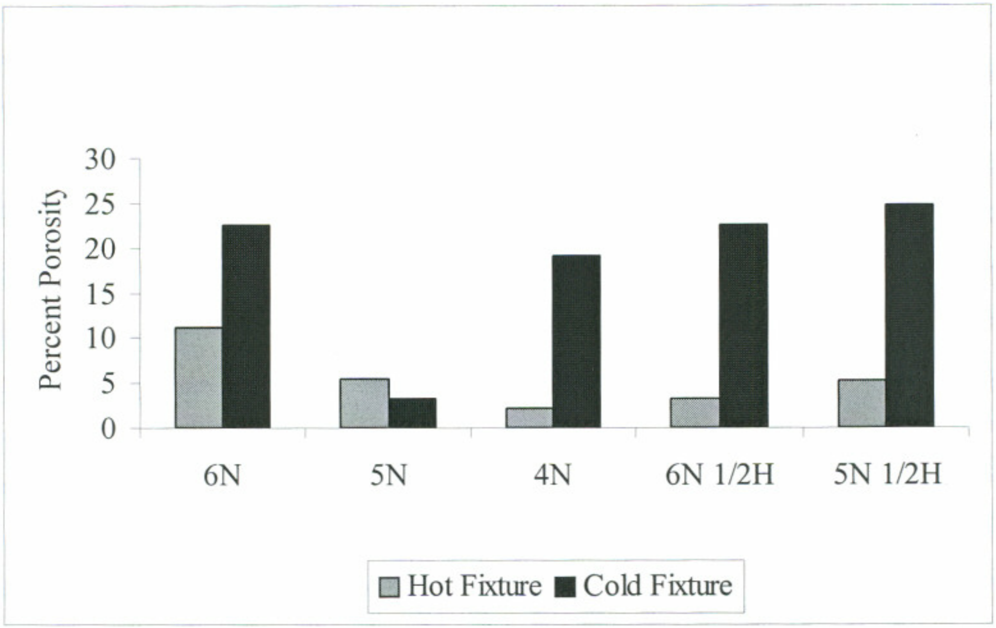

Figure 3.67. Porosity of Nanomyte^{TM} WC-12 wt% Co, hot fixture and cold fixture.

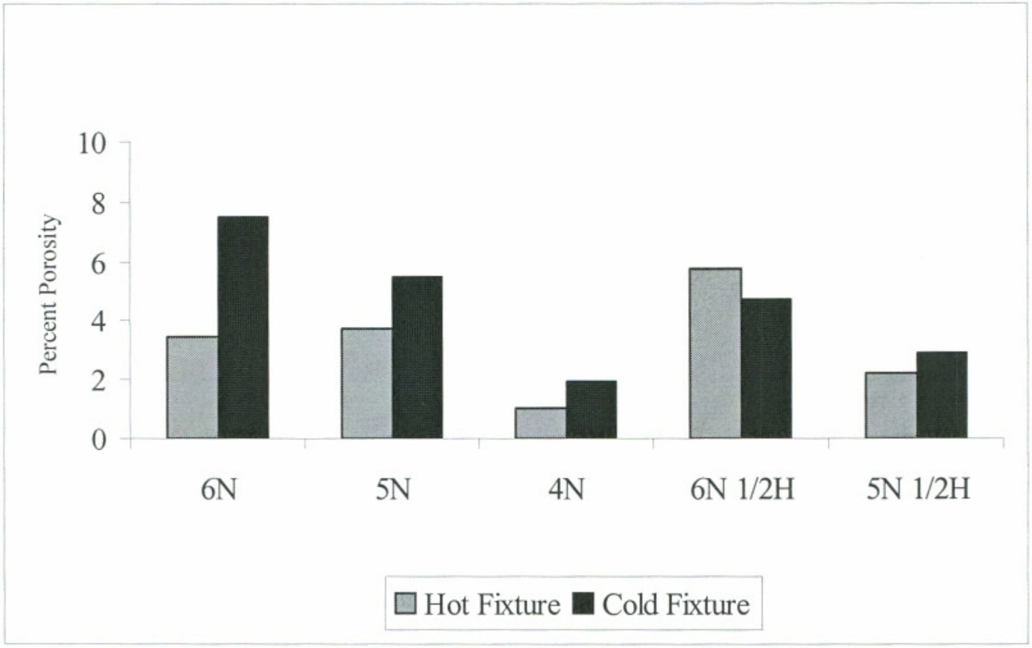

Figure 3.68. Porosity of Nanodyne^{TM} 12 wt% Co Large Cut, hot fixture and cold fixture.

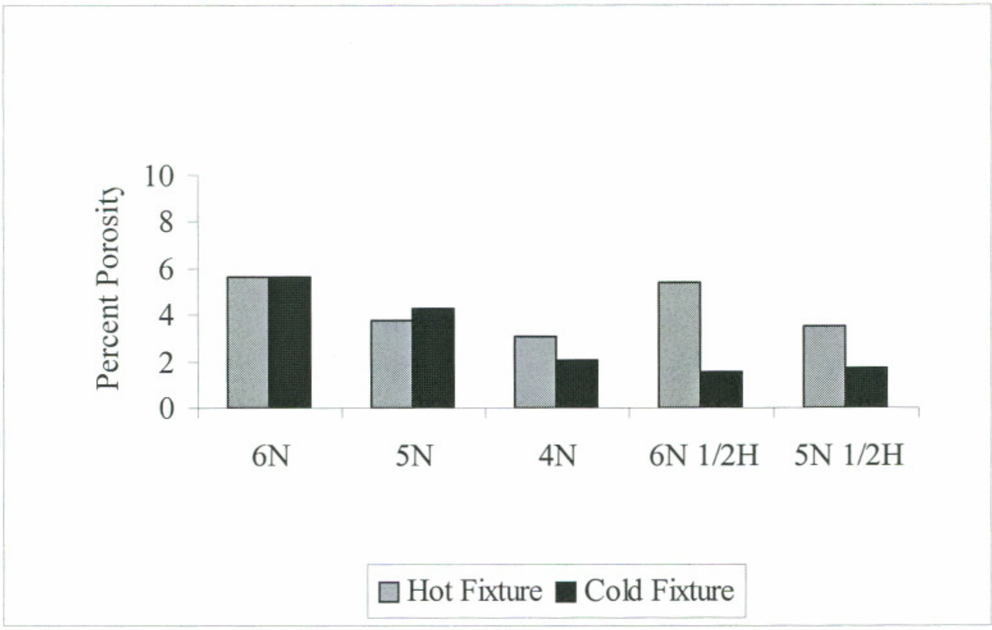

Figure 3.69. Porosity of Nanodyne^{TM} 12 wt% Co Small Cut, hot fixture and cold fixture.

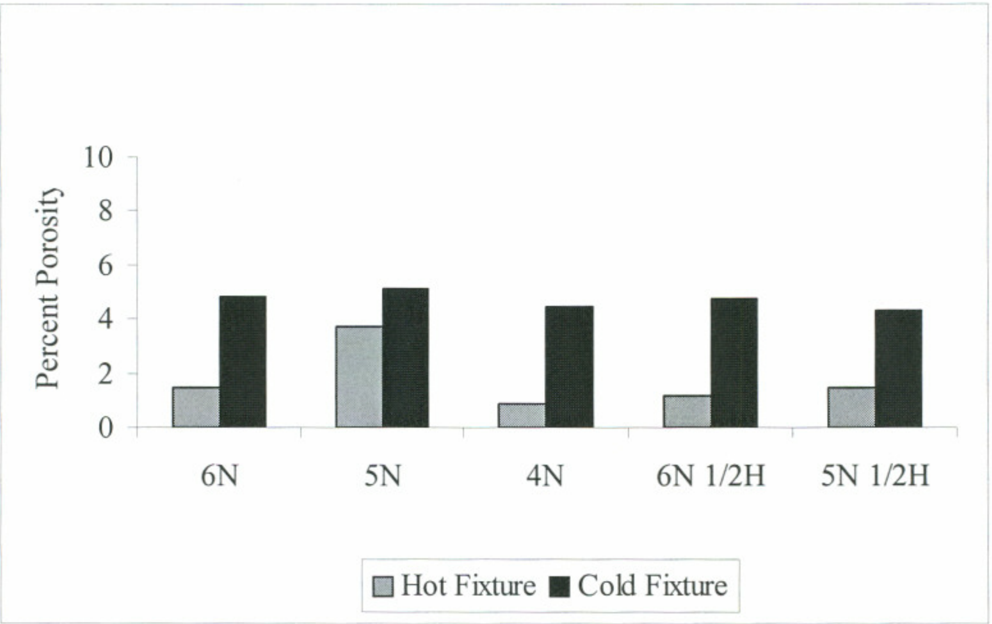

Figure 3.70. Porosity of Osram-Sylvania 12 wt% Co, hot fixture and cold fixture.

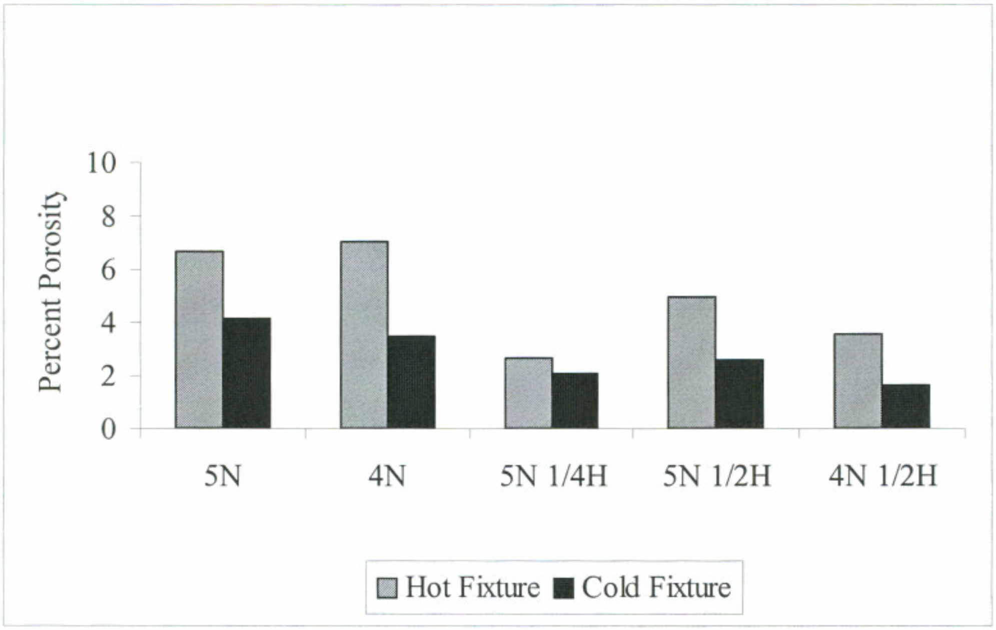

Figure 3.71. Porosity of Osram-Sylvania 18 wt% Co, hot fixture and cold fixture.

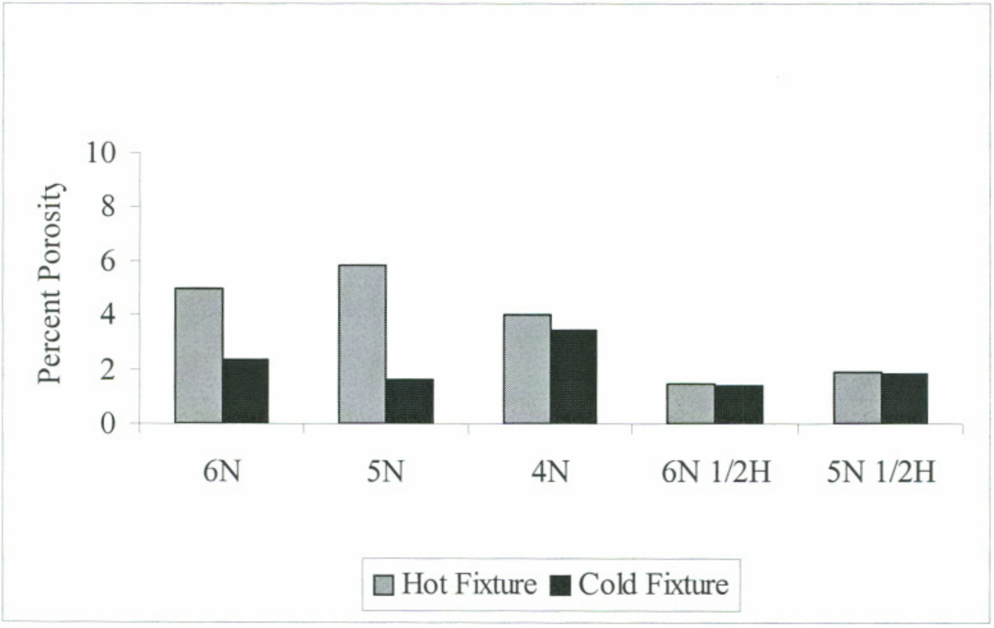

Figure 3.72. Porosity of Nanodyne™ 15 wt% Co, hot fixture and cold fixture.

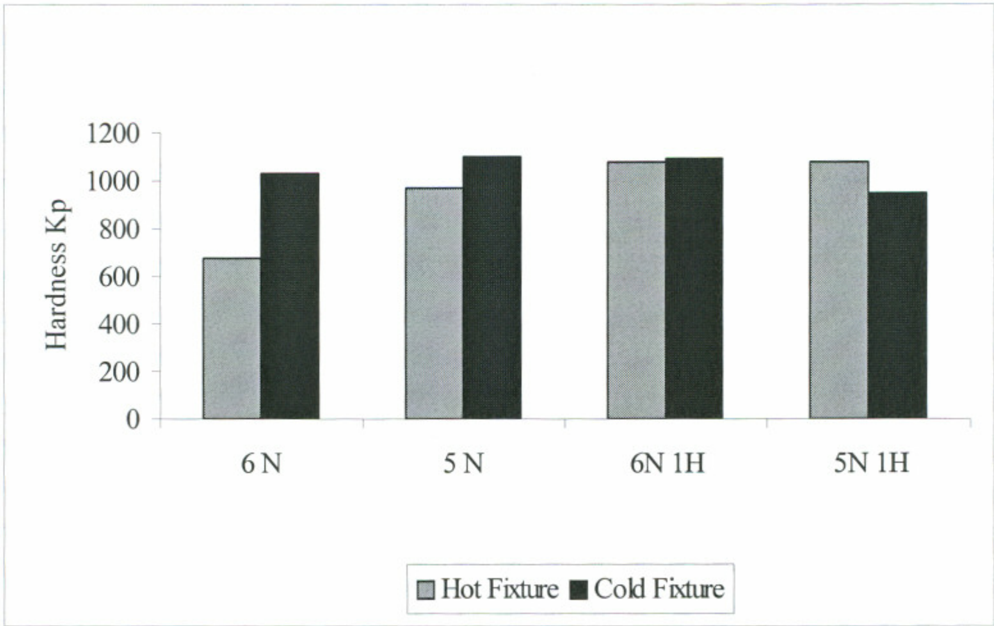

Figure 3.73. Hardness of Metco 2004 WC-12%Co, hot fixture and cold fixture.

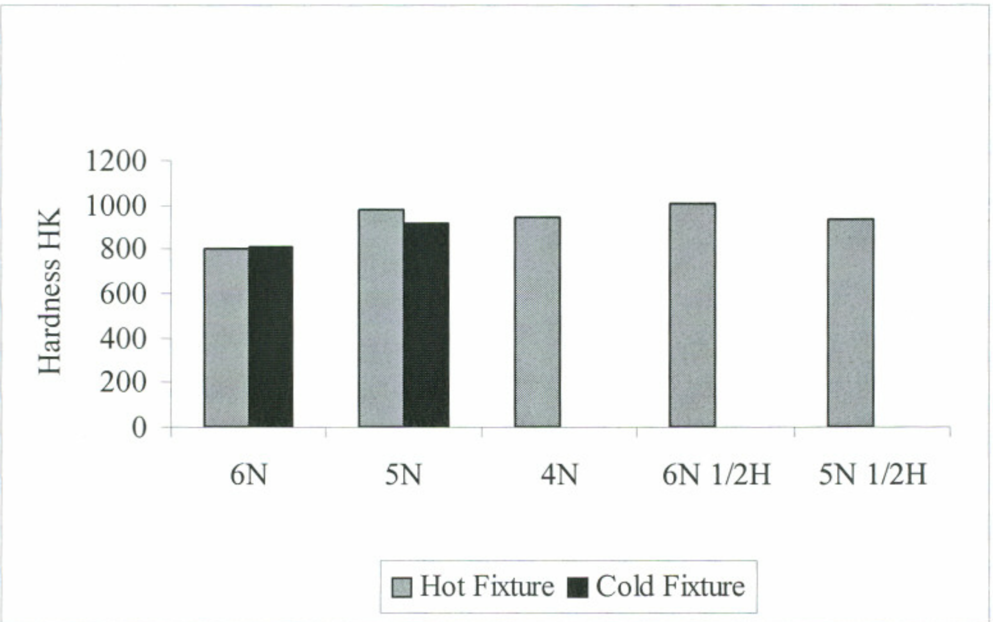

Figure 3.74. Hardness of Nanomyte^{TM} WC-12%Co, hot fixture and cold fixture.

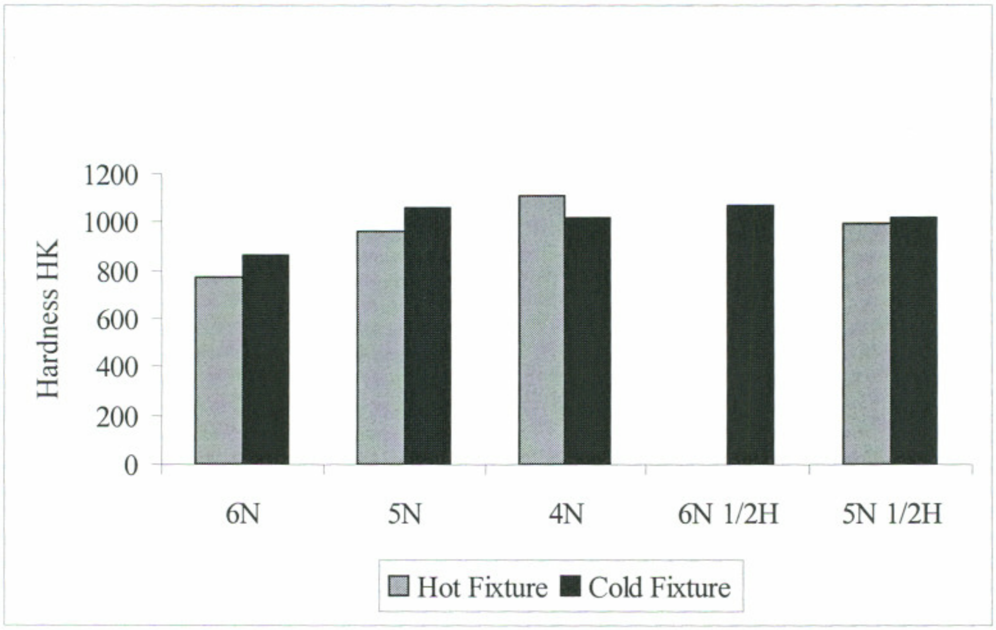

Figure 3.75. Hardness of Nanodyne^{TM} 12 wt% Co Large, hot fixture and cold fixture.

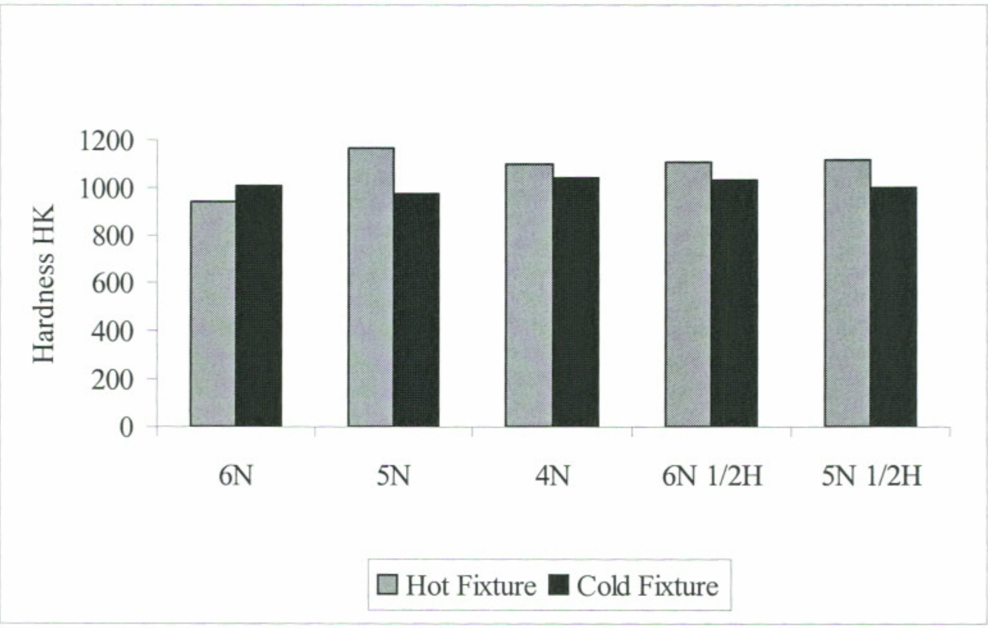

Figure 3.76. Hardness of Nanodyne^{TM} 12 wt% Co Small, hot fixture and cold fixture.

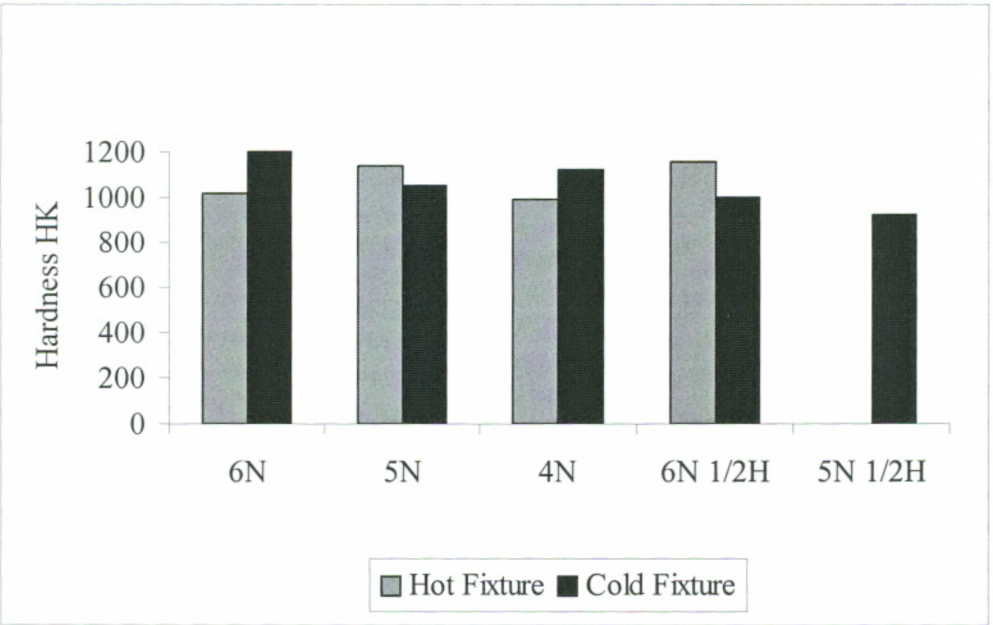

Figure 3.77. Hardness of Osram-Sylvania 12 wt% Co, hot fixture and cold fixture.

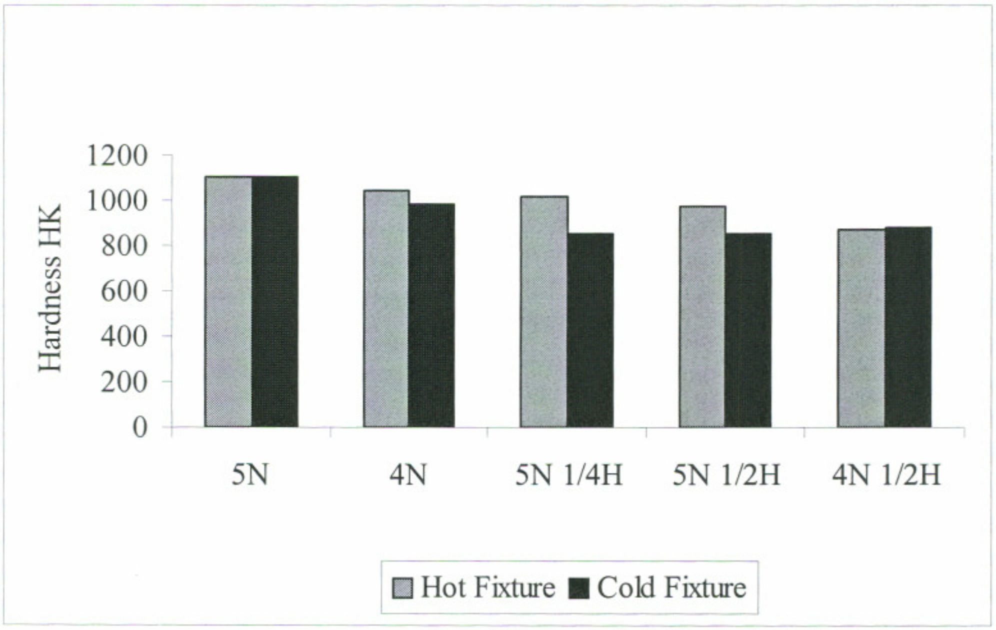

Figure 3.78. Hardness of Osram-Sylvania 18 wt% Co, hot fixture and cold fixture.

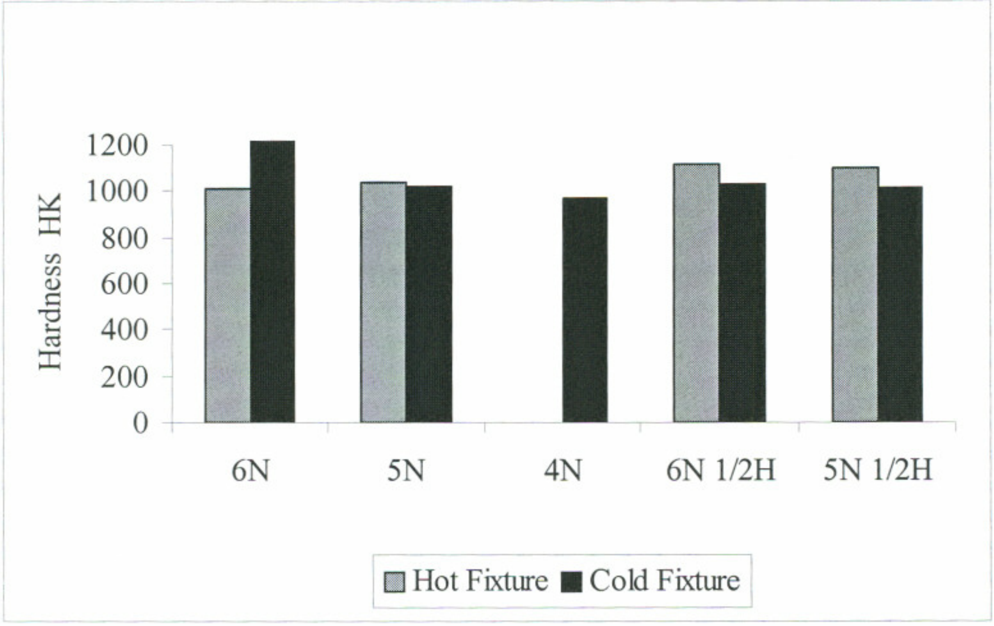

Figure 3.79. Hardness of Nanodyne™ 15 wt% Co, hot fixture and cold fixture.

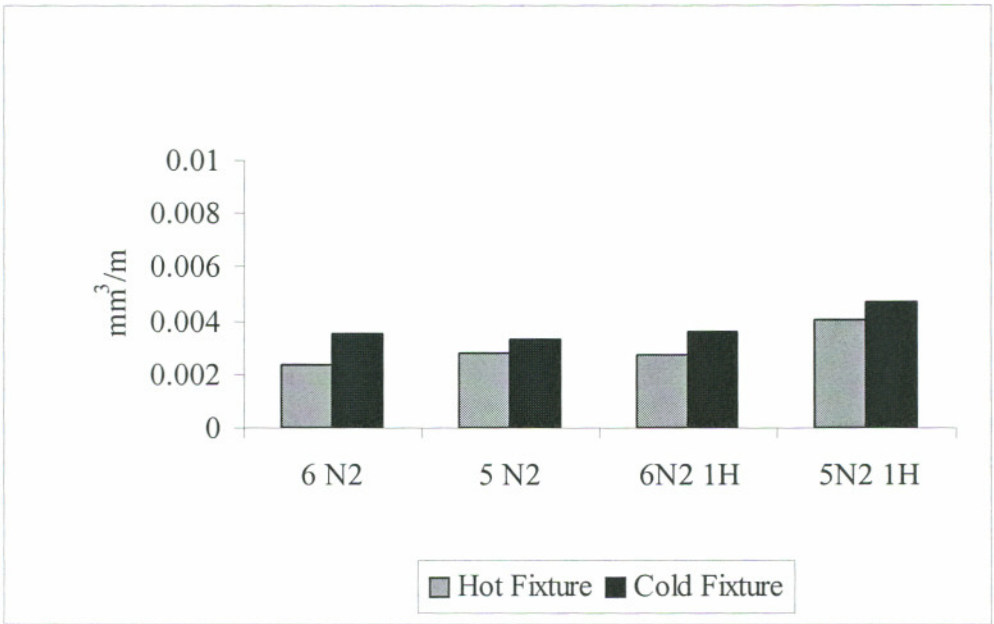

Figure 3.80. Wear Rate of 2004 WC-12 wt% Co, hot fixture and cold fixture.

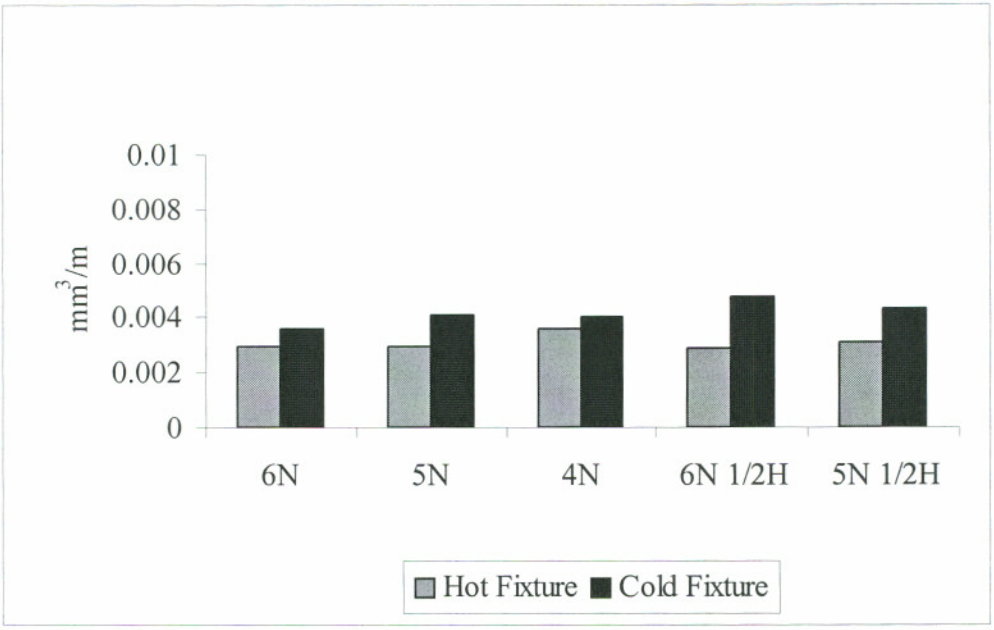

Figure 3.81. Wear Rate of Nanomyte^{TM} WC-12%Co, hot fixture and cold fixture.

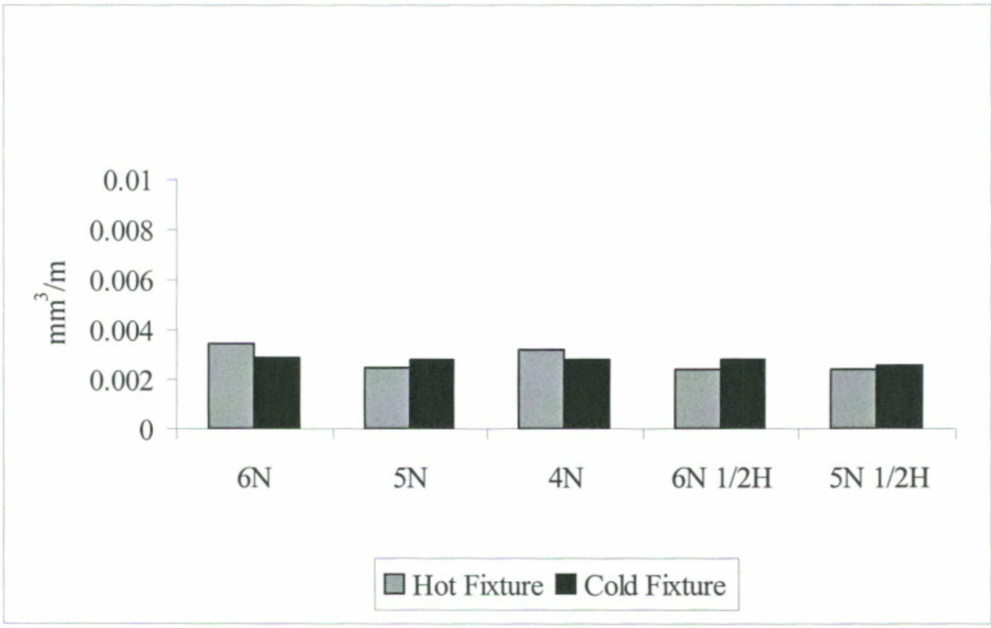

Figure 3.82. Wear Rate of Nanodyne^{TM} 12 wt% Co large cut, hot fixture and cold fixture.

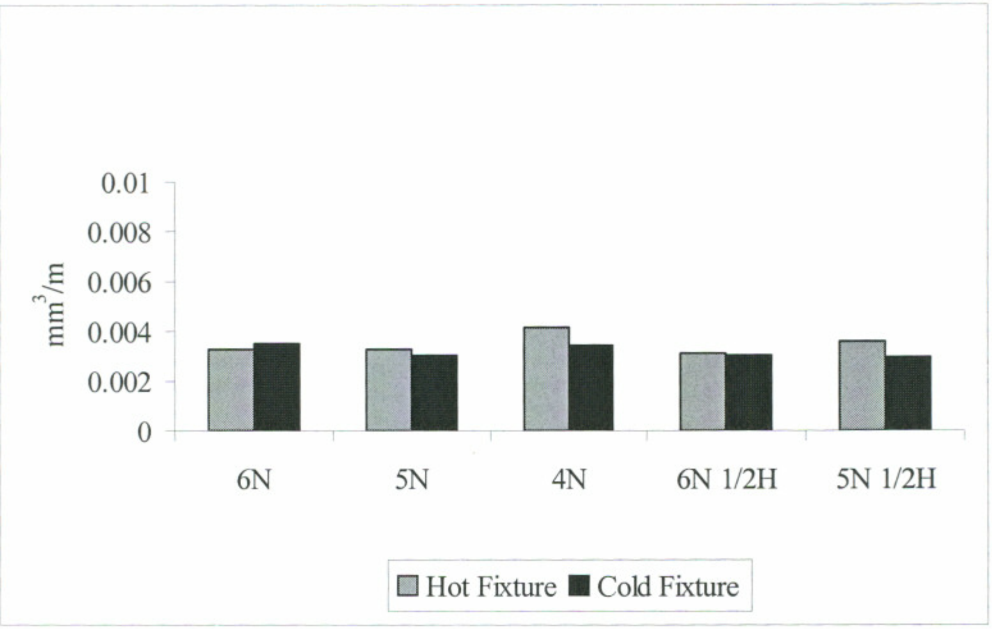

Figure 3.83. Wear Rate of Nanodyne™ 12 wt% Co small cut, hot fixture and cold fixture.

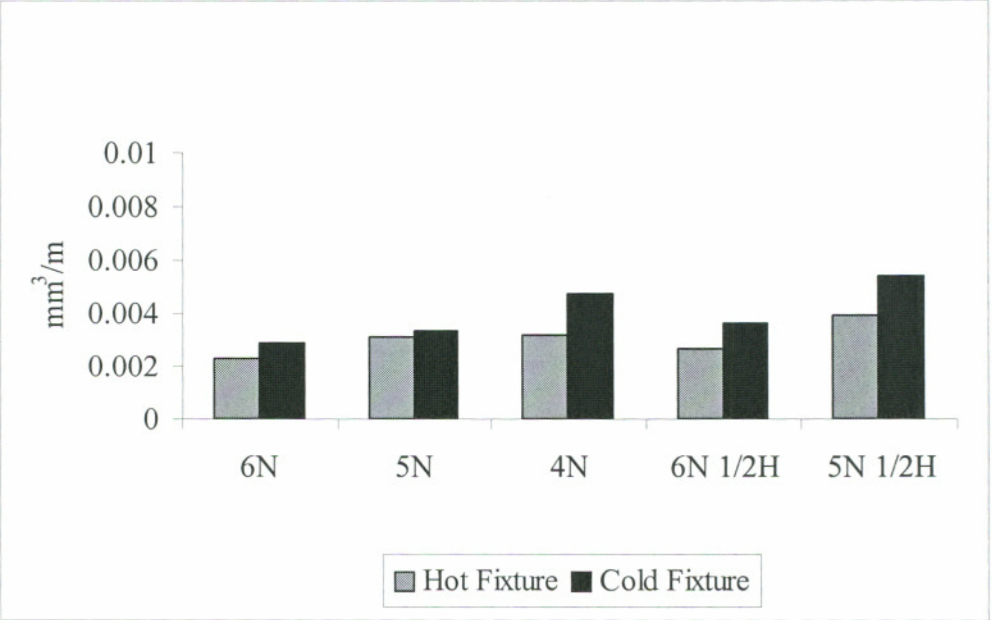

Figure 3.84. Wear Rate of Osram-Sylvania 12 wt% Co, hot fixture and cold fixture.

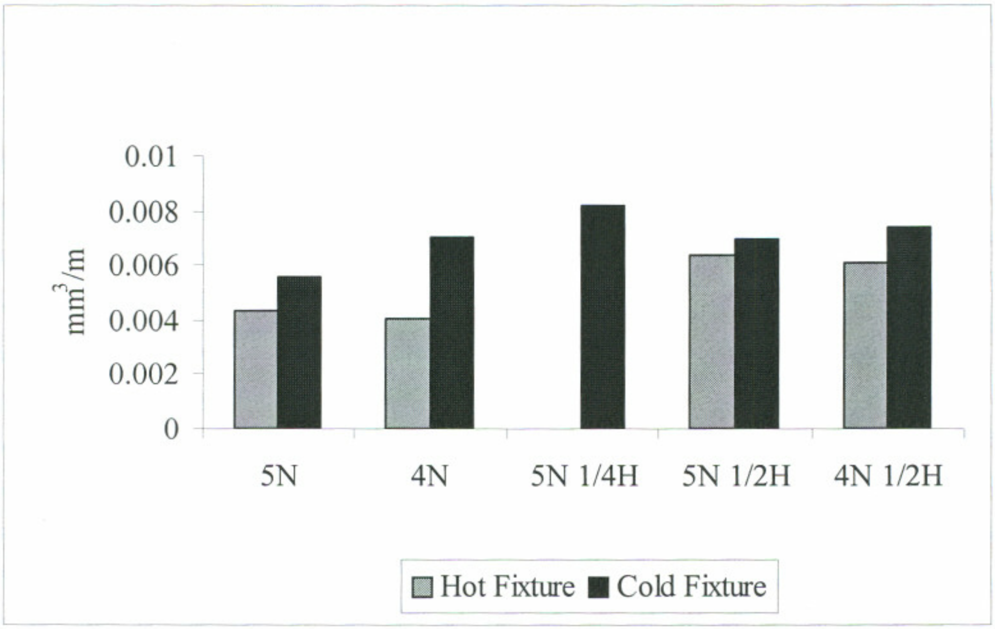

Figure 3.85. Wear Rate of Osram-Sylvania 18 wt% Co, hot fixture and cold fixture.

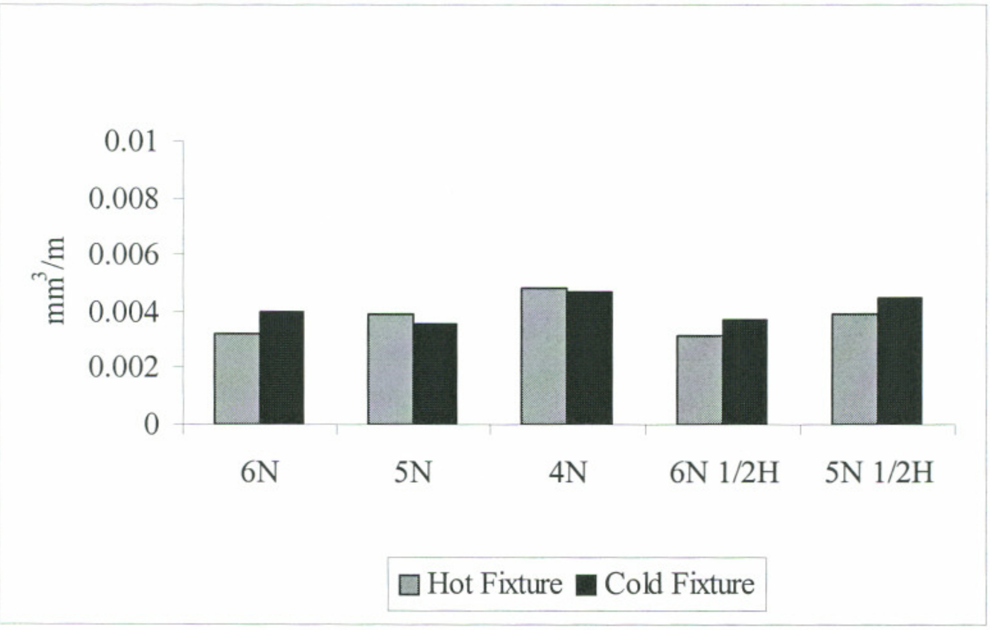

Figure 3.86. Wear Rate of Nanodyne^{TM} 15 wt% Co, hot fixture and cold fixture.

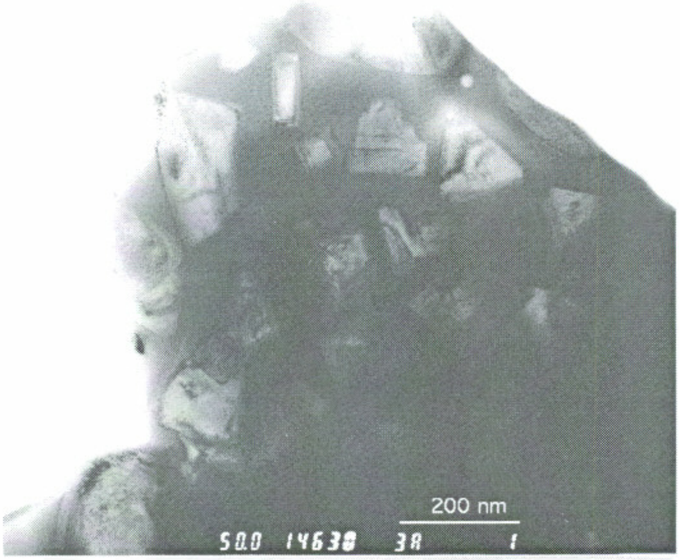

Figure 3.87. TEM image of sprayed coating showing WC particles in matrix, 50000X.

Figure 3.88. TEM image of sprayed coating showing WC particles in matrix, 100000X.

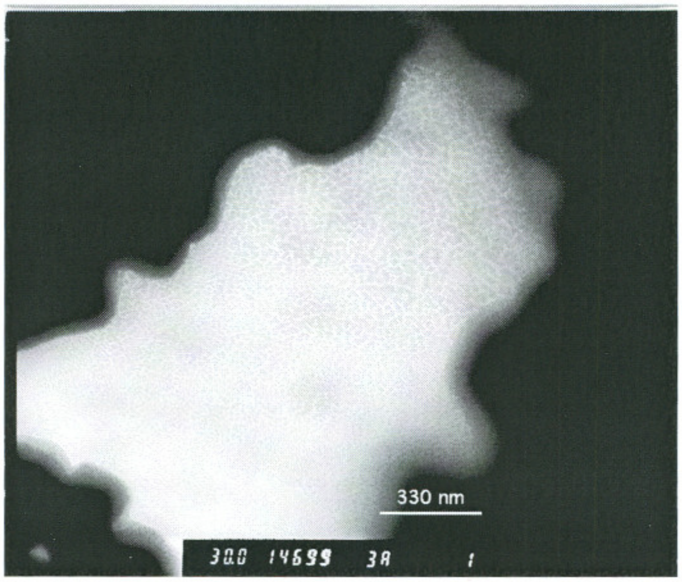

Figure 3.89. TEM image of matrix showing glassy appearance, 30000X.

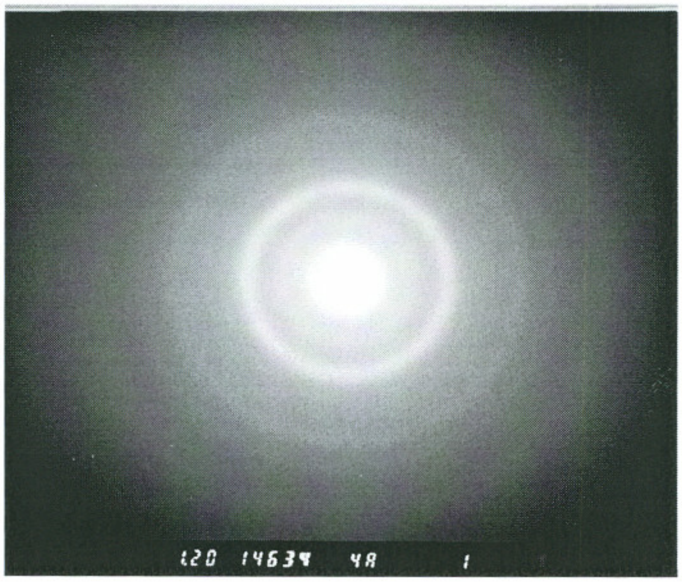

Figure 3.90. Diffraction pattern of matrix from Figure 3.90.

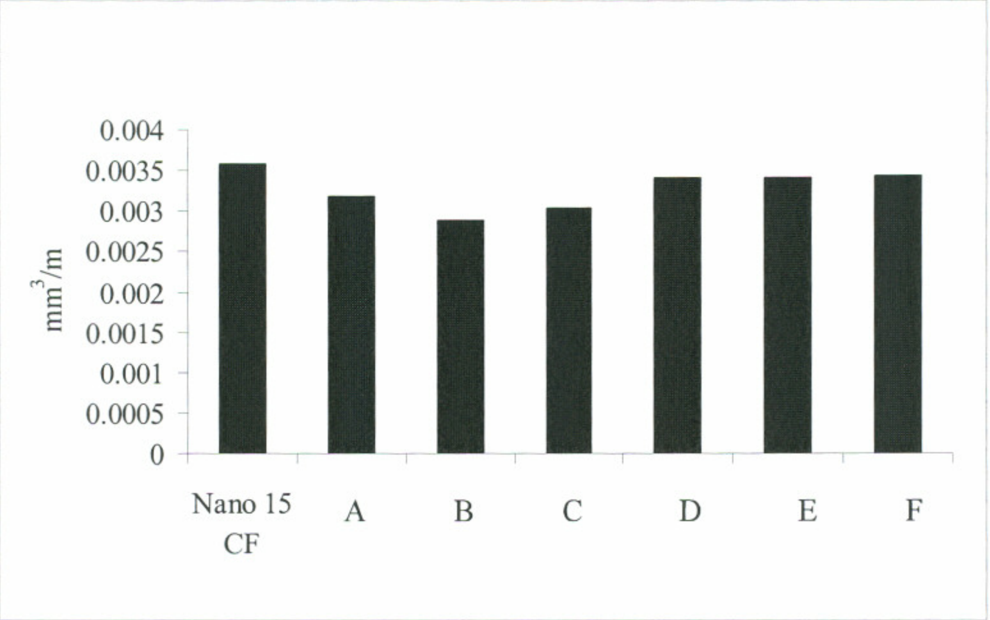

Figure 3.91. Wear rate of non-heat treated Nanodyne™ 15 wt% Co coatings compared to those heat treated for one hour at 200° C (A-C) and 400° C (D-F).

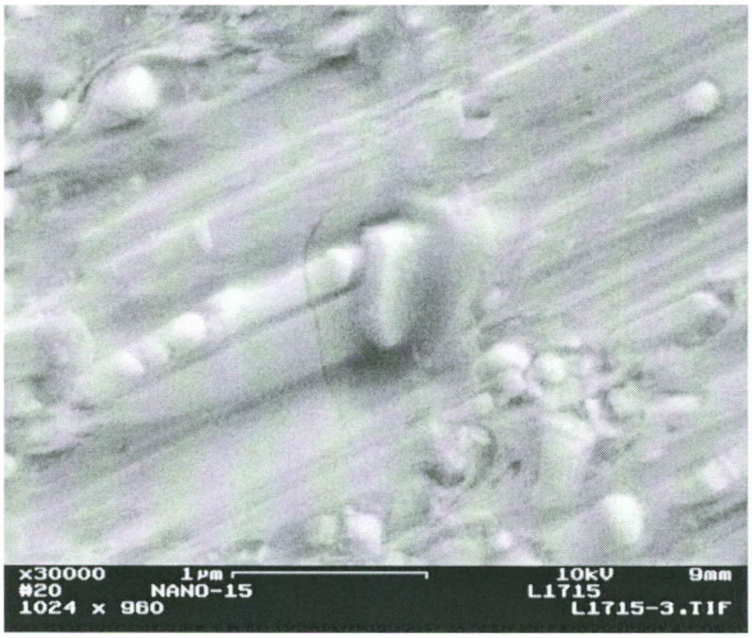

Figure 3.92. FESEM image of Nanodyne™ WC-15 wt% Co powder B cross section 30000X, showing ductile flow in matrix.

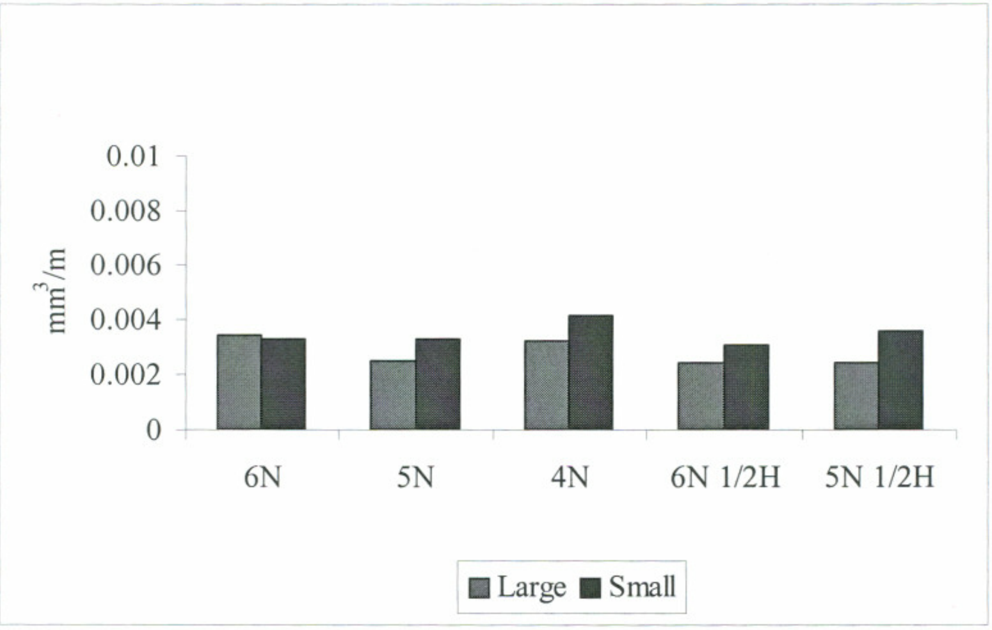

Figure 3.93. Wear Rates of Large vs. Small Nanodyne™ 12 wt% Co, hot fixture.

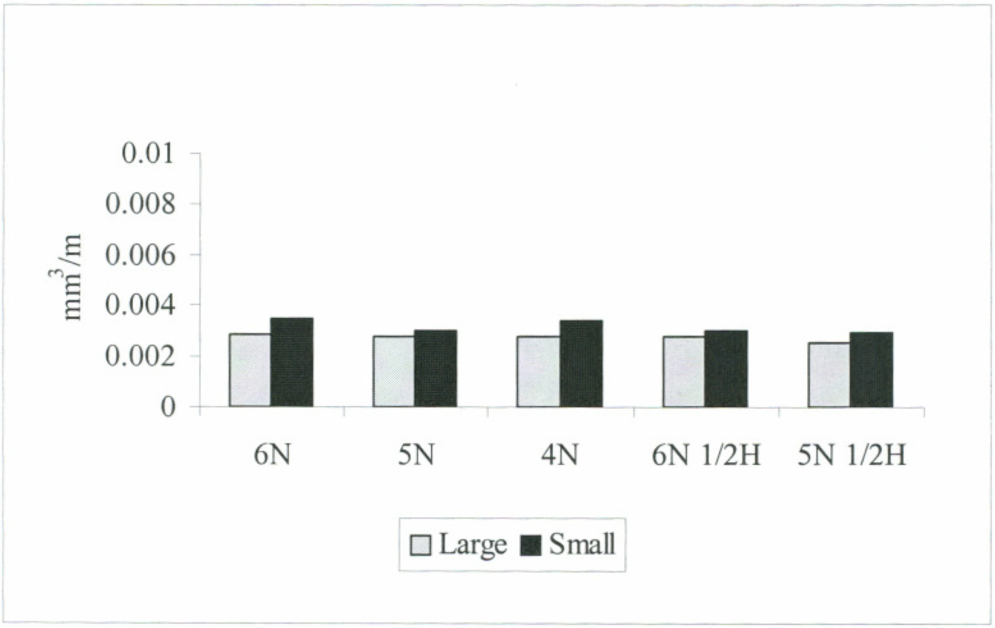

Figure 3.94. Wear Rates of Large vs Small Nanodyne™ 12 wt% Co, cold fixture.

Figure 3.95. Optical photomicrograph cross section of Nanodyne™ 12 wt% Co, Large Cut showing less then full melting, 200X.

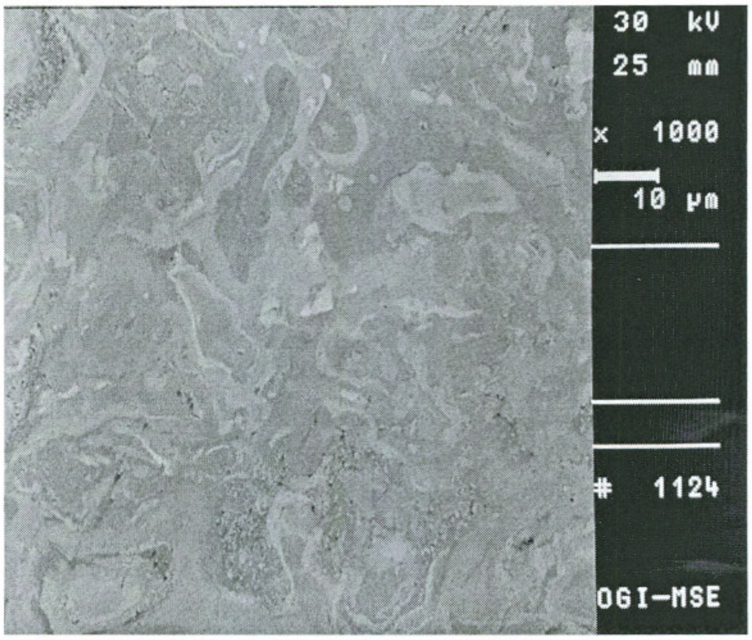

Figure 3.96. SEM micrograph of the wear scar for Osram-Sylvania 18 wt% Co sprayed with hydrogen resulting in the melting of carbides.

4.0 DISCUSSION

The focus of this thesis was the microstructural characterization and abrasive wear behavior of WC-Co plasma sprayed coatings. The discussion will focus on a number of variables that influenced the wear rate of the coatings. The discussion consists of four areas of interest; microstructure, reduction/oxidation, property comparisons and wear. The various powders and coatings in this study were compared. The effect of hydrogen, oxygen, and carbon were examined . The relationships between trends in the hardness, porosity and wear rates for the coatings were examined. Finally, the abrasive wear mechanism is discussed, and a potential wear relationship is presented.

4.1 Coating Microstructure

Both microstructure and properties of the sprayed coatings were examined. While all of the coating were observed optically and many were examined with the SEM. It is not possible or even desirable to fully document the microstructure of all the coatings. The cross sections that are shown illustrate the characteristic microstructure of the coatings as well as some of the changes that occur based on the spraying conditions. The coating properties examined were hardness and wear rate.

4.1.1 Coating Microstructure

There were a variety of microstructural features of interest in the coating, porosity, unmelted particles, overmelted particles, etc. However, the focus of this work on the wear properties of the coatings. So the coating images emphasize the carbides and the matrix. Of particular interest are the effect of hydrogen on the coating microstructure and the carbide-rich and carbide-poor regions.

As the carbide size decreased it was not always possible to distinguish the individual carbides in the coatings with optical methods. However, in all of the coatings shown sprayed in the nitrogen-only condition, there were easily visible regions of carbides. The addition of hydrogen to the plume, with the same amount of nitrogen resulted in a significant decrease in the size and frequency of the carbide-rich regions when compared to the nitrogen only condition. In the case of the Osram-Sylvania - 18 wt% Co coating sprayed with hydrogen there does not appear to be any carbide-rich regions remaining (Figure 3.96). Images of the wear scar in BSE mode show that there are areas that are of high Z value that no longer have discrete carbides. Carbides are shown to be standing proud from the matrix in all cases. The increase in the amount of non-discrete carbides was expected to increase the material loss due to the relative softness of these phases.

Carbide-rich and carbide-poor regions differ in the amount and type of wear. In the carbide-rich regions it can be seen that the carbides stand proud and that the matrix is removed around them. This creates a surface of hard carbides. Where there are fewer carbides it can be seen that there is an increase in the abrasive wear of the surface. The wear scar can be thought of as an image of wear arrested. Different regions of the scar show different morphology. These morphology can be thought of as being spread over the area of the wear scar in a random way. This is not strictly true, as there will be some regions of preferential deposition due to the way the powder was fed into the plume.

It has been shown by various authors that distribution in the plume of powder particles is effected by the particle loading, stochastic particle interactions and particle size distribution and morphology. The effects of the location of the injectors, their angle in respect to the plume, the carrier gas velocity, and gravity cannot be neglected either.

The coating microstructure is such that interpenetrating skeletons of carbide and cobalt do not occur. This is the major difference between the sintered and sprayed coatings, and the lack of a 3-D carbide skeleton limits the achievable properties of the coatings. For example in the sintered WC-Co hardness of 2200 HV have been reported, in the sprayed coatings the highest hardness achieved in this study was 1200 HK_{500}.

The lack of long range carbide/carbide interfaces limits the potential hardness and wear resistance of the coatings. It is not unexpected that the values of the hardness and wear resistance do not compare to the values achieved in sintered material. The isolated nature of the carbides in the sprayed coatings means the carbides act more like particulate reinforcements rather than providing the structure as they would in a sintered material.

Both Stewart and Usmani [10, 69] observed a decrease in the wear resistance of the coating with a decrease in the carbide size. Harvey et al. [86] suggested in their work that there was a direct correlation between the high wear rates and the high levels of amorphous W-C-Co phase in the ribbon like structures (melted decarburized WC). The reason that there was a decrease in the wear resistance with decreasing carbide size was due to the greater degradation of the carbide of the smaller carbides. With careful control of the spraying process it is possible to create coatings that are no worse than a conventional coating with the same weight percentage carbide.

4.2 Reducing Agents

It was thought in developing this investigation that reducing the degree of decarburization in the coatings might result in significant improvement in the properties of the coatings. This was approached by adding carbon and hydrogen. Carbon was added to a powder with good flow characteristics to act as a getter for the oxygen entrained in the plume. Hydrogen was added to the plasma gas and was intended to produce reducing conditions in the plume, limiting decarburization and potentially improving the coating properties. The following reactions are some of the possible steps in the decarburization of the tungsten carbide.

$$2WC \rightarrow W_2C + C \tag{31}$$

$$W_2C + O \rightarrow W_2(C,O) \tag{32}$$

$$W_2(C,O) \rightarrow 2W + CO \tag{33}$$

$$4Co + 4WC + O_2 \rightarrow 2Co_2W_4C + 2CO \tag{34}$$

$$3Co + 3WC + O_2 \rightarrow Co_3W_3C + 2CO \tag{35}$$

$$12Co + 12WC + 5O_2 \rightarrow 2Co_6W_6C + 10CO \tag{36}$$

As mentioned in the introduction the first set of reactions (Equations 31-33) are thought to only occur on the surface of the particle. These reactions proceed at a very slow rate until liquid WC is present. The melting and boiling points of the materials are such that a significant loss of Co could also occur by the time the powder is heated sufficiently to melt the carbide. The second set of reactions (Equations 34-36) would be diffusion limited and occur primarily in the presence of liquid Co and solid WC. These two sets of reactions result in different types of compounds being formed in the coating.

The first set of reactions will result in the presence of W in the coating. The second set of reactions would result in the formation of one of the eta carbides. In both reaction sequences, oxygen plays a significant role. The reducing agents were intended to limit the role of oxygen in the material. The reaction that was assumed to have occurred with the carbon in the plume was:

$$C + O_2 \rightarrow CO_2 \tag{37}$$

or

$$C + O \rightarrow CO \tag{38}$$

These reactions serve two purposes: they remove oxygen from the plume which limits the amount of oxygen available for the decarburization; and the presence of the CO and CO_2 could serve to limit the forward reactions of Equations 31-33. However, due to the time scale and the turbulence/fluid dynamics of the plume, equilibrium is never reached and so the reverse reaction may not occur.

It was expected that the amount of carbon added was insufficient to cause an increase in the amount of carbon in coating. CO and CO_2 formation reactions would change the balance of the decarburization reactions by removing oxygen from the plume, therefore, limiting the oxygen assisted decarburization of the coating. The inclusion of carbon had two effects. There was a decrease in the amount of decarburization. The addition of carbon to the powder decreased the coating thickness. It was assumed that 1 to 4 weight percent of carbon would not make a significant difference in the way the coating was formed. However, the addition of carbon resulted in a large decrease in the coating thickness, limiting the usefulness of a carbon addition. Figure 4.1 shows a slight improvement in the wear rate of the coatings when compared to the same conditions without the addition of carbon, also see Table 4.1.

It was unclear why there was such a large drop in the deposition efficiency with the carbon addition. The addition of the carbon lowered the mass of powder flowing into the plume, which would have decreased the relative deposition efficiency. The combustion of the carbon may have also caused some scattering as the powder was injected into the plume. If different spraying conditions, or a different equipment set up had been used, it may be possible to achieve the improvements in the wear rate with the addition of the carbon without the decrease in deposition efficiency. The amount of carbon in the WC-Co powders was in the 5.0-5.3 wt% range, shown in Table 3.5. It was assumed that there was no free carbon in the powders, and this was supported by the fact that the XRD did not detect free carbon. Many of the powders were sintered and agglomerated and as such any free carbon would have formed graphite.

The amount of carbon expected in each of the coatings will vary by the amount of cobalt in the starting powder. There is 6.12 wt % carbon bound in stoichiometric WC. All of the WC in the starting powders were assumed to be stoichiometric. This seemed to be reasonable assumption to make in light of the narrowness of the phase field as evidenced by the phase diagram (Figure 1.1). Table 3.5 shows the 'ideal' amount of carbon in the starting powders, the amount of carbon that was detected in the coating, and the amount of carbon that was retained. The trends shown in Table 3.5 were as expected. Higher cobalt contents, larger carbides and full coverage of the carbides resulted in a minimization the of carbon loss [36, 66, 69]. With those criteria, the conventional material would be expected to have the minimum amount of carbon loss and only 30% of the carbon was lost. The coating made from the powders containing the nanoscale carbides had the characteristics to maximize the carbon loss; i.e. small carbides and a porous powder morpohlogy with poor carbide coverage. This particular powder had lost 67% of the carbon in the spraying process. The carbon loss in the coating with submicrometer carbides was higher than might be expected especially in the case of the 12 wt% Co powder, which also lost 67% of carbon. The 18 wt% Co powder faired better with only a loss of 49% of carbon.

The comparisons of the phase degradation done by XRD show that there is much less degradation in the case of vacuum plasma sprayed WC-Co coating when compared to coatings sprayed in atmosphere. So it was assumed that the carbon is lost in the plume, following the reactions presented by Finke et al.

The Osram Sylvania WC-18 wt% Co powder which had carbon added to the feedstock also was analyzed for carbon. The addition of carbon to the feedstock powder decreased the loss of carbon in the coatings. This was either due to a suppression of the decarburization reactions by giving the oxygen another source of carbon to react with or due to the actual addition of carbon to the coating.

The carbon added to the feedstock powder in this study was carbon black not crystalline graphite. Where the carbon added to the feedstock powder went is uncertain. Carbon sublimes at 3652° C, which is a higher temperature then was experienced by the powders that formed the coatings. The small size of carbon could have allowed greater acceleration of the particles so that they would not have had enough time in the plume to cause sublimation and might have been included in the coating. Conversely, the very small size of carbon also means it has a large amount surface area with which to react with the entrained oxygen. A third scenario is that the carbon black was too small to efficiently enter the plume, at the injection angle used for the powders, and a majority of the carbon bounced back out of the plume. Neither the optical nor SEM observations of the cross sections of these coatings revealed the presence of carbon inclusions, though it is possible that the carbon was removed during the polishing process.

The commonality in the carbon loss results can be linked to a combination of factors; the morphology of the particle, the cobalt content of the particle, and the size of the carbides in the powder.

The conventional powder had the most carbon retained in the coating. Furthermore, the XRD traces of the coatings made from this powder show very little phase degradation (Table 3.9). There is a slight presence of the W_2C but no evidence of tungsten, although Co-W solid solution would not show up in XRD. Both Stewart and Jia observed regions in the matrix that had 20-23wt% W. The chemistry data, Table 3.7, also did not show a large drop in the amount of W in the coatings corresponding with the loss of carbon.

The submicrometer WC powders were very similar powders with only the cobalt composition differentiating them. The expected trend of higher cobalt composition showing less decarburization was observed. However, without more testing it is difficult to understand the significance of this trend.

The powder containing the nanoscale carbides had the greatest amount of carbon loss. The small size of the carbides meant that it had the largest surface area of carbides. Degradation of the carbides is controlled by diffusion. More surface area means that there was more surface area to react with and this, combined with the decrease in the diffusional distances, means that reactions would occur faster. The effect of the reduction in carbide on the surface area of the carbides assuming the same total volume is illustrated on Table 1.2.

The FESEM observations of the cross sections of the powder containing nanoscale carbides show a very porous powder with poor coverage of the carbides by cobalt, Figures 3.56 and 3.57. This further increases the surface area of the carbide available for reaction. The XRD of this powder differed from the rest in that it did not produce a cobalt peak in the diffraction pattern. This suggests that the cobalt in the starting powder was amorphous which explains the odd globular shape of the cobalt around the carbides. The high porosity, poor cobalt coverage, and small carbide size all contribute to the carbon high loss in the resulting coating.

4.2.1 Hydrogen

The use of hydrogen in the plume was investigated as a means to eliminate the decarburization of the powder in flight by creating a reducing atmosphere in the plasma jet. The reaction mechanisms for the formation of W_2C and W were presented previously. The removal of carbon from WC only occurs when the particles are exposed to high temperature and oxygen for a significant time. Finke et al. [56] suggested that the reactions would not proceed at a significant speed until the WC melted. Images of the coatings sprayed with nitrogen and hydrogen when compared to the coatings sprayed only with nitrogen, show fewer carbides. There were fewer carbides observed in the coatings that were sprayed with N_2/H_2 versus N_2 only. This was assumed to be due to the increased temperature that the particles would experience with the addition of hydrogen to the plume. This would be mainly due to the increase in the thermoconductivity of the plume with the inclusion of hydrogen. This would have increased the heat flux to the particles leading to increased melting of the carbides in the plume, which could decrease the wear resistance of the coatings either through the formation of the W_2C and W or through dissolution of the WC into the matrix [35, 87].

The increase in the temperature and thermoconductivity of the plume with the addition of hydrogen promotes the overheating of the powder particles. As a result, the net effect of the addition of hydrogen to the plume was a decrease in the wear resistance of the coating due to the loss of WC particles. The predominate morphology of the decarburized carbides was much more rounded than the carbides in the starting powder. The most obvious example of this can be seen by comparing the carbides in the starting powder of the Metco 2004 powder with the carbides in the wear scar of the coating, (Figures 3.32, 3.33, and 4.2 and 4.3). The carbides in the starting powder were prismatic, the carbides in the coatings were more rounded. From these images it is clear that there was sufficient heating in the plume to melt some of the carbides.

The work done on sprayed WC-Co coatings has indicated that the loss of carbon is not detrimental in terms of wear resistance until the carbon loss exceeds 60% [66]. The loss of WC carbide is partially compensated by increasing the hardness of the matrix by the dissolution of W and C. This observation again illustrates the importance of the matrix properties.

4.3 Oxidation of Nanoscale Carbide Powders

Though no quantitative studies were performed, the Nanodyne™ WC-15 wt% Co powder containing the nanoscale carbides was found to react in a furnace at 300°C. The submicrometer and micrometer carbide containing powders did not react at the same temperature. The reacted powder changed in color from black to green and, over time, eventually turned blue. This was assumed to indicate that the powder was transforming from the carbide to a mixture of WO_2 (yellow) and WO_3 (blue), and finally transforming completely to WO_3. In general the literature on the oxidation of WC discusses the formation of WO_3, and does not mention the formation of WO_2 [59, 60, 84]. Roebuck's experiments ran to completion and as such the thermodynamically stable tungsten oxide, (WO_3) was the only oxide of interest. In other work focusing on the oxidation of WC-Co, WO_3, Co_2O_3 (black), Co_3O_4 (black), and $CoWO_4$ (blue) were all identified with XRD [88]. Another study by Lofaj found that oxidized WC-Co formed WO_3, and CoO (pink) in the oxidized layers but did not note any presence of any other oxides [89]. The formation of WO_2 would be slightly favored over the formation of WO_3 on a per mol of oxygen basis their energies of formation are -379kJ vs -356kJ. However, per mol of WC, the energy of formation at 800°C for WO_3 is -534 kJ vs -379 kJ for WO_2, [90, 91]. The increased particle surface reactions with decreasing carbide size agrees well with the findings of Roebuck et al in their studies of the oxidation of WC [59, 60, 84].

4.4 Property Comparisons

The effect of hardness and porosity on wear and each other was evaluated. The data set was inclusive of all of the acceptable coatings sprayed and thus represents a wide range of spray conditions. The data has substantial scatter and few trends were observed. The effect of the different spray conditions on the various powders made it difficult to evaluate the inter-relationships between material properties (hardness and porosity) and extrinsic behavior (wear). Due to the large amount of scatter in the data, it is unclear as to the degree that the decomposition of the carbide had on the properties of the coatings.

4.4.1 Porosity vs. Hardness

The hardness of the coatings is plotted against their porosity in Figure 4.4. Only a weak relationship between the hardness and porosity of the coatings is observed. There is a wide range of hardness for the same amount of porosity in coatings with similar carbide sizes, and cobalt contents. There does seem to be a general, if broad, trend toward lower hardness with increasing porosity. Figure 4.5 shows the same data constrained to the 12 wt% Co powders. Coatings sprayed on the hot fixture had higher hardness for the same nominal amount of porosity as coatings sprayed on the cold fixture. The large solid powder had a lower hardness than the small solid powder sprayed on the hot fixture. Coatings using the large and small solid powder as feedstock sprayed on the cold fixture had nearly the same porosity and hardness. The Osram-Sylvania - 12 wt% Co powder showed the unusual trend of having nearly constant porosity and widely varying hardness.

The data would indicate that there is not a strong relationship between hardness and porosity. However it must be pointed out that there are flaws with the way the porosity was measured in this study. The polishing process was standardized for all coatings which had a wide range of microstructures. At least some of the porosity measured by image analysis was caused by pullout. So the real amount of porosity in the coatings may have been lower than the measured amount. This was a much more significant problem with coatings that containing micrometer carbides that did not have full melting of the splats, i.e. Metco 12 wt% Co, and the Nanomyte^{TM} powders.

4.4.2 Porosity vs. Wear Rate

Figure 4.6 illustrates the relationship between the porosity on wear rates in the coatings. The range of porosities in these coatings was not so great as to overly effect the wear rate of the coatings. The 18 wt% Co coatings did show an anomalous trend of decreasing wear rate with increasing porosity. The reason for this trend is unclear, although, the low porosity coatings may have had lower porosity due to excessive melting. This trend may mean that the deposition conditions were not sufficiently optimized for the 18 wt% Co powders. Figure 4.7 shows the porosity wear rate of the coatings containing submicrometer carbides and 12 wt% Co and there was a broad clustering of wear rates regardless of porosity. Most of the coatings tended have porosities of less than 5 percent, which may not be large enough to distinguish between them in low stress abrasive wear. At high loads, with harsh abrasives, the porosity would be expected to effect the wear rate by providing crack initiation centers. However, the dry sand rubber wheel abrasion test with Ottawa silica sand was not severe enough for that to be apparent.

4.4.3 Hardness vs. Wear Rate

Wear equations by Archard and Khruschov assume some relationship between hardness and wear rate. Under classical abrasive wear theory it was expected that, as the hardness of the coating increased, the wear rate of the coating would decrease. Figure 4.8 is a plot of hardness vs. wear rate for all of the coatings. This plot shows that there is not a strong relationship between hardness and wear rate, or at least not a simple one. With only the 12 wt% Co coatings plotted (Figure 4.9), the data shows a weak relationship between hardness and wear rate. The highest hardness coating and the lowest hardness coating did not have a substantial difference in their wear rate, even though the difference was 425 HK_{500}. The weakness of the hardness/wear rate relationship may be due in part to the wide range of powder characteristics. To examine that possibility, the two Osram-Sylvania powders were plotted against each other (Figure 4.10). As shown in Figure 4.10, a relationship between hardness and wear rate is more evident. However, the softest Osram-Sylvania - 12 wt% Co coating was not much softer than the softest 18 wt% Co coating; yet had twice the wear rate. This suggests that the relationship between hardness and wear rate is more complicated than expected from simple abrasive theory as depicted by Khruschov's wear equation.

4.4.4 Hardness and Porosity

The coatings in general had hardness values between 900 and1200 HK_{500}. There was not a strong relationship between hardness and porosity even for coatings with the same carbide size sprayed on the same fixture (Figure 4.11). The data does not tend to show the expectation that lower porosity results in higher hardness. The lower porosity coatings tended to be coatings sprayed with hydrogen in the plume and, as previously noted, the addition of hydrogen to the plume caused overmelting. The lower porosity coatings tended to have a larger percentage of matrix phase, which due to the diffusion of W into the matrix, may have been harder then the pure cobalt would have been. However, the increase in hardness of the matrix was overshadowed by the decrease in the number of carbides in the coatings. Furthermore, the coatings were very heterogenous, with both carbide-rich and carbide-poor regions that varied in hardness. That variation in hardness may have swamped out any effect of porosity on the hardness of the coating.

What was not observed was a trend for the coating containing smaller carbides to be substantially harder than the larger carbide containing coatings. The predictions of the Hall-Petch relationship, that the nanoscale carbide containing coating should be harder than the coatings containing micrometer or submicrometer carbides was not seen within the data set. The increased hardness of the nanocarbides has been reported in the case of the sintered material [32, 92]. The absence of an increase in hardness in the case of the small carbides in a thermally sprayed coating was likely due to the relative percentage of matrix and the lack of WC/WC interfaces.

Sintered nanoscale WC-Co has been shown to have an increase in the hardness and wear resistance over sintered WC-Co with conventional sized carbides. Sintered WC-Co has been described as being comprised of two interpenetrating skeletons; one comprised of WC and the other comprised of Co. TEM studies have shown that WC/WC bonds are present in sintered materials. In the sprayed material these bonds are much less common and never are able to develop to the same extent as in the sintered material. The sintered material could be thought of as a three dimensional fiber reinforced composite. The sprayed material, due to the lack of WC/WC bonds, would be better described as a particulate reinforced composite. Another way of thinking about this difference is via the contiguity (C), which is used to calculate the properties of sintered WC-Co. In sprayed WC-Co the contiguity is much lower then in sintered WC-Co, in fact almost zero. This can be seen in the images of the carbide-rich regions of the worn coatings, where there is clearly significant spacing between the carbides. In small regions of the coatings, there are regions that have very high concentrations of carbides and the carbides appear to be butting up next to each other. In this case there could be WC/WC bonding, but these regions are rare in the sprayed coating.

The rule of mixtures which can be used to estimate the hardness of the composites, predicts that the increase in the cobalt content should decrease the bulk hardness of the coating. Calculation of hardness for the sintered WC-Co, due to the effects the WC skeleton, has the additional factor of contiguity. Sprayed coatings are better modeled as a particulate reinforced composites and as such the standard rule of mixtures in more applicable. The rule of mixtures in the latter case would be a linear relationship between the hardness of Co and the hardness of WC and their relative volume percentages. There is a 15 volume percent difference in the amount of WC versus Co in the 18 wt% and the 12 wt% coatings. The rule of mixtures would predict that there would be 15% difference between the hardness of the two coatings. Due to the large amount of variability in the hardness data, this was difficult to observe. The coatings made from the 18 wt% powders were not noticeably softer than the coatings made from the 12 wt% powders in the best cases.

4.5 Abrasive Wear

There are numerous factors that influence the abrasive wear of the coatings. This thesis focused on the carbide size and cobalt content. The effect on the wear resistance due to the reduction in the carbide size was the initial motivation for this study. Cobalt content in sintered WC-Co cermets controls several important properties. In sintered WC-Co, the cobalt content controls the fracture toughness of the material. However, this is less studied in WC-Co coatings. Thus the relationship between the cobalt content and the carbide size should be critical in determining the fitness of the coating for a particular application.

The raw wear data has been presented in the results section. In this section the effect of selected variables on the wear rate will be evaluated. The SEM and FESEM images of the wear surface will be used to explain the wear mechanism. The equal pressure and equal wear modes that were presented in the introduction will be further discussed. Finally, a model for predicting the wear of the coating under low stress abrasive wear will be presented.

4.5.1 Effect of Carbide Size on Wear

The initial reason for looking at the fine grained WC was for the potential improvement in the wear resistance of the WC-Co coatings. Figure 4.12 shows the best wear rates for each of the powders that produced reasonable coatings sprayed on the cold fixture. The wear rate range for the 12 wt% Co coatings was 0.0031 to 0.0029mm^3/m, see Table 4.2. The coatings with micrometer size carbides had slightly higher wear rates than the coating with submicrometer carbides for the same initial percentage of cobalt. However, the difference was so small as to be well within the expected range due to experimental error (± 10%). A powder with good spraying characteristics, whether it contained micrometer or submicrometer carbides, resulted in low wear rates with no substantial drop in wear rate as the carbide size decreased. The powder containing a reasonable percentage of nanoscale carbides had intermediate to poor spraying characteristics and, they had a higher wear rates than the coatings containing micrometer-size carbides for comparable spray conditions.

A comparison of the best hot fixture wear rates revealed a change in this trend, Figure 4.13. As discussed in an earlier section, there was an decrease in the wear rate of the coatings from the cold fixture to the hot fixture. The exact reason for this decrease in the wear rate was not clear, but all coatings made from powders containing 12 wt% Co tended to have very similar wear rates. The range of values for the wear rates for these coatings were 0.0024 to 0.0022mm^3/m, which is a small enough range that all the values must be considered identical see Table 4.3.

4.5.2 Wear Scar Topography

Images of the wear scar were taken with both the SEM and FESEM. Only coatings sprayed on the cold fixture were imaged. The images show the microstructures of the coatings from a surface perspective, rather than in cross section. The microstructural features seen in the cross section can be related to the features seen in the wear scar in a qualitative way. The cross sectional images showed both rich and poor carbide regions. These regions are evident in the wear scar images as well. The wear scar images reveal differences in coatings and help explain the change in the wear rate between the different coatings. There were several features that are of importance in the microstructure of these coatings: unmelted particles, carbides surrounded by matrix, and overheated splats in which the carbides have melted. Due to their aspect ratio some microstructure features are more evident in the wear scar than in the cross sections.

Coatings made from the conventional powder containing micrometer sized carbides and the powder containing the nanoscale carbides were compared. Both groups the coatings were sprayed on the cold fixture and had the lowest wear rate for their group. Splat size depended on the condition and the size of the powder particle. In some cases there was a very wide range in powder sizes and the resultant splats varied in size. In general though, the splats were 10 to 20 μm wide and less then 2 μm thick. The images (Figures 4.14-20) show a small area of a single splat.

4.5.3 Field Emission Scanning Electron Microscopy of Metco 2004

The image in Figure 4.14 shows the carbide-poor region, small scale wear grooves and wear debris. The regular shaped object in the center of the images is probably an uprooted carbide sitting on the surface of the coating. Figure 4.15 shows a cracked carbide. Figure 4.16 shows the worn topography in a carbide-poor region, where the central feature is a high Z material containing tungsten and a previously melted and decomposed carbide. Also of note are the cracks around the feature, so while it is wearing at a higher rate than the other carbides it is still fracturing the surrounding matrix. Figure 4.17 shows a carbide-rich region in the coating. There were numerous fractured and unfractured carbides. Figure 4.18 focused on a particular carbide from the previous image, clearly showing the fracturing in the carbide. Also of note in this image is the dark line around the carbide indicating that the carbide is not fully bonded to the matrix. It is possible that this was due to the difference in the thermal expansion of the materials, the cobalt receding from the carbide as it cools, the fractured carbide was loosening from the matrix, or the matrix was deforming around the carbide.

4.5.4 Field Emission Scanning Electron Microscopy of Nanodyne™ 15 wt% Co

Figure 4.19 shows the ductile feature of the wear scar, where the matrix material has moved around the carbides. The carbides seem to be acting like particle in a fluid flow, where there is bow wave in front of the particles and a wake behind. The scratches are on a very fine scale (less then 60 nm), the size of the carbides ($\approx$100 nm) or less. Also observed was a regularly shaped pore, which is likely where a carbide was plucked from the matrix. A few carbides were seen to be standing proud and these carbide-rich regions did not show any other signs of wear.

Figure 4.20 shows a wear groove where a carbide has been removed from the matrix. The groove continues intersecting a small group of carbides. The carbides show no evidence of damage from the groove running through their midst. However, they do not stop the groove either as it continues on the other side of the carbides. The carbides seem to be resistant to wear as the scratches continue on the other side of the area covered by the carbides.

This suggests that these coatings, with the carbide-rich and carbide-poor regions, are only highly wear resistant in the carbide-rich regions. The carbide-poor regions around the carbide-rich regions are not protected at all due to their proximity to the carbide-rich regions.

The coatings were made up of splats melted from powder particles that had experienced a wide range of temperature conditions. The coating was a large scale average of all of these splats. Depending on the conditions that the individual powder particle experienced, an area of high carbide density was the result of either unmelted or undermelting, which retains the most carbides but does not adhere well. Overmelting of the splats resulted in melting of the carbides and loss of cobalt. This resulted in splats with high Z value, indicating W or W_2C and a lack of cobalt. The degradation of the carbides has been related to poor wear resistance by Stewart and Qiao [35, 69, 89, 93, 94]. The abrasive particles in this case are small enough that the carbide-rich regions are not providing any protection to the carbide-poor regions. The idea that the abrasive particles would be supported by dozens if not hundreds of carbides appears to hold true for the small particle wear. This is not to say that the silica sand is not being supported by hundreds of carbides for the contact area is just too large for that not to be the case. However, the smaller wearing debris of uprooted carbides are able to wear the carbide-poor regions without being stopped by the carbide-rich regions.

The wear scars illustrate the actual wear mechanism of the material. The use of the FESEM allowed for high resolution images of the micrometer and nanoscale carbides to be obtained. There were several general observations that could be made about the wear scar in all of the cases. It was assumed that the difference between the hot and cold fixture would be a question of the extent of the wear as opposed to a change in mechanism by which the wear occurs. The abrasive, in all cases, was Ottawa silica sand, 50-70 mesh size. Figure 4.21 shows that the sand was in the 212-300 μms range.

This sand was a 'rounded' sand with a narrow distribution of sizes. This images shows that the sand is not perfectly smooth, rounded is a description of the sand and is a relative term when compared to the other sand abrasives used by Avery [95-97]. The sand has asperities that are much smaller than the size of sand particle [98]. A perfectly smooth sand particle would cause wear in the coating that would result in large grooves that were on the same size scale as the sand. The Ottawa silica sand is shown to not be perfectly smooth but have a significant amount of asperities on it's surface. Figure 4.22 is an asperity of the Ottawa silica sand broken off in a wear groove in steel. The wear groove in this case is approximately 10 micrometers in size, if the material were harder the size of the wear groove would be substantially reduced. The asperities on the silica sand are small enough that they could wear a single splat. There were not large areas of material removal corresponding to the size expected from wear caused by the whole grains of the Ottawa silica sand.

What is revealed by the SEM and more clearly by the FESEM images was that grooves in the wear scar were much smaller than could be conveniently accounted for by just the wear of the Ottawa sand. The images show the submicrometer size of the wear grooves. The evidence suggests that the wear was not solely caused by the sand but also caused in some part by the removal of carbides from the matrix. The subsequent dragging of the carbides through the (relatively) soft matrix phase has been clearly shown. Figures 4.32, 4.34 and 4.37 also showed a difference in the wear mechanism between the micrometer and nanoscale carbides. Some of the micrometer sized carbides in the wear scar were fractured and the nanoscale carbides observed in the wear scar did not show any sign of fracture. Rather it seemed that the smaller carbides were uprooted and pulled out of the coating.

The coatings that had the lowest wear rates for the extremes of WC particle size were observed to see if there was an effect of carbide size on the wear mechanism of the coatings. None of the coatings observed showed evidence of wear grooves through the carbides. Though in the case of the worn coatings made with micrometer sized carbides, fracture and fragmentation was observed (Figures 4.32, 4.34 and 4.35). The matrix showed distinctive grooving and displacement of material in all of the wear scars was observed (Figures 4.31, 4.36-37). In white cast irons with over 30 volume percent carbide the increase in the wear rate was due an increase in microcracking of the carbides [71]. A similar microcracking is seen in the micrometer scale WC particles. As the volume percent of cobalt is reduced it is expected that the same trend observed in white cast iron would be seen in WC-Co. At some point microcracking and spalling will become the predominant wear mechanism. No signs of cracking was observed in the nanoscale carbides. It should be possible to see an increase in wear resistance due to lower cobalt composition in th coating containing the nanoscale carbides without the microcracking that would otherwise limit the utility of a further decreasing percentage cobalt. Furthermore, a decrease in carbide size results in a decrease in the cobalt mean free path, for the same percentage cobalt. So whether the wear is controlled by microcracking or is controlled by mean free path the reduction in carbide size should result in the increased wear resistance.

The wear scars did not show a large difference in the wear surface appearance between the micrometer, submicrometer and nanoscale carbide containing coatings. The wearing particle in this case is Ottawa silica sand, which is approximately 250 μm in diameter. The largest carbide observed was on the order of several micrometers in diameter, the smallest carbides were in the range of 100 nm making them 200 to 2000 times smaller than the abrasive, respectively.

The size effect study by Misra and Finnie would indicate that the carbides in all cases are so much smaller then the abrasive that there would not be a change in the wear mechanism due to abrasive size [99]. A change in wear mechanism might be expected if the size ratios were substantially different, such a having smaller abrasives or larger carbides.

4.5.5 Effect of Cobalt Percentage on Wear Rate

The carbide size has been shown to not have a major influence on the wear rates once the variation in cobalt contents was taken into account. The powder that contained the nanoscale carbides was a 15 wt% Co. To compare the wear rate of the various carbide sizes, a way to compensate for the cobalt content had to be developed. The Osram-Sylvania powders (WC-12 wt% Co and WC-18 wt% Co) were very similar. Their powder size distribution and carbide size were essentially identical. This allowed for a comparison of the wear rates in which the only variable was the cobalt content. Figures 4.17 and 4.18 show the lowest wear rate of the Osram-Sylvania powders. The difference in the wear rates was initially surprising. The doubling of the wear rate due to a change in 6wt% cobalt seemed out of place. The weight loss rate as a wear rate does not tell the whole story as there was a large difference between the densities of the materials. Even so, there was only a 15% difference in volume of cobalt between the two powders. Wear rate, as predicted by Khruschov's rule of mixtures for the wear rate of composites (Eq. 27), would predict that the difference in the wear rate between the two coatings would be between 18% to 23%. This range of wear rates was obtained by assuming the wear resistance of the carbide was 6 times and 60 times that of the cobalt, respectively. No matter how high relative wear resistance of the carbide phase was to the cobalt phase it is not possible with Khruschov's equation to get a difference greater than 24% for the coatings in question.

The difference in the hardness between the carbide (2000 HK) and the abrasive (650 HK) is large enough for it to be reasonable to think that the carbide is not wearing at all or, at least, very little when compared to the matrix. Images from the previous section show the matrix material loss dominated. The ratio of the matrix area that is involved in the wear, to the carbide area that is immune to the wear, should give some insight into the relative wear rates of the coatings.

A WC/Co volume ratio predicted coating wear in a reasonable fashion. This relationship should hold so long as the assumptions that govern it are not violated, most importantly that the carbide is not being worn, or worn at a much lower rate than the matrix. The WC/Co volume ratio will predict relative wear rates so long as the abrasive is softer than the carbide. This means that this relationship cannot be used to predict the wear rate if another abrasive were used, such as SiC or diamond.

The expected relationship between the wear rate and cobalt mean free path is not evident in sprayed material. Using the WC/Co volume ratio to predict the wear rate of a 12 wt% Co from the 15 wt% Co wear rate of 0.0032 mm^3/m to 0.0022 mm^3/m, which compares favorably to the wear rate of the 12 wt% Co coatings with the micrometer and submicrometer carbides. The lack of difference in wear rate as the carbide size in the coatings dropped indicates that cobalt mean free path was not a controlling factor in determining the wear rate of the coating.

As the grain size of the carbide decreases, the binder mean free path will also decrease. As long as the volume percentage of the binder is the same there is a linear decrease in the binder mean free path as the carbide size is reduced. Work by Jia, et al. [32-34, 92] with a sintered nanoscale WC-Co showed a strong relationship between the mean free path and the wear rate of the material. Coatings sprayed in this study did not show the same relationship between the decrease in carbide size, hence mean free path, and the wear rate of the coatings.

The reason for this discrepancy may be due to the heterogeneity of the sprayed coatings, with carbide-rich and carbide-poor regions, and/or the lack of WC/WC bonds which would imply a lack of a three dimensional skeleton of WC.

4.5.6 Equal Pressure (EP) and Equal Wear (EW) Modes

The two modes, EW and EP, constitute upper and lower limits of the wear resistance of a composite or a multiphase material, provided that assumptions of the model are fulfilled, as discussed in the introduction section. The theory is based on proposed micromechanisms involved in the wear process and results in two equations expressing linear and inverse rules of mixture. The dependence of the wear on the amount of reinforcing phase in the coatings change based on which mode of wear the coatings would experience. The micromechanisms in this derivation provide useful insight about the wear of multiphase materials and the role of the matrix and the reinforcing phase in the overall wear.

Improvement in the strength of the matrix can have a dramatic improvement on the wear rate [77-79]. A more wear resistant matrix improves the overall wear resistance of the composite, beyond the marginal increase in the composite's wear resistance due to the matrix contribution. Additionally, the harder matrix enhances the protection of the reinforcing particles by decreasing the risk of discrete removal i.e. digging out, loosening or cracking, consequently transforming the wear mode in the direction of the more favorable EW mode. Thus, despite the extremely large difference in the wear resistance between the matrix and the reinforcement in these composites, the relatively modest differences between the matrices can have a significant impact on the wear resistance of the composite.

The WC-Co worn in low stress abrasive wear with the DSRW would be expected to be in EP wear for several reasons [77-79]. The size of the reinforcement is much smaller than the wearing particle in all cases. Three body abrasive wear with the rubber wheel allows the conformity of the surfaces. Unfragmented reinforcing particles may be removed as a part of larger wear debris. Since they are removed without direct contact with the abrading particles they do not have an effect on the wear resistance for the matrix or the load distribution. When the matrix surrounding the reinforcing phase is removed by wear, the particles are gradually exposed to higher stresses and receive gradually diminished support from the matrix. At some point the particles either fracture or loosen and are subsequently easily removed from the surface.

4.6 Volume wear relationships

Since the rule of mixtures and the EP and EW wear equation are based on volume percentages, looking at these materials in terms of volume percentages may be more useful. To that end, Table 4.4 was constructed to equate the weight percentages and the volume percentages of the individual phases, and volume ratio of the phases.
This table presents the idealized volume percentages in the coatings, which have been shown to vary from the actual volume percentages found in the coatings. The most significant departure from the ideal volumes, the overmelting of the carbides, has been shown to result in poor wear resistance. Properly chosen conditions would minimize overmelting and the coatings would approach the idealized volumes.

Table 4.4 shows the problem of thinking about the properties of these materials on a weight percentage basis. The large difference in the densities of cobalt and WC results in a density ratio of 1:1.75. The effect that this has on the volume percentage of WC and Co relative to the weight percentage can be seen in Figures 4.23 and 4.25.

Because the carbides are small and regular it is reasonable to assume that the volume percentages would also describe the relative amount of surface area of each of the phases. The final column in Table 4.4 is of the volume ratios in coatings. This was a useful way to think about the surface of the coating as it was being worn. From the wear scar images it is clear that the carbides are standing proud and the cobalt is behaving in a ductile manner. While many of the physical properties can be predicted with the rule of mixtures and using the volume ratios, the wear rate has been shown to be more complex in its behavior. The WC/Co volume ratio is an easy and quick way of thinking about the coating. In this instance it describes the relative volume of the highly wearing matrix phase to be the less vulnerable carbide phase.

The data in Table 4.4 and in the following figures are based on ideal volumetric ratios (assuming no porosity). This means that they do not take into account any degradation of the material. The effect of increasing the amount of the matrix or decreasing the amount of carbide can be easily understood as changing the relative amounts of the matrix to carbide. The large difference between the wear rate of the Osram-Sylvania - 12 wt% Co and the Osram-Sylvania - 18 wt% Co can be explained in terms of the WC/Co volume ratio. The difference in the volume percent carbide and cobalt is only 15%, but their WC/Co volume ratios are 3.17 versus 1.59, almost exactly the 2:1 ratio of their lowest wear rates. Figure 4.25 shows the WC/Co volume ratio versus Co wt% and Figure 4.26 shows the WC/Co volume ratio versus the Co volume percentage. These figures illustrate the effect of changing the amount of the cobalt in the composite with respect to the WC/Co volume ratios.

As was previously discussed, the difference between the Osram-Sylvania - 12 wt% Co and the Osram-Sylvania - 18 wt% Co could not be explained with Khruschov's wear equation. For a variety of reasons already discussed, the coatings are not expected to be in EW wear but in EP wear. A generic curve for EP wear would create a curve very similar to the curve generated by the WC/Co volume ratio, see Figure 1.9. Figure 4.27 is a plot of the actual versus the predicted wear rate of the coatings. The curve is the WC/Co volume ratio, with the wear rate of Osram-Sylvania - 12 wt% Co was set to one. The percentages of cobalt were assumed to be the same as the starting powder. For these coatings, the chemistry data was collected and can be seen in Table 3.7. Figure 4.28 shows the same curve with the actual cobalt content and not the expected cobalt content. While both of these curves were close, there is a near perfect match between the actual and the predicted wear rates. Figure 4.28 follows the same format for the same powders sprayed on the hot fixture. The predicted wear rate is very close to the actual wear rate for assumed wt% of cobalt.

Chemistry data was not obtained for the coatings sprayed on the hot fixture, but it is very likely that the wt% of cobalt was not changed due to a change in the fixture. Figure 4.30 shows the actual versus predicted wear rate for the assumed corrected wt% of cobalt. The 15 wt% Co coating had a slightly higher wear rate than would be predicted.

The WC/Co volume ratio has been shown to be a reasonable predictor of the relative wear rates of the coatings. Figure 4.25 show the WC/Co volume ratio for the coatings from 1 wt% Co to 25 wt% Co. Using this ratio, it is possible to predict the relative wear rates of coating with cobalt wt% ranges from 5 wt% Co to 20 wt% Co. Figure 4.31 shows the predicted relative wear rates normalized to 12 wt% Co, where Figure 4.48 is a similar curve with the wear normalized to 18 wt% Co.

The wear rate of a theoretical coating could be predicted through the use of the WC/Co volume ratio. These plots have utility beyond the specific set of wear conditions used in this study. The relationship between the WC/Co volume ratio is a relationship between the coatings and that can be applied to other wear conditions than the ones used in this study; as long as the assumptions of the three body abrasive wear are not violated and that the abrasive was softer than the carbide. The harder the abrasive the flatter the EP wear curve will become as the difference in the relative wear resistance of the cobalt and the carbide decreases.

Table 4.1. Osram-Sylvania 18 wt% Co powder with weight percentage of carbon added to feedstock.

Condition (CFM)	**Weight %Co added**	**Wear rate (mm^3/m)**	**Hardness (HK)**
5N	1%	0.00502	1031
4N	1%	0.00624	958
5N	2%	0.00481	1017
4N	2%	0.00693	954
5N	3%	0.00521	1025
4N	3%	0.00623	994
5N	4%	0.03025	N/A
4N	4%	0.00533	950

Table 4.2. Best wear rates of coating sprayed on the cold fixture.

Powder	**Wear Rate (mm^3/m)**
Metco 2004 12 wt% Co	0.00312
Nanomyte™ 12 wt% Co	0.00358
Osram-Sylvania12 wt% Co	0.00292
Osram-Sylvania18 wt% Co	0.00557
Nanodyne™ 12 wt% Co - Large Cut	0.0028
Nanodyne™ 12 wt% Co - Small Cut	0.00295
Nanodyne™ 15 wt% Co	0.00357

Table 4.3. Best wear rates of coatings sprayed on the hot fixture.

Powder	**Wear Rate (mm^3/m)**
Metco 2004 12 wt% Co	0.00236
Nanomyte™ 12 wt% Co	0.0029
Osram-Sylvania12 wt% Co	0.00226
Osram-Sylvania18 wt% Co	0.00406
Nanodyne™ 12 wt% Co - Large Cut	0.0024
Nanodyne™ 12 wt% Co - Small Cut	0.00308
Nanodyne™ 15 wt% Co	0.00318

Table 4.4. Volume and volume percentages with respect to wt% Co.

WT%	**Volume**	**Density**	**Volume % Cobalt**	**Volume % WC**	**Volume ratio WC/Co**
1%	1.01	15.51	1.77	98.23	55.37
2%	1.02	15.40	3.58	96.42	26.90
3%	1.02	15.28	5.43	94.57	17.41
4%	1.03	15.17	7.32	92.68	12.67
5%	1.04	15.06	9.24	90.76	9.82
6%	1.05	14.95	11.21	88.79	7.92
7%	1.05	14.84	13.22	86.78	6.57
8%	1.06	14.74	15.27	84.73	5.55
9%	1.07	14.63	17.37	82.63	4.76
10%	1.08	14.53	19.51	80.49	4.12
11%	1.08	14.43	21.71	78.29	3.61
12%	1.09	14.33	23.95	76.05	3.18
13%	1.10	14.23	26.24	73.76	2.81
14%	1.11	14.13	28.59	71.41	2.50
15%	1.11	14.04	30.99	69.01	2.23
16%	1.12	13.94	33.45	66.55	1.99
17%	1.13	13.85	35.97	64.03	1.78
18%	1.14	13.76	38.55	61.45	1.59
19%	1.14	13.67	41.19	58.81	1.43
20%	1.15	13.58	43.90	56.10	1.28
21%	1.16	13.49	46.68	53.32	1.14
22%	1.17	13.40	49.53	50.47	1.02
23%	1.17	13.31	52.46	47.54	0.91
24%	1.18	13.23	55.46	44.54	0.80
25%	1.19	13.15	58.54	41.46	0.71

Table 4.5. WC/Co volume ratios relative to 12 and 18 wt% Co.

WT%	**WC/Co volume ratios relative to 12 wt% Co**	**WC/Co volume ratios relative to 18 wt% Co**
1%	17	34.74
2%	8.47	16.88
3%	5.48	10.92
4%	3.99	7.95
5%	3.09	6.16
6%	2.49	4.97
7%	2.07	4.12
8%	1.75	3.48
9%	1.50	2.98
10%	1.30	2.59
11%	1.14	2.26
12%	1.00	1.99
13%	0.89	1.76
14%	0.79	1.57
15%	0.70	1.40
16%	0.63	1.25
17%	0.56	1.12
18%	0.50	1.00
19%	0.45	0.90
20%	0.40	0.80
21%	0.36	0.72
22%	0.32	0.64
23%	0.29	0.57
24%	0.25	0.50
25%	0.22	0.44

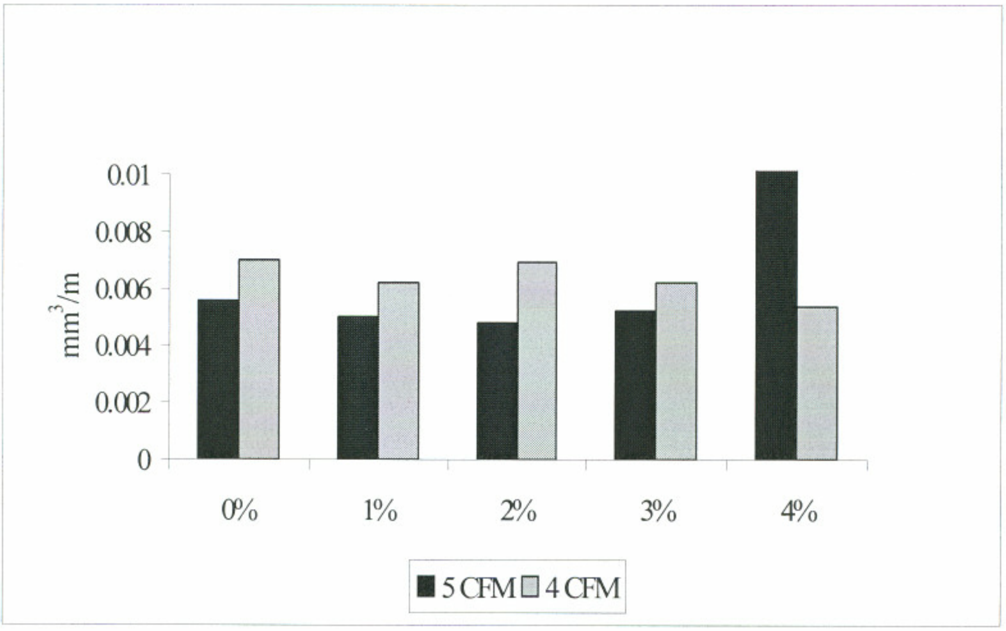

Figure 4.1. Wear Rate of Nanodyne™ 15 wt% Co with the addition of 1 to 4 wt%C to powder.

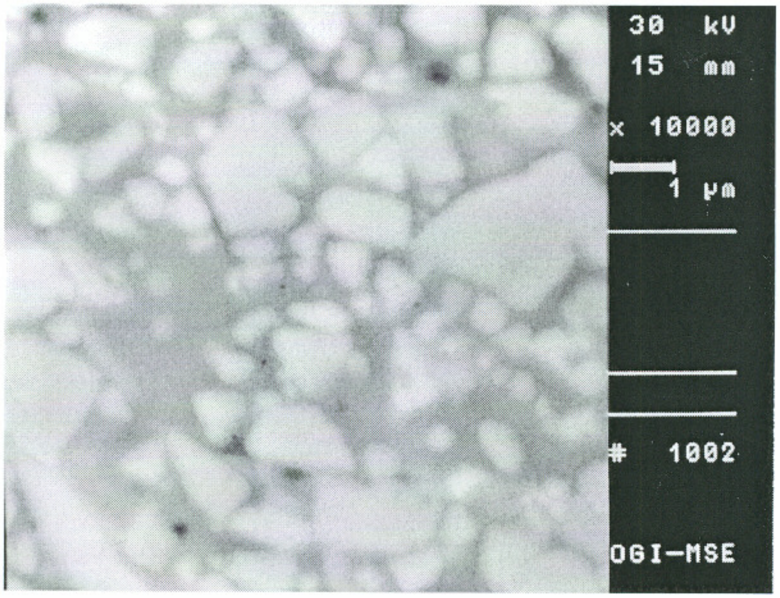

Figure 4.2. SEM image of Metco 2004 WC-12 wt% Co cross section showing no fracture in as sprayed carbides, 10000x

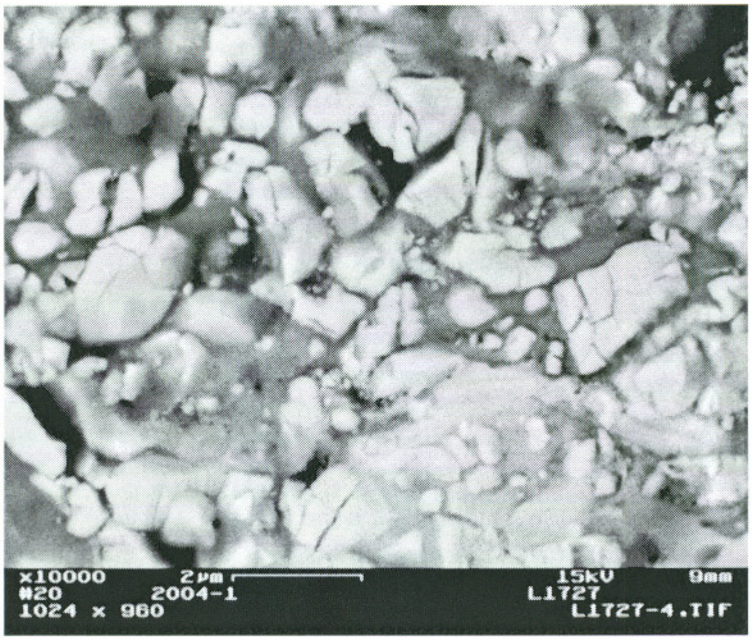

Figure 4.3. FESEM image of Metco 2004 WC-12 wt% Co wear scar showing as sprayed carbides, 10000x.

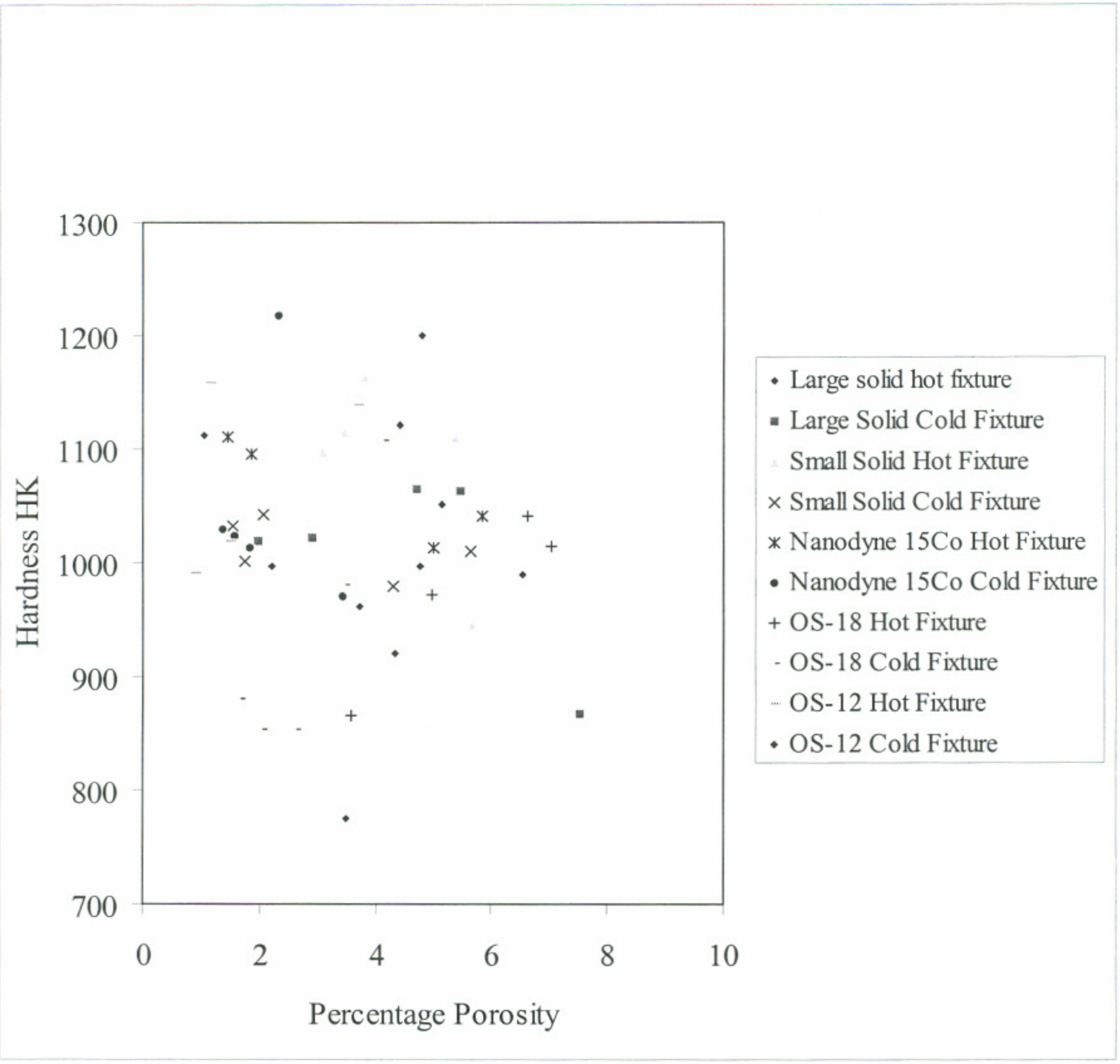

Figure 4.4. Hardness vs. porosity for all coatings and fixtures.

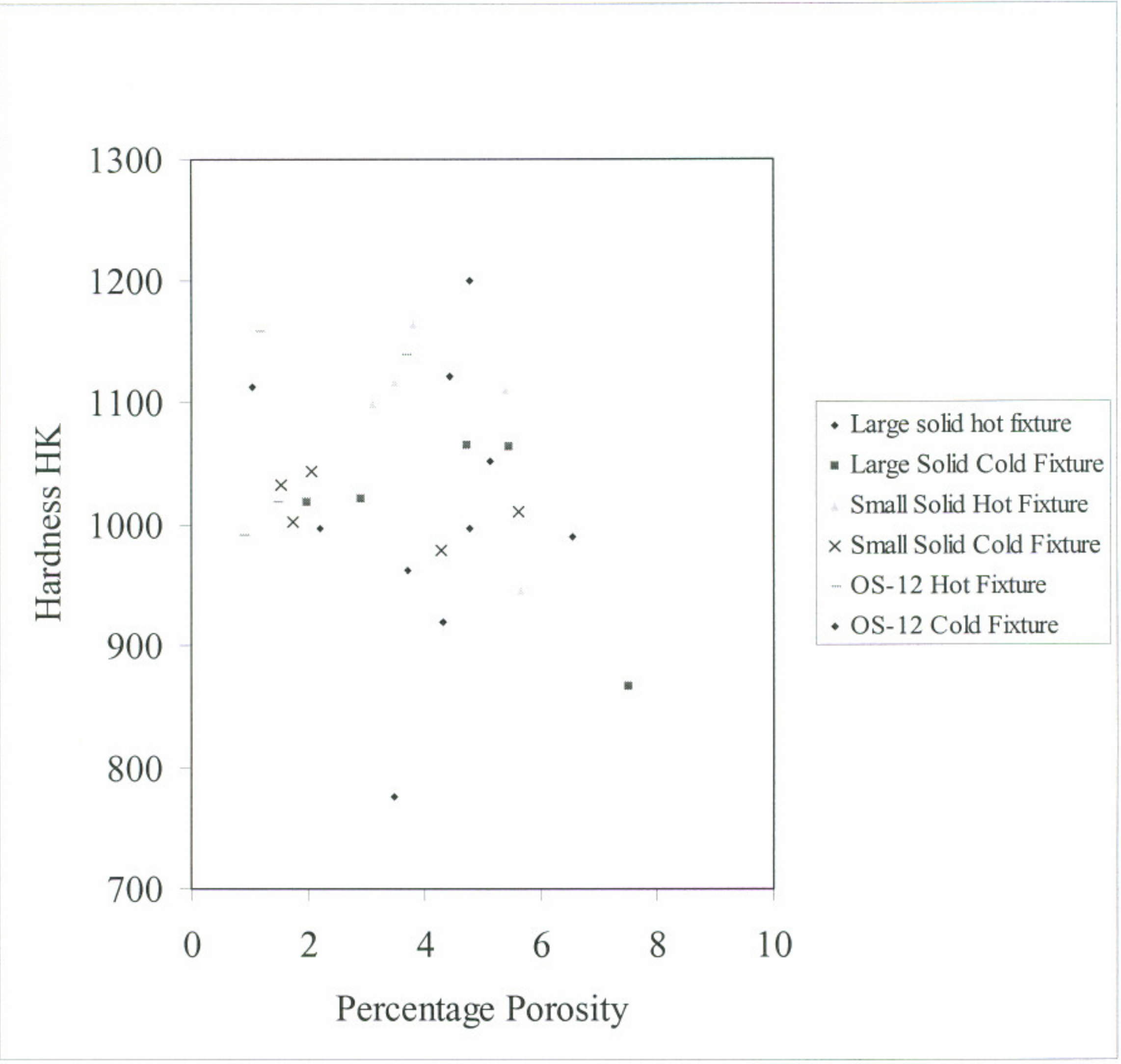

Figure 4.5. Hardness vs. porosity for coatings containing submicrometer carbides and 12 wt% Co hot and cold fixtures.

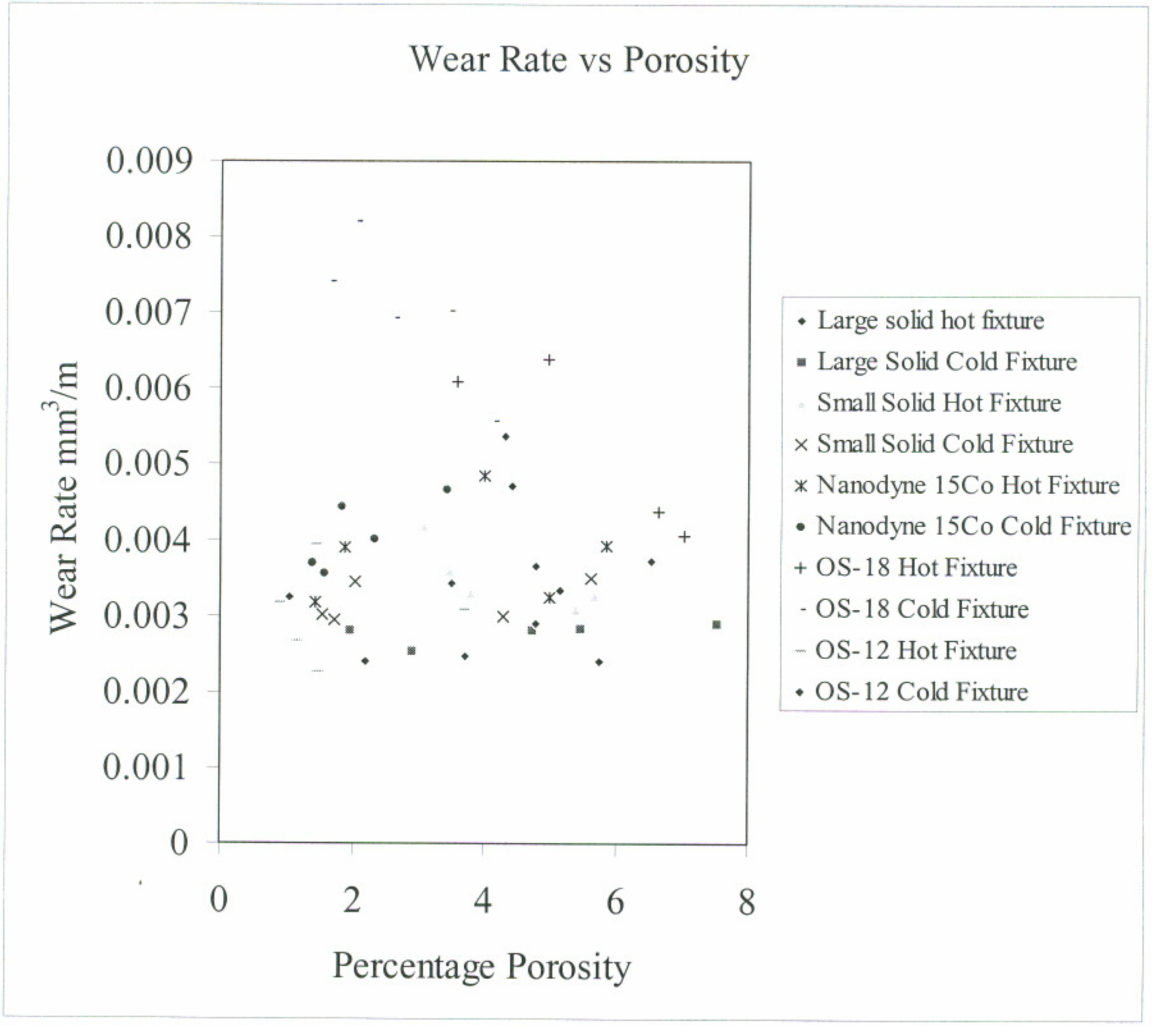

Figure 4.6. Wear rate vs. porosity for all coatings and fixtures.

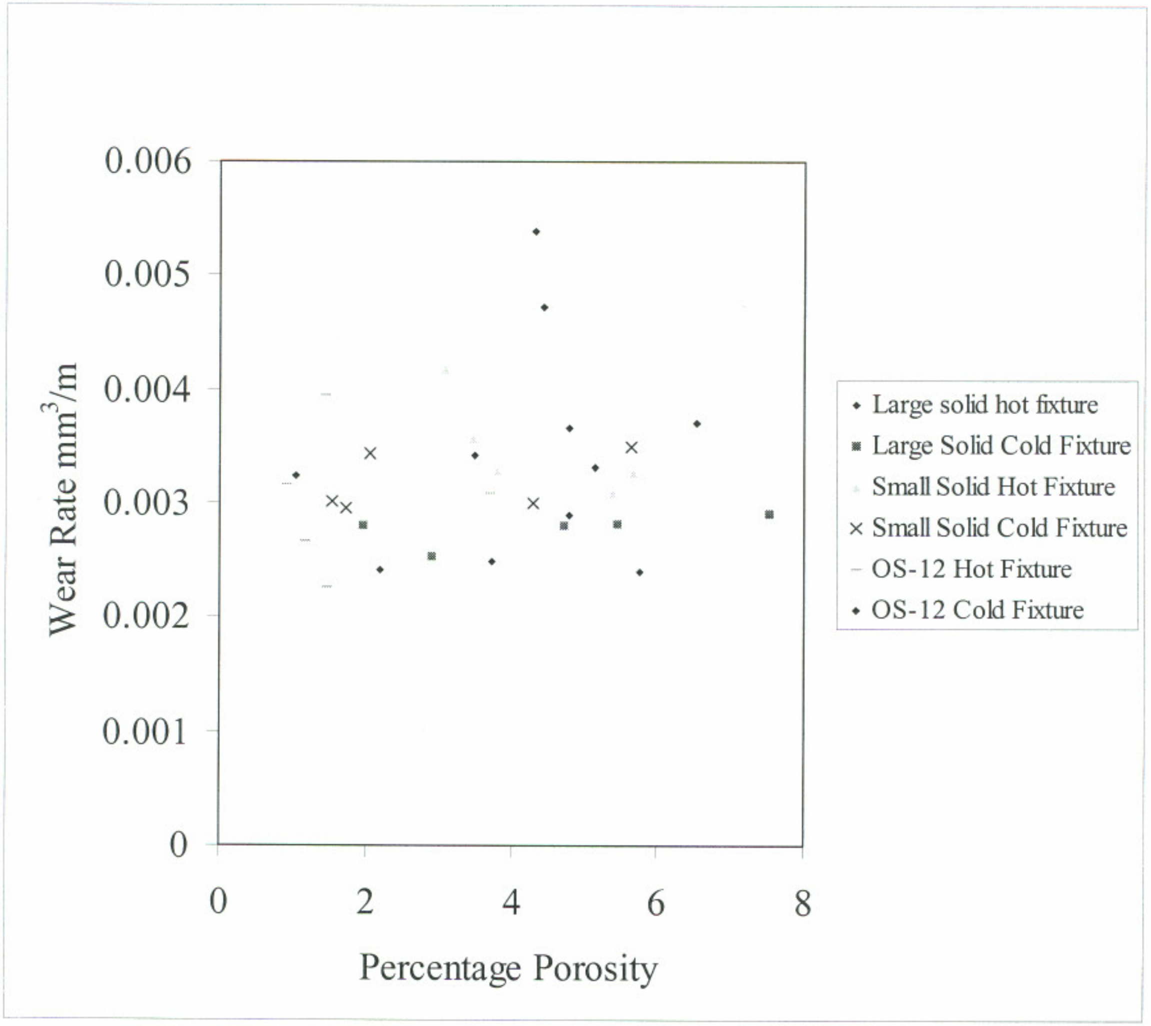

Figure 4.7. Wear rate vs. porosity for coatings containing submicrometer carbides and 12 wt% Co hot and cold fixtures.

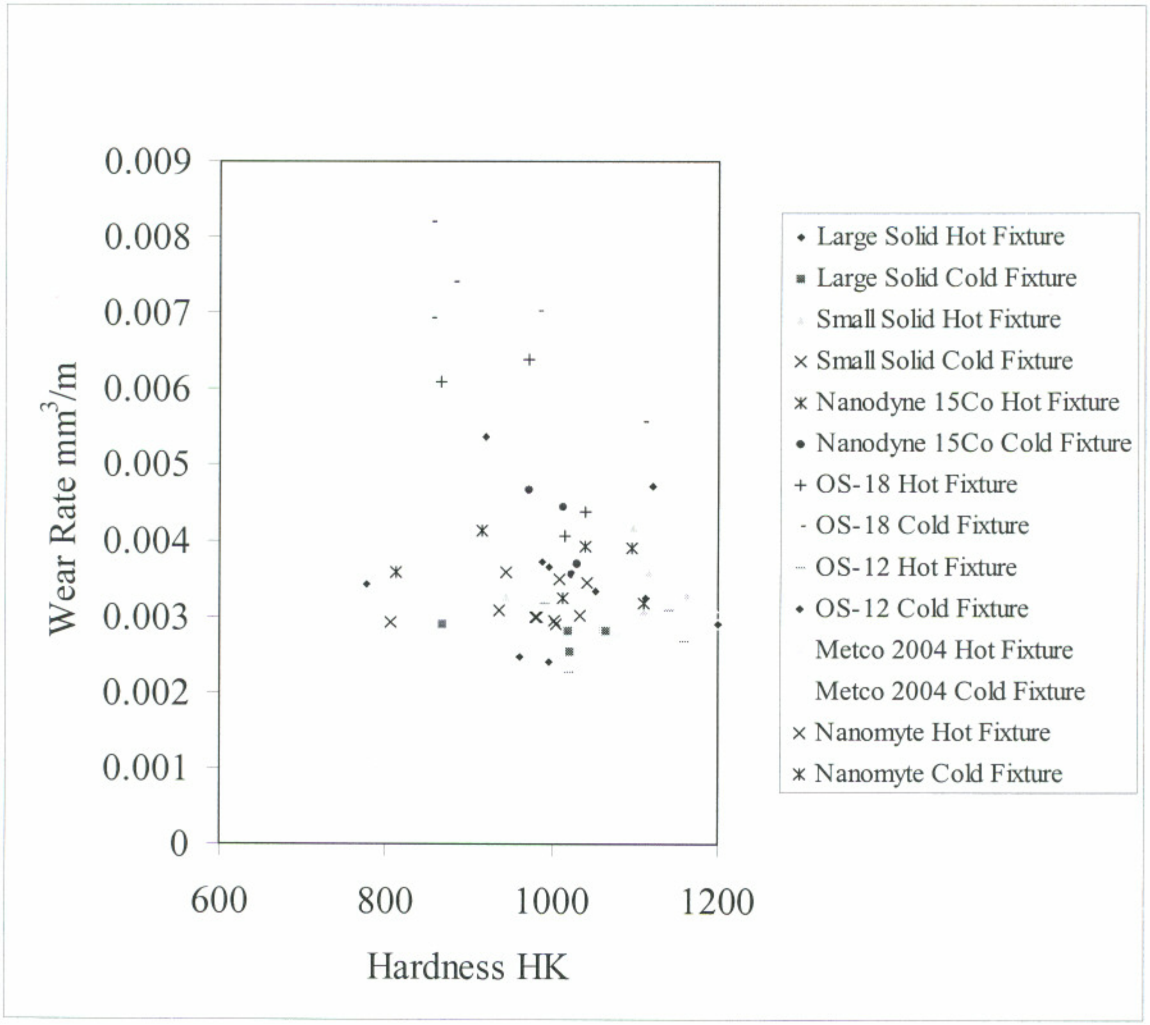

Figure 4.8. Hardness vs. wear rate for all coatings and fixtures.

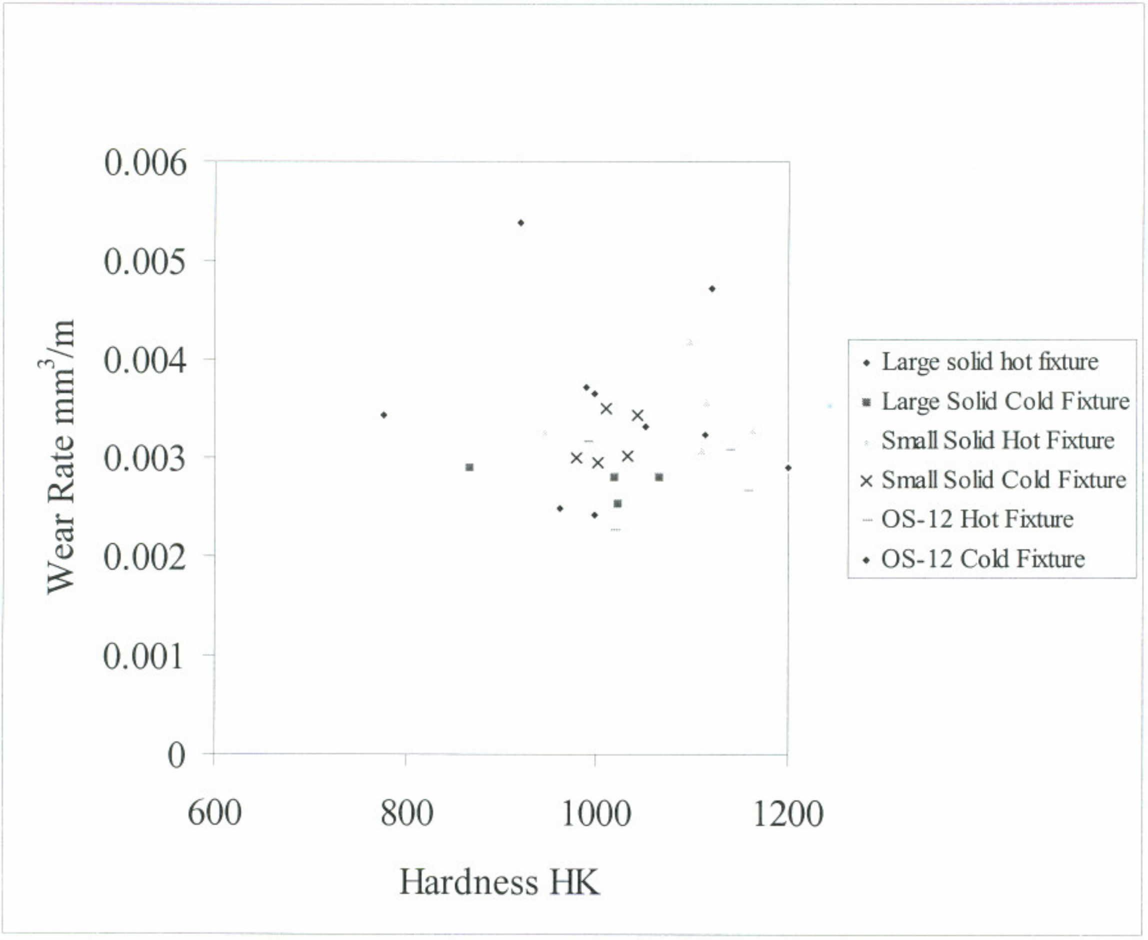

Figure 4.9. Hardness vs. wear rate for coatings containing submicrometer carbides and 12 wt% Co hot and cold fixtures.

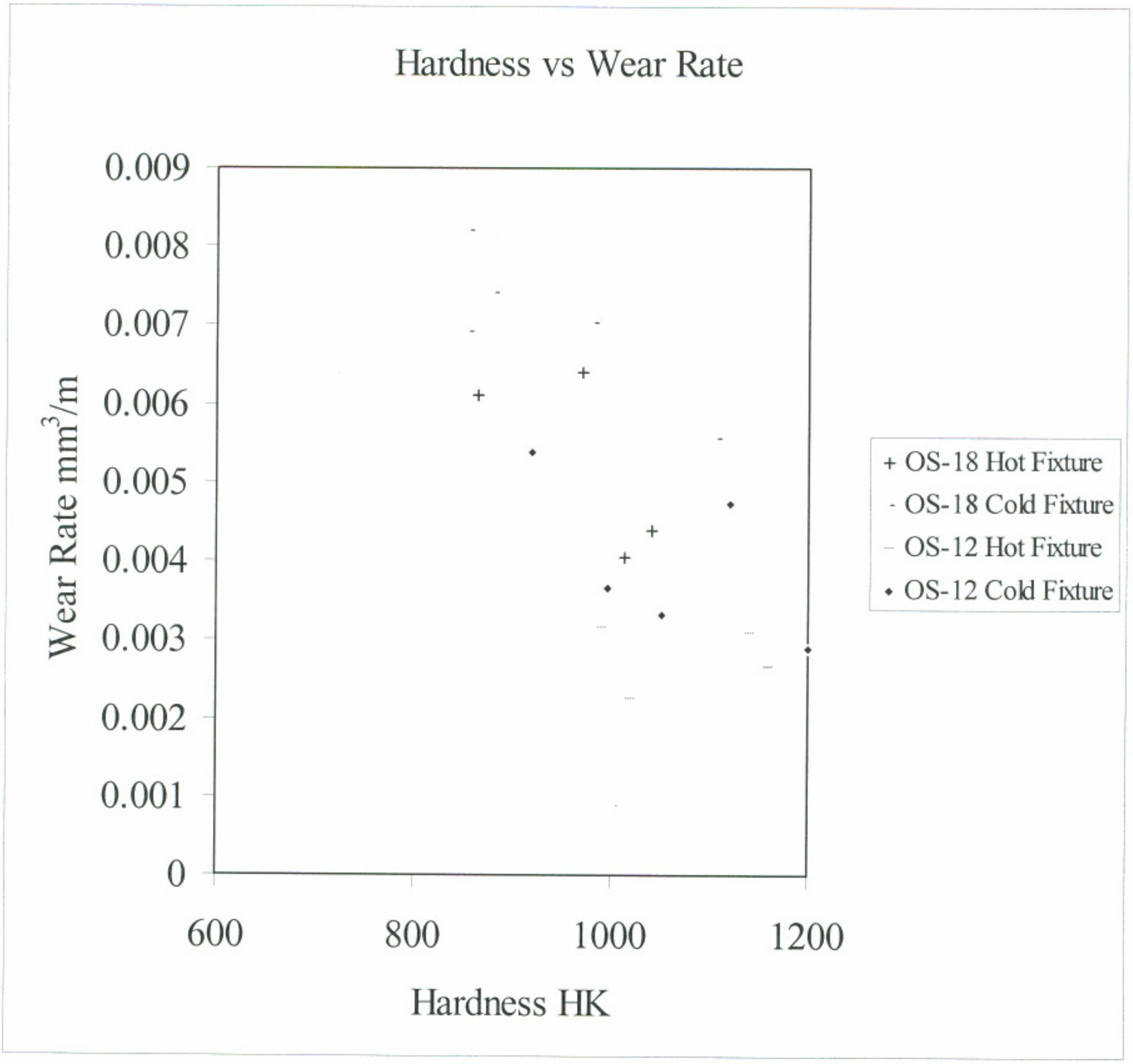

Figure 4.10. Hardness vs. wear rate for Osram-Sylvania 12 wt% Co and Osram-Sylvania 18 wt% Co, hot and cold fixtures.

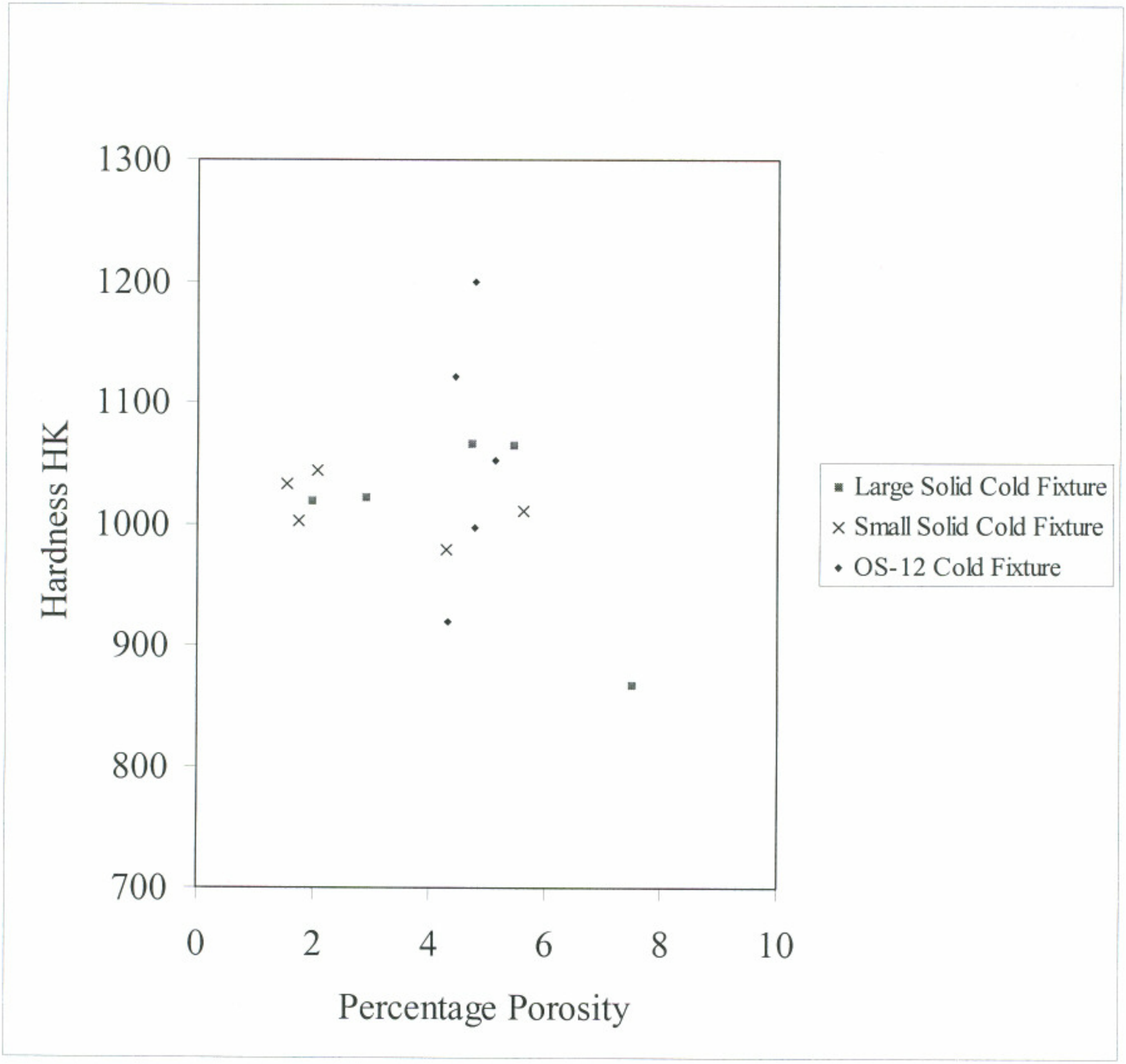

Figure 4.11. Hardness vs. porosity for coatings containing submicrometer carbides and 12 wt% Co, cold fixture.

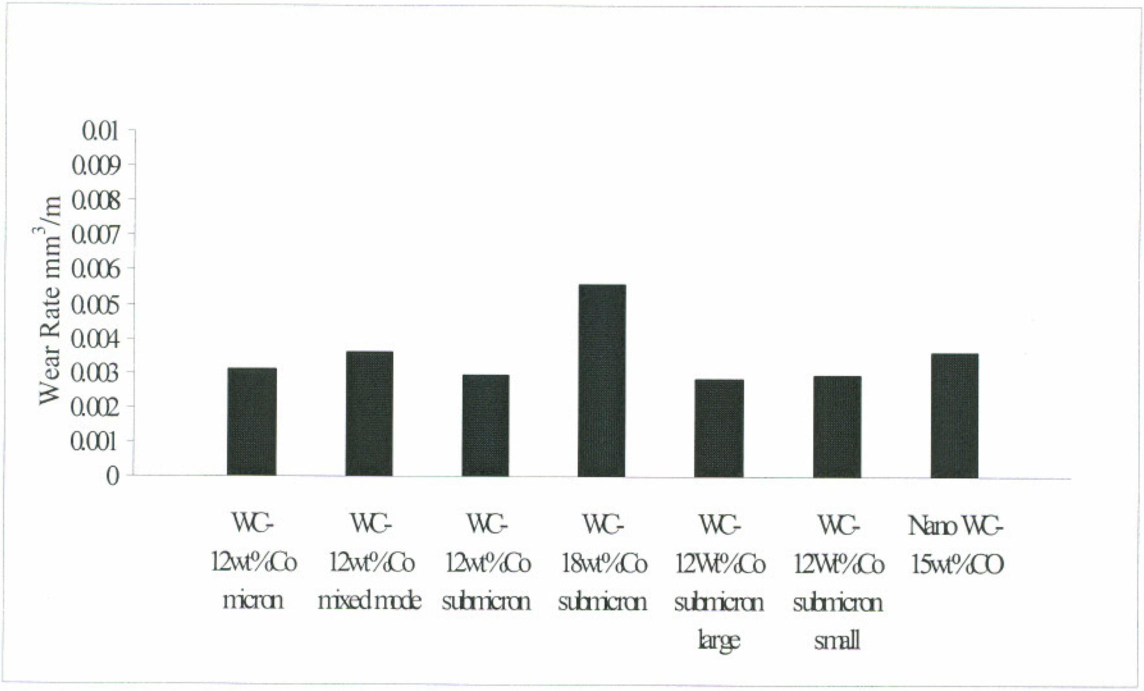

Figure 4.12. Lowest wear rates for each of the coatings sprayed on the cold fixture.

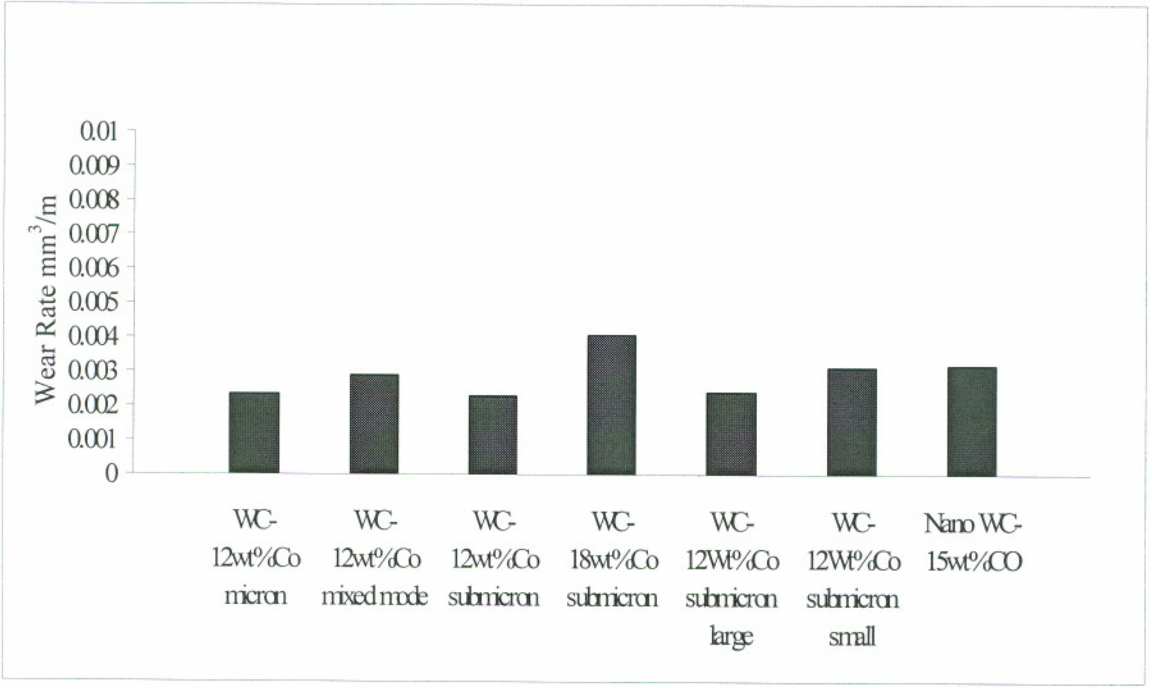

Figure 4.13. Lowest wear rates for each of the coatings sprayed on the hot fixture.

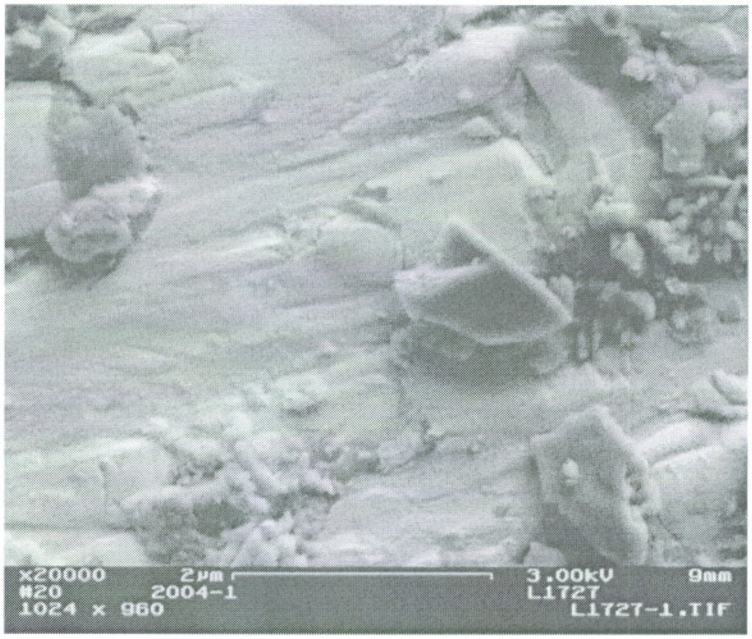

Figure 4.14. FESEM image of Metco 2004 WC-12 wt% Co wear scar, 20000x.

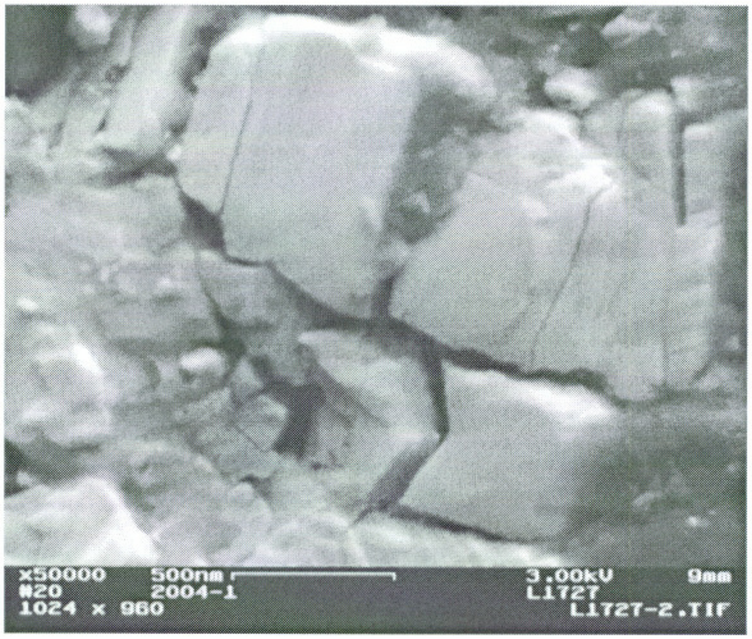

Figure 4.15. FESEM image of Metco 2004 WC-12 wt% Co wear scar, 50000x.

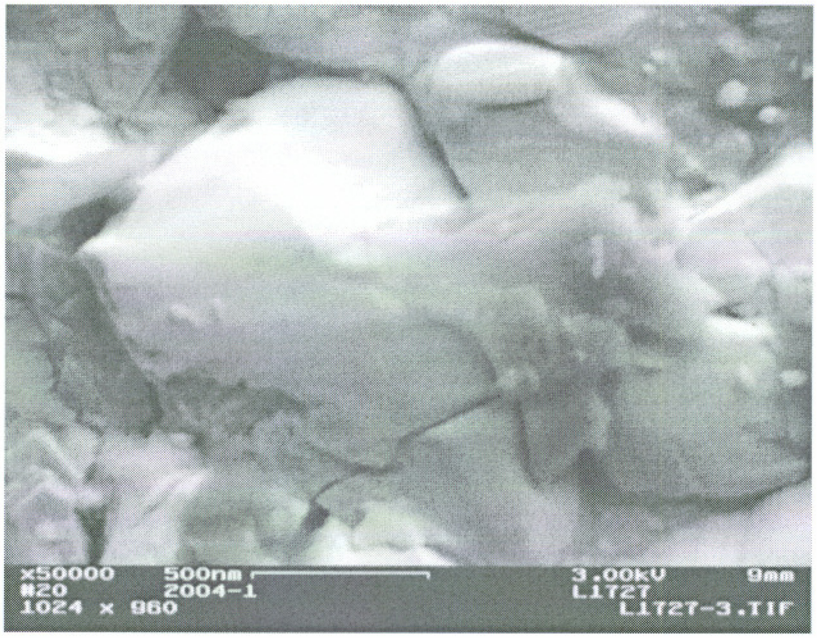

Figure 4.16. FESEM image of Metco 2004 WC-12 wt% Co wear scar, 50000x.

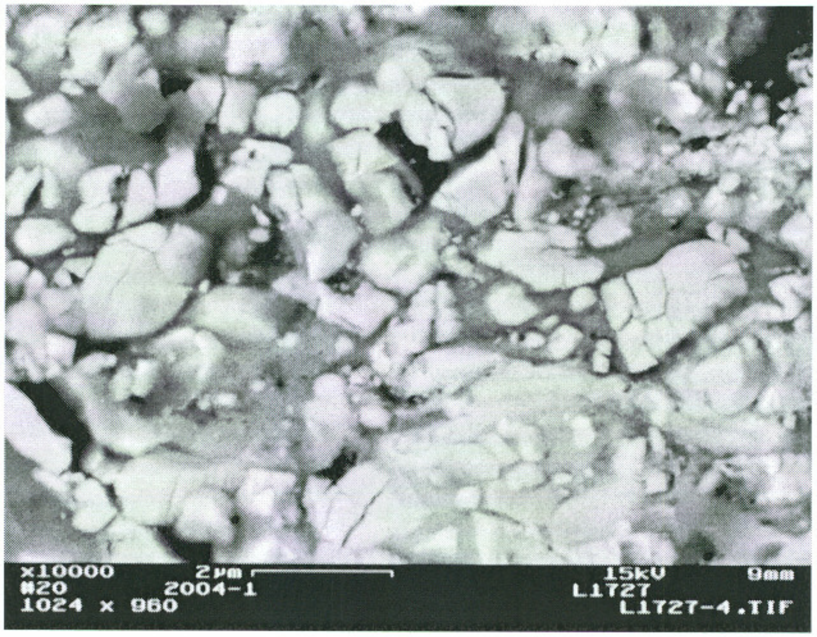

Figure 4.17. FESEM image of Metco 2004 WC-12 wt% Co wear scar, 10000x.

Figure 4.18. FESEM image of Metco 2004 WC-12 wt% Co wear scar, 30000x.

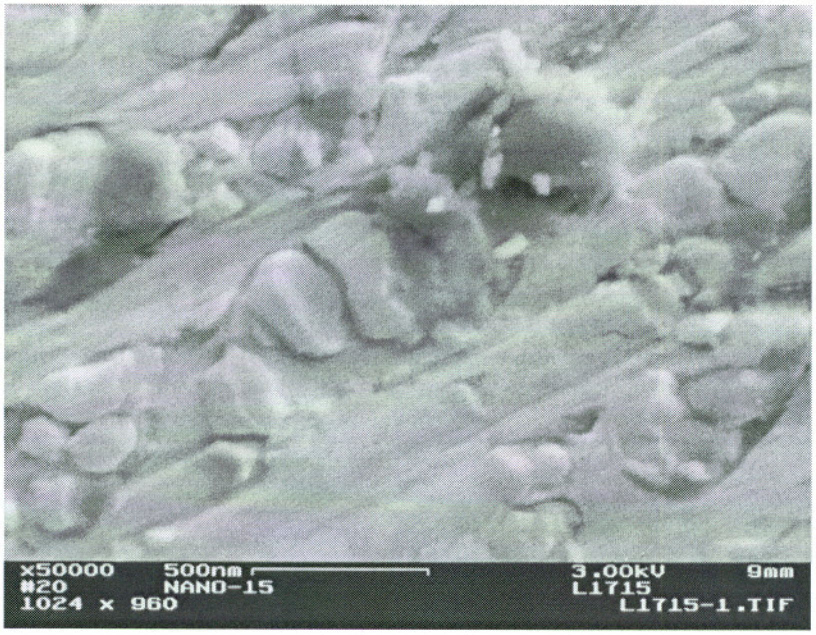

Figure 4.19. FESEM image of Nanodyne™ 15 wt% Co wear scar, 50000x.

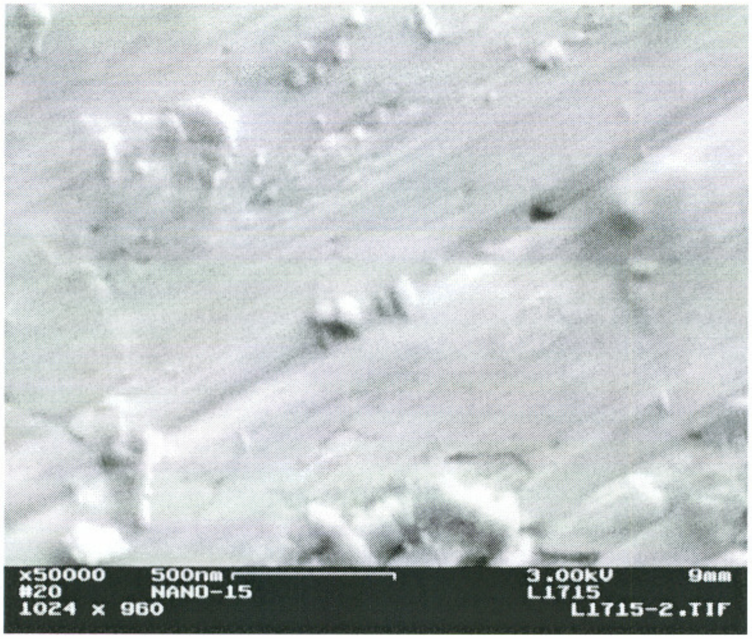

Figure 4.20. FESEM image of Nanodyne™ 15 wt% Co wear scar, 50000x.

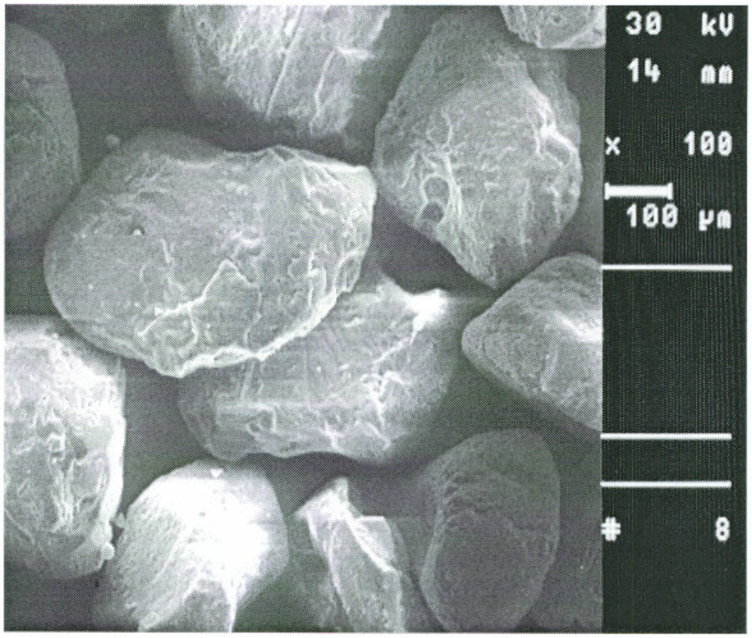

Figure 4.21. SEM image of Ottawa silica sand particles, 100X.

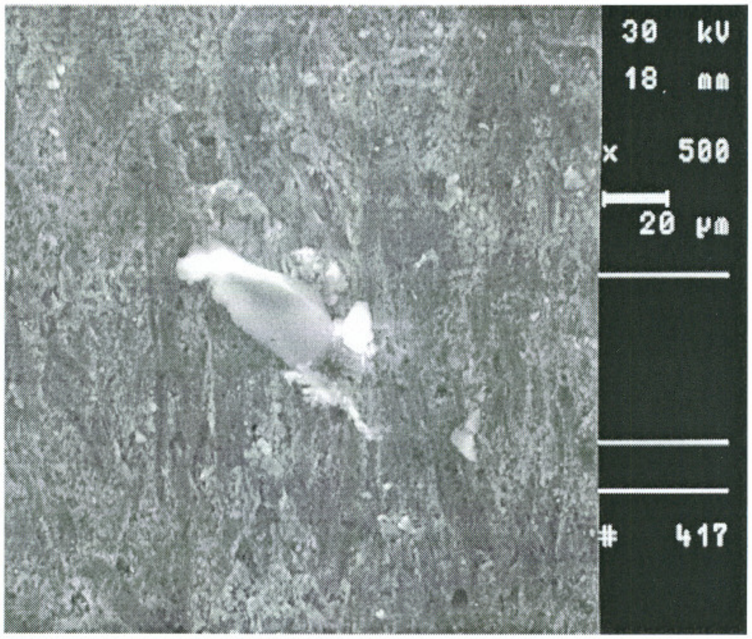

Figure 4.22. SEM image of an Ottawa silica sand fragment wearing a groove in 1040 steel, 500x.

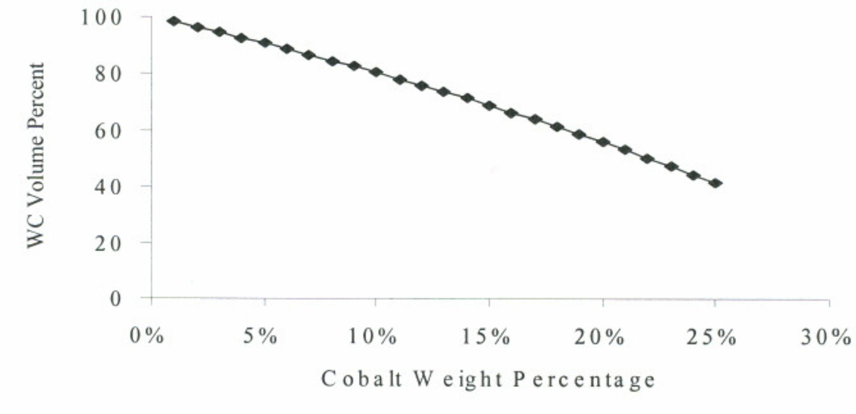

Figure 4.23. Volume of WC in composite in respect to the weight percentage of cobalt.

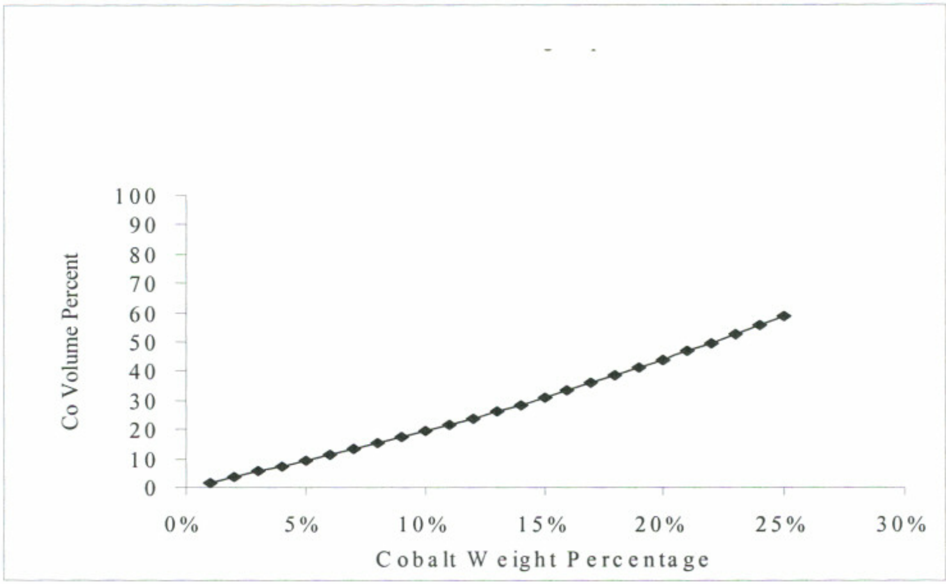

Figure 4.24. Volume of cobalt in composite in respect to the weight percentage of cobalt.

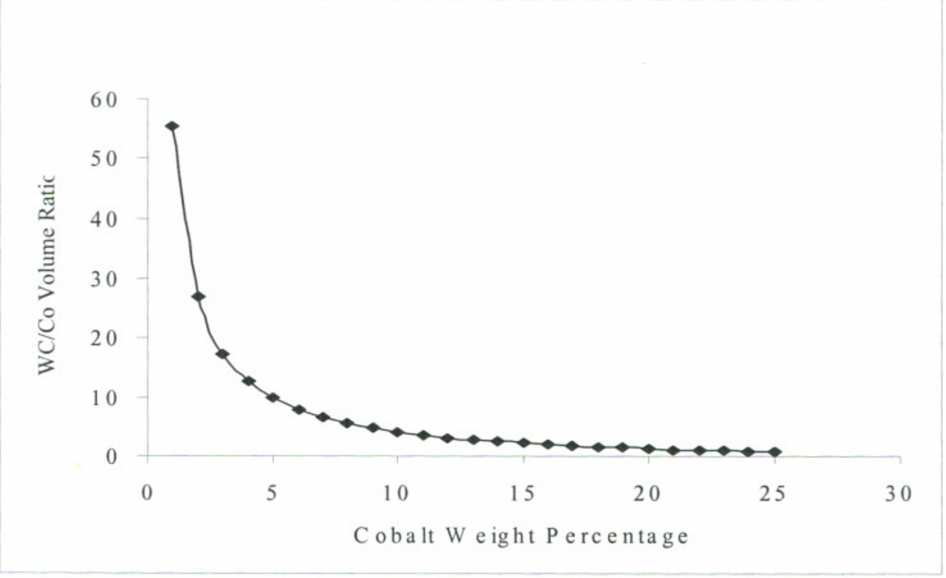

Figure 4.25. WC/Co volume ratio in the composite plotted against the cobalt weight percentage of the composite.

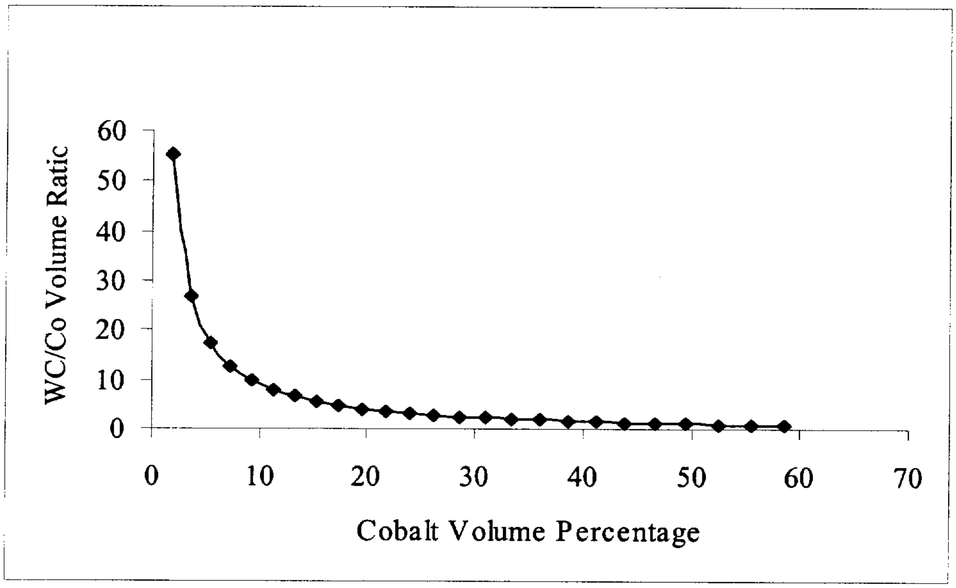

Figure 4.26. WC/Co volume ratio in the composite plotted against the cobalt volume percentage of the composite.

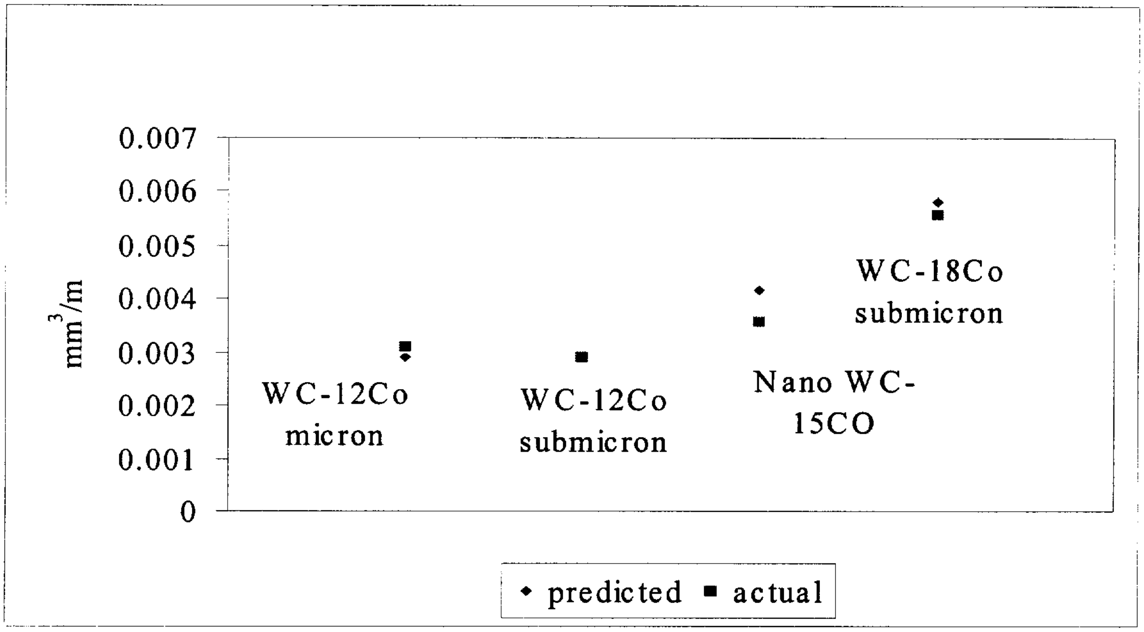

Figure 4.27. Actual vs. predicted wear rates for selected coatings sprayed on the cold fixture, normalized to Osram-Sylvania 12 wt% Co.

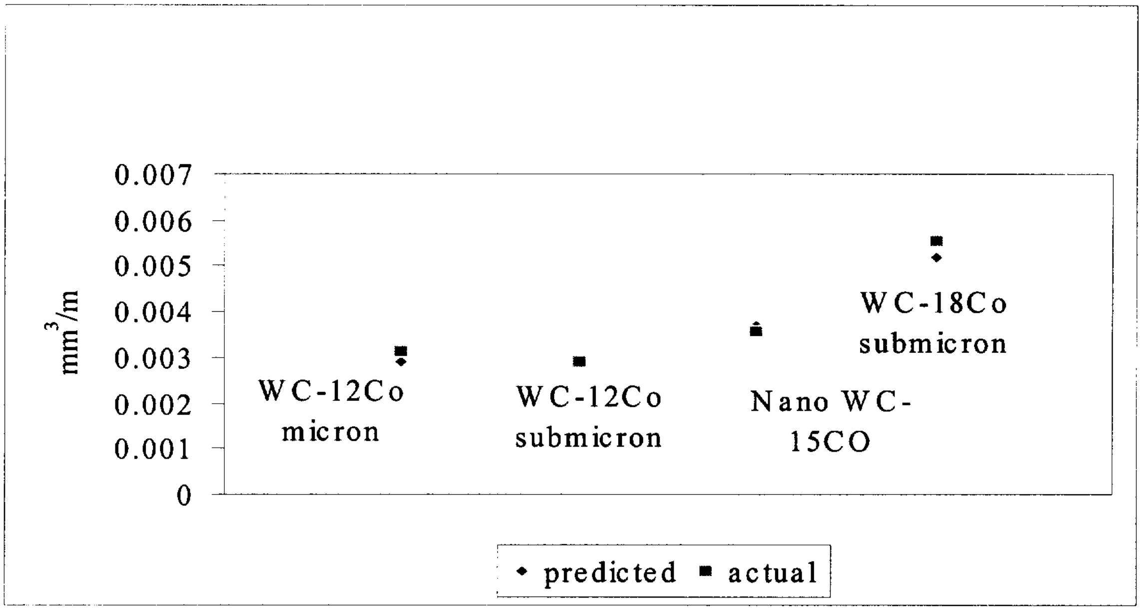

Figure 4.28. Actual vs. predicted wear rates for selected coatings sprayed on the cold fixture reflecting the amount of cobalt remaining in the sprayed coatings, normalized to Osram-Sylvania 12 wt% Co.

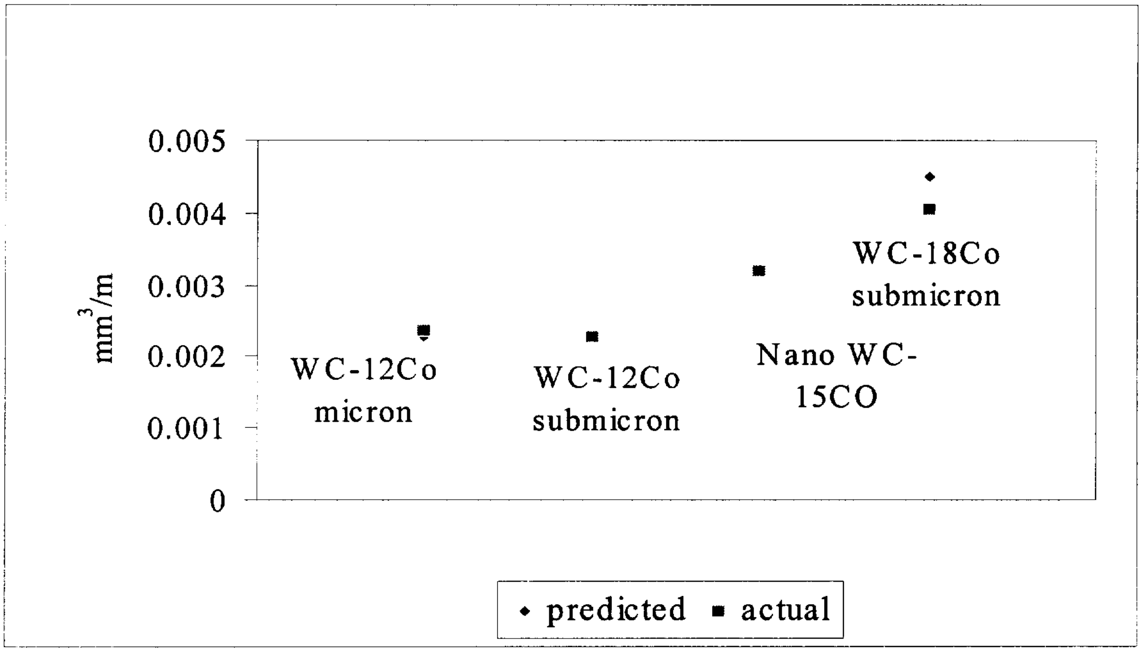

Figure 4.29. Actual vs. predicted wear rates for selected coatings sprayed on the hot fixture, normalized to Osram-Sylvania 12 wt% Co.

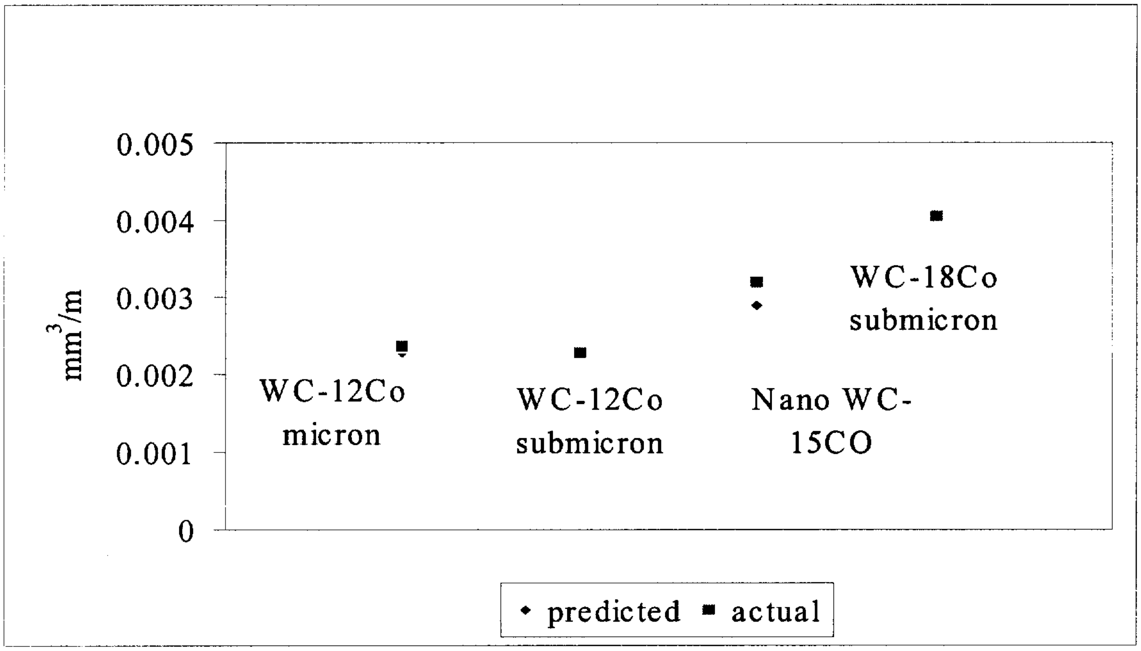

Figure 4.30. Actual vs. predicted wear rates for selected coatings sprayed on the hot fixture reflecting the amount of cobalt remaining in the sprayed coatings, normalized to Osram-Sylvania 12 wt% Co.

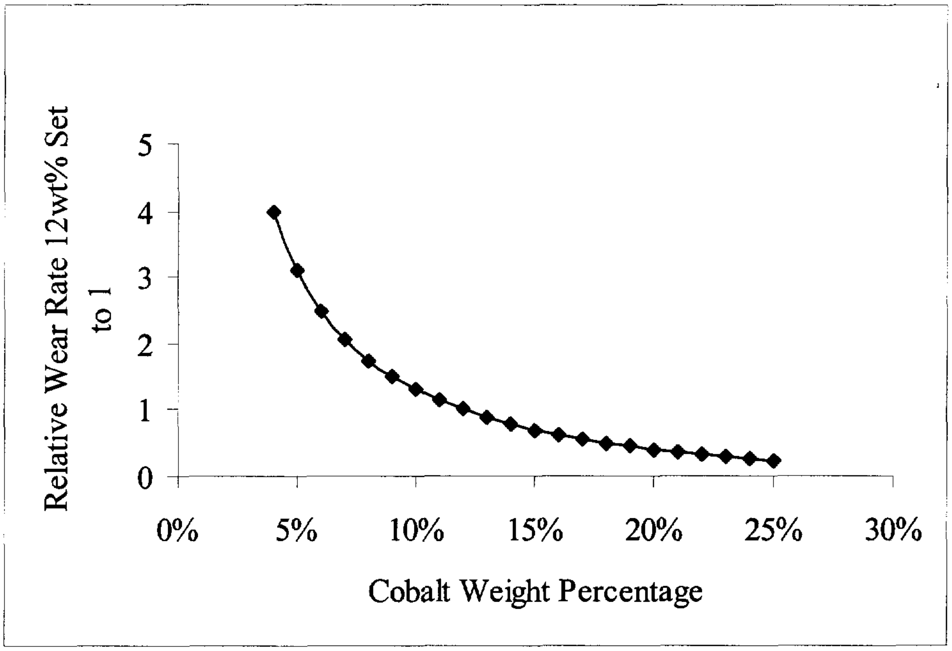

Figure 4.31. Predicted WC/Co volume ratio vs. Co weight percentage, normalized to 12 wt%.

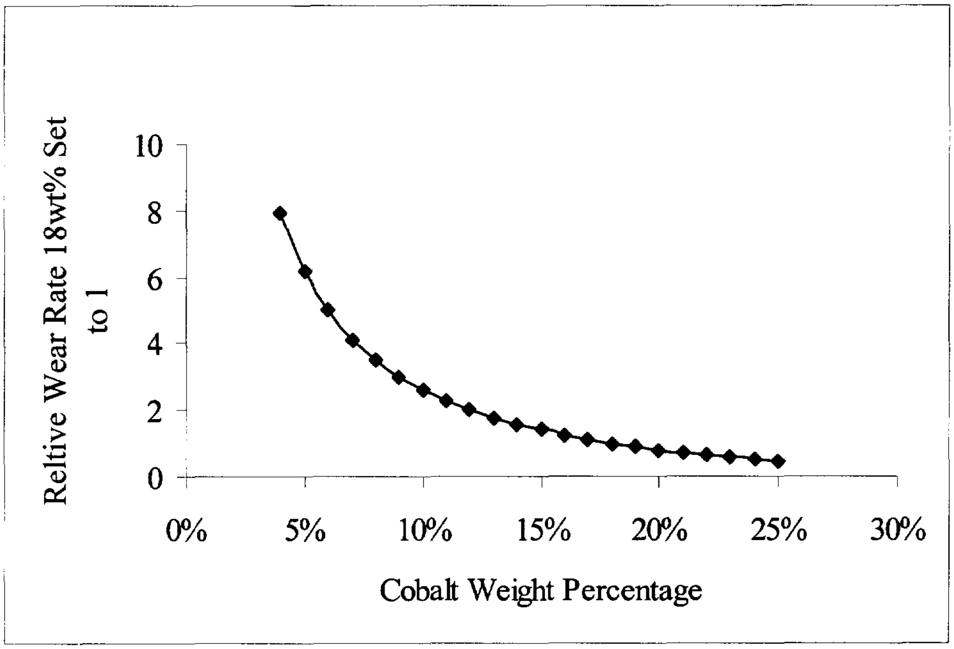

Figure 4.32. Predicted WC/Co volume ratio vs. Co weight percentage, normalized to 18 wt%.

5.0 CONCLUSIONS

Coatings composed of a variety of carbide sizes and cobalt contents were sprayed with a high energy plasma spray system. The feedstock powder was evaluated in terms of size distribution, external morphology, internal morphology, and initial carbide size. The microstructure of the sprayed coatings were examined, also porosity, hardness and wear rates of the coatings were evaluated. Two different fixtures were used to evaluate the effect of cooling rate on the coatings. SEM, FESEM, TEM, XRD, and chemical analysis were performed to further characterize the coatings.

Cobalt content was found to be the major influence on the wear rate of the coatings. The lowest wear rates for coatings with the same cobalt content tended to have the same wear rate regardless of the size of the WC particles. The decrease in the carbide size did not affect the wear rate of the coatings. The wear rate was controlled by the amount of matrix in the coating. This was true for the range of cobalt compositions tested and would likely continue to be true for coatings tested in low stress abrasive wear with relatively soft abrasives where the abrasive cannot cause grooving in the reinforcement phase.

Wear rates of the coatings were found to be related to each other by their WC/Co volume ratio. This volume ratio is approximately equal to the surface area ratio of the carbides to the matrix. The volume ratio provides a simple way to predict the change in wear rate due to changing cobalt compositions in the coatings. The reinforcement/matrix volume ratio has been used in white cast irons to predict wear, though will not accurately predict wear rate relationships in sintered WC-Co.

The wear mechanism was shown consist of removal of the matrix and crushing and /or discrete removal of the carbides for the micrometer sized carbides. The nanoscale carbides were never seen to exhibit micro-cracking of the carbides, the wear mechanism was discrete removal of whole carbides and matrix grooving. This evidenced by to the FESEM wear scar images which showed the ductile groves in the carbide-poor regions and no sign of grooving in the carbide-rich regions.

The addition of hydrogen to the plume gas had the effect of increasing the amount of matrix in the coating by increasing the melting the occurred in the coating. This would be expected to increase the strength of the matrix by solid solution strengthening, but the decrease in the amount of carbides in the coating resulted in an overall decrease in the wear resistance. Carbon additions to the feedstock were found to decrease the loss of carbon from the coating. The utility of the additional carbon was overshadowed by the subsequent decrease in coating thickness.

The hot fixture was shown to have improved wear resistance when compared to the same coatings sprayed on the cold fixture. This was attributed to the greater time at temperature that coatings sprayed on the hot fixture experienced. The coatings sprayed on the cold fixture that were heat treated, and in the best case had the same wear rate as the same coating sprayed on the hot fixture.

REFERENCES

1. Exner, H.E., "Physical and chemical nature of cemented carbides", *International Metals Review*, v. 4, 1979: pp. 149-173.

2. Raghunathan, S., R. Caron, and J. Freiderichs, "Tungsten carbide technologies", *Advanced Materials & Processes*, v. 4, 1996: pp. 21-23.

3. Viswanadham, R.K. and P.G. Lindquist, "Transformation-toughening in cemented carbides: Part 1. Binder composition control", *Metallurgical Transactions A*, v. 18A, 1987: pp. 2163-2173.

4. Viswanadham, R.K. and P.G. Lindquist, "Transformation-toughening in cemented carbides: Part 2. Thermomechanical treatments", *Metallurgical Transactions A*, v. 18A, 1987: pp. 2175-2180.

5. Kakeshita, T. and C.M. Wayman, "Martensitic transformations in cermets with a metastable austenitic binder 1: WC-(Fe-Ni-C)", *Materials Science and Engineering*, v. A141, 1991: pp. 209-219.

6. Krawitz, A.D., D.G. Reichel, and R.L. Hitterman, "Residual stress and stress distribution in a WC-Ni composite", *Materials Science and Engineering*, v. A119, 1989: pp. 127-134.

7. Olivares, J.L. and I.C. Grigorescu, "Friction and wear behavior of thermally sprayed Nichrome-WC coatings", *Surface and Coatings Technology*, v. 33, 1987: pp. 183-190.

8. Nishimura, T., O. Ishibashi, and S. Imasato, "Some properties of WC-Co-Ni-Cr cemented carbides", *Nippon Tungsten Review*, v. 20, 1987: pp. 53-60.

9. Wayne, S.F., J.G. Baldoni, and S.T. Buljan, "Abrasion and erosion of WC-Co with controlled microstructures", *Tribology Transactions*, v. 33, n. 4, 1990: pp. 611-617.

10. Usmani, S., S. Sampath, and D.L. Houck, "Effect of carbide grain size on the sliding and abrasive wear behavior of thermally sprayed WC-Co coatings", *Tribology Transactions*, v. 40, n. 3, 1997: pp. 470-478.

11. McCandlish, L.E., B.H. Kear, and B.K. Kim, "Processing and properties of Nanostructured WC-Co", *Nanostructured Materials*, v. 1, 1992: pp. 119-124.

12. Fang, Z. and J. Eason, "Study of nanostructured WC-Co Composites", *Proceedings of the 13th International Plansee Seminar*, 1993: pp. 625-638.

13. McCandlish, L.E. and P. Seegopaul, "Development and applications of nanostructured tungsten carbide/cobalt powders", *Advances in Hard Material Production: Proceedings of the 1996 European Conference on Advances in Hard Materials Production*, 1996: pp. 93-100.

14. Siegel, R.W. and G.J. Thomas, "Grain boundaries in nanophase materials", *Ultramicroscopy*, v. 40, 1992: pp. 376-384.

15. Siegel, R.F. and G.E. Fougere, "Grain size dependent mechanical properties in nanophase materials", *Grain Size and Mechanical Properties Fundamentals and Applications*, Materials Research Society, Boston, MA, 1994: pp. 219-230.

16. Siegel, R.W., "Nanostructured materials: mind over matter", *Nanostructured Materials*, v. 4 n. 1, 1994: pp. 121-138.

17. Siegel, R.W. and G.E. Fougere, "Mechanical properties of nanophase metals", *Nanostructured Materials*, v. 6, n. 4, 1995: pp. 205-216.

18. Siegel, R., " Mechanical properties of nanophase materials", *Synthesis and Properties of Mechanically Alloyed and Nanocrystalline Materials, 20-24 May, 1997, Rome, Italy,* 1997: pp. 851-860.

19. Adrievskii, R.A., "Properties of nanocrystilline refractory compounds", *Powder Metallurgy and Metal Ceramics*, v. 32, n. 11/12, 1994: pp. 935-941.

20. Suryanarayana, C.M., D. Mukhopadhyay, S.N. Patankar, and F.H. Froes, "Grain size effects in nanocrystalline material", *Journal of Materials Research,* v. 7, n. 8, 1992: pp. 2114-2118.

21. Suryanarayana, C. and F.H. Froes, "The structure and mechanical properties of metallic nanocrystals", *Metallurgical Transactions A*, v. 23A, n. 4, 1992: pp. 1071-1081.

22. Suryanarayana, C., "Nanocrystalline materials", *International Materials Reviews*, v. 40, n. 2, 1995: pp. 41-64.

23. Schuh, C.A., T.G. Nieh, and T. Yamasaki, "Hall-Petch breakdown manifested in abrasive wear resistance of nanocrystalline nickel", *Scripta Materialia*, v. 46, 2002: pp. 735-740.

24. Roebuck, B. and E.A. Almond, "Deformation and fracture processes and the physical metallurgy of WC-Co hardmetals", *International Materials Reviews*, v. 33, n. 2, 1988: pp. 90-110.

25. Henjered, A., M. Hellsing, H.O. Andren, and H. Norden, "Quantitative microanalysis of carbide/carbide interfaces in WC-Co base cemented carbides", *Materials Science and Technology*, v. 2, 1986: pp. 847-855.

26. Vicens, J., M. Benjdir, G. Nouet, A. Dubon, and J.Y. Laval, "Cobalt Intergranular segregation in WC-Co composites", *Journal of Materials Science*, v. 29, 1994: pp. 987-994.

27. Sale, F., "Thermochemistry and phase equilibria in the W-O, W-C and related W-Co containing ternary phases", *Journal of the Less Common Metals*, v. 100, 1984: pp. 277-297.

28. Sara, R.V., "Phase equilibria in the system tungsten - carbon", *Journal of the American Ceramics Society*, v. 48, n. 5, 1965: pp. 251-257.

29. Shin, Y., "Effects of microstructure on hardness and Palmqvist toughness of WC-Co alloys", *Materials Science and Engineering*, v. A105/106, 1988: pp. 377-382.

30. Lee, H.C., and J. Gurland, "Hardness and deformation of cemented carbide", *Journal of Materials Science and Engineering*, v. 33, 1978: pp. 125-133.

31. Wayne, S.F., and S. Sampath, "Structure/ Property relationships in sintered and thermally sprayed WC-Co", *Journal of Thermal Spray Technology*, v. 1, n. 4, 1992: pp. 307-316.

32. Jia, K., *The Effect of Fine Microstructure on the Wear and Relevant Mechanical Properties of Cemented Carbide*, PhD Dissertation, Department of Material Science and Engineering, Stevens Institute of Technology, Hoboken, NJ, 1996: p.199.

33. Jia, K., and T.E. Fischer, "Abrasion resistance of nanostructured and conventional cemented carbides", *Wear*, v. 200, 1996: pp. 206-214.

34. Jia, K., and T.E. Fischer, "Sliding wear of conventional and nanostructured cemented carbides", *Wear*, v. 203-204, 1997: pp. 310-318.

35. Stewart, D.A., P.H. Shipway, and D.G. McCartney, "Abrasive wear behaviour of conventional and nanocomposite HVOF-sprayed WC-Co coatings", *Wear*, v. 225-229, 1999: pp. 789-798.

36. Subrahmanyam, J., M.P. Srivastava, and R. Sivakumar, "Characterization of plasma sprayed WC-Co coatings", *Materials Science and Engineering*, v. 84, 1986: pp. 209-214.

37. Li, C.J., A. Ohmori, and Y. Harada, "Formation of an amorphous phase in thermally sprayed WC-Co", *Journal of Thermal Spray Technology*, v. 5, n. 1, 1996: pp. 69-73.

38. Verdon, C., A. Karimi, and J.L. Martin, "A study of high velocity oxy-fuel thermally sprayed tungsten carbide based coatings. Part 1: Microstructures", *Materials Science and Engineering*, v. A246, 1998: pp. 11-24.

39. Yamasaki, T., P. Schloßmacher, K. Ehrlich, and Y. Ogino, "Formation of amorphous electrodeposited Ni-W alloys and their nanocrystalization", *Nanostructured Materials*, v. 10, n. 3, 1998: pp. 375-388.

40. Milman, Y.V., S. Luyckx, and I.T. Northrop, "Influence of temperature grain size and cobalt content of the hardness of WC-Co alloys", *International Journal of Refractory Metal and Hard Materials*, v. 17, 1999: pp. 39-44.

41. Milman, Y.V., S. Luyckx,I.T. Northrop, S. Chugunova, and V. Goncharuck, "Low and high temperature hardness of WC-6wt% Co alloys", *International Journal of Refractory and Hard Materials*, v. 15, 1997: pp. 97-101.

42. Sturgeon, A.J., "High velocity oxy-fuel spraying promises better coatings", *Metals and Materials*, v. 8, n. 10, 1992: pp. 547-548.

43. Parker, D.W., and G.L. Kutner, "HVOF thermal spray upgrades power turbines", *Welding Design & Fabrication*, v. 67, n. 12, 1994: pp. 20-24.

44. Sobolev, V.V., "Formation of splat morphology during thermal spraying", *Materials Letters*, v. 36, 1998: pp. 123-127.

45. Sobolev, V.V., and J.M. Guilemany, "Effect of substrate deformation on the droplet flattening in thermal spraying", *Materials Letters*, v. 35, 1998: pp. 324-328.

46. Sobolev, V.V., and J.M. Guilemany, "Influence of wetting and surface effects on splat formation during thermal spraying", *Materials Letters*, v. 37, 1998: pp. 132-137.

47. Safai, S., and H. Herman, "Microstructural investigation of plasma sprayed Al-coatings", *Thin Solid Films*, v. 45, 1977: pp. 295-307.

48. Sampath, S., and H. Herman, "Rapid solidification and microstructure devolpment during plasma spray deposition", *Journal of Thermal Spray Technology*, v. 5, n. 4, 1996: pp. 445-456.

49. Heimann, R.B., *Plasma Spray Coating: Principles and Applications*, pub. by Weinheim, New York, 1996.

50. Leigh, S.H., and C.C. Berndt, "Quantitative evaluation of void distributions within a plasma sprayed ceramic", *Journal of the American Ceramic Society*, v. 82, n. 1, 1999: pp. 17-21.

51. Nakamura, T., G. Qian, and C.C. Berndt, "Effects of pores on mechanical properties of plasma-sprayed ceramic coatings", *Journal of the American Ceramic Society*, v. 83, n. 3, 2000: pp. 578-584.

52. Fauchais, P., and A. Vardelle, "Thermal plasmas", *IEEE Transactions on Plasma Science*, v. 25, n. 6, 1997: pp. 1258-1280.

53. Karimi, A., C. Verdon, and G. Barbezat, "Microstructure and hydroabrasive wear behaviour of high velocity oxyfuel thermally sprayed WC-Co(Cr) coatings", *Surface and Coatings Technology*, v. 57, n. 6, 1993: pp. 81-89.

54. Khan, M.S.A., and T.W. Clyne, "Microstructure and abrasion resistance of plasma sprayed cermet coatings", *Proceedings of the 9th National Thermal Spray Conference*, ed. by C.C. Berndt, ASM International, Metals Park OH, 1996: pp. 113-122.

55. Hartfield-Wunsch, S.E., and S.C. Tung, "The effect of microstructure on the wear behavior of thermal spray coatings", *Proceedings of the 7th National Thermal Spray Conference,* ed. by C.C. Berndt, ASM International, Metals Park, OH, 1994: pp. 19-24.

56. Finke, J.R., W.D. Swank, and D.C. Haggard, "Comparison of the characteristics of HVOF and plasma thermal spray", *Proceedings of the 7th National Thermal Spray Conference,* ed. by C.C. Berndt, ASM International, Metals Park, OH, 1994: pp. 325-330.

57. Jarosinski, W.J., M.F. Gruninger, and C.H. Londry, "Characterization of tungsten carbide cobalt powders and HVOF coatings", *Proceedings of the 1993 National Thermal Spray Conference*, ed. by C.C. Berndt and T.F. Bernecki, ASM International, Metals Park OH, 1993: pp. 153-157.

58. Wang, Y., and P. Kettunen, "The optimization of spraying parameters for WC-Co coatings by plasma and detonation-gun spraying", *Proceedings of the 13th International Thermal Spray Conference*, ed. by C.C. Berndt, ASM International, Metals Park, OH, 1992: pp. 575-580.

59. Roebuck, B., and A. Almond, "Measurement of particle size of ultrafine (submicrometre) WC powders". *Powder Metallurgy*, v. 29, n. 2, 1986: pp. 119-124.

60. Roebuck, B., "Dependence of oxidation rate of WC powder on the particle Size", *Journal of Materials Science*, v. 21, n. 6, 1986: pp. 2033-2042.

61. Roebuck, B., M.G. Gee, and E.G. Bennett, "Modeling hardness variations in WC/Co hard metals with a wide grain size distribution", *European Conference on Advances in Hard Materials Production Proceeding, Turin, Italy*, European Powder Metallurgy Association, 1999: pp. 221-227.

62. Roebuck, B., "Measuring WC grain size distribution", *Metal Powder Report*, v. 54, n. 4, 1999: pp. 20-24.

63. Nolan, D., P. Mercer, and M. Samandi, "Microstructural stability of thermal sprayed WC-Co composite coatings in oxidizing atmospheres at 450C", *Eleventh International Conference on Surface Modification Technologies, Paris, France*, ed. by T.S. Sudarshan, 1997: pp. 212-222.

64. Warren, A., A. Nylund, and I. Olefjord, "Oxidation of tungsten and tungsten carbide in dry and humid atmospheres", *International Journal of Refractory Metals and Hard Materials*, v. 14, 1996: pp. 345-353.

65. Nerz, J., B. Kushner, and A. Rotolico, "Microstructural evaluation of tungsten carbide-cobalt coatings", *Journal of Thermal Spray Technology*, v. 1, 1992: pp. 147-152.

66. Schwetzke, R., and H. Kreye, "Microstructure and properties of tungsten carbide coatings sprayed with various HVOF spray systems", *Proceedings of the 15th International Thermal Spray Conference, Nice, France*, 1998: pp. 187-192.

67. Lim, L.C., S.C. Lim, M.O. Lai, S.F. Chong, and S. Alli, "Annealing of plasma sprayed WC-Co coatings", *Surface and Coating Technology*, v. 79, 1996: pp. 151-161.

68. Guo, D.Z., F.L. Li, J.Y. Wang, and J.S. Sun, "Effects of post-coating processing on structure and erosive wear characteristics of flame and plasma spray coatings", *Surface and Coatings Technology*, v. 73, 1995: pp. 73-78.

69. Stewart, D., *Studies on the Abrasive Wear Behaviour of HVOF WC-Co Coatings*, PhD Dissertation, University of Nottingham: Nottingham, UK. 1998: p. 316.

70. Zum Gahr, K.H., "Relationship between abrasive wear rate and the microstructure of metals", *Proceedings of the Conference on Wear of Materials*, ed. by K. Ludema, ASME, 1979: pp. 266-274.

71. Zum Gahr, K.H., *Microstructure and Wear of Materials*, Elsevier, New York, 1987.

72. Misra, A. and I. Finnie, "Correlations between two-body and three-body abrasion and erosion in metals", *Wear*, v. 68, 1981: pp. 33-39.

73. Larsen-Basse, J. and E.T. Koyanagi, "Abrasion of WC-Co alloys by quartz", *Journal of Lubrication Technology*, v. 101, 1979: pp. 208-211.

74. Khruschov, M.M. and M.A. Babichev, "Resistance to abrasive wear of structurally inhomogeneous materials", *Friction and Wear in Machinery*, v. 12, 1958: pp. 5-23.

75. Khruschov, M.M., "Principles of abrasive wear", *Wear*, v. 28, 1974: pp. 69-88.

76. Garrison, W.M., "Khruschov's rule and the abrasive wear resistance of multiphase solids", *Wear*, v. 82, 1982: pp. 213-220.

77. Axen, N., and S. Jacobson, "A model for the abrasive wear resistance of multiphase materials", *Wear*, v. 174, 1994: pp. 187-199.

78. Axen, N., and B. Lundberg, "Abrasive wear in intermediate mode multiphase materials", *Tribology International*, v. 28, n. 8, 1995: pp. 523-529.

79. Axen, N., and I.M. Hutchings, "Analysis of abrasive wear and friction behaviour of composites", *Materials Science and Technology*, v. 12, 1996: pp. 757-765.

80. *Binary Alloy Phase Diagrams. Volume 1*, ed. by T.B. Massalski, ASM International, Metals Park, OH, 1990.

81. Villars, P., A. Prince, and H. Okamoto, *Handbook of Ternary Alloy Phase Diagrams. Volume 5*, ASM international, Metals Park, OH, 1995: pp. 6590-6602.

82. Misra, A., and I. Finnie, "A classification of three-body abrasive wear and design of a new tester", *Wear*, v. 60, 1980: pp. 111-121.

83. Grigoroudis, K., and D.J. Stephenson, "Modeling low stress abrasive wear", *Wear*, v. 213, 1997: pp. 103-111.

84. Roebuck, B., E.A. Almond, and J.L.F. Kellie, "Characterization of the particle size of cubic transition metal carbides by measurement of the rate of oxidation", *Horizons of Powder Metallurgy: Part I*, Verlag Schmid, 1986: pp. 123-126.

85. Yamamoto, T., M. Olsson, and S. Hogmark, "Three-body abrasive wear of abrasive ceramic materials", *Wear*, v. 174, 1994: pp. 21-31.

86. Harvey, M., A. Sturgeon, F. Blunt, and S. Dunkerton , "Investigation into the relationship between fuel gas selection, wear performance and microstructure of HVOF sprayed WC-Co coatings", *International Thermal Spray Conference.* 1995: pp. 471-476.

87. Qiao, Y., *Mechanical and Tribological Properties of Thermal Sprayed WC-Co Coatings*, PhD Dissertation, Department of Materials Science and Engineering, Stevens Institute of Technology, Hoboken, NJ, 2001: p. 203.

88. Bhaumik, S.K., R. Balasubramaniam, G.S. Upadhyaya, and M.L. Vaidya, "Oxidation behaviour of hard and binder phase modified WC-10 Co cemented carbides", *Journal of Materials Science Letters*, v. 11, n. 21,1992: pp. 1457-1459.

89. Lofaj, F., and Y.S. Kaganovskii, "Kinetics of WC-Co oxidation accompanied by swelling", *Journal of Materials Science*, v. 30, 1995: pp. 1811-1817.

90. Kubaschewski, O., E.L. Evans, and C.B. Alcock, *Metallurgical Thermochemistry*, Pergamon Press, London, 1967.

91. *The Oxide Handbook*, ed. by G.V. Samsonov, Plenum Press, New York, 1973.

92. Jia, K., and T.E. Fisher, "Microstructure, mechanical properties and wear resistance of WC/Co nanocomposites", *Nanophase and Nanocomposite Materials II, 1996, (Materials Research Society Symposium*, v. 457), 1997: pp. 303-308.

93. Shipway, P.H., and I.M. Hutchings, "The role of particle properties in the erosion of brittle materials", *Wear*, v. 193, 1996: pp. 105-113.

94. Stewart, D.A., P.H. Shipway, and D.G. McCartney, "Influence of heat treatment on the abrasive wear behaviour of HVOF sprayed WC-Co coatings", *Surface and Coatings Technology*, v. 105, n. 1-2, 1998: pp. 13-24.

95. Avery, H.S, "The nature of abrasive wear", *1975 SAE Off-Highway Vehicle Meeting*, Society of Automotive Engineers, 1975: pp. 1-15.

96. Avery, H.S., "Classification and precision of abrasion tests", *Proceedings of the International Conference on Wear of Materials*, ed. by K. Ludema, ASME, 1977: pp. 148-157.

97. Avery, H.S., "Analysis of the rubber wheel abrasion test", *Proceedings of the International Conference on Wear of Materials*, ed. by K. Ludema, ASME, 1981: pp. 367-378.

98. Blickensderfer, R., B. Madesen, and J.H. Tylczak, "Comparison of several types of wear tests", *Proceedings of the International Conference on Wear of Materials*, ed. by K. Ludema, ASME, 1985: pp. 313-323.

99. Misra, A. and I. Finnie, "On the size effect in abrasive and erosive wear", *Wear*, v. 65, 1981: pp. 359-373.

Biographical Sketch

Graham Alfred Tewksbury

EDUCATION

Ph.D. Materials Science and Engineering
OGI School of Science & Engineering
Oregon Health & Science University, Portland, OR

B.A. Chemistry
Lawrence University, Appleton, WI

PRESENTATIONS

"Effect of Carbide Size on High Energy Plasma Sprayed Tungsten Carbide Cobalt," Thermec 2000 Conference, Las Vegas, 2000.

"High energy plasma spraying of Conventional and Nanoscale WC(Co) powder," United Engineering Foundations Conference, Quebec City, 1999.

"Evaluation of Retained apparent shear strength properties in adhesives based on epoxy and cyanate ester chemistries," SAMPE Anaheim CA,1997.